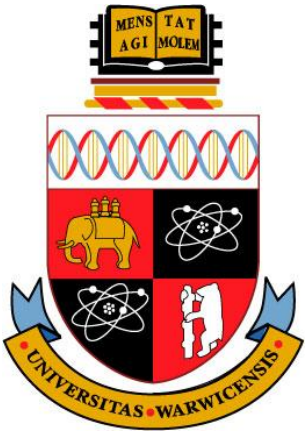

The potential for using combined electrical impedance and ultrasound measurements for the non-invasive determination of temperature in deep body tumours during mild hyperthermia

By

Md. Naimul Islam

Thesis

Submitted to the University of Warwick
for the degree of

Doctor of Philosophy

Department of Physics

May 2012

THE UNIVERSITY OF WARWICK

Contents

List of Tables

List of Figures

Acknowledgements

First and foremost I wish to express my deepest gratitude from the bottom of my heart to my supervisor Prof. Adrian J. Wilson, who has actively supported me throughout this thesis with his patience, knowledge and expertise in experimental works. This research work would not have been completed or written without his invaluable assistance, support and guidance. I simply could not wish for a better or friendly supervisor.

In my daily work, I have been blessed with friendly, cheerful and helpful group members. Thanks to Adam H. Aitkenhead and Kay Guest for helping me at the beginning of this research. Special thanks to Sakil Zuberi and Tung Fai Yu (Nixon) for sharing ideas and invaluable assistance for the last 3 years. I feel privileged to have friends like Sakil and Nixon and it has been really a wonderful and entertaining moment for me to have your company.

I would like to convey my thanks to the Commonwealth Scholarship Commission for providing me the financial support to continue this work. Thanks to the Department of Physics, University of Warwick for offering me the postgraduate research position and providing me the support and equipment that I have needed to produce and complete my thesis.

I also wish to express my love and gratitude to my beloved wife and my parents for their understanding, patience and endless love, through the duration of my PhD study. Special thanks to my son, Shifwat for keeping me fresh by giving so much entertainment specifically, after returning home from the office.

Declarations

I hereby declare that the thesis "The potential for using combined electrical impedance and ultrasound measurements for the non-invasive determination of temperature in deep body tumours during mild hyperthermia" is my own independent research work except where specifically referenced in the text and has not been previously submitted for any other degree. The research work for this thesis was carried out in the department of Physics at the University of Warwick from October 2008 to March 2012.

Some contents (results of chapter 2) from this thesis have been published in the following paper:

Islam, N., Rabbani, K. S. and Wilson, A. J. The sensitivity of focused electrical impedance measurements, ***Physiological Measurements*** 31(8) S97-S109.

In addition, further materials (particularly the results of chapter 4 and 5) have been submitted for publication in the Journal of ***Physiological Measurements*** and corrections are in progress based on the referees' comments.

Materials of this thesis have also been presented by the author at the following conferences:

Islam, N., Rabbani, K. S., and Wilson, A. J. Sensitivity of Focused Electrical Impedance Measurements. 10th International Conference on Biomedical Applications of Electrical Impedance Tomography (EIT 2009) 16th-19th June 2009, University of Manchester, UK.

Islam, N. and Wilson, A. J. Preliminary results on using electrical impedance to determine tissue composition in support of non-invasive temperature measurement. 12th International Conference on Electrical Impedance Tomography (EIT 2011) 4th-6th May 2011, University of Bath, UK.

Signature: ……

Date: ……..

Abstract

The effectiveness of mild hyperthermia in improving the outcome of radiotherapy and chemotherapy treatment is well established for surface tumours (e.g. an average improvement of 20% in the 5 years survival rate using mild hyperthermia in conjunction with radiotherapy). However, to apply this technique to deep body solid tumours clinically, a non-invasive thermometry method is needed. Several approaches have been proposed for non-invasive thermometry in the past but none were capable of providing 3D temperature distributions in-vivo with the required accuracy. In this thesis, the potential for determining the temperature in a deep body solid tumour during mild hyperthermia by combining ultrasound propagation velocity and electrical impedance measurement techniques has been investigated.

Simultaneous ultrasound propagation velocity and electrical impedance measurements were made in-vitro on liver, fat and layered fat-liver samples as the temperature was increased to mild hyperthermia levels (45°C max.). From the ultrasound measurements a linear correlation was found between the percentage of fat in the sample and the change in ultrasound propagation velocity with temperature ($-0.12 ms^{-1}°C^{-1}\%^{-1}$, $r^2 = 0.93$). Analysis of the data from the multi-frequency electrical impedance measurements showed that the magnitude of the electrical impedance measured at 256kHz normalised to the magnitude of the electrical impedance measured at 8kHz gave a linear correlation with the percentage of fat in the sample ($0.003\ \%^{-1}$, $r^2 = 0.72$) but no statistically significant correlation between the fat content and the temperature coefficient at 256kHz ($r^2 = 0.007$, $p > 0.05$). These results support an approach of using high to low frequency impedance ratios to determine the percentage of fat in the tissue and then this together with an ultrasound propagation velocity measure to detect the change in the temperature of the tissue. Application of this technique is limited by the variation in the change in ultrasound propagation velocity with temperature between tissue samples found in this study but the origins of this are unclear. In addition, further improvements in the spatial sensitivity of the tetrapolar impedance measurements are necessary to ensure an adequate spatial determination of fat content.

Abbreviations

ADC	Apparent Diffusion Coefficient
APC	Antigen Presenting Cell
AR PSD	Auto Regression Power Spectral Density
ATP	Adenosine Triphosphate
CaP	Prostate Cancer
CT	Computed Tomography
DAC	Digital to Analogue Convertor
DC	Dendritic Cell
DNA	Deoxyribonucleic Acid
EIT	Electrical Impedance Tomography
EPROM	Erasable Programmable Read Only Memory
FET	Field Effect Transistor
FFT	Fast Fourier Transform
FIM	Focused Impedance Measurement
FUS	Focused Ultrasound Surgery
FWHM	Full Width Half Maximum
HIFU	High Intensity Focused Ultrasound
HILP	Hyperthermic Isolated Limb Perfusion
HSP	Heat Shock Protein
MRI	Magnetic Resonance Imaging
MOSFET	Metal Oxide Semiconductor Field Effect Transistor
NI	National Instrument
NK	Natural Killer
PRFS	Proton Resonance Frequency Shift
PZT	Lead Zirconate Titanate
SNR	Signal-to-noise ratio
TOF	Time of Flight
TPIM	Tetrapolar Impedance Measurement
TTL	Transistor Transistor Logic
USB	Universal Serial Bus
VCCS	Voltage Controlled Current Source

1 Introduction

1.1 Heating the patient: a promising approach in cancer treatments?

The use of high temperatures to treat a disease has existed for many centuries. In the splendour of the Roman Empire, thermal baths were common, often with complete facilities for the treatment of diseases involving the use of humid and dry heat applied locally or to the whole body (Habash *et al.*, 2006). The oldest one reported (Nielsen *et al.*, 2001; Habash *et al.*, 2006; van der Zee, 2002; Strohbehn and Douple, 1984) probably dated around 3000 B.C. which was found in the Egyptian Edwin Smith surgical papyrus, where a bath in hot desert sand was prescribed for the ill. Parmenides (520–450 B.C.), a Greek physician and philosopher (Wolf, 2008) said –

''Give me a chance to create a fever and I will cure any disease'' back around 500 B.C.

Many hyperthermia researchers like to mention Hippocrates (460–370 BC); in particular, the method he described in one of his aphorisms – the use of hot-irons in cauterisation (van der Zee, 2002). Over the centuries various applications of high temperature were found, for example fever was artificially induced with the help of pyrogenic substances to fight infectious diseases (Nielsen *et al.*, 2001; van der Zee, 2002; Moss, 1996; Strohbehn and Douple, 1984; Coley, 1991). In the Middle Ages, growths on the skin were burned away with a red-hot iron and fever was considered to be a purging agent that purifies and detoxifies the body (Wolf, 2008).

In the last decades of the nineteenth century, hyperthermia underwent a renaissance triggered by observations that some patients with a high fever due to erysipelas demonstrated spontaneous regression of tumours (Strohbehn and Douple, 1984; Coley, 1991). This inspired the American surgeon William B. Coley (1862-1936) to develop his 'Mixed Bacterial Toxin' for the treatment of cancer (Straube and Arthur, 1994b; Ralph W. Moss, 1996). He also conjectured that the increase in body temperature not only mobilized the body's own immune systems to fight off the infection but also destroyed the tumour at the same time.

At present the term 'hyperthermia' literally refers to the treatment of mainly malignant diseases by administering heat in various ways. In general it is categorised into the following three different modalities based on the temperature level and time duration:

Diathermia: Heating up to 41°C, applied in physiotherapy for treatment of rheumatic diseases.

Mild Hyperthermia: The temperature of a part of the body or the whole body is raised in the range 40–43˚C. It is usually applied as an adjunct to already established treatment modalities normally radiotherapy and / or chemotherapy. Definitions of temperature range for mild hyperthermia vary in the literature, but the key requirement is that the temperature is well below the necrotic threshold (also defined in section 1.1.5.2). This type of hyperthermia has applications in oncology for cancer treatment and there is a renewed interest in it due to its effectiveness in improving cancer-treatment outcomes.

High Temperature Hyperthermia: Very high temperatures (>50°C) is used to destroy cells within a localized section of tumour. This type of hyperthermia is also known as **High Intensity Focused Ultrasound (HIFU) or Focused Ultrasound Surgery (FUS).** The high temperature is generated for a short period of time usually within the focal region of a megahertz ultrasound field, with surrounding areas remaining largely unheated. HIFU is used in oncology for the treatment of prostate, liver, kidney, and breast cancer. It offers an excellent management for the prostate cancer (CaP) (ter Haar, 2007; Hacker *et al.*, 2005). HIFU is also used to seal punctured blood vessels and halt blood flow in vessels (Hynynen, 1996; Rowland, 1997).

1.1.1 Basis for hyperthermia in cancer treatments

The microenvironment of malignant tumours is characterised by a reduction of blood flow and blood vessel density which in turn results in low pH (acidosis), low pO2 (hypoxia) and energy deprivation, which is not found in benign tissues (Hildebrandt *et al.*, 2002). Low metabolic rate and inhomogeneity of blood perfusion in the cells of a malignant tumour plays a paramount role in determining the energy status and in making of a hostile metabolic microenvironment (Vaupel and Keller, 1995; Hildebrandt *et al.*, 2002; van der Zee, 2002). These micro-environmental changes in malignant tissues especially, the low pH, energy depletion, and change of nutritional status, make cells more sensitive to hyperthermia which leads in turn to disturbances in the metabolic processes of dividing and maintaining cells, including the failure of the repair systems of the cells (Vaupel and Keller, 1995). These biological rationales for hyperthermia in cancer therapy are discussed in the following sections.

1.1.1.1 Tumour vasculature and differential heating

The tumour growth depends upon the development of neovasculature which differs from normal vasculature in a number of ways. Whereas normal vasculature is arranged in a hierarchy of evenly spaced, well differentiated arteries, arterioles, capillaries, venules and veins, the tumour vasculature is unevenly distributed and chaotic (Nagy *et al.*, 2009; Peterson, 1978).

The tumour neovasculature develops from the pre-existing normal host vessels and morphologically resembles large, elongated, and often dilated tortuous vessels. The host vessels per unit tumour mass do not increase in number, thus leading to a reduction of available exchange area for oxygen, nutrients, hormones, growth factors, and waste products (e.g. hydrogen ions, lactic acid, necrosis products) (Vaupel *et al.*, 1989). In addition during tumour growth, some of the pre-existing host vessels incorporated in the tumour mass disintegrate, are obstructed, or are compressed. Due to these vascular irregularities, substantial regional variations in blood flow occur within a tumour (Peterson, 1978; Song, 1984). The blood flows in a tumour varies with tumour size; a substantial decrease in blood flow per gram of tissue has been observed with increasing tumour volume (Peterson, 1978).

Normal tissue perfusions rates vary substantially depending on organ or tissue type. The blood flow rates in normal tissues (except the breast or liver tumours (Beaney *et al.*, 1984)) are reported to be 2.5 to 30 times greater than the tumour flow rates (Shibata and MacClean, 1966).

Blood flow plays an important role in heat dissipation, especially in large well-perfused tissue masses, whereas in small tissue masses, heat loss via thermal diffusion becomes prominent at very low blood flow rates. The blood flow in muscle (and skin) increases markedly with temperature. Research in animals indicates an increase of muscle and skin blood flow up to 5- or 10-fold or more at temperatures of 42–44°C, but little change is seen in tumour blood flow (Song *et al.*, 1980). Increases in blood flow of this magnitude in human skin, muscle, and fatty soft tissue allow the differential heating of some tumours or tumour regions when heat is deposited equally in tumour and normal tissue (Vaupel and Kelleher, 1990). If the blood flow of a particular normal tissue is found to be relatively high and constant among patients, the differential heating of some lesions may be anticipated. However, variations in blood flow within tumours and at the normal/tumour tissue margin preclude uniform heating (Dudar and Jain, 1984).

1.1.1.2 pH and thermal sensitivity

The second major rationale for hyperthermia in cancer is based on the low pH of tumours compared to normal tissues. Low pH may occur secondary to an elevated rate of glycolysis which is commonly exhibited by tumour tissues under both aerobic and anaerobic conditions (Aisenberg, 1961). The average pH in tumours is lower than the pH in normal tissue by approximately 0.3 to 0.4 pH units (van den Berg *et al.*, 1982). Reduction in the pH of the extra-cellular medium below 7.0 results in a marked reduction in the fraction of cells surviving 42°C heat treatment. In general, the magnitude of the pH-sensitizing effect is most pronounced in the 41˚C–43˚C temperature range and decreases at higher temperature (Gerweck, 1977).

1.1.1.3 Energy status and thermal sensitivity

Under condition of extreme nutrient deprivation, cell death occurs rapidly at 37°C (Gerweck *et al.*, 1984). Nutrient deprivation probably give rise to the necrotic foci which are observed in tumours as the radial distance from functioning capillaries increases (Thomlinson and Gray, 1955). Between the nutrient-rich capillaries and the necrotic zone, viable cells reside within a gradient of decreasing oxygen and glucose concentration. Decreasing oxygen and glucose concentration prolongs the cell regeneration time and causes a redistribution of cells in their cycle (Koch *et al.*, 1973). As a consequence, the toxicity of cell-cycle specific drugs or other agents may substantially be modified. In addition, local tissue hypoxia may severely limit the toxicity of drugs, the effect of which is mediated by activated oxygen species (free radicals). The presence or absence of either glucose or oxygen alone has little effect on thermal sensitivity (Gerweck *et al.*, 1984). However, when the supply of both nutrients is sufficiently reduced to bring about a reduction in intra-cellular ATP levels, thermal sensitivity is markedly enhanced (Gerweck, 1985).

1.1.2 Thermo-radiotherapy

One of the most important findings from in vitro studies on heat in tissue was that hyperthermia and radiation act in a combined way (Hildebrandt *et al.*, 2002). This combination induces an increase in cell killing even at lower temperatures, which is not the case when hyperthermia is administered alone. This so-called thermal ‘radiosensidization’ results in a reduction of the radiation dose (Hildebrandt *et al.*, 2002). There are several mechanism which are responsible for the supra additive effect of the combination of radiotherapy and hyperthermia. The additive effect comes from the sensitivity of cells in the hypoxic, low pH areas, cells with impaired nutrient supply, and the cells in S-phase

(DNA synthesis) (Raaphorst, 1990). It appears most pronounced in S-phase cells that are usually resistant to radiation alone (Raaphorst, 1990). Mild hyperthermia temperatures increase blood circulation in the tumours due to the body's response to the stimulus of heat. This increased blood flow result in an improvement of tissue oxygenation, which then results in a temporally increased radio-sensitivity (Song *et al.*, 1997). Radiotherapy destroys tumour cells substantially through the formation of hydrogen and oxygen free radicals that attack tumour cell DNA. Oxygen-starved cells are three times more resistant to ionizing radiation than normal cells. It has been demonstrated that low oxygen levels (hypoxia) in human tumours is directly linked to the failure in achieving local tumour control through ionizing radiation, and the degree of oxygen deficiency in cancerous tumours is the key predictor of the efficacy of radiotherapy.

While oxygen free radicals attack cancer cell DNA, hyperthermia acts further to create an accumulation of proteins in the cell nucleus that bind to the nuclear matrix followed by a disruption of the repair of radiation-induced DNA damage (Kampinga and Dikomey, 2001). Hyperthermia increases the effectiveness of the ionizing radiation during the growth cycle of cancer cells. During the cell division (S phase) the cancer cells are aggressively resistant to the effects of ionising radiation, but they are susceptible to the destructive effects of hyperthermia.

The 'thermal enhancement ratio' (the ratio of T(0) at 37°C to the T(0) at an elevated temperature, where T(0) is the time to reduce survival from 1 to 0.37, since the cell survival is exponentially related to the treatment time at all temperatures) for radiation-induced cell killing increases with higher temperatures and longer exposures times and decreases with longer time-intervals between the two modalities. In vivo studies have shown that the effect of radiotherapy can be enhanced by a factor of between 1.2 and 5 (Marino and Cividalli, 1992) making hyperthermia probably the most potent radio-sensitizer known to date.

1.1.3 Thermo-chemotherapy

For chemotherapy drugs dependent on blood transport for delivery, hyperthermia enhances blood flow in tumour tissues which eventually increases the uptake of chemotherapy drugs in the tumour membranes (van der Zee, 2002). Hyperthermia also induces disassembly of the cytoskeleton, which enlarges the tumour pores allowing easier drug entry (Hildebrandt and Wust, 2007). So, once delivered, mild hyperthermia temperatures can act as drug activator, accelerating chemical reactions through heat and

drawing essential oxygen molecules to tumour tissue for chemical reactions with the drug. Hyperthermia interacts with a wide range of chemotherapy drugs including doxorubicin, mitomycin C, mitoxantrone, bleomycin, cisplatin, nitrosoureas and cyclophosphamide (van der Zee, 2002; Skibba *et al.*, 1982; Gerad *et al.*, 1984). Hyperthermia has demonstrated the ability to enhance drug toxicity in cells which are otherwise resistant to many drugs used in chemotherapy.

Hyperthermia also acts as a valuable companion therapy when chemotherapy drugs encapsulated as 'liposomes' are injected. Research has shown that when a liposome-encapsulated drug is used in combination with hyperthermia, drug penetration can dramatically increase (Hildebrandt *et al.*, 2002). Research is also being conducted on heat-activated liposomes that use hyperthermia temperatures as the release mechanism for the encapsulated drug when they reach the tumour (Hildebrandt *et al.*, 2002) reducing the toxic effect of the drug on normal tissues.

Hyperthermia is also employed synergistically with chemotherapy in strategies to treat bulky tumours. The cores and other regions of these tumours are often difficult to penetrate with drugs because of the low blood flow in up to one third of the mass of the tumour. Chemotherapy has limited efficacy against blood starved cells. Hyperthermia is able to destroy the cancer cells in blood-deficient regions of the tumour while the drug permeates tissues with higher blood flow nearer the surface, providing improved disease control (van der Zee, 2002).

The 'thermal enhancement ratio' depends on temperature and exposure times. The effect of the drugs can be enhanced by a factor of between 1.2 to 10 and an extremely high thermal enhancement ratio of 23 was even observed for in vivo application of certain types of drugs (Skibba *et al.*, 1982). However, the therapeutic gain of the clinical combination of hyperthermia and chemotherapy will depend on the temperature rise in the organs for which the used drug is toxic. Eventually, the successful effect of regional/local hyperthermia in chemotherapy will depend on the heating methods.

1.1.4 Thermo-immunotherapy

Nowadays, hyperthermia is also used as an adjunct to cancer immunotherapy (Skitzki *et al.*, 2009). It has been shown that improved anti-tumour immune response can be achieved with the addition of mild hyperthermia. The molecular mechanism responsible for the improved immune reactivity observed with the addition of hyperthermia include the

generation of Heat Shock Proteins (HSPs), the activation of antigen presenting cells and changes in lymphocyte trafficking (Calderwood *et al.*, 2005).

1.1.4.1 Hyperthermia induced HSPs as modulators of the immune system

HSPs are a family of stress (temperature) induced proteins with several critical cellular functions. HSPs work as central mediators of a variety of cellular functions under physiological conditions, as they are key regulators of cellular protein activity, turnover and antibody trafficking (Calderwood and Ciocca, 2008).

HSPs are present in many of tumour types but their activities are complicated and diverse and may function to confer several survival benefits of cancer cells (Calderwood and Ciocca, 2008). HSPs have also been implicated in mediating resistance to potentially cytotoxic hyperthermia in a process termed thermotolerance (Li and Werb, 1982). Tumour cell depends upon HSPs for several critical functions and therefore controlling HSP expression is an attractive and potential therapeutic approach (Tamura *et al.*, 1993).

The immune system takes the advantages of the ability of HSPs to act as 'danger signals', thus allowing the generation of an amplified immune response (Todryk *et al.*, 2000). HSPs released from stressed or dying cells activate dendritic cells (DCs), transforming them into mature antigen-presenting cells (APC). Mild-hyperthermia may take advantage of tumour cell HSPs by inducing their release from tumour cells and augmenting DC priming then against tumour antigens (Bleifuss *et al.*, 2008; Schueller *et al.*, 2003). It has also been reported that hyperthermia alone can enhance antigen display by tumour cells, thus rendering them even more susceptible to programmed immune clearance (Takahashi *et al.*, 1995).

HSP-peptide complexes isolated from cancer cells, as well as HSPs complexes bound to tumour antigens, clearly have the potential of being cancer vaccines. An autologous, tumour-derived HSP-peptide vaccine can be generated by applying mild-hyperthermia or thermal ablation to tumours sites without the need for ex vivo manipulations, but such techniques has yet to be systematically evaluated (Skitzki *et al.*, 2009).

1.1.4.2 Improvement of dendritic cell (DC) and natural killer (NK) cell function by hyperthermia

The release of HSPs from tumour cells can activate dendritic cell (DC) which can serve as a potent activating signal for quiescent APCs (Somersan *et al.*, 2001). Moreover HSPs are able to mediate the cross-priming of tumours antigens (Bendz *et al.*, 2007). In tumour cells

exposed to temperatures in the mild hyperthermia range (42°C for 4h) prior to lysing, DC activation and cross-priming were significantly enhanced with the application of heat (Shi *et al.*, 2006). Enhanced cross-priming was directly attributed to increased expression of HSPs in hyperthermia-treated cells (Shi *et al.*, 2006).

Tumour-primed DCs are clinically used as a cancer vaccines and hyperthermia has been used in combination with intra-tumoural injection of DCs to treat melanomas (Tanaka *et al.*, 2005). Due to the ability of HSPs to activate DCs directly by chaperoning tumour antigens upon their release (Bendz *et al.*, 2007), it is possible that both local and regional immune stimulation can be achieved with hyperthermia. Tumours treated with combination of hyperthermia and intra-tumoural DC injections exhibited significant growth inhibition compared with controls.

Natural Killer (NK) cells which are considered as an important mediator of innate anti-tumour immunity have been reported to be responsive to hyperthermia (Dayanc *et al.*, 2008; Burd *et al.*, 1998). In clinical trials, exposure to mild hyperthermia resulted in improved endogenous NK cell cytotoxicity to several cancer types (Zanker and Lange, 1982). The distribution of NK cells throughout the body could also be altered by whole body hyperthermia, suggesting mobilization and possibility for improved immune surveillance (Blazickova *et al.*, 2000).

1.1.4.3 Enhancement of immunotherapies by hyperthermia

Hyperthermia can tightly regulate the leukocyte trafficking at multiple levels (Chen *et al.*, 2009). Hyperthermia has been demonstrated to regulate adhesion molecule expression on selected vascular endothelial sites (Chen *et al.*, 2009). Hyperthermia can also augment the lymphocyte entry across the endothelial layer (Chen *et al.*, 2006; Evans *et al.*, 2001). The combined effects of hyperthermia on lymphoid tissue endothelium and lymphocytes can promote immune surveillance and increase the probability of naive lymphocytes leaving the circulation and encountering their cognate antigen - an effect displayed by the level of DCs in lymphoid organs (Skitzki *et al.*, 2009; Ostberg and Repasky, 2000; Atanackovic *et al.*, 2006).

Hyperthermia acts at multiple levels to improve lymphocyte and endothelial interactions via complex complementary mechanisms involving a variety of trafficking molecules. Increased leukocyte migration in inflammatory models appears to be elicited by exposure to hyperthermia. The synergy between local HSP peptide release and chemokine

production may serve to amplify immune responses at tumour sites exposed to hyperthermia (Takeda *et al.*, 2008).

The circulation of lymphocytes through lymphoid tissues may be mandatory for the generation of cancer immunity. So, hyperthermia has been shown to improve immune surveillance by T-cells (Chen *et al.*, 2006) and to increase DC trafficking to lymph nodes (Ostberg *et al.*, 2001).

Hyperthermia may also act as a useful adjunct to adoptive transfer regimens by increasing the entry of adoptively transferred lymphocytes into lymphoid compartments (Skitzki *et al.*, 2009).

1.1.5 Characteristic of hyperthermia cell death

1.1.5.1 Different modes of cell death

Chemotherapy drugs and radiation have antineoplastic properties- an ability to induce (directly or in directly) either apoptotic (programmed) of necrotic cell death.

Necrosis is marked by a passive pathological cell damage which is sometimes followed by an inflammatory response originating from the surrounding tissue. Necrotic cell death begins with the disruption of membranes or organelles within the cell and finally the cell membrane disintegrating. The constituents of necrosed cells are not phagocytosed by the surrounding cells; instead they remain in place until removed by mononuclear phagocytes. An influx of these phagocytes may be stimulated by necrosis, since necrosis tends to provoke an immune response (Bold et al., 1997). In addition, necrosis generally occurs to individual cells scattered throughout a volume of tissue.

Apoptosis represents a genetically controlled active death. It tends to occur to individual cells scattered throughout a region of tissue. It may be activated by cell damage or physiologically, thereby contributing to maintaining tissue haemostasis as well as preventing severe cell damage that may lead to sustained viral infection or cancer. When a cell dies via apoptosis, the process begins with the cell nucleus breaking into discrete fragments which disperse throughout the cell. Within a few minutes of this occurring the cell splits into membrane enclosed bodies, and over the next few hours each of these is phagocytosed and ingested by nearby cells. In apoptosis, potential lethal stimuli like cytotoxic drugs, radiation, viruses, or starvation, activate a cascade of specific cysteine proteases, the so-called caspases, in different ways. Each of these signalling pathways can be boosted in the mitochondria. Regulation of programmed cell death is controlled through

the expression of a number of genes with activating (e.g. bax gene family) or inhibiting (e.g. bcl gene-family) properties.

1.1.5.2 Hyperthermia induced apoptosis and necrosis

Hyperthermia can induce both necrotic and programmed cell death depending on temperature level.

Hyperthermia produces an enhancement of apoptosis within tissue, when the temperature is increased to above approximately 42˚C for periods of 30 minutes or more (Raaphorst, 1990; Habash *et al.*, 2006). This type of hyperthermia is commonly referred to as mild hyperthermia as discussed in section 1.1. The value of this threshold temperature may vary depending on tissue type, but cytotoxicity changes sharply as the threshold is exceeded, with cytotoxic and non-cytotoxic temperatures differing by as little as 0.2˚C (ter Haar, 1999a). At temperatures slightly above the threshold, the enhancement of apoptosis is accompanied by other changes to the cell-cycle, with cellular reproduction slowing down or ceasing. The heat sensitivity of cells is dependent on their phase in the cell-cycle, being most sensitive during the S-phase (DNA synthesis) and M-phase (mitosis) (Hildebrandt *et al.*, 2002) with the result that sensitivity tends to be high for rapidly proliferating tissues (such as tumours) relative to normal tissue (Kerr *et al.*, 1994).

Hyperthermia produces an enhancement of necrosis when tissue is heated to temperatures > 46˚C for periods of 30 minutes or more (Kerr *et al.*, 1994). The required heating time decreases as the temperature is increased (Dewhirst *et al.*, 2003), and when temperatures of about 60˚C are applied, coagulative necrosis occurs within 1-2 seconds (ter Haar, 1999b). Hyperthermia of this type is used for tissue ablation and is commonly performed using high intensity focused ultrasound (HIFU) therapy and therefore is sometimes referred to as focused ultrasound surgery (FUS) as discussed in section 1.1.

The susceptibility of cultured cells to apoptosis has been demonstrated, in particular, in a number of experiments using cultured cancerous cell lines. Yonezawa and co-workers (Yonezawa *et al.*, 2002) explicitly reported that out of various soft tissues and osteosarcoma cell lines apoptosis could only be induced by heating up to 43˚C in a single cultured cell line of malignant fibrous histiocytoma. The findings from this work (Yonezawa *et al.*, 2002) indicated that at least some types of cells exhibit different susceptibility to apoptotic cell death induced by heat. Above a clearly identified temperature, but tissue specific, temperature is more likely to induce necrosis cell death instead.

In summary, both apoptosis and necrosis provide routes that may be utilised in the treatment of cancer for killing tissue within solid, localised tumours. It should be noted however, that these cell death pathways also mean that excessive heating of healthy tissue during hyperthermia treatments must be avoided, as otherwise normal cells will also be killed by the hyperthermia.

1.1.6 Hyperthermia and toxicity

Experimental studies have shown that most normal tissues are not directly damaged when the temperature over an hour treatment does not exceed 44°C (Fajardo, 1984). However during local hyperthermia it is not always possible to avoid higher temperatures due to the heterogeneity of the temperature distribution and the limits of thermometry (van der Zee, 2002).

During hyperthermia, the patients could feel some painful hot spots (van der Zee, 2002). Toxicity from superficial hyperthermia is usually skin burns (van der Zee *et al.*, 1999). If the temperature is too high in the subcutaneous fat or muscle, an increased pressure can be felt in the area (van der Zee, 2002). Some randomised studies have shown that when hyperthermia is used with radiotherapy, there is no increase in acute or late toxicity from the treatment (van der Zee *et al.*, 2000; Wust *et al.*, 1995; Lee *et al.*, 1995). However, the toxicity of chemotherapy is enhanced and it depends on the temperature in the drug-sensitive tissues. Toxicity from whole body hyperthermia depends not only on the temperature, but the patient's physical conditions during treatment (van der Zee, 2002). It is suggested that during any application of hyperthermia, it is always best to avoid pressure sites, since hypoxic normal tissues will be more sensitive to hyperthermia (van der Zee, 2002).

1.1.7 Clinical benefits of hyperthermia

Hyperthermia in combination with radiotherapy has been shown to be the most effective cancer treatment therapy available now for breast cancer, inflammatory breast cancer (IBC), prostate cancer, head and neck cancers, throat cancer, bladder cancer, skin, colon, thyroid and others (Bicher and Wolfstein, 2006).

Valdagni and Amichelli (Valdagni and Amichetti, 1994a) reported that hyperthermia added to ionizing radiation in patients with stage IV recurrent breast and head and neck tumours improved the complete response (tumour disappears or elimination of any evidence of cancer or no residual disease following the treatment) from 41% to 83%, local relapse-free

survival from 24% to 68% and overall survival at 5 years from 0% to 53%, as compared to radiotherapy.

Overgaard and co-workers (Overgaard *et al.*, 1996) reported that the addition of hyperthermia to radiotherapy increased the complete response rate of recurrent malignant lesions from 35% to 62%, and local relapse-free survival at five years from 28% to 46%, as compared to radiotherapy alone. Vernon and co-workers (Vernon *et al.*, 1996a) reported that combination of hyperthermia and radiotherapy increased the complete response to treatment from 41% to 59% and local relapse free survival from 30% to 50% in patients with superficial localized breast cancer (phase III). Lee and his co-workers (1996) reported their findings on carcinoma of the head and neck region, carcinoma of the breast and on malignant melanoma showing that interstitial hyperthermia in combination with radioactive seeds produced complete response to treatment in 89% of patients and partial response in 11% of patients, with a two-year actuarial local control rate of 74%.

Algan and co-workers (Algan *et al.*, 2000) reported a 5-year overall survival of 73%, with a median survival of 88 months in treating advanced or recurrent adenocarcinoma of the prostate by combining external beam radiotherapy with local mild hyperthermia.

van der Zee (van der Zee, 2002) reported a complete response rate for bladder cancer increased from 51% to 73%, a complete response rates for advanced cervical cancer increased from 57% to 83%, and the overall 3 year survival increased from 27% to 51% when mild hyperthermia used in combination with radiotherapy.

Similarly, an improvement in the 3-year survival rate was reported by Welz and co-workers (Welz *et al.*, 2005) when treating recurrent chest wall disease in breast cancer with mild hyperthermia and radiotherapy. The 3-year overall survival rate was 85% and disease free survival rate was 69%.

Recently, Bicher and Wolfstein (Bicher and Wolfstein, 2006) evaluated the effectiveness of hyperthermia combined with radiotherapy in patients suffering from early stage cancers (phase III or less) of the breast, head and neck and prostate; and found better results than those reported in previous studies comparing the radiotherapy alone with radiotherapy and mild hyperthermia (van der Zee, 2002; Valdagni and Amichetti, 1994b; Vernon *et al.*, 1996b; Algan *et al.*, 2000; Welz *et al.*, 2005; Bicher and Wolfstein, 1990a, b). Breast tumours showed a complete response rate to treatment of 82% with a further 18% showing a partial response (50% reduction in the size of the tumour) (Bicher and Wolfstein,

2006). The complete response rate to radiotherapy and hyperthermia for head and neck tumours was 88% and for prostate tumours was 93% (Bicher and Wolfstein, 2006). Recurrence rate was also low when a complete response to treatment was achieved. For breast cancer this stood at 15%, for head and neck tumours 12% and for prostate tumours 14%. Dissemination (metastatic disease) rates were comparable. They were 23% for breast tumours, 13% for head and neck and 14% for prostate tumours. Projected 5 year survival rates were 80% for breast patients, 88% for head and neck and 87% for prostate patients.

Work where a combination of hyperthermia and chemotherapy is applied is scarce, but the results reported are also promising. Use of a simultaneous combination of cistaplatin and hyperthermia in recurring cervical cancer following radiation treatment resulted in a 50% response rate to treatment (de Wit *et al.*, 1999), while without hyperthermia the response rate was expected to be around 15%. Witkamp and co-workers (Witkamp *et al.*, 2001) reported that patients with metastatic colorectal cancer (phase III) had a 45% 2 year and 23% 3 year survival rate when hyperthermia was used with chemotherapy, while a 10% to 20% 2 year survival rate was found when only chemotherapy or palliative surgery was used. A phase II study on hyperthermia in combination with pre- and/or postoperative chemotherapy in high risk sarcomas have demonstrated an impressive 5-year overall survival rate (van der Zee, 2002). A long term (>2 year) overall survival rate of 20% to 30% was also reported by Verwaal and co-workers (Verwaal *et al.*, 2003) for peritoneal carcinomatosis of colorectal region when hyperthermia used as an adjunct to chemotherapy comparing to 1 year overall survival rate of 13% to 20% of chemotherapy alone.

Recent research by Issels and his co-workers (Issels *et al.*, 2010) suggested that the addition of regional hyperthermia to chemotherapy reduced the risk for recurrence or death by 42%. This phase III study included patients with high risk of tissue sarcoma who were randomly assigned to etoposide 250 mg/m^2, ifosfamide 6 g/m^2, adriamycin 50 mg/m^2 (EIA) at four cycles every three weeks alone or to EIA plus regional hyperthermia both before and after local therapy. Patients assigned to chemotherapy plus regional hyperthermia survived an estimated 120 months before disease progression, while this was 75 months for patients assigned to chemotherapy alone. The overall survival rate increased in patients who completed all four cycles of chemotherapy plus eight hyperthermia treatments when compared with those treated with chemotherapy alone. Patients assigned to combined treatment were 44% less likely to die during follow-up compared

with those assigned to chemotherapy alone. At two years, 76% of patients assigned to regional hyperthermia were alive without local progression compared with 61% of patients assigned to chemotherapy alone. Tumour shrinkage occurred in 12.7% of patients assigned to chemotherapy, but 28.8% assigned to the combined therapy. Not all treatment were successful but tumour growth occurred in only 6.8% of those assigned to combined therapy, whereas tumour growth occurred in 20% of those assigned to chemotherapy alone.

1.2 Current heating techniques for hyperthermia

There are many heating techniques for hyperthermia. All these can be categorised as mainly non-ultrasonic and ultrasonic heating techniques. In the following section all these techniques are briefly described.

1.2.1.1 Non-ultrasonic heating techniques

Non ultrasonic heating techniques include radiative heating, perfusion techniques, magnetic nano particles, convective heating, radio frequency ablation and electromagnetic heating. Each of these techniques is briefly discussed below.

Radiative heating technique is mainly applied for whole body hyperthermia (WBH). It uses infra-red radiators to increase the temperature. A detail of this technique has been reported in the work of Hildebrandt and Wust (Hildebrandt and Wust, 2007). Two main types of radiative applicators are in use – with the patient positioned within either a 'closed-chamber' or an 'open-chamber'. These two types of applicator each have their own advantages: closed chamber devices allow the environment within the chamber to be tightly controlled in terms of humidity, while open-chamber devices allow more convenient access to the patient during treatment (Roemer, 1999). In addition, differences in the frequencies of the infra-red radiation exist between the various applicators, which affects the penetration depth of the radiation into the patient. Localised heating is not possible with radiative heating techniques.

Hyperthermia can be applied through perfusion techniques. In this technique, heat is applied to an isolated organ by controlling the temperature of the blood using a perfusion circuit external to the body. The technique may be used for organs such as the lung, pleura or liver, or for isolated limbs, in which case the treatment is called Hyperthermic Isolated Limb Perfusion (HILP) (Moreno-Ramirez *et al.*, 2010; Knorr *et al.*, 2006). Perfusion techniques give good temperature control and are generally used as an adjunct to

chemotherapy, enabling higher drug concentrations to be used in comparison to standard chemotherapy since the drug may be delivered to the organ or limb in isolation from the rest of the body. Perfusion techniques have fewer side effects than other techniques of hyperthermia. However, perfusion techniques have some disadvantages as well. It can damage nerve cells (Wust *et al.*, 2002) and highly localized heating is not possible with this heating technique.

Convective heating techniques involve heat transfer to tissue from a heated medium which is in contact with the tissue, such as wax or water bath. This technique may be used either for WBH or for heating of individual limbs. It is commonly used for creating hyperthermia in laboratory work on small animals (Song, 2005). It has some adverse effects on humans and is sometimes associated with excess toxicity (Hildebrandt *et al.*, 2005).

Heating can be done with magnetic nanoparticles. In this method of heating, a colloid of magnetic particles is injected into tumour and activated by an alternating magnetic field (typically at 50–100 kHz for humans or higher frequencies for studies on mice, thus producing heat) (Wust *et al.*, 2006b; Tseng *et al.*, 2009). The technique uses iron-oxide nanoparticles to maximise the heating efficiency, and surface coatings are used to delay targeting by the immune system (Salloum, 2009). Highly localised heating patterns can be achieved by administering the nanoparticles within a target region, but the treatment is invasive.

Radio frequency ablation uses electrodes which are either placed on the surface of the body or inserted via catheter into the target region, and a radio-frequency (RF) current, typically at 100–500kHz (Baronozio and Hager, 2006) is applied between them. RF excitation of ions within the tissue produces frictional heating. RF heating techniques are typically used for ablation since the heating can be confined to a highly localised region. Using a single interstitial electrode, the power deposition in the surrounding tissue is inversely proportional to the square of distance (Curley, 2001), so the temperature decreases rapidly away from the electrode. The region to be ablated is typically larger than the volume that can be lesioned by a single electrode, and therefore either several electrodes must be used, or a single electrode must be repeatedly repositioned to allow multiple lesions to be created within the target volume. RF heating techniques are therefore invasive, and may require surgery to provide access for the treatment of deep tumours.

Electromagnetic heating also called microwave techniques may be used to provide non-invasive, regional heating of tissue and this is the most widely used technique for mild hyperthermia. Various applicators have been developed for heating various parts of the anatomy. Examples include planar arrays for regional superficial hyperthermia of the chest and abdomen (Johnson, 2006), phased arrays such as hypercolar for localized heating within the head and neck (Paulides *et al.*, 2007) and array designed for intra-cavitary applications (Debicki *et al.*, 1995). The operating frequencies of the devices in these examples lie within the range of 400–1000MHz, which is typical for other types of microwave applicators. Electromagnetic heating techniques are limited by the penetration depth and the spatial resolution that can be achieved. High frequencies (>400 MHz) allow for good localisation of the heating, but only for a shallow heating depth (<2cm); conversely, low microwave frequencies allow for greater depth of heating but give poor spatial resolution (Lagendijk, 2000).

1.2.1.2 Ultrasonic heating techniques

In many applications, particularly deep body applications ultrasonic heating techniques can give a number of benefits over the non-ultrasonic heating techniques. Specifically, it can provide highly localised non-invasive heating of tissue over a wide range of depths (Hynynen, 1992; Aitkenhead *et al.*, 2008; ter Haar, 2007; Diederich, 1996). However, this heating technique has some limitations as well. The two major limitations are: they are not suitable for heating where gas filled cavities exist, such as lung, since the ultrasound is reflected at the tissue/gas interface and they are also not suitable for heating regions close to bone, since there may be unwanted heat deposition at the bone/tissue interface (Roemer, 1999) .

FUS, also called HIFU is the method of destroying tissue non-invasively by using a tightly focused ultrasound beam to create a rapid rise in temperature to above 60°C at a targeted location (discussed in section 1.1), hence producing the formation of a lesion of ablated tissue. Because of tight focus and low treatment times, the energy deposited in the surrounding tissue is low, hence leaving surrounding tissue largely unaffected. FUS is considered as an attractive method of destroying cancerous tissue since it can be done non-invasively which eliminates the potential complications that exist with surgery. However, the problems of focusing the beam through inhomogeneous tissue structures and superficial body structures such as the ribs have limited its applications to date. HIFU can damage tissue mechanically (via cavitation) or thermally depending on the focal intensity and the pulse duration. For ultrasound surgery, cavitation is normally avoided,

since the formations of gas bubbles disrupts the ultrasonic field and make precise prediction of the lesion volume difficult. However, Hu and co-workers (Hu *et al.*, 2007) reported that mechanical damage to tissue during HIFU can give additional benefits by inducing a systemic anti-tumour immune response.

In contrast, mild hyperthermia (section 1.1) involves raising the tissues temperatures by a smaller amount and for longer periods of time in order to improve the efficacy of some other modes of treatment, such as radiotherapy or chemotherapy, without necessarily reaching cytotoxic temperatures.

The design of an ultrasound transducer for mild-Hyperthermia or HIFU depends on the specific application. Three basic types of transducer are normally considered: extracorporeal transducers; intra-cavitary transducers; and interstitial transducers. An overview of the design approaches for ultrasound transducers are discussed in the following paragraphs all of which are based on the use of piezoelectric materials.

Extra-corporeal devices:

Extracorporeal ultrasound devices enable an ultrasound field to be created within tissue, thus generating heat due to the absorption of the ultrasound. The energy deposition may be aimed at a localised region by focussing the ultrasonic field, and this can be achieved using either physically focused single element devices or phased arrays.

Single element transducers are most commonly used in HIFU treatment where focusing is done through the use of an element with a concave surface (Wu *et al.*, 2001, 2002). Such physically focused elements can provide fields with characteristics well suited to the requirements of HIFU: the position of the focus relative to the transducer is well known aiding the targeting of the ablative treatment; the focal geometry for any transducer is simple to predict given the dimensions of the element; and the single element design maximises the focal intensity that can be achieved for a given transducer diameter, since the entire concave face of the element contributes to the field. The simple design of a single element transducer avoids potential sources of problems that exist in phased arrays, such as the need for multiple independent drive channels and the potential problems caused by inter-element cross-coupling.

However, single elements transducers are impractical for mild hyperthermia. To maintain an elevated and well-controlled temperature distribution (typically 42±0.5°C) within a region of tissue, the intensity and location of the focus needs to be adjusted during

treatment in order to respond to changes in the temperature distribution in the tissue. For a single element transducer, control of intensity is straightforward since the drive conditions can be modified, but there is no control of the position of the focus as that is determined by the geometry of the transducer. Moving the positions of the focus require physical movements of the transducer, and the mechanical system required for this may not respond fast enough or be accurate enough to control the temperature adequately (Aitkenhead, 2008; Cain and Umemura, 1986).

Ultrasound transducers based on phased arrays can be electronically focused and steered around the volume to be heated. So these types of transducers are more suitable for the treatment of tumours deep within the body. There are several styles of phased array transducers for deep tissue hyperthermia, with each style having different capabilities. Concentric-ring arrays (Fjield *et al.*, 1996) and combined concentric-ring sector vortex (Cain and Umemura, 1986) arrays provide the ability to move the focal region along the central axis of the transducer and are able to produce a focal region with an annular geometry suitable for optimal heating to a region of tissue. In contrast, sparse arrays of randomly distributed discrete elements afford maximum flexibility in terms of steering the beam in 3 dimensions with minimal grating lobes (Daum and Hynynen, 1999; Gavrilov and Hand, 2000). Overall geometry of the most of the proposed array designs is based on a hemi-spherical shell which helps produce an inherently focused beam. Recently, Hand and co-workers (Hand *et al.*, 2009) showed a randomised phased array device consisting of 254 1MHz elements on a spherical shell of radius of curvature 130mm and 170mm diameter. The phased array device of Hand and co-workers (Hand *et al.*, 2009) was capable of steering a single focus laterally to at least ±15mm off axis and axially to more than ±15mm from the centre of curvature of the array, whilst maintaining low intensity levels of the secondary maxima away from the targeted area. However, nowadays it is considered that a transducer with all the elements in a plane would be more appropriate for use on many parts of the body. The main advantages of planar arrays are that they allow for a relatively straightforward construction, and that they may allow closer placements of the transducer to the surface of the patient than is possible with a curved array (Aitkenhead, 2008). The majority of reported sparse arrays for deep tissue applications are intended for HIFU, so there is a lack of designs aimed at mild hyperthermia. However, both have the same requirements, in terms of adequate control of the focal region. Aitkenhead and co-workers (Aitkenhead *et al.*, 2008) showed that a planer phased array transducer consisting of 15 elements was suitable for mild hyperthermia deep within the body and achieved a good

focal region with high intensity ultrasonic field. They further suggested that an array of 60 elements driven by 550V peak to peak pulses was capable of producing a peak focal intensity of 50Wcm^{-2} at a depth of 60mm in tissue, which would be appropriate for mild hyperthermia as an adjunct to radiotherapy or chemotherapy.

Intra-cavitary devices:

Several research works have been reported on the design and characterisation (Diederich and Hnynen, 1989; Diederich and Hynynen, 1990) of intra-cavitary ultrasound transducers, such as devices for rectal and vaginal applications. These types of devices differ from extra-corporeal devices in two ways. Clearly, the physical dimensions of the intra-cavitary devices are limited by the nature of the application and so intra-cavitary devices are generally smaller than extra-corporeal devices, and intra-cavitary devices are generally aimed at regions closer to the transducer than the typical target depths for extra-corporeal devices. Despite these two differences, intra-cavitary devices follow the same design principles as extra-corporeal transducers.

Mechanical movement of an intra-cavitary device is limited. Many intra-cavitary arrays are based on phased arrays rather than single element to allow control over the pattern of the heat delivery with minimal mechanical movement of the device (Saleh and Smith, 2005a). It is common for the intra-cavitary arrays to incorporate a water jacket surrounding the applicator to cool the transducer and prevent overheating of the tissue directly in front of it (Smith *et al.*, 2001; Sanghvi *et al.*, 1999).

Interstitial devices:

As well as the non-invasive ultrasonic devices mentioned already, interstitial devices have been reported which may be inserted directly into tissue. While these devices are invasive, they provide good control of the heat localisation and minimise the heating of healthy tissue which would lie between other non-invasive ultrasound transducer and the target region (Nau *et al.*, 2000). As with extra-corporeal and intra-cavitary devices, the use of external cooling layers in conjunction with interstitial devices has been investigated to reduce the heating of the tissue in contact with the applicator and thereby increase the penetration of the heat in the radial direction (Nau *et al.*, 2000). Other cooling systems have been described, including routing the water coolant through the internal core of the applicator rather than around the outside in order to cool the piezoelectric device itself rather than the tissue (Deardorff and Diederich, 2000).

The relative merits and demerits of the different heating techniques used for hyperthermia are compared and shown in Table 1-1.

Table 1-1 Showing the relative merits and demerits of different heating techniques used for hyperthermia.

Heating techniques	Advantages	Disadvantages
Non-ultrasonic :		
Radiative heating	• Convenient to the patient • Environment can be easily controlled	• Localised heating is not possible
Perfusion	• Suitable for specific organs such as lung, pleura or isolated limbs (HILP) • Good temperature control • Can be used as an adjunct to chemotherapy • Fewer side effects comparing to other techniques	• Highly localised heating is not possible • Can damage nerve cells
Convective	• Whole body or individual limbs can be heated • Normally used for laboratory work or small animals	• Can produce adverse effects on humans (e.g. severely disturbed thermoregulation) • Associated with excess toxicity
Magnetic nano particles	Highly localised heating patterns can be achieved	Invasive technique
Radio frequency ablation	• Typically used for ablation • Highly localised heating is possible	• Invasive technique since a radio antenna is inserted into the body • For deep body tumours surgery is required
Electromagnetic/ microwave	• Most widely used technique • Non-invasive	• Low penetration depth • Low spatial resolution
Ultrasonic heating techniques :	• Ultrasound transducer can be designed and made according to the applications (e.g. extracorporeal devices, intra-cavitary devices (rectal & vaginal application), interstitial devices (inserted directly into the tissue) etc.). • Highly localised heating of tissue is possible over a wide range of depths • Minimum heating of healthy tissue	• Not suitable for heating of gas filled cavities such as lung • Not suitable for heating regions close to bone • Cooling of the transducer can be required to prevent surface heating

1.3 Current techniques for temperature measurements

The efficacy of hyperthermia can be evaluated from the knowledge of the properties of the heating modality employed, its measurements and the anatomy and physiology of the

patient in the region of the target. In fact, the efficacy of hyperthermia, in the sense of achieving and maintaining a desired temperature distribution cannot be assured solely on the basis of prior measurements whether in the laboratory or in the clinic. It is certainly the case that in vivo temperature measurements will be required during each and every mild hyperthermia treatment.

Two approaches to thermometry are identified. The first is invasive in which the temperature measurements are made at specific and predetermined points within the heated region. From practical point of view, the number of measurement sites for this approach is clearly limited. The alternative is a non-invasive method, which in principle is capable of yielding three dimensional temperature maps. The latter is best suited to hyperthermia applications. Although many techniques have been investigated for non-invasive temperature measurement none have yet been identified which combine the necessary spatial and temperature resolution over clinically relevant volumes.

Because of the limited thermometry some researchers proposed that information about the temperature distributions achieved could be obtained by hyperthermia treatment planning (Lagendijk, 2000; De Bree *et al.*, 1998; Van Leeuwen *et al.*, 2000). Treatment planning can provide a complete 3D temperature distribution in the treatment area and can deal with the complex relation between heating system, perfusion, discrete vasculature and anatomy of tissue. However, it cannot predict the temporal changes in tissue characteristics over long periods and therefore is unsuitable for mild hyperthermia.

1.3.1 Invasive temperature measurements

There are several techniques available for invasive temperature measurements during hyperthermia where the measurement technique used depend on heating technique employed. For a particular invasive temperature measurement technique for a particular heating modality it is necessary to understand the underlying physical principles of operation. Such information will help to evaluate the extent of compatibility with heating technique and the anatomical region of interests. Some of the major characteristics of the invasive thermometry techniques used in hyperthermia will now be described.

Thermocouples are the most common devices for measuring temperature in the clinical environment because of their low cost, ease of fabrication, small size, adequate accuracy, adequate linearity, adequate stability and the possibility of combining them into arrays. It is reported that in the clinical environment over 60% studies still rely on the use of thermocouples for temperature measurement (Dunscombe *et al.*, 1989). However, the

major drawback of thermocouples is their interactions with strong electromagnetic fields. In addition, they suffer from thermal smearing due to heat conduction in their metallic leads. Moreover, depending on their coating and packaging they can also interact with ultrasonic field (Hynynen *et al.*, 1983).

Thermistors are extremely sensitive and stable devices (Dunscombe *et al.*, 1989). When thermistors are connected to the measurement electronics through high impedance leads, they will neither perturb nor be perturbed by the electromagnetic fields (Dunscombe *et al.*, 1989). Multisensory probes of a micrometre size have been fabricated which are suitable for clinical use (Engler *et al.*, 1987).

Fibre optic temperature measurements are also available in hyperthermia which involves various sensing materials including phosphors, semiconductors or liquid crystal and fibre optic links which offer environmental and the use of remote instrumentation (Wickersheim and Mei, 1987). These devices are minimally perturbing to the electromagnetic fields since there is no interaction with electromagnetic fields at radio frequencies. This type of thermometer can be fitted into the smallest catheters and measurements can be localised a small volume within the tissue (Dunscombe *et al.*, 1989).

For mild hyperthermia where a temperature of 42°C is to be maintained, a high accuracy thermometry system is required. It is recommended that thermometry system for clinical use during local or regional mild hyperthermia should be calibrated to an accuracy of 0.2˚C with a precision of 0.1˚C (Dunscombe *et al.*, 1989). The temperature accuracy of 0.2˚C implies effective thermal contact between the sensor and the tissue being monitored. Poor thermal contact can impair measurement accuracy particularly when temperatures are changing rapidly. Another intrinsic property of a thermometry system that should be considered is its stability. The frequency of calibration of the thermometry is chosen such that the stability, precision, and accuracy of the system are guaranteed. In addition for any types of invasive thermometry its susceptibility to humidity and method of sterilization should be considered.

There are several problems associated with the invasive temperature measurement techniques. Interference from RF fields with the sensitive electronics (which conditions and records the signals from the temperature sensor) has been a long recognized difficulty of making temperature measurements (Dunscombe *et al.*, 1989). Many thermometry systems have been designed with shielding and filtering configurations aimed at eliminating this

problem (Horseman *et al.*, 1983). In addition to the interference with metallic thermometers, there are problems associated with self-heating (Constable *et al.*, 1987; Dunscombe *et al.*, 1988).

A further effect can be significant when the temperature sensor assembly is thermally conducting. Smearing or distortion of the temperature distribution can occur due to the conduction along the sensor (Lyons *et al.*, 1985). Such an effect is clearly more significant in temperature gradients such as found frequently in tissue close to large blood vessels; in the penumbra of heating field and near the edges of the heating volume (Lagendijk, 1982). Thermal lag due to the insulating properties of the encapsulating medium within which the temperature sensor is located can become clinically significant. Sometimes a tracking technique is employed to maximize the temperature information obtained per insertion (Engler *et al.*, 1987). In this approach, sufficient time must be allowed at each location for thermal equilibrium to be attained which will depend on the time constant of the sensor within its encapsulation (Waterman, 1985).

An additional problem has been identified when performing temperature measurements in ultrasonic fields. The interaction of the field with plastic catheters has been observed (Waterman *et al.*, 1990; Fessenden *et al.*, 1984; Hynynen *et al.*, 1983).

The aim of thermometry in hyperthermia is by measurement and/or predictive modelling to determine the distribution of temperature in 3 dimensions. Due to a lack of homogeneity of temperature achievable with almost all heating modalities, the positional accuracy of invasive thermometry is of vital importance.

With the exception of whole body hyperthermia, temperature gradients of between 1 and 10˚C cm^{-1} are characteristic of clinical hyperthermia heating technology (Samulski *et al.*, 1987). The lower value is achievable with regional heating techniques while higher values are typical of gradients encountered during the application of interstitial techniques near the surface of externally heated sites and, in general, near tumour / normal tissue boundaries. The reproducibility of setup from treatment to treatment should ideally be better than 2mm and the position of the temperature sensors with respect to both patient's anatomy and applicator must be considered (Dunscombe *et al.*, 1989).

In the absence of other constraints, it is clear that thermometry will be more reproducible if the locations of measurements are in regions where large temperature gradients are not

expected. Large blood vessels which could constitute significant heat sinks may require special consideration if they lie within the intended therapeutic volume of heating field.

The use of linear arrays of sensors is a convenient technique for increasing the temperature information which can be obtained from the insertion of one catheter. An alternative method which employs only one thermometer to reach the same objective is a linear tracking technique (Gibbs, 1983). The recommended precision of positioning is unlikely to allow temperature measurements to be made at locations separated by more than about 5mm routinely. In addition to considering the precision of location of temperature measurement, the absolute accuracy must also be considered.

Finally, it is necessary to identify the locations of temperature measurement relative to the patient's anatomy and the applicator position before clinical treatment commences. The specification of a temperature distribution to be achieved during clinical hyperthermia cannot be realized without a clear and accurate description of the location of measurement. Several techniques are used for identifying the location of a temperature measurement. Computed tomography (CT) in the presence of radio-opaque skin markers to indicate applicator position is universally applicable when available. Stereo or orthogonal X-ray films taken with the probe catheter filled with a radio opaque substance can be employed to identify the position of the catheter in 3 dimensions. Other imaging techniques such as ultrasound and MRI can also be used to help identify catheter location.

1.3.2 Non-invasive temperature measurements

At present, the possible non-invasive temperature measurement techniques include: microwave temperature measurement, magnetic resonance imaging (MRI) temperature measurement, Infrared or near infrared temperature measurement, computerised simulation of the temperature field, ultrasound temperature measurement and electrical impedance temperature measurement. Each has advantages and disadvantages and will now be considered in more detail

1.3.2.1 Non-invasive temperature measurement using MRI

The temperature sensitivity of magnetic resonance (MR) has been recognised for a long time (Bloembergen *et al.*, 1948). More recently, MRI has been proposed for monitoring temperature distribution non-invasively (Bertsch *et al.*, 1998; Rieke and Pauly, 2008; Yuhua *et al.*, 2010). MRI has many temperature sensitive parameters which can show the changes of temperature as well as the histological changes to tissue. Several methods have been developed and demonstrated based on MRI to measure temperature changes. These

methods can be separated into two categories: endogenous and exogenous. Endogenous methods depend on the inherent thermosensitive properties of the tissue in the body, while exogenous methods depend on thermosensitive contrast agents that need to be injected into the body.

There are some endogenous tissue properties that have been used to measure temperature change by MRI. In principle, temperature changes can be detected by their effect on the relaxation times (T_1 and T_2), spin density, diffusion constant and the water proton resonant frequency shift (PRFS).

The temperature dependence of the T_1 relaxation time has been known since the theory was developed by Bloembergen and his co-workers (Bloembergen *et al.*, 1948) and was first investigated for non-invasive thermometry by Parker and co-workers (Parker *et al.*, 1983). Work done on detecting temperature changes in T_1 relaxation time have shown that this increases by approximately 1.0%/°C to 2.0%/°C (e.g. 1.0%/°C in fat, 1.4%/°C in bovine muscle, 1–2%/°C in liver etc.) (Bertsch *et al.*, 1998; Rieke and Pauly, 2008). However, any technique that measures T_1 can be used; and T_1 weighted GRE or Look Locker sequences have also been used (Germain *et al.*, 2002). There are some disadvantages of T_1 based MR thermometry. It does not have sufficient sensitivity to measure the small temperature changes required for mild hyperthermia treatment. Moreover, T_1 based methods are only linear for a small temperature range (43–45˚C) and T_1 in tissue changes differently with increasing and decreasing temperature (Lewa and Majewska, 1980) and hence there is a hysteresis in the relationship (particularly in muscle) between the signal intensity and the temperature (Jolesz *et al.*, 1988).

Similarly, an increase in T_2 relaxation time with increasing temperature has been observed in aqueous solution. However, in tissue the sensitivity of T_2 to temperature specifically, at higher temperatures is reduced by a significant factor compared to pure water and the temperature dependence of T_2 can be masked by other factors. Additionally, there is a different temperature sensitivity to increasing and decreasing temperatures due to thermal coagulation as there is with T_1 based MR thermometry (Rieke and Pauly, 2008). Yuhua and co-workers (Yuhua *et al.*, 2010) proposed a T_2 based MR thermometry using the CPMG (Carr-Purcell-Meiboom-Gill) sequence (the style of this sequence is: $\pi/2$-τ-π-2τ-π-2τ-....). They showed that with the help of nonlinear curve fitting techniques, temperature can be assessed during clinical hyperthermia.

A change of proton density or spin density with temperature has also been used to monitor temperature by MRI (Goldhaber *et al.*, 1993). The proton density depends linearly on the equilibrium magnetization, M_0, which in turn depends on the Boltzmann thermal equilibrium. The proton density in the tissue itself does not change with temperature but rather the susceptibility, χ_0, which reflects the ratio of parallel and antiparallel spin populations. The susceptibility is inversely proportional to the absolute temperature, T, which is known as Curie law. So the temperature sensitivity of equilibrium magnetisation, M_0, is inversely proportional to temperature and changes by -0.30 ± 0.01%/°C (Rieke and Pauly, 2008) between 37°C and 80°C. From the change in susceptibility a relative temperature is calculated. However, this method requires a high signal-to-noise ratio (SNR) because of its small −0.3%/°C temperature dependency. It is also necessary to eliminate the effects from changes in T_1 relaxation time. To do this a long repetition times close to 10s is required, which makes the method less useful for real-time applications. In fast imaging sequences, changes in susceptibility are difficult to separate from the effects due to changes in relaxation times (Rieke and Pauly, 2008). In addition, susceptibility also varies with tissue types and there is a hysteresis effect. Therefore, temperature monitoring of tissue based on the exploitation of relaxation times and proton density (susceptibility) parameter appears less promising.

The diffusion method measures changes in the apparent diffusion coefficient (ADC), which increases with increasing temperature by about 2%/°C (Rieke and Pauly, 2008). Standard diffusion sequences can be used, with segmented EPI sequences being ideal for body imaging (Gellermann *et al.*, 2006). Non-invasive temperature measurement by the diffusion method has very high sensitivity, but acquisition times are relatively long and in vivo implementations suffer from an extremely high sensitivity to motion (Rieke and Pauly, 2008). It has been suggested that single-shot echo planar imaging (Bleier *et al.*, 1991) and line-scanning techniques (Morvan *et al.*, 1993) can be used to reduce the acquisition time and motion sensitivity of this method. An additional complication is that the temperature dependence of diffusion becomes nonlinear when tissue conditions change. The mobility of water in tissue depends on barriers such as cellular structure, proteins, and membranes. Heat induced changes like protein coagulation, therefore, can lead to large changes in the diffusion coefficient (Rieke and Pauly, 2008). In fatty tissue lipid suppression is necessary because fat has a different change in diffusion coefficient with temperature (Rieke and Pauly, 2008). Moreover, temperature measurements in fat are difficult due to the low diffusion coefficient in fat. Apart from SNR advantages at high field strengths and changes

in relaxation times, temperature imaging based on the diffusion coefficient is independent of field strength.

Non-invasive temperature monitoring with proton resonance frequency (PRF) is the most sensitive among the endogenous MRI parameter techniques in detecting small changes, which results in higher precision than that achieved by other methods. The temperature sensitivity of the PRF was first observed by Hindman in 1996 (Hindman, 1966) and first implemented for MR temperature monitoring by Ishihara and his co-workers (Ishihara *et al.*, 1995) and De Poorter and his co-workers (De Poorter *et al.*, 1995). Temperature imaging based on PRF shift has evolved into two techniques, spectroscopic imaging and phase mapping methods (Rieke and Pauly, 2008). The ability of spectroscopic imaging to determine absolute temperatures makes it a unique tool for non-invasive temperature measurements, but has currently limited applicability for real-time temperature monitoring during mild hyperthermia due to its low temporal and spatial resolution. In the following section the phase mapping methods will be discussed in details.

The proton resonant frequency shift (PRFS) occurs when the hydrogen bonds in water lengthen with increasing temperature, as this increases the magnetic shielding of the protons by the electrons in the hydrogen bond. These changes in the shielding decrease the resonant frequency of the water protons, which results in a decrease in the phase of the water signal, which is dependent on the echo time (TE) as the temperature increases. Fortunately, the frequency changes are linear with temperature, with many in vivo and in vitro experiments showing that most tissues have a sensitivity of approximately 0.01ppm/˚C. These phase changes can be measured by acquiring phase sensitivity images using gradient echo or offset spin-echo sequences. In order to eliminate temperature-independent contributions, e.g., due to B_0 field inhomogeneities, one or more images are usually acquired before heating and subtracted from images during heating. The phase difference images are proportional to the temperature dependent PRF change and to the echo time, TE, and can be converted to a temperature change by the following equation 1-1.

$$\boldsymbol{\Delta T} = \frac{\boldsymbol{\phi(T) - \phi(T_0)}}{\boldsymbol{\gamma \alpha B_0 TE}} \qquad 1\text{-}1$$

Where ϕ(T) is the phase in the current image, ϕ(T_0) is the phase of a reference (baseline) image at a known temperature, γ is the gyromagnetic ratio, α is the PRF change coefficient,

B_0 is the magnetic field strength, and TE is the echo time, which can be optimized to increase the phase contrast-to-noise ratio.

However, there are some other effects that influence temperature measurements with PRF, such as magnetic field drift (B_0), the composition of tissue, the electrical conductivity, and the motion drift which will be summarised here.

Complications of PRFS thermometry due to B_0 field shift:

Large errors in the estimated temperature can occur when the main magnetic field (B_0) drifts significantly during the scan time, creating significant non-temperature related phase shifts in water (Wyatt, 2010). These phase shifts due to field change are inseparable from phase changes due to temperature and resulting in error in temperature measurements using PRFS methods. A maximal specification of the rate of magnetic field drift in a modern commercial MRI magnet is 0.1ppm/hour, or approximately 6.4Hz/hour at 1.5T. The resonant frequency of water also changes at -0.01ppm/˚C, or approximately 0.64Hz/˚C at 1.5T, meaning that an hour long mild hyperthermia treatment could have up to 10˚C of temperature error due to B_0 drift alone, if not corrected. Considering that the maximum temperature change for a typical mild hyperthermia treatment is between 6–8˚C, field drift could be a significant problem for accurate measurement of temperature change. There have been many methods (Gellermann *et al.*, 2005; De Poorter *et al.*, 1995; Wust *et al.*, 2006a; El-Sharkawy *et al.*, 2006) developed to correct for the field drifts seen during mild hyperthermia treatments. Unfortunately, none of these methods are robust. Therefore, a robust method needs to be developed and optimized to correct for these field drifts before a technique based on the PRFS technique is clinically viable (Wyatt, 2010).

Complication of PRFS thermometry in fatty tissue

It is considered that the PRF shift is independent of tissue type except for adipose tissue (Hynynen *et al.*, 2000). In water (aqueous tissues), the dependence of the PRF on temperature is attributed to changes in the hydrogen bonds, which is absent in fat. Therefore, fat has very small or negligible temperature sensitivity (≈ 0.000045ppm/˚C), which causes difficulty in using the PRFS approach for thermometry inside fatty tissue (Kuroda, 2005). Many biological tissues are composed of both water and fat (De Poorter *et al.*, 1995). The presence of lipid modifies the phase difference obtained in thermometry experiments and this leads to temperature errors. To overcome this problem, lipid suppression (Weidensteiner *et al.*, 2003) or selective excitations (Rieke and Butts Pauly,

2008) are commonly used on high-field scanners. However, at field strength of 0.5T and below chemically selective excitation or suppression is difficult due to the small difference in spectral shift between water and fat (Rieke and Pauly, 2008).

Complications of PRFS thermometry due to motion

Motion is the most prevalent problem for temperature monitoring with PRF phase mapping (Rieke and Pauly, 2008). Motion artefacts can be divided into two categories, intrascan motion and interscan motion, where the classification is based on the timescale of the motion with respect to the image acquisition time. Intrascan motion is caused by movement of an object during MR image acquisition, resulting in a poor quality image with blurring and ghosting artefacts (Rieke and Pauly, 2008). These motion artefacts can be reduced by accelerating the image acquisition. Interscan motion occurs due to motion or displacement of an object between the acquisitions of consecutive images. If motion is present between the acquisitions of the images and the images are not registered to a baseline image, artefacts in the temperature maps will occur (Rieke and Pauly, 2008). Unfortunately, many of the target areas for thermometry are in the abdomen, where motion is always present. A major source of motion, especially for the upper abdominal organs, is respiration. Respiration not only displaces the organs but also changes the susceptibility field. Even without tissue motion in the image region, lung filling can change the background phase enough to render temperature measurements based on subtraction impossible (Salomir *et al.*, 2003). Without respiratory motion, there is heat-induced tissue motion (e.g. caused by thermal coagulation), which can be observed without any other source of motion being present. Different strategies to overcome the problem with motion have been proposed including averaging or fitting K-space data, real-time adjustment of the field (shimming), field change estimation from calculating differences in tissue position and the use of navigator echoes for respiratory gating. Whilst many correction method have been developed, none of these are robust, with each correction method has its limitations (e.g. gating can fail when respiratory cycle is irregular, the use of navigation echoes is restricted to rigid body motion and may not be optimal for complex organ displacements or deformations).

Among the endogenous MR thermometry methods, PRFS is preferred, due to linearity of the frequency change, the tissue independence, and the high sensitivity (Wlodarczyk *et al.*, 1998). However, both diffusion and T_1 relaxation have advantages making them useful in specific situations (Rieke and Pauly, 2008). Both methods can be made less sensitive to B_0

field inhomogeneity by using spin echo techniques, while PRFS methods are restricted to sensitive gradient echo methods (Wlodarczyk *et al.*, 1999). The T_1 measurement is relatively motion resistant since images can be registered between measurements unlike the PRFS and diffusion methods (Rieke and Pauly, 2008).

In recent years, temperature sensitive contrast agents have attracted interest for guiding thermal therapies, including paramagnetic thermosensitive liposomes, paramagnetic lanthanide complexes, and spin transition molecular materials (Rieke and Pauly, 2008). These exogenous contrast agents can change the thermosensitive MRI parameters, typically giving a much higher sensitivity than that obtained with endogenous methods described above (Pakin *et al.*, 2006; Hekmatyar *et al.*, 2005). Paramagnetic thermosensitive liposomes are composed of gadolinium or manganese based compound enclosed by a phospholipids membrane (Fossheim *et al.*, 2000). Below a distinct gel-to-liquid crystalline phase transition temperature (T_m), the liposomes do not allow water exchange through the membrane. Above T_m the membrane becomes water permeable, yielding fast exchange conditions and therefore relaxation enhancement. Different paramagnetic lanthanide complexes such as $DOTMA^-$ (1,4,7,10-tetraazacyclododecane-1,4,7,10-tetramethyl-1,4,7,10-tetraacetate) and $TmDOTMA^-$ (thulium 1,4,7,10-tetraazacyclododecane-1,4,7,10-tetramethyl-1,4,7,10-tetraacetate) have chemical shifts that are very much greater than the water ^1H shift, e.g., $TmDOTMA^-$ has a temperature coefficient of 0.57 ppm/°C, which is nearly 60 times that of water (Pakin *et al.*, 2006; Hekmatyar *et al.*, 2005). Another kind of paramagnetic lanthanide complex referred to as PARACEST (paramagnetic chemical exchange saturation transfer) has also been investigated for temperature imaging (Woessner *et al.*, 2005). Spin transition molecular materials are bistable molecular complexes that switch from a spin S = 0 diamagnetic state to an S = 2 paramagnetic state at a temperature given by its chemical composition (Muller *et al.*, 2003). Temperature sensitive contrast agents have attracted interest in recent years and have been evaluated in animal experiments. However, MR thermometry based on temperature sensitive contrast agents is dependent on a homogeneous accumulation and retention in the target tissue, which is often difficult to achieve (e.g. in necrotic tumours). Therefore, temperature measurements might not be representative for the temperature distribution in the tumour. In addition, the nontoxicity of the agents has to be demonstrated for in vivo applications.

Overall, the non-invasive temperature measurement using MRI can be considered as an attractive method for FUS/HIFU because of the short treatment times and that the effect of

ablation can be seen immediately after the application of high intensity ultrasonic field. However, the MRI approach is of little value for controlling the mild hyperthermia treatment delivery.

1.3.2.2 Microwave Radiometry

The technique of microwave radiometry in the application to non-invasive thermometry is based on the detection of electromagnetic radiation in the microwave region emitted from a hot body (Foster and Cheever, 1992; Leroy *et al.*, 1998). Any material body at a temperature above that of absolute zero will emit thermal radiation, the spectrum of which is directly related to the temperature of the body. For living human tissue, at a temperature around 37˚C, spectral emission is most intense in the mid-infrared at about 9.7μm (Togawa, 1985). At a microwave frequency of 3GHz (10cm wavelength), a typical frequency used in microwave radiometry (Leroy *et al.*, 1998), the emitted intensity is approximately 10^8 times less than that at the peak (Togawa, 1985). However, with sensitive enough equipment this radiation can be detected and a temperature resolution of 0.1˚C achieved (Edrich *et al.*, 1980). At microwave wavelengths the penetrations depth through human tissue is the order of several centimetres, much deeper than the few millimetres or less that is characteristic of the mid-infrared range (Godik and Gulyaev, 1991). Spatial resolution is however, compromised by the use of longer wavelengths: at a wavelength of 3 cm the spatial resolution has been reported to be 2cm (Edrich *et al.*, 1980).

Microwave radiometry detects the average power emitted from a particular volume of the medium beneath the antenna. The received signal depends on many factors such as the temperature distribution in the measured volume and its dielectric properties (Cheever and Foster, 1992). The effective depth of sensing, i.e. the depth at which the signal is e^{-1} that at the surface, depends on the antenna geometry: a longer antenna increases the effective depth at the cost of resolution (Cheever and Foster, 1992). The radiometric temperature (known as brightness temperature) is determined by a complex two-step process (Leroy *et al.*, 1998). Initially, the received radiation field pattern of antenna is estimated by assuming it to be the same as the absorbed field distribution seen in the medium where antenna to be used to transmit energy into the medium (Cheever and Foster, 1992). Subsequently, the temperature is found by applying an inverse process to the radiometric data, which has been weighted by the antenna field distribution. There are many inverse technique used for recovery of the temperature distribution in biological tissue (Foster and Cheever, 1992). Some require the use of multi-frequency radiometers (Mizushina *et al.*, 1993), whilst others depend on a fixed-frequency, multi-angle method (Montreuil and Nachman, 1991).

Gustav and Troitsky (Gustov and Troitsky, 1985) investigated the non-invasive measurement of cranio-cerebral temperatures in healthy adults by the use of microwave radiometry. The system they used was reported to measure temperature to an accuracy of 0.1˚C. In this study, the brain temperatures at a depth of 5–6cm were measured directly for three patients during surgery. The radiometric temperature measured at the corresponding site prior to surgery was found to differ only 0.4–0.8˚C. Recently, there has been interest in the application of microwave radiometry to monitoring neonatal brain temperature during hypothermic treatment (Han *et al.*, 2001).

Foster and Cheever (Foster and Cheever, 1992) discuss the relative advantages and disadvantages of microwave thermometry. In their opinion, the advantages include the comparative simplicity of the hardware, e.g. in comparison to magnetic resonance systems and the potential for greater tissue-depth temperature determination compared to infra-red thermographic techniques. Another obvious advantage is the inherent safety of the technique, since no external field is applied to the tissue. Amongst the disadvantages, Foster and Cheever (Foster and Cheever, 1992) conclude the relatively poor temporal and spatial resolution of the measurements, susceptibility to interference from other electrical signals and the possibility that the radiometric signal may reflect temperature dependent changes in tissue dielectric properties as well as tissue temperature changes.

1.3.2.3 Ultrasound thermometry

Ultrasound is an attractive method for temperature monitoring because it is non-ionizing radiation, convenient, and inexpensive and has relatively simple signal processing requirements. This method may be useful for temperature estimation if a temperature-dependent ultrasonic parameter can be identified, measured and calibrated. The most common methods for using ultrasound uses either (1) echo shifts due to changes in the speed of sound and thermal expansion, (2) changes in the attenuation coefficient or (3) changes in backscattered energy from tissue inhomogeneities (Arthur *et al.*, 2005).

The use of echo shifts has gained popularity in the last decade. By tracking scattering volumes and measuring the time shift of received echoes, researchers have been able to predict the temperature from a region of interest both theoretically and experimentally in phantoms in isolated tissue regions in vitro and preliminary in vivo studies. However, the disadvantage of this method is that a prior knowledge of both speed of sound and the thermal expansion coefficients is required (Arthur *et al.*, 2005).

Acoustic attenuation also depends on temperature, but the significant changes occur only at higher temperatures (>50°C), which may lead to its use in thermal ablation therapies (Damianou *et al.*, 1997). Minimal changes in attenuation occurred at lower temperature (<50°C) reduce its attractiveness for use in mild hyperthermia (Techavipoo *et al.*, 2004).

Models and measurements based on the change in backscattered energy suggest that, over the clinical hyperthermia temperature range, changes in backscattered energy are dependent on the properties of individual scatters or scattering regions (Arthur *et al.*, 2005). Calibration of the backscattered energy from different tissue regions is an important parameter of this technique. According to some researchers, the backscattered energy from scatterers could change by as much as 5dB over the temperature change 37–50°C (Straube and Arthur, 1994a).

A number of researchers evaluated techniques based on the change in the velocity of ultrasound as a method of monitoring temperature changes during hyperthermia therapy (Miller *et al.*, 2002; Miller and Bamber, 2004; Miller *et al.*, 2004; Seip and Ebbini, 1995). Miller and Bamber (Miller and Bamber, 2004) used ultrasound to measure temperature distribution due to the heat-induced sound speed changes in soft tissue of diagnostic ultrasound. In their measurement, they considered the sound speed in a medium as a function of temperature. They used an ultrasound scanner to interpret heat induced sound speed changes as displacements. They measured these apparent displacements by echo tracking and used to produce a 2D image of temperature rise. They got a good spatial and temporal resolution comparable to diagnostic ultrasound. They got good sensitivity in ex vivo bovine liver with a temperature resolution of 1°C, starting from room temperature; however the sensitivity was likely to be poor in liver with a significant fat content. Miller and Bamber (Miller and Bamber, 2004) also pointed out that the commonly quoted temperature sensitivity 0.04%°C^{-1} was only applicable to liver, and importantly, over the narrow temperature range of 35–50°C. Above 50°C the temperature sensitivity reverses (Bamber, 2007).

Seip and Ebbini (Seip and Ebbini, 1995) used the diagnostic ultrasound in an attempt to measure tissue temperature non-invasively. They established a relation between temperature and frequency changes in the spectrum of reflected ultrasound pulses. They assumed that the biological tissue consists of a semi-regular lattice of discrete scatters, separated by some average distance, ***d***, over a certain region of interest. The frequency spectrum of back-scattered ultrasound pulses from tissue will therefore contain harmonics

of some 'fundamental 'tissue frequency that will be related to ***d***. This fundamental frequency (***f*** $_1$) is determined from the time taken for the ultrasound pulse to travel the minimum possible distance which depends on both d and the speed of sound c in the tissue (***f*** $_1$ = **c**/2***d***) (Weng *et al.*, 1992). Since ***d*** and the speed of sound, ***c***, in tissue will change with temperature, and their temperature coefficients will vary between different tissue types, ***f*** $_1$ will also depend on tissue temperature (Seip and Ebbini, 1995). However, ***f*** $_1$ for most tissues does not fall within the frequency pass band of typical diagnostic transducers; therefore, Seip and Ebbini (Seip and Ebbini, 1995) investigated the temperature dependence of its visible harmonics. Autoregressive model based methods were used in the estimation of Δf. It was shown that the harmonic frequency changes Δf extracted from the AR PSD are linearly proportional to the temperature changes ΔT of the medium being heated, with the proportionality constant being determined by changes in the speed of sound with temperature and the linear coefficient of thermal expansion of the tissue. They predicted the change in temperature of a dog's thigh in vivo due to ultrasonic heating by this method and found a reasonable agreement between these and invasive measurements of temperature using a thermocouple (Seip and Ebbini, 1995). The standard deviation of the estimated results was however, quite high at 0.5˚C, which the authors believed to be due to movement artefacts. They found that the AR PSD estimation technique has a temperature resolution on the order of 0.4˚C, and spatial temperature resolution on the order of 3.0mm. These resolutions are adequate for current hyperthermia treatments.

Mass-Moreno and co-workers (Maass-Moreno *et al.*, 1996) used a similar technique to predict tissue temperature in turkey breast, and the related temperature changes to the time shifts in the received ultrasound echoes. In between periods of heating with a high-intensity ultrasound beam, pulses were sent and received and the echo times recorded for the different temperature. They noticed that the relationship between pulse-echo time and temperature related changes remained constant for a temperature increase of approximately 10˚C, but as the temperature peaked the relationship appeared to change. The authors attributed this non-linearity to a result of irreversible tissue alterations at high temperatures (Maass-Moreno *et al.*, 1996).

1.3.2.4 Electrical impedance temperature measurements

Electrical impedance measurement has also been proposed as a technique for determining the temperature during hyperthermia treatments for cancer (Conway *et al.*, 1985; Conway, 1987; Esrick and McRae, 1994; McRae and Esrick, 1993; Gersing, 1999; Paulsen *et al.*, 1994;

Paulsen and Jiang, 1997; Moskowitz *et al.*, 1994). Impedance changes with temperature due to changes in the conductivity in the extra- and intra-cellular fluids. The commonly quoted electrical conductivity change in the tissue in the low radiofrequency range due to temperature is approximately 2% $°C^{-1}$ (Conway *et al.*, 1985; Conway, 1987) and most of the researchers looking at electrical impedance measurement techniques used this assumption and suggested this as means of determining tissue temperature non-invasively during mild hyperthermia. However, there are also other factors, which may affect the impedance changes with temperatures and those factors need to be considered properly during non-invasive temperature estimation. Esrick and McRae (Esrick and McRae, 1994) reported that in addition to the conductivity changes, impedance changes due to changes of permeability of the cellular membrane and heat induced oedema or changes in cellular volume with temperatures. Gersing (Gersing, 1999), in his work on the temperature measurements of skeletal muscle and tumours (DS sarcoma) during hyperthermia showed that extra-cellular fluid volume changes due to vasodilation with temperature has the same order of effect on impedance changes as the change in conductivity. He also suggested that this extra-cellular fluid volume changes occurred concurrently with heating in normal tissue but was delayed in cancerous tissue.

The temperature estimation in hyperthermia using electrical impedance technique has poor temperature resolution. The commonly reported temperature resolutions based on this technique is of 10˚C (Paulsen *et al.*, 1994; Moskowitz *et al.*, 1994). Paulsen and Jiang (Paulsen and Jiang, 1997) suggested that a temperature resolution of 2°C was possible by the electrical impedance method using an optimised image reconstruction algorithm, where the conductivity as well as the permittivity distributions in tissue are recovered. However, in mild hyperthermia, temperature resolution of at least 1°C is clinically required, which is difficult to achieve with electrical impedance imaging even when the enhanced image reconstruction approach is used. Several non-invasive temperature measurement methods are compared in Table 1-2.

Table 1-2 Showing the relative merits and demerits of several non-invasive temperature measurement techniques.

Non-invasive temperature measurement techniques	Advantages	Disadvantages
MRI thermometry (Several MRI parameter such as relaxation times (T1 & T2), spin density, diffusion constant and proton resonant frequency shift can be used to measure temperature non-invasively using MRI)	• Sensitive in detecting small temperature changes • For soft tissue sarcomas temperature resolution of 0.5°C to 1°C can be achieved • Attractive method for FUS/HIFU because of the short treatment times and the effect of ablation can be seen immediately after the application of the high intensity ultrasonic field	• Magnetic field drifts, tissue composition (fatty tissue), electrical conductivity and motion drifts (peristalsis or respiration) create artifacts in the thermal data and cannot easily be corrected. • Not suitable for use in abdomen and pelvis • Limited applicability in real time temperature monitoring because of the low temporal resolution. • Not appropriate for controlling the mild hyperthermia treatment delivery • Very expensive and non-portable
Microwave thermometry	• Simple hardware • Safe – as no external field is applied	• Poor temporal and spatial resolution • Susceptibility to interference from electrical signals • Radiometric signals may reflect temperature dependent changes in tissue dielectric properties as well as tissue temperature changes.
Ultrasound thermometry	• Good temporal and spatial resolution • Temperature resolution of 1°C can be achieved in homogeneous cellular tissues. • Non-ionizing radiation • Inexpensive • Simple signal processing • Suitable for mild hyperthermia	• Sensitivity is poor in fat • Application is limited in gas filled cavities (such as lung) and close to bone.
Electrical impedance temperature measurements	• Safe – no known side effects. • Portable. • Inexpensive • Very good temporal resolution (in the order of milliseconds)	• Poor temperature resolution - typically quoted as 2-10°C, so not suitable for mild hyperthermia • Poor spatial resolution comparing to other methods

1.4 Some unresolved Challenges in hyperthermia

Despite the average 20% improvement in 5 years survival rate using mild hyperthermia in conjunction with radiotherapy (discussed in section 1.1.7), a number of challenges must be met before mild hyperthermia in combination with radiotherapy can be considered as a standard treatment modality for deep body solid tumours. Many clinical trials are being conducted to evaluate the effectiveness of hyperthermia. Some of these trials are focused

on a combination of hyperthermia with other therapies (van der Zee, 2002; Skitzki *et al.*, 2009; Wust *et al.*, 2002; Hildebrandt and Wust, 2007) whilst others studies focus on improving hyperthermia treatment in terms of heating (Aitkenhead *et al.*, 2008) and thermometry techniques (Lagendijk, 2000; Arthur *et al.*, 2005; Seip and Ebbini, 1995).

To get optimum benefit from hyperthermia, a criterion for the selection of optimum heating and thermometry needs to be available. There are a large range of heating modalities and measurement techniques currently used in hyperthermia.

Researchers are currently more concerned with the heating techniques and their potential application to the patients. Present heating technology gives very non uniform patterns of energy deposition. Even if energy deposition were uniform, physiological effects (blood flow) and differences in thermal properties (e.g. thermal conductivity) among different tissues would generally result in a very non uniform temperature distribution.

There is limited progress in design and implementation of clinical thermometry for hyperthermia. Temperatures are routinely measured invasively, but only sparse measurements can be made. The limited number measurement may result in less information than is necessary in order to assess thermal dosimetry properly. With the advent of multi-element heating devices (Aitkenhead *et al.*, 2008; Hand *et al.*, 2009), there is an increased need for temperature measurements that can provide detailed feedback about temperature distributions. This information in real time would considerably improve the ability to deliver consistently effective temperature distributions. To meet the capability of present and forthcoming heating technologies of hyperthermia, a clinically useful method is needed to measure 3D temperature distributions to within 0.5°C in $1cm^3$ volumes (Arthur *et al.*, 2005).

There are several approaches to non-invasive thermometry proposed but none is fully clinically usable because none of the proposed non-invasive thermometry can provide temperature distributions in three dimensions throughout the course of a clinical treatment. The temperature data acquired during the clinical treatment form the most valuable record of the treatment which will act as the source data for characterizing the heating session. Such data will enable researchers to determine the thermal dose required to achieve maximum benefits in terms of tumour control. With the currently available thermometry techniques, the complete temperature in vivo cannot be determined and this

is limiting the appropriate application of hyperthermia alone or in conjunction with chemo- or radiotherapy.

It remains a topic of considerable research to devise methods of determining the complete temperature distributions from the limited measurements possible in clinic. However, in designing and implementing a clinical thermometry for hyperthermia, the high degree of temperature non-uniformity in human tissue must be considered. Therefore, despite the impressive biological effects, the use of hyperthermia is held back by the major problems related to the delivery of heat and its measurements which are sometimes aptly phrased as:

"The biology is with us, the physics are against us".

1.5 Potential for simultaneous use of Electrical Impedance and Ultrasound propagation measurements to assess temperature non-invasively

The aim of this research is to explore the use of electrical impedance and ultrasound propagation velocity measurements simultaneously to assess temperature in deep body tumours non-invasively during mild hyperthermia.

From the mid-1980s when work on methods of producing controlled hyperthermia as an adjunct to radiotherapy really started, measuring the temperature of the heated volume has always presented a significant – and still unresolved – challenge. All temperature measurements currently used are invasive, which is not appropriate for a routine clinical tool (section 1.3.1). Several non-invasive temperature measurement techniques have been proposed but none achieves the required standard for clinical mild hyperthermia and each has its own drawbacks (section 1.3.2).

Preliminary works on the non-invasive temperature measurements by electrical impedance method in tissue as discussed in section 1.3.2.4 showed that the observed impedance changes were not simply due to changes in conductivity of the intra- and extra-cellular fluids but also due to intra- and extra-cellular fluid volume changes and membrane conductance changes (Esrick and McRae, 1994). As discussed in section 1.3.2.4, extra-cellular volume changes resulting from vasodilatation was considered to be the primary effect giving rise to impedance changes (Gersing, 1999). Brown and co-workers (Brown *et al.*, 2000a) has shown that lumped parameter models of tissue can be used with multi-frequency electrical impedance measurements to separate data from extra- and intra-

cellular space. Paulsen and Jiang (Paulsen and Jiang, 1997) suggested that improvements in the image reconstructions technique could reduce the errors in temperature prediction from the order of 10˚C reported by many workers to 2˚C (section 1.3.2.4). In addition, the region of negative sensitivity found by Brown and co-workers (Brown *et al.*, 2000b) may mask impedance changes related to temperature and this needs further investigation if electrical impedance measurement is considered as the non-invasive temperature measurement technique.

As discussed in section 1.3.2.3, a number of workers have proposed that the change in the propagation velocity of ultrasound as the method of monitoring temperature changes during hyperthermia therapy (Seip and Ebbini, 1995; Miller *et al.*, 2004). Moreover, techniques based on this have widely been investigated in the field of high intensity focused ultrasound (HIFU) ablation techniques (ter Haar, 1999a). However, Miller and co-workers (Miller *et al.*, 2002) pointed out that changes in propagation velocity are different in different tissues and different in the same tissues from different species. The majority of temperature measurement works based on ultrasound propagation velocity has been carried out on excised tissue samples and therefore, changes in tissue due to physiological processes was not observed.

If electrical impedance and ultrasound propagation velocity measurements are used simultaneously, these will be sensitive to both the physical changes (resistivity, density) and physiological changes (active increases in the intra- and extra-cellular fluid volumes and changes in membrane conductance) in the tissue. Modelling how these physical and physiological processes change both the observed electrical impedance and ultrasound propagation velocity has the potential to estimate the different component of the changes with temperature. Essentially, the simultaneous measurements of these physical and physiological changes in tissue with temperature by electrical impedance and the ultrasound propagation velocity measurements may give a non-invasive thermometry, and this will be the first attempt to combine two approaches to non-invasive temperature measurement. This thesis explores the novel approach of combining these two measures for non-invasive thermometry during hyperthermia.

2 Multi-frequency Electrical Impedance Measurements

Mapping the electrical impedance distribution in a tissue volume is possible with Electrical Impedance Tomography (EIT) techniques which use multiple surface electrodes (Grimnes and Martinsen, 2000). In electrical impedance tomography (EIT), an alternating current of about 1mA is injected in one pair of electrodes and voltages are measured from the other pairs. Current injection is then, moved between another, commonly adjacent, pair of electrodes so that all electrode pairs are used. It has been shown that the images of the internal electrical conductivity distribution based on the information of the injected current and measured potentials on the surface of the body can be reconstructed using image reconstruction algorithms (Barber and Brown, 1986; Lionheart, 1999; Lionheart, 2004). Initial work used a single frequency within the range of 20–50kHz; however, the fundamental problem of electrical impedance tomography (EIT) is that the absolute impedance is difficult to determine accurately because of the uncertainty in the position of the electrodes (Grimnes and Martinsen, 2000). With the introduction of multi-frequency electrical impedance tomography (EIT), the possibility of tissue characterization based on impedance spectroscopy has been realised (Wilson *et al.*, 2001; Brown *et al.*, 1994; Riu *et al.*, 1992; Riu *et al.*, 1995). In addition, if the impedance varies significantly with frequency between different organs and tissues, frequency difference imaging techniques became possible. The images will be based on the characteristics changes of impedance with frequency rather than the absolute value of impedance. Indexes such as the relation between measured data at two frequencies may be used to characterise the tissue (Brown *et al.*, 1994), though it is difficult to choose two frequencies to match all tissue types due to differences of dispersion frequencies of tissues. Brown and co-workers (Brown *et al.*, 1994) used seven frequencies from 9.6 to 614kHz in a 16 electrode thorax measurement to observe the impedance changes with frequency. They (Brown *et al.*, 1994) also derived indexes using 9.6kHz data as the reference and suggested that it is possible to identify tissue types on the basis of their impedance spectrum and the differences in the impedance spectrum at 2 frequencies.

2.1 EIT Imaging

The temperature measurement technique used in mild hyperthermia in addition to having the required accuracy of less than 1°C must also be capable of measuring the temperature distribution within the tumour volume. Images, known as Electrical Impedance Tomography (EIT) images, have been constructed from tetrapolar electrical impedance measurements. The first EIT images were constructed using a modified x-ray CT 'back

projection' algorithm based on a linear approximation described by Barber and Brown (Barber and Brown, 1986) and later modified by others (Santosa and Vogelius, 1990; Bernestein and Casadio, 1996). The mathematicians consider EIT reconstructions problem as an inverse problem. The approach, to some extent obeys the following procedure: the problem is nonlinear so linearize it, the linear problem is ill posed so regularize it (using the zeroth-order Tikhonov (Vauhkonen *et al.*, 1998), discrete Laplacian filter (Polydorides and Lionheart, 2002), NOSER priors (Cheney *et al.*, 1990; Graham and Adler, 2007)), and since the linear approximation cannot reconstruct large contrast or complex geometries, apply the process iteratively (Lionheart, 2004). The iterative algorithms have been based on a variety of techniques including least squares (Borcea *et al.*, 1996; Borcea, 2001; Dobson and Santosa, 1994; Kallman and Berryman, 1992), the variational method (Wexler *et al.*, 1985; Kohn and Vogelius, 1987; Kohn and McKenney, 1990; Woo *et al.*, 1993) and statistical inversion (Kaipio *et al.*, 2000; Vauhkonen *et al.*, 2001).

Paulsen and Jiang (Paulsen and Jiang, 1997) proposed a hybrid method combining the least square and total variational minimization method which can provide higher quality image reconstructions than either method alone. This hybrid algorithm (Paulsen and Jiang, 1997) can simultaneously recover both the conductivity and permittivity distribution under a variety of simulation conditions and in the presence of significant amounts of noise (>1% noise level, even with 10% noise level image can be recognizable). Moreover, this hybrid algorithm (Paulsen and Jiang, 1997) was used to estimate temperature and can dramatically reduce the maximum temperature errors to 2°C relative to more than 10°C in previous thermal simulations with the condition that a priori anatomical information is used (section 1.3.2.4, chapter 1). Though, this technique still lacks enough sensitivity to be able to recover highly accurate thermal profile (to within 0.1°C), it has much more promising potential for EIT to use as a non-invasive thermal tracking method in clinical hyperthermia.

Several other approaches for EIT image reconstructions have been proposed, incorporating many refinements to improve the image reconstruction (Lionheart, 2004), However, such refinements were not widely accepted because of a lack of agreement on which of the refinements gave the best improvements and how these refinements could be combined into a single algorithm. To address this issue, a 2D linear reconstruction algorithm for lung EIT, called GREIT (Graz Consensus Reconstruction algorithm for EIT) has been implemented based on a consensus of multi-disciplinary researchers in the area (Adler *et al.*, 2009).

However, most of the EIT image reconstruction algorithms proposed to date are capable of reconstructing two dimensional (2D) EIT image. So there remains a major problem with three dimensional (3D) EIT image reconstructions because of the currents within the body. In most cases, data are collected on a three dimensional body and the image reconstruction performed assuming the body was two dimensional (Barber and Brown, 1984). However, data measured on a three dimensional body (unless multiple planes of electrodes are used (Metherall *et al.*, 1996)) cannot be fitted accurately to any two dimensional conductivity distribution (Lionheart, 1999). Moreover, attempts to fit a two dimensional model result in errors of position and shape of anomalies (Globe, 1990). The reason for the two dimensional image reconstructions assumption is that some researchers considered that the injected currents are confined to the two dimensional electrode planes. The current spread in three-dimensions means that it flows through off plane structures which has significant effect on the reconstructed images (Rabbani and Kabir, 1991).

Several electrode configurations are used for EIT imaging, however, they are all based on tetrapolar measurements because of its ability to minimise the impact of electrode contact impedance on the measurements, whilst it has been used in a number of research areas such as respiratory system (Brown *et al.*, 1994), cardiac system (Newman and Callister, 1999), cervical neoplasia (Brown *et al.*, 2000a), fat and lean body mass estimation (Segal *et al.*, 1988), tissue characterisation (Shallof and Barber, 1997) etc.. There is very little information in the literature about the sources of errors, when making tetrapolar impedance measurements. The spatial sensitivity of tetrapolar impedance measurements is complex having regions of negative sensitivity, which may introduce large errors when measuring the heterogeneous materials (Brown *et al.*, 2000b).

If electrical impedance measurement techniques are to be part of a new technique for measuring temperature during mild hyperthermia, then a better understanding of, and a way of controlling the spatial sensitivity of the measurement is required. In this chapter, spatial sensitivity distributions of different electrode configurations for making tetrapolar electrical measurements are investigated using computer simulations.

2.2 Sensitivity analysis of Electrical Impedance Measurements

2.2.1 Introduction

As discussed in the previous section electrical impedance measurements on the human body have found a variety of applications in clinical diagnosis and research including the measurement of physiological functions (Zhang *et al.*, 1986), the assessment of tissue characteristics (Brown *et al.*, 2000a; González-Correa, 1999) and imaging (Wilson *et al.*, 2001). Over the past two decades much work has focused on the potential uses of multi-frequency electrical impedance imaging. However, multi-frequency tetrapolar electrical impedance measurements have the potential to form a non-invasive or minimally invasive probe into tissue structure at the cellular level as electrical impedance measurements at multiple frequencies can be related to tissue structure through the use of lumped parameter models such as the Cole-Cole model (Cole and Cole, 1941). To date, this approach has only been applied to surface tissues (Brown *et al.*, 2000a; González-Correa, 1999), however, the ability to characterise tissue structures deep within the body through spatially localised measurements would have considerable potential in addressing non-invasive temperature measurement. The major problem in achieving this is the complex spatial sensitivity distribution of tetrapolar impedance measurements (Brown *et al.*, 2000b) coupled with tissue inhomogeneities.

Geselowitz (Geselowitz, 1971) modelled the sensitivity distribution of tetrapolar impedance measurements by considering the vector current densities from pairs of electrodes (which he termed lead fields). He (Geselowitz, 1971) showed that the sensitivity at a point can be defined as the scalar or dot product of the lead fields (vector current densities are associated with both current injection and voltage measurement electrode pairs) resulting from unity current injection between two pairs of electrodes. The reciprocity theorem applies so that the current injection and potential measurement electrode pairs can be interchanged without changing the measured transfer impedance. If J_1 and J_2 are the current densities resulting from the current injections, I_1 and I_2 between the current drive and voltage measurement electrodes respectively, then the sensitivity, S, at a point for the tetrapolar impedance measurement can be calculated as:

$$\boldsymbol{S} = \frac{\boldsymbol{J_1} \cdot \boldsymbol{J_2}}{\boldsymbol{I_1 I_2}} \qquad \text{2-1}$$

where, (.) represent the dot product of the two current densities.

Calculating transfer impedance is difficult. An analytical solution is only possible for simple geometries whilst finite element methods can be used to give numerical solution for more complex geometries. Using vector interpretation of Geselowitz's theory (Geselowitz, 1971) in a semi-infinite homogeneous medium, Brown and co-workers (Brown *et al.*, 2000b) investigated the sensitivity profile for an electrode geometry. In their work with the electrodes placed at the corners of a square, Brown and co-workers (Brown *et al.*, 2000b) showed that the average sensitivity in the plane at the electrode surface was zero, that there were regions of negative sensitivity which extended down beneath the electrodes into the measurement volume to a depth of half of the electrode spacing; and that there was a maxima in the average sensitivity of a plane parallel to the plane of the electrodes at a distance of one-third of the electrode spacing from the plane of the electrodes (Brown *et al.*, 2000b). The first of these findings explains why tetrapolar impedance measurements are not dominated by surface effects and hence why it is possible to investigate the characteristics of tissue within the body. For example, tetrapolar impedance measurements have been used in conjunction with Cole-Cole models to characterise accessible epithelial tissues (Brown *et al.*, 2000a; González-Correa, 1999).

In this chapter, the previously validated model based on Geselowitz's lead theory (Brown *et al.*, 2000b) has been applied to investigate the spatial distribution of the sensitivities in tetrapolar impedance measurements (TPIM) and to the recently proposed focused impedance measurement (FIM) method for the different electrode configurations and compare the resultant sensitivity distributions between the two methods.

2.2.2 Materials and methods

In tetrapolar impedance measurements, electrodes can be configured on a surface in various geometrical patterns. Figure 2-1 shows the possible electrode positions and the combinations of current drive and voltage measurement to create tetrapolar measurements. From the sensitivity analysis of different tetrapolar electrode configurations, the optimal electrode configuration can be chosen, which localizes the sensitivity to a particular zone of interest and maximises the sensitivity to the centre of that zone. For tetrapolar measurements, conventionally electrodes are placed in a line; where the outer pair forms the drive electrodes and inner pair forms the receive electrodes. This electrode configuration is denoted as TPIM-8. An electrode configuration of this geometrical pattern was used in imaging and modelling respiratory related electrical impedance changes (Brown *et al.*, 1994). In another tetrapolar electrode configuration,

instead of placing all the four electrodes in a line, the inner two receive electrodes are just offset from the line of the outer pair of drive electrodes in opposite directions and placed at corners of one of the diagonals of a hypothetical square (Rabbani *et al.*, 1999), a configuration denoted TPIM-6. This type of configuration is used for cardiac system (Newman and Callister, 1999). Electrodes can also be placed at the corners of a hypothetical square, where the drive and the receive electrode pairs are on opposite sides of the square, denoted as TPIM-4. This is the most widely used electrode configuration for tetrapolar measurements on epithelial tissue (Brown *et al.*, 2000b).

Recently, a technique called Focused Impedance Measurement (FIM) has been proposed in which two tetrapolar measurements are summed to maximise the sensitivity of the measurement to a region beneath the electrodes (Rabbani *et al.*, 1999). Three different electrode configurations, using eight, six (Rabbani *et al.*, 1999) and 4 electrodes (Rabbani and Karal, 2008), have been identified for making FIM measurements. Experimental results from electrolytic tanks performed using the six- and four- electrode configurations have shown that both these electrode configurations produce a maxima in the measurement sensitivity in the central region beneath the electrodes. However, the spatial, and in particular the depth, resolution of these measurements did not allow the spatial sensitivity distributions achieved by FIM to be investigated in detail. Further, the relationship between the characteristics of these maxima, the electrode configuration and the electrode spacing remained unknown.

The three different electrode configurations for making FIM using eight, six and four electrodes are shown in Figure 2-1. For each electrode configuration, the sensitivity of the FIM is the sum of the sensitivities for two tetrapolar impedance measurements (M_1 & M_2).

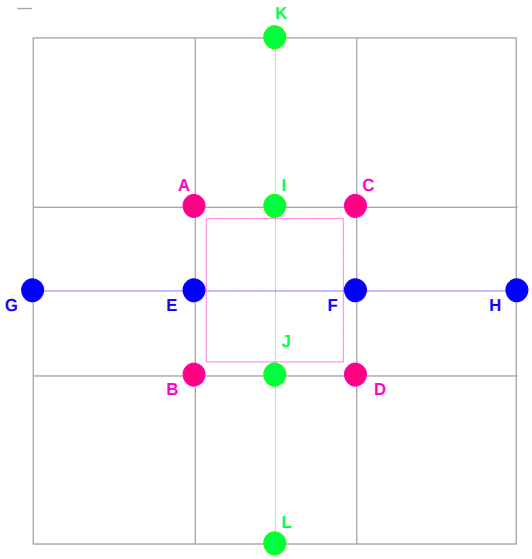

Tetrapolar measurements with different electrode configuration	
Electrode configurations	Measurements
TPIM-8	Drive Electrodes: G H / Drive Electrodes: K L Receive Electrodes: E F / Receive Electrodes: I J
TPIM-6	Drive Electrodes: G H / Drive Electrodes : K L Receive Electrodes: A D / Receive Electrodes:B C
TPIM-4	Drive Electrodes: A B / Drive Electrodes: A C Receive Electrodes: C D / Receive Electrodes: B D

FIM measurements with different electrode configuration. In each case, the FIM is given by M1+M2		
Electrode configurations	Measurement 1 (M1)	Measurement 2 (M2)
FIM-8	Drive Electrodes: G H Receive Electrodes: E F	Drive Electrodes: K L Receive Electrodes: I J
FIM-6	Drive Electrodes: G H Receive Electrodes: A D	Drive Electrodes: K L Receive Electrodes: B C
FIM-4	Drive Electrodes: A B Receive Electrodes: C D	Drive Electrodes: B D Receive Electrodes: A C

Figure 2-1 Showing electrode positions to create different configuration for tetrapolar and focused impedance measurements (FIM). Individual measurements to create tetrapolar and focused impedance measurement are shown. Two sets of measurements for each tetrapolar configuration are shown. The FIM measurement is given by summing the two individual measurements M1 and M2.

In the eight-electrode configuration, the electrodes are arranged in two groups of four electrodes such that straight lines through the two groups of electrodes form a cross with equal length arms. For each group of 4 electrodes the tetrapolar measurements (denoted TPIM-8) are made by driving current through the outer pair of electrodes with measurements of the voltage made through the inner pair of electrodes. The FIM (denoted FIM-8) is then the sum of the measurements from the two inner pairs of electrodes. For a six-electrode FIM, the drive electrodes are in the same positions as they are for the eight-electrode configuration. If these are considered to be placed at the centre of the sides of a square, then the single pair of receive electrodes are placed at the corners of a smaller concentric square. The position of the receive electrodes (at either A & D, or B & C, Figure 2-1) notionally corresponds to the intersection of isopotential lines between the two pairs of drive electrodes (Rabbani *et al.*, 1999). The two tetrapolar impedance measurements (denoted TPIM-6) are made from the same pair of receive electrodes with the drive swapped between the two pairs of drive electrodes. The FIM (denoted FIM-6) is the sum of the two tetrapolar impedance measurements. For the 4 electrode configuration (denoted FIM-4), the electrodes are placed at the corners of a square and the two tetraplolar impedance measurements (denoted TPIM-4) are made with the drive and receive electrodes positioned on opposite sides of the square. The focused impedance

measurement (denoted FIM-4) is the sum of measurements made from the two orthogonal directions across the square.

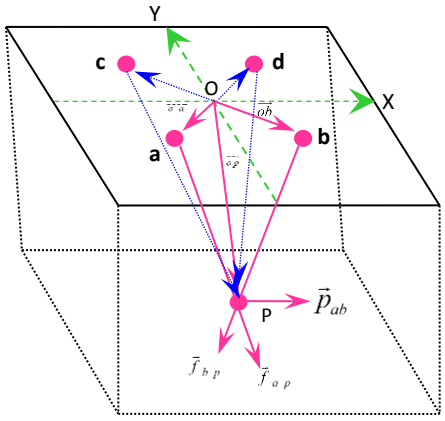

Figure 2-2 Geometry used for Geselowitz's sensitivity analysis (Brown *et al.*, 2000b; Islam *et al.*, 2010)

According to Geselowitz's lead field theory (Geselowitz, 1971), the sensitivity of a tetrapoloar impedance measurement at a point, p, can be defined as the scalar product of the vector current densities (the lead fields) for unit current injection between the two pairs of electrodes (equation 2-1). For a homogeneous medium, it can be shown that the vector lead fields are determined by the vector paths from the electrode to the point p, where the sensitivity is to be determined (Brown *et al.*, 2000b). The geometry shown in Figure 2-2 with four electrodes at a, b, c and d is considered for the analysis. The lead field at point p for a current injection through electrodes a and b is given by $\vec{P}_{ab} = \vec{f}_{ap} + \vec{f}_{bp}$, where $\vec{f}_{ap}$ and $\vec{f}_{bp}$ are the vector current densities resulting from current injection at electrodes a and b respectively. If the origin of the axis system is o, then $o\vec{a}$ and $o\vec{p}$ are the vectors from this origin to the electrode a and the point p, respectively. If a semi-infinite homogeneous medium was considered for the geometry shown in Figure 2-2, then the vector current density can be calculated. In that case, the vector current density $\vec{f}_{ap}$ should have the direction given by $(\overrightarrow{op} - \overrightarrow{oa})$ and a magnitude proportional to the magnitude ap^{-2} (by the inverse square law). The magnitude of the vector $\overrightarrow{ap}$ is calculated as $|ap| = sqrt(sum((\overrightarrow{op} - \overrightarrow{oa}).\hat{}2))$. The unit vector giving the direction of the vector current density $\vec{f}_{ap}$ is given by: $(\overrightarrow{op} - \overrightarrow{oa})./ap$. Therefore, $\vec{f}_{ap}$ can be calculated using:

$$\vec{f}_{ap} = \frac{\overrightarrow{op} - \overrightarrow{oa}}{|\overrightarrow{op} - \overrightarrow{oa}|^3}$$

Similarly, $\vec{f}_{bp}$ can be calculated as

$$\vec{f}_{bp} = -\frac{\overrightarrow{op} - \overrightarrow{ob}}{\left|\overrightarrow{op} - \overrightarrow{ob}\right|^3}$$

The sign of vector current density $\vec{f}_{bp}$ changes because the electrode b has current of opposite polarity than electrode a. Thus, the lead field from electrodes a and b is given by $\vec{P}_{ab} = \vec{f}_{ap} + \vec{f}_{bp}$. The vector current densities at point p resulting from a current injection at the other electrodes (c and d) can be calculated in an identical manner. If the lead fields for current injected at electrode pairs a, b and c, d are $\vec{P}_{ab}$ and $\vec{P}_{cd}$ respectively, then the sensitivity of the tetrapolar impedance measurement at point p, P_s, for unit current injection is given by:

$$P_s = \vec{P}_{ab} \cdot \vec{P}_{cd}$$

To find the sensitivity for a focused impedance measurement, the sensitivity for the two individual tetrapolar impedance measurements are summed. It should be noted that values of P_s are calculated from the vector distances between the electrodes and a point within a semi-infinite volume and are thus independent of boundary conditions, which would not be the case if the sensitivity were calculated by finite element or finite difference techniques, where a bounded volume is used.

Using Matlab™, the sensitivity was calculated for all three TPIM electrode configurations for a 200mm sided cube on a mesh with 1mm spacing and the sensitivity for FIM was obtained from the summation of two TPIM measurements. The simulation assumes a semi-infinite homogeneous isotropic medium. Real tissues are not homogeneous, nor in many cases isotropic, and therefore lead fields determined using the geometric approximation described above will contain errors dependant on the degree and type of homogeneity and isotropy. In addition, part of the inhomogeneity of real tissues is their cellular structure giving electrical impedance which is frequency dependant. This frequency dependence is not modelled in the sensitivity analysis. For the eight-electrode FIM configuration, six drive electrode spacings (Dr8) between 30mm and 60mm were used at intervals of 6mm. For each of these six drive electrode spacings, the sensitivity was calculated for receive electrode spacings between 6mm and (Dr8-6)mm at intervals of 6mm. In all cases electrodes were symmetrically placed around the origin as shown in Figure 2-2. For the six-electrode FIM configuration, six drive electrode spacings (Dr6) between 30mm and 60mm were used at intervals of 6mm. For each of these six drive electrode spacings, the

sensitivity was calculated for receive electrode positions, where the horizontal and vertical coordinates were the same, and varied between 6mm and (Dr6-6)mm at intervals of 6mm. For the four-electrode FIM configuration, the electrodes can be thought to be positioned at the corners of a square, where the drive electrode spacing is the same as the receive electrode spacing. For this configuration electrode spacings of 6 to 62mm at 2mm intervals were used. Since the sensitivity of a focused impedance measurement is the sum of the sensitivities for two tetrapolar impedance measurements, the sensitivity of the equivalent tetrapolar measurement was also calculated.

For all the electrode configurations and spacings studied, the electrodes were centrally placed on one side of the 200mm sided cube (the *x, y* plane) with the *z* direction representing the distance (depth) into the measured volume. The sensitivity of planes parallel to the plane of electrodes was assessed by summing the sensitivity values on those planes. For each electrode configuration and spacing analysed the average sensitivities of planes spaced at 1mm intervals in the z direction were calculated down to a depth of 200mm. These were used to investigate whether the previous finding of a plane with a maximum average sensitivity existed in other tetrapolar electrode configurations and in the three FIM electrode configurations. Regions of negative sensitivity were identified in the sensitivity data for each electrode configuration and spacing studied and the perpendicular distance in the *z* direction to where these regions of negative sensitivity ceased to exist was determined. Previous work has shown that the pattern of sensitivity within the medium was complex with multiple peaks in the sensitivity beneath the electrodes (Brown *et al.*, 2000b) but did not examine the spatial distribution of sensitivity. The FIM technique aims to maximise the sensitivity beneath the centre of the electrode configuration. With increasing depth into the measured volume, the peaks beneath the electrodes get smaller and the sensitivity beneath the centre of the electrode configuration increases. Initially, the sensitivity in this central area commonly consists of multiple peaks but with increasing depth these merge to a single maximum. Therefore, for each electrode configuration and spacing, the minimum distance from the plane of the electrodes to the plane where this single maximum occurred was identified. In order to assess the spatial size of the peak beneath this single maxima its full width half maximum (FWHM) size was measured for its largest dimension in the *x* or *y* direction. In addition, the ratio of the sensitivity at this single maximum to the mean sensitivity on the plane on which it occurs was also investigated. For both the FWHM and sensitivity analyses, the depth at which the single maximum occurred was investigated in terms of the electrode spacing. The previous work (Brown *et al.*, 2000b)

used a TPIM-4 electrode configuration, where the spacing between the receive electrode spacing and the drive-receive electrode spacing are the same. In the TPIM-6 and TPIM-8 electrode configurations this is no longer the case. Therefore, the relationship between the measures of sensitivity distribution and both the receive electrode spacing and the drive-receive electrode spacing was investigated. A graphical analysis was used to investigate the relationships and the Pearson-r product moment correlation used to quantify them.

2.2.3 Results of sensitivity analysis

Computer simulation of Geselowitz's lead field theory (Geselowitz, 1971) shows different sensitivity distributions for different configurations of tetrapolar and focused impedance measurements. As expected, all electrode combinations for both tetrapolar and focused impedance measurements showed complex patterns of sensitivity within the measured volume. All the configurations of tetrapolar and focused impedance measurements gave zero, positive and negative values of sensitivity. There are peaks in the sensitivity, particularly beneath the electrodes, and it is in these regions that areas of negative sensitivity occur (Figure 2-3).

2.2.3.1 Tetrapolar impedance measurement sensitivity results

The simulation results for all tetrapolar electrode configurations and spacings showed a peak in the average sensitivity of planes parallel to and beneath the plane of the electrodes. For all the tetrapolar electrode configurations, a plot of the depth of the plane with the maximum average sensitivity against the drive-receive electrode spacing showed a straight line relationship (r^2 =0.97, 0.89 and 0.98 for TPIM-8, TPIM-6 and TPIM-4 respectively) where points from the different electrode configurations were overlapping and following the same trajectory. The Pearson r analysis for the pooled data from all the electrode configurations gave a value of r^2 of 0.99 and a line-of-best-fit analysis showed this maxima to be at a plane 0.3 times the drive-receive electrode spacing beneath the plane of the electrodes (Figure 2-4). For the TPIM-8 and TPIM-6 electrode configurations, the depth of the plane with the maximum average sensitivity was uncorrelated with the receive electrode spacing (r^2 = 0.48 & 0.31, respectively). All tetrapolar electrode configurations showed regions of negative sensitivity beneath the electrodes.

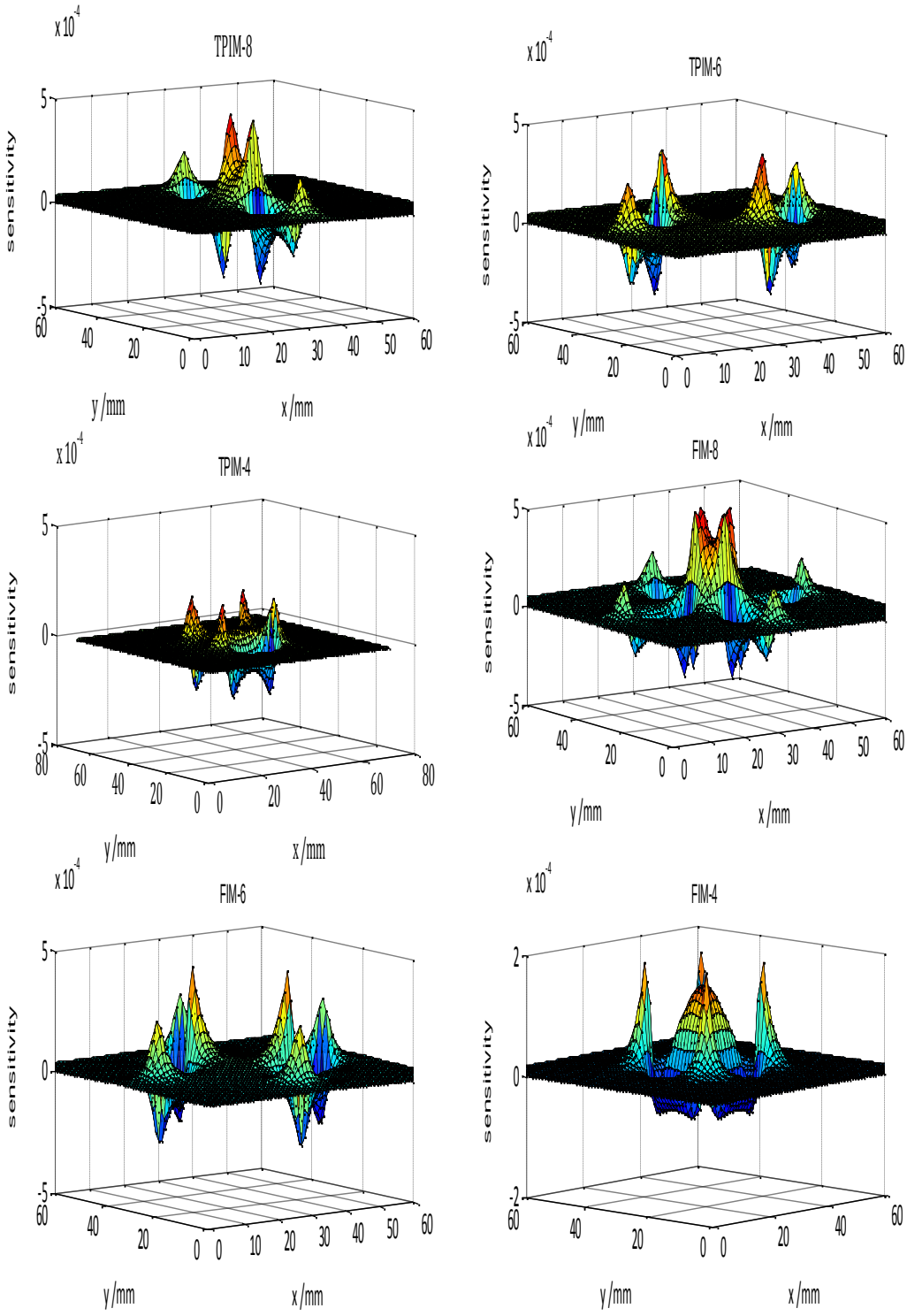

Figure 2-3 The sensitivity distribution for tetrapolar and FIM measurements having approximately the same drive-receive electrode spacing (18mm) at a plane depth of 2mm. For the TPIM-8 and the 8 electrode FIM configuration the drive electrode spacing was 48mm and the receive electrode spacing 12mm. For the TPIM-6 and the 6 electrode FIM configuration the drive electrode spacing was 48mm and the receive electrode spacing was 25.5mm measured across the diagonal. For the TPIM-4 and the 4 electrode FIM configuration the electrode spacing was 18mm.

Graphs of the depth to which these region of negative sensitivity extend against drive-receive electrode spacing showed a linear relationship (r^2 = 0.98, 0.96 and 1 for TPIM-8, TPIM-6 and TPIM-4 respectively) with values from the different electrode configurations following the same trajectory (Figure 2-5). Analysing the pooled data from all electrode configurations showed the depth to which these regions of negative sensitivity extend into the measured volume to be highly correlated to the drive-receive electrodes spacing (r^2 = 0.99) and a line-of-best-fit analysis showed that the depth of planes with negative sensitivity extend 0.5 times the drive-receive electrode spacing into the measured volume (Figure 2-5). For the TPIM-8 and TPIM-6 electrode configurations no correlation was found between the depth to which regions of negative sensitivity extend into the measured volume and the receive electrode spacing (r^2 = 0.50 and 0.19, respectively).

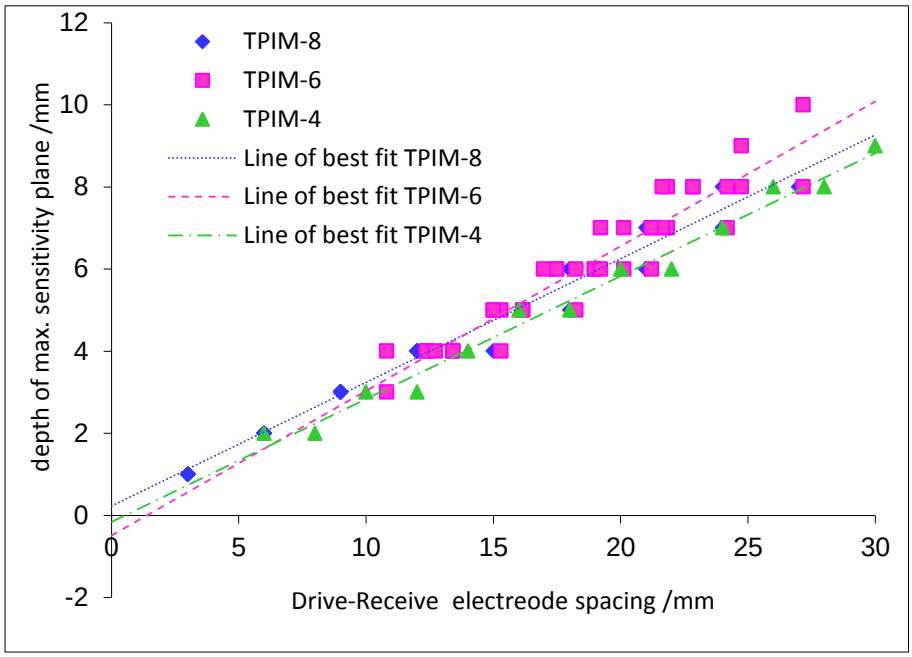

Figure 2-4 Showing the depth of the plane at which the maximum sensitivity occurs against the drive-receive electrode spacing for the different tetrapolar electrode configuration.

The depth into the measured volume at which a single maxima in the sensitivity existed beneath the centre of the electrode configuration for the TPIM-8 and TPIM-6 electrode configurations was difficult to analyse because there were a high proportion of electrode spacings ($^{26}/_{39}$ for TPIM-8 and $^{26}/_{39}$ for TPIM-6) for which no single peak existed at a depth of 200mm into the measured volume. Therefore, no further analyses were done on these data. For the TPIM-4 electrode configuration, a single maxima existed for all the electrode spacings analysed and the depth of the plane at which this occurred was found to be correlated with the electrode spacing (r^2 = 0.99). A graph showed a straight line relationship

with the electrode spacing where the slope of the line-of-best-fit was calculated to be 0.23 (Figure 2-8). A correlation was found (r^2 = 0.99) between the FWHM size of the single maxima beneath the electrode and the electrode spacing. A graph showed a straight line relationship between the two and analysis gave the slope of the line-of-best-fit as 0.41 (Figure 2-9).

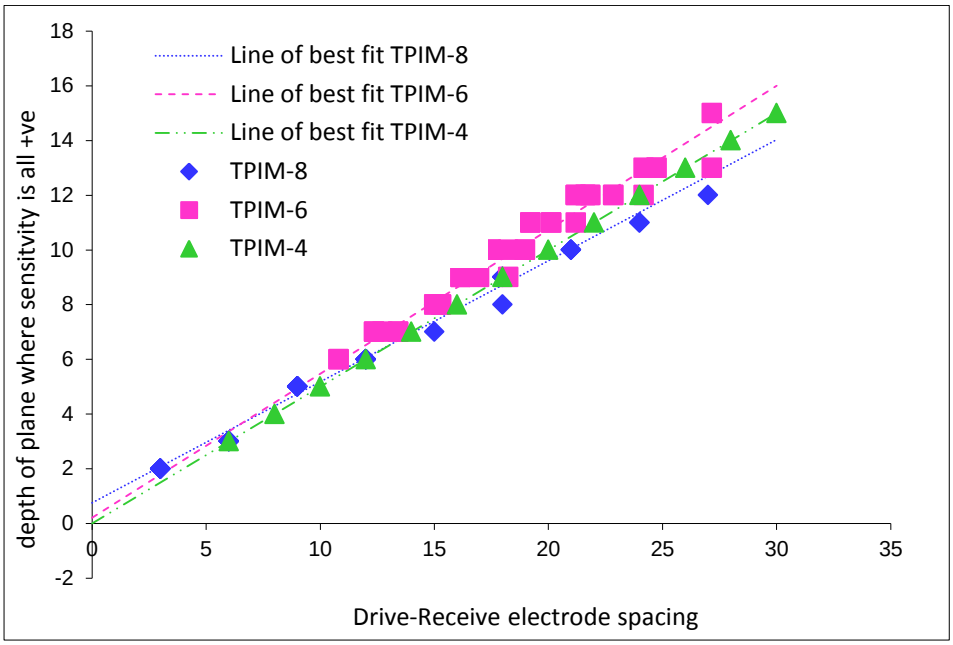

Figure 2-5 Showing the depth at which regions of negative sensitivity cease against drive-receive electrode spacing for the different tetrapolar electrode configurations.

An analysis of the ratio of sensitivity at the single maximum to the mean sensitivity on the plane at which it occurs against receive electrode spacing for the TPIM-4 electrode configuration showed that this ratio was proportional to the inverse of the square of the electrode spacing (Figure 2-10).

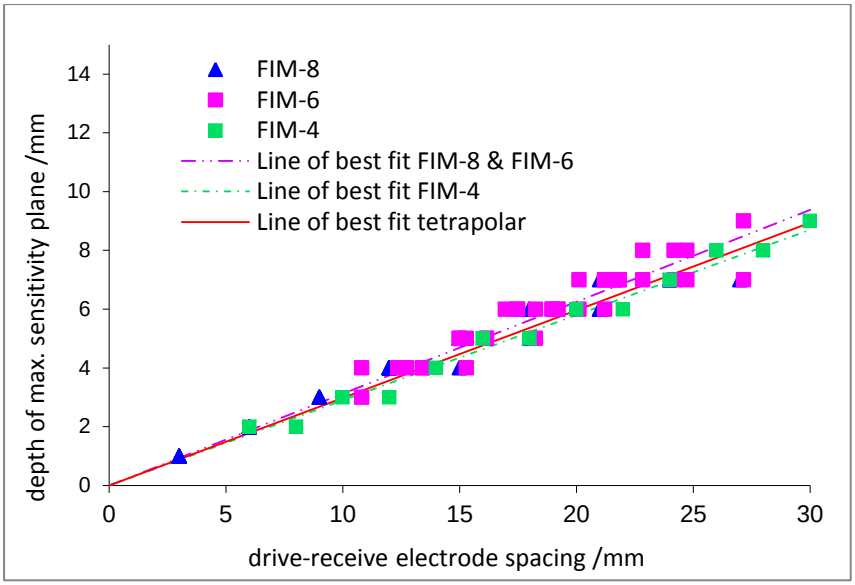

Figure 2-6 Showing the depth of the plane at which the maximum in the mean sensitivity occurs against the drive-receive electrode spacing for the different FIM configurations.

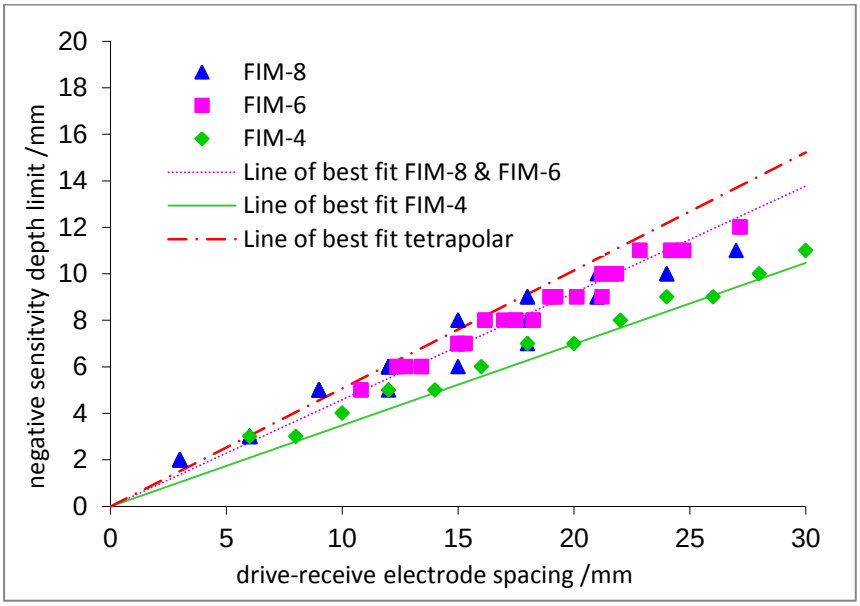

Figure 2-7 Showing the depth at which regions of negative sensitivity cease against the drive-receive electrode spacing for the different FIM electrode configurations.

2.2.3.2 Focused impedance measurement sensitivity results

All FIM electrode configurations and spacings showed a peak in the average sensitivity of planes parallel to and beneath the plane of the electrodes. No correlation was found between the depth of the maximum average sensitivity plane and the receive electrode spacing for the FIM-8 and FIM-6 electrode configurations (r^2 = 0.48 & 0.31, respectively).

A plot of the depth of the maximum average sensitivity plane against the drive-receive electrode spacing (Figure 2-6) showed an almost straight line relationship. The data points for the FIM-8 and FIM-6 configurations were overlapping and analysis for the combined data set showed a correlation (r^2 = 0.97) with the slope of the line-of-best-fit being 0.31. The data points for the FIM-4 electrode configuration were consistently below those for the other two electrode configurations and analysis of these data showed a good correlation (r^2 = 0.99) with the slope of the line-of-best-fit being 0.29. A χ^2 analysis comparing values predicted from the line-of-best-fit for the FIM-8 and FIM-6 data sets against the measured values for the FIM-4 configuration showed no significant difference ($p>0.05$) and therefore, a single line-of-best-fit could have been used. As expected from the previous result, the values of the average sensitivity for the planes where this was maximum varied as the inverse of the square of the drive-receive electrode spacing (χ^2 test, $p < 0.05$) and comparing modelled values against predicted values from the curve fitting analysis for the three electrode configurations showed no difference in the sensitivity values obtained between them (χ^2, $p > 0.05$). All electrode combinations showed that the values obtained were double those obtained from the equivalent single tetrapolar measurement. The peaks of negative sensitivity seen in Figure 2-7 reduce in magnitude with increasing depth.

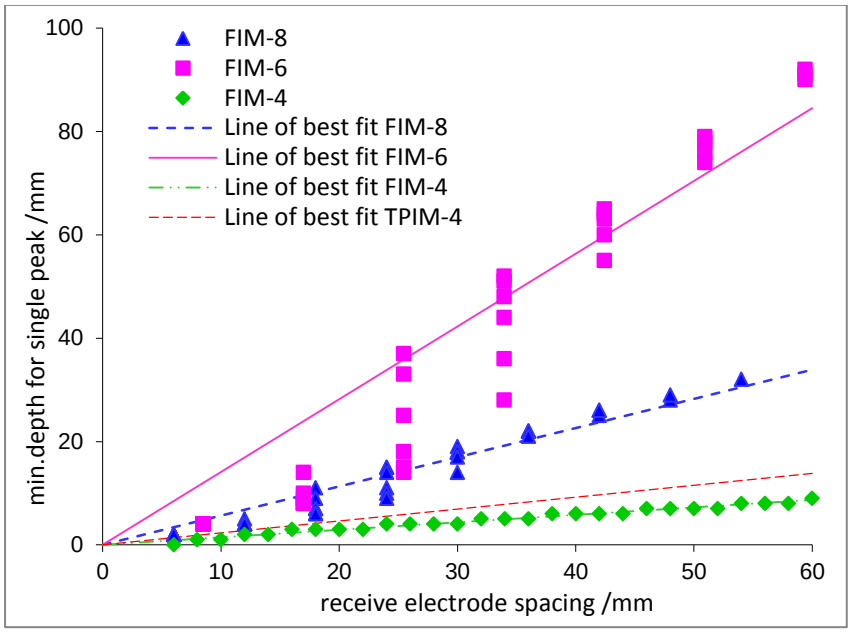

Figure 2-8 Showing the depth at which there is a single peak in the sensitivity distribution beneath the centre of the electrode configuration as a function of the receive electrode spacing. The line-of-best-fit for the 4 electrode tetrapolar electrode configuration (TPIM-4) is shown for comparison.

Analysis showed no correlation between the depth to which regions of negative sensitivity extend and the receive electrode spacing for either the FIM-8 or FIM-6 electrode configurations (r^2 = 0.44 &0.13, respectively). However, the plot of the depth at which the sensitivity becomes all positive against the drive-receive electrode spacing showed a straight line relationship for each electrode configuration (Figure 2-7). Once again, the FIM-8 and FIM-6 data sets overlaid each other but the FIM-4 data clearly followed a different path. Analysis of the pooled FIM-8 and FIM-6 data gave a value of r^2 of 0.99 for the correlation between the depth at which the sensitivity became all positive and the drive-receive electrode spacing. A line-of-best-fit analysis gave the slope of this relationship to be 0.46. A correlation analysis also demonstrated a correlation between the depth at which the sensitivity became all positive and the drive-receive electrode spacing for the FIM-4 electrode configuration (r^2 = 1.00) but with the slope of the line-of-best-fit being 0.35. Figure 2-7 also shows that the depth to which regions of negative sensitivity occur is reduced by using the FIM electrode configurations compared to the tetrapolar electrode configurations.

With increasing depth the sensitivity beneath the centre of the electrode configuration increases relative to other sensitivity values on the same plane. A correlation analysis between the depth at which a single maxima existed beneath the centre of the electrode configuration and the drive-receive electrode spacing showed no significant correlation for either the FIM-8 or FIM-6 electrode configurations (r^2 = 0.60 & 0.08, respectively). Plots of the minimum depth at which the single maxima occurred and the receive electrode spacing (Figure 2-8) showed a linear relationship for each of the electrode configurations, but with a different slope for the line-of-best-fit for the different configurations: 0.56, 1.41 and 0.14 for the FIM-8, FIM-6 and FIM-4 configurations respectively. Thus, the minimum depth was greatest for the FIM-6 configuration and least for the FIM-4 configuration.

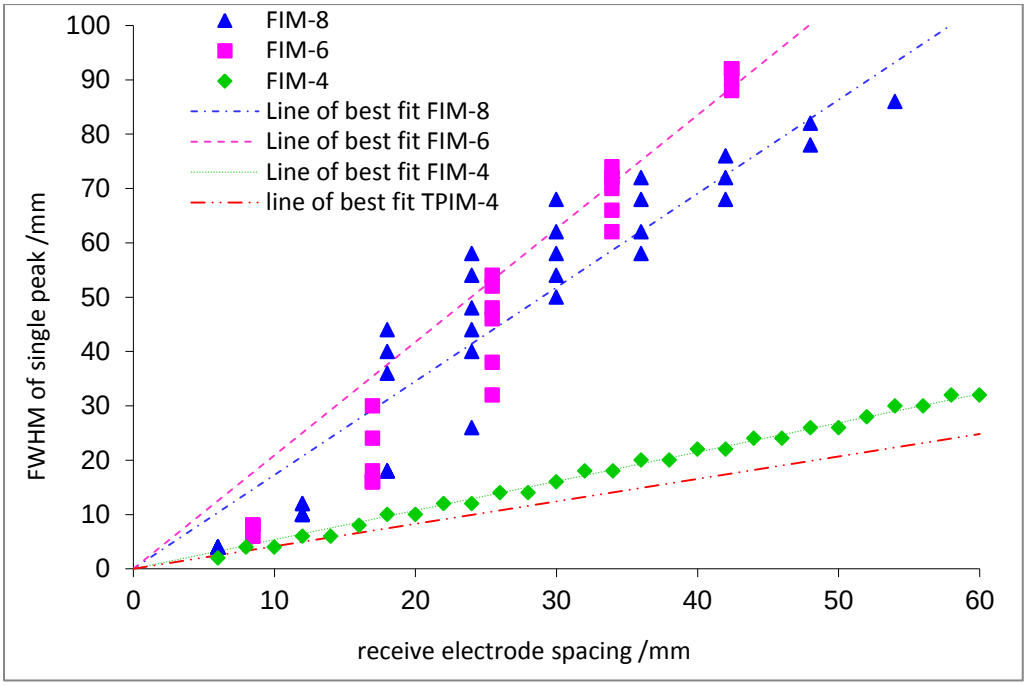

Figure 2-9 Graph shown the FWHM for the peak beneath the centre of the electrode configuration as a function of the predicted receive electrode spacing. The line-of-best-fit for the 4 electrode tetrapolar electrode configuration (TPIM-4) is shown for comparison.

A plot of the FWHM for this single peak (Figure 2-9) showed a significant correlation with the receive electrode spacing for all electrode configurations. The multiple results at particular values of the drive-receive electrode spacing represent identical values of this spacing obtained as the drive electrode spacing is increased. These results show that for any electrode configuration the width of the peak beneath the electrodes is dependent on the receive electrode spacing but that the relationship between the FWHM of the peak and electrode spacing is dependent on the electrode configurations. For the FIM-8 and FIM-6 data sets, the slope of the line-of-best-fit between the receive electrode spacing and the FWHM of the peak was of 1.7 and 2.1, respectively (r^2 = 0.97and 0.99, respectively). There was no correlation between the FWHM of the peak and the drive-receive electrode spacing for either the FIM-8 or the FIM-6 electrode configurations (r^2 = 0.51& 0.07, respectively). The FIM-4 data followed a very different path showing a correlation with the receive electrode spacing (r^2 = 0.99) but with the slope of the line-of-best fit between the receive electrode spacing and the FWHM of the peak being 0.54.

A plot of the ratio of the sensitivity at the single maxima to the mean sensitivity on the plane at which it occurs against receive electrode spacing is shown in Figure 2-10. Since the sensitivity distribution pattern is complex, the ratio of the 'single peak' sensitivity beneath the electrode plane to the 'mean sensitivity' of that plane is a measure of the spatial

sensitivity of the FIM technique. (e.g. its ability to measure the impedance spectrum within a localised region such as a tumour). It can be seen that this ratio rapidly decreases with increasing electrode spacing, but that analysis showed no consistent relationship between the two for the different electrode configurations. Specifically, the ratio was not proportional to the inverse of the square of the receive electrode spacing. A graph of the ratio against drive-receive electrode spacing showed no consistent relationship for any of the electrode configurations.

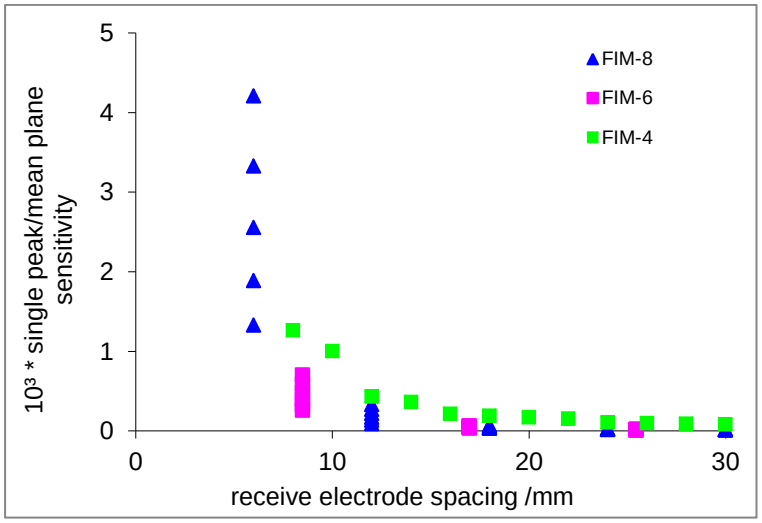

Figure 2-10 Showing the relationship between the ratio of the single peak sensitivity to the mean sensitivity on the plane at which it occurs against receive electrode spacing.

2.2.4 Discussions

The previous work on electrode configurations using Geselowitz's lead theorem found a mean sensitivity at the surface layer of zero, a maximum in the average sensitivity of a plane at $^1/_3$ of the electrode spacing and regions of negative sensitivity down to $^1/_2$ of the electrode spacing (Brown *et al.*, 2000b). Whilst not formally part of the current work, the first of these findings from the previous work was confirmed – that the average sensitivity on the electrode plane is approximately zero irrespective of electrode placement. The previous modelling work and the modelling described in this chapter for sensitivity analysis have assumed a homogeneous medium. Whilst the results of this work provide a valuable insight into the relationships between the electrode positions and the spatial distribution of measurement sensitivity for addressing electrical impedance measurement problems, the human body consists of tissues which are non-linear, inhomogeneous and arranged in a complex geometry. Therefore, care should be exercised in extrapolating general results obtained here to specific electrical impedance measurement problems and the predictions

should be verified either by a finite element method (FEM) analysis using the specific application geometry or measurement on phantoms approximating the application geometry and tissues.

The previous work looking at the sensitivity of tetrapolar impedance measurements using a geometrical approach to determining the lead fields (Brown *et al.*, 2000b) had electrodes placed at the corners of a square, where drive current was applied to one side of the square and voltage measurements made from the opposite side of the square (Figure 2-1, TPIM-4 electrode configuration and Figure 2-2). The findings for the tetrapolar electrode configurations in the current work suggest that the previously identified linear relationships for the plane with the maximum average sensitivity and the depth into the measured volume where regions of negative sensitivity exist are true for any symmetrical electrode placements on a surface but that the relationship is with the drive-receive electrode spacing, a fact that was not apparent from the previous work since the drive-receive and receive-receive electrode spacings are the same for 4 electrodes arranged in a square. The zero sensitivity at the surface plane results from there being equal positive and negative sensitivity values on the plane which sum to zero. The size and magnitude of the regions of negative sensitivity rise and then fall with increasing depth giving rise to the peak in the sensitivity of a plane at a depth determined by the drive-receive electrode spacing. The finding for negative sensitivity regions in this work is consistent with the sensitivity of bipolar impedance measurements always being positive as the depth of negative sensitivity regions decreases as the drive-receive electrode spacing decreases. In the limit, the spacing between drive and receive electrodes becomes zero and the measurement will be a bipolar one in which there are no regions of negative sensitivity. Although there is a maximum in the average sensitivity of a plane at a depth equal to 0.3 times the drive-receive electrode spacing for the TPIM-8 and TPIM-6 electrode configurations, it is important to note that the spatial distribution of sensitivity in that plane is regional with large multiple peaks. Therefore, the measured impedance value will also be sensitive to spatial inhomogeneities in the resistivity of the media at this depth. For the TPIM-4 configuration the depth at which a single peak occurs is less than the depth at which the maximum sensitivity plane occurs and therefore, the maximum average sensitivity corresponds to the presence of a single dominant peak in the sensitivity. However, it should be noted that there are still regions of negative sensitivity at this and greater depths down to half the electrode spacing. The lack of a well-defined single peak in the sensitivity at large distances beneath the electrodes for the TPIM-8 and TPIM-6 electrode configurations has implications for

number of applications of electrical impedance as the TPIM-8 electrode configuration has been used to measure respiration and the TPIM-6 configuration used to measure cardiac output. Complex tissue geometry coupled with very regional sensitivity peaks will give poor estimates of impedance changes within the body.

For all the FIM electrode configurations analysed in the current work, a maximum in the average sensitivity of a plane was found at a depth of approximately one-third of the drive-receive electrode spacing, but no correlation was found between the depth at which the maximum in the average sensitivity occurred and the receive electrode spacing for the FIM-8 and FIM-6 electrode configurations. For the FIM-8 and FIM-6 electrode configurations regions of negative sensitivity was found down to approximately half of the drive-receive electrode spacing, which is consistent with the previous findings of Brown and co-workers (Brown *et al.*, 2000b) and the findings reported in this chapter for the equivalent tetrapolar electrode configurations. Once again, no correlation was found with the receive electrode spacing. For the FIM-4 electrode configuration the regions of negative sensitivity was found down to approximately one-third of the drive-receive electrode spacing. The difference in the results between the FIM-8 and FIM-6 electrode configurations and the FIM-4 electrode configuration is because in the FIM-4 configuration an electrode used for voltage detection in one measurement is used to drive current in the second measurement. For small depths within the medium, the magnitude regions of negative sensitivity lie beneath the electrodes. With increasing depth, the largest magnitude regions of negative sensitivity lie between the two receive electrodes whilst in the other direction (between a drive and a receive electrode), the sensitivity is positive. In FIM-4, the line between the two drive electrodes in one measurement becomes the line between a drive and a receive electrode in the other (Figure 2-1) and summing regions of negative sensitivity in one measurement with regions of positive sensitivity in another reduces the depth at which the regions of negative sensitivity disappear.

The aim of the focused impedance measurement is to produce a maxima in the sensitivity beneath the electrodes. The depth at which there was a single maxima in the sensitivity beneath the centre of the electrode configuration was analysed for all the electrode configurations considered. For this analysis there were clear differences between the three electrode configurations with the depth at which there was a single maxima in the sensitivity beneath the centre of the electrode configuration for the FIM-8, FIM-6 and FIM-4 electrode configurations being 0.56, 1.41 and 0.14 of the receive electrode spacing

respectively. Once again the effect of common drive and receive electrodes can be seen in the results for the FIM-4 electrode configurations. It should also be noted that for the FIM-8 and FIM-6 electrode configurations this single peak occurs below the level at which the regions of negative sensitivity have disappeared and below the level at which the maxima in the average sensitivity of a plane has occurred. However, for the FIM-4 electrode configuration, the single maxima in the sensitivity beneath the centre of the electrode configuration was found above these levels. The size of the peak beneath the single maxima was also found to be dependent on the receive electrode spacing with the size being roughly the same for the FIM-8 and FIM-6 configurations despite the depth into the measured volume for the FIM-6 configuration being approximately double that for the FIM-8 electrode configuration for the same receive electrode spacing. It should be noted that for a given drive-receive electrode spacing, the receive electrode spacing will be larger for FIM-6 than for FIM-8; thus, for a given drive-receive electrode spacing, the FWHM will always be greater for FIM-6 than FIM-8, although these are uncorrelated. Whilst the ratio of the single peak sensitivity to mean sensitivity at that plane (Figure 2-10) was found to vary as the inverse of the electrode spacing squared for the TPIM-4 electrode configuration, no consistent relationship was found between the electrode spacing and the ratio for any of the FIM electrode configurations. Importantly, these results showed that not all the electrode spacings for the TPIM-6 and TPIM-8 tetrapolar electrode configurations contained a single peak in the sensitivity within the depth modelled (200mm), whereas all the focused impedance configurations did. Therefore, whilst no direct comparison between the tetrapolar and focused impedance results are possible for the six and eight electrode configurations for this measure, the finding of a lack of single peak in the sensitivity distribution for these tetrapolar electrode configurations does mean that the corresponding FIM electrode configurations do have an advantage in terms of the spatial distribution of sensitivity. For the four electrode configuration the FIM measurement gave a small overall improvement in the peak sensitivity when compared with the equivalent tetrapolar measurement.

2.2.5 Summary

The findings presented in this chapter for the FIM-8 and FIM-6 electrode configurations are consistent with the previous findings since the receive electrode spacing for electrodes arranged in a square is identical to the drive-receive electrode spacing. In terms of the pattern of sensitivity beneath the electrodes, this work has established that the important parameter for determining the maxima in the average sensitivity of a plane and the depth

to which regions of negative sensitivity occur is the drive-receive electrode spacing; whilst the existence of a single peak beneath the centre of the electrode configuration is determined by the receive electrode spacing.

The complex resistivity distributions of the body coupled with complex sensitivity distributions of the tetrapolar measurement technique have the potential to produce unreliable estimates of transfer impedance. All FIM electrode configurations produce a peak in the maximum sensitivity of a plane at a depth of approximately $^1/_3$ of the drive-receive electrode spacing. Since there is no difference in the value of this maximum sensitivity for the different FIM electrode configurations with the same drive-receive electrode spacing, no particular electrode configuration has an advantage in terms of improving the overall sensitivity of the measurements. The difference between the electrode configurations lies in the depth to which regions of negative sensitivity exist and the depth at which the positive peak beneath the electrodes becomes dominant. Both the FIM-8 and FIM-6 electrode configurations have negative sensitivity peaks down to a depth of approximately ½ the drive-receive electrode spacing, whilst the FIM-4 has negative sensitivity peaks down to only approximately $^1/_3$ the drive-receive electrode spacing. This, together with the existence of a dominant positive peak at 15% of the receive electrode spacing must be considered an advantage. An FIM-4 electrode configuration used in conjunction with a 'stand-off' electrode of an appropriate thickness as proposed by Bertemes-Filho and co-workers (Bertemes-Filho *et al.*, 2003) would produce a well-defined distribution of sensitivity within the tissue. The finding for the FIM-6 electrode configuration that the positive peak beneath the centre of the configuration does not dominate until a depth of 1.4 times the receive electrode spacing is of concern as this electrode configuration would give the poorest estimate of the transfer impedance in a medium with complex regional variations in resistivity.

3 Materials and Methods

In this chapter, the instruments used for both the ultrasound and multi-frequency electrical impedance measurements and the details of measurement technique are described. The data acquisition and data processing for both the ultrasound and electrical impedance measurements are also discussed. The results from some preliminary ultrasound and electrical impedance measurements are also presented at the end of this chapter.

3.1 Ultrasound Instrumentation

A pulse transmitter/receiver specifically designed in-house for ultrasound transducer testing was used to drive the ultrasound transducer as well as to receive the reflected ultrasound signals. The pulse transmitter/receiver provided a single channel 320V drive and a single channel receive circuit. The block diagram of the instrument is given in Figure 3-1. It has two separate sections– the drive section generates a high voltage pulse to drive the PZT transducer and the receive section which amplifies the reflected ultrasound signal detected by the PZT using a FET input amplifier. A brief description of the pulse transmitter/receiver instrument is given in the following paragraphs.

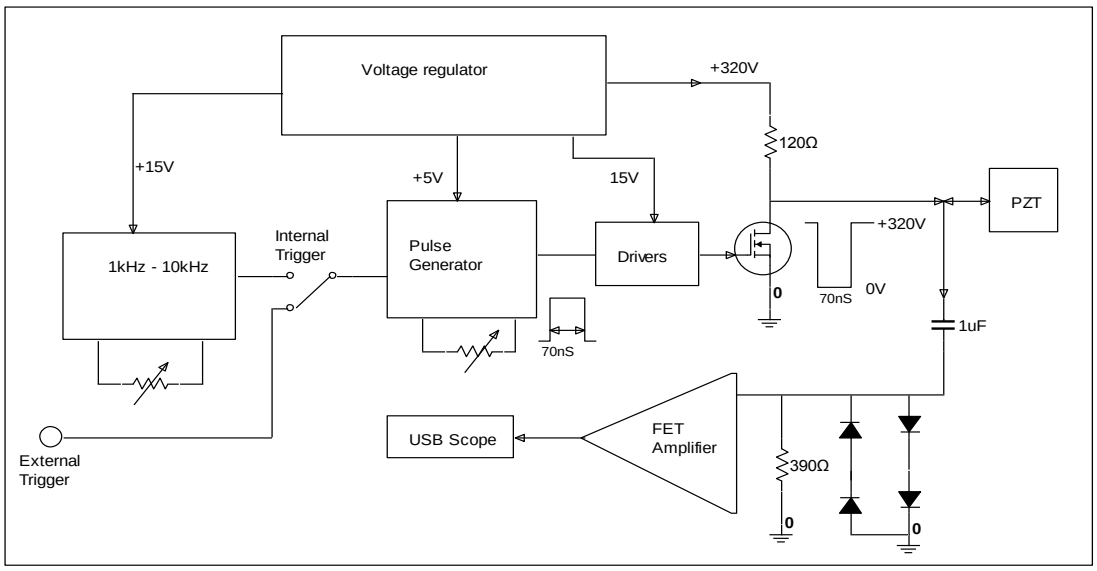

Figure 3-1 The block diagram of the pulse transmitter/receiver instrument for the ultrasound application.

The voltage regulator provides multiple levels of DC voltages to drive the various sections of the pulse transmitter/receiver circuit, including the high voltage supply for the PZT. A variable width square edged pulse is used to drive the PZT element, which is generated by the pulse generator where the width of the pulse is controlled by a variable resistor. The smallest duration pulse that could be generated was 70ns. The pulse generator circuit can

either be internally or externally triggered. For internal triggering, a variable frequency clock (1kHz – 10kHz) is used to trigger the pulse generator where the frequency is controlled by a second variable resistor. For external triggering, a TTL pulse is supplied to the pulse generator circuit (minimum duration 50ns).

The output from the pulse generator is taken to a driver circuit, the output of which is taken to the gate of the FET that drives the PZT element. An n channel enhancement mode power MOSFET was used to get the high voltage (320V) pulse necessary to drive the PZT element. The FET is operated in switching mode so that the pulse used to drive the FET is square edged.

In the pulse transmitter/receiver circuit the same PZT element is used to receive the reflected ultrasound signal. The voltage at the input to the FET amplifier includes the drive pulse voltage and four diodes together with a blocking capacitor were used to limit its input voltage to $\pm 1.4V$.

3.1.1 Optimisation of the drive electronics for the ultrasound measurements

Traditionally, ultrasound transducers are driven with a narrow pulse to exploit the natural resonant properties of PZT. Mechanical damping to produce the required pulse shape is achieved by placing material of the appropriate acoustic impedance behind the PZT element within the transducer. The long term aim of the work described in this thesis, if successful, is to use the same ultrasound transducer elements for temperature measurement and heating during mild hyperthermia. The previously described phased array transducer with randomly distributed elements demonstrated the feasibility of using ultrasound to create mild hyperthermia in deep body tumours (Aitkenhead *et al.*, 2008) and the aim was to use the same arrangement for mounting the PZT element in this work as that used in the phased array. The PZT elements in the phased array transducer were air backed allowing the PZT to ring undamped after application of the drive pulse avoiding any loss of energy due to absorption in the backing layer (Persson and Hertz, 1985). However, for ultrasound propagation measurements where the same element is to be used for transmission and echo detection, this results in unwanted ringing of the transducer at 1MHz due to the high Q of the PZT material. In order to be able to use an undamped transducer for the work described in this thesis, there was a need to optimise the drive pulse to minimise the ringing of the transducer. To investigate the optimisation of the drive pulse, a single element transducer was made using the same technique as that described by Aitkenhead (Aitkenhead, 2008).

A 10mm diameter circular element PZT (SP-8) was mounted on a Perspex frame (Figure 3-2). The Perspex frame was machined to house a 10mm diameter PZT element at its centre. The front surface of the frame was recessed around the hole to contain the PZT element to allow a matching layer of thickness of approximately 1mm to be incorporated into the PZT transducer. A hole was drilled in the recessed region to provide common connection to the front surface of the PZT transducer. Araldite 2020 (resin : hardener = 100 : 30) was used to provide a matching layer on the front surface of the transducer. The matching layer was cured at low temperature for a long periods of time (>48 hours) to minimise air bubbles becoming trapped in it. The matching layer was ground back (using wet abrasive paper) to the surface level of the Perspex frame once it had hardened. The completed Perspex frame was then housed in a diecast aluminium case. A coaxial cable (RG178B/U) was used to make electrical connections to the transducer. The cable entered the transducer from the top of the aluminium casing and was connected to a strip board inside the casing. Thin wires were run from the strip board and soldered to the rear and front face of the PZT element to make the active and common connections to the transducer element, respectively.

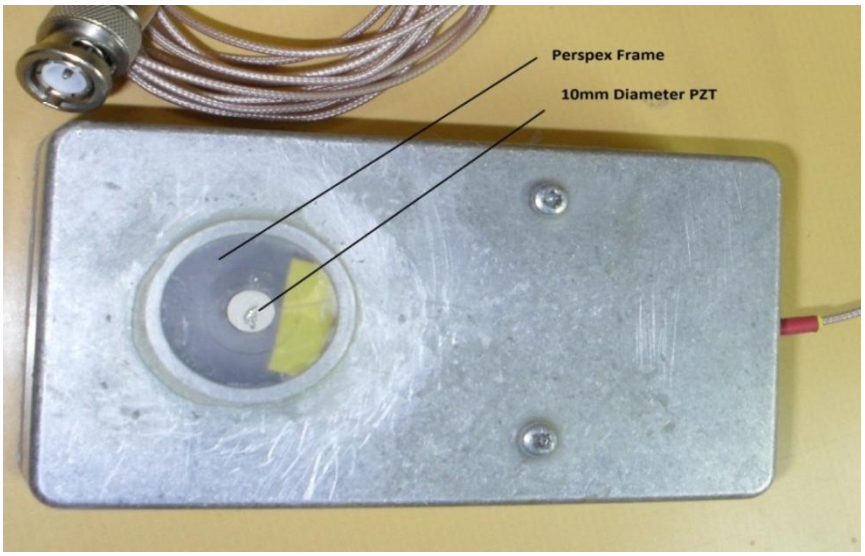

Figure 3-2 The 10mm diameter circular element transducer fitted in a Perspex frame and housed in an aluminium case.

The PZT transducer was tested in a water tank and the electro-mechanical characteristics were measured. The transducer was driven by a narrow (70ns) pulse and showed 'ringing' for 25µs after the pulse was applied, measured using a Tektronix digital oscilloscope and using a NI high speed digitiser connected to a computer through the USB port (USB-5233). However, to support mild hyperthermia it is necessary to make measurement at tissue

depths less than 10mm which corresponds to a time of flight of about 13µS (assuming ultrasound propagation velocity of 1500ms^{-1} in soft tissue). The signal from the 10mm diameter circular element transducer during the first 25µS after the transmission is showed in the Figure 3-3.

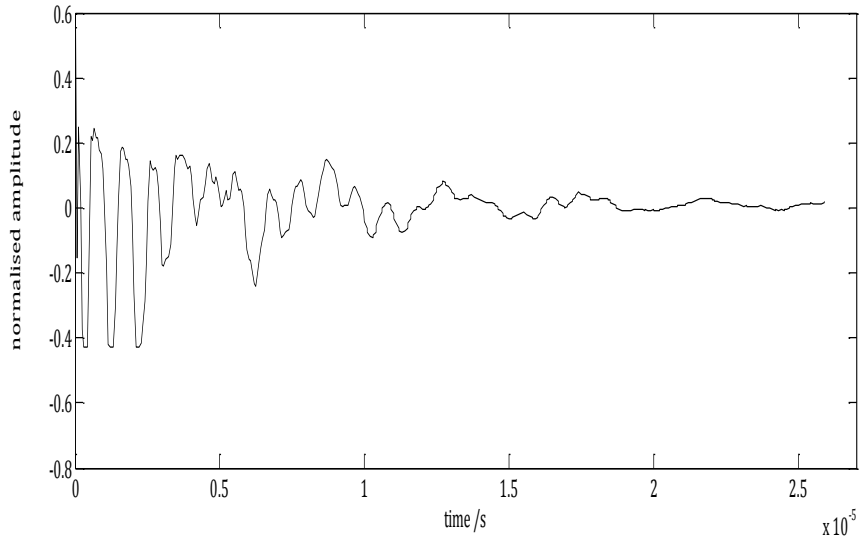

Figure 3-3 Ultrasound signal from the 10mm diameter circular element PZT-8 transducer following excitation with a 70ns pulse.

The magnitude of the FFT of this signal also showed activity at about 200kHz as well as at 1MHz, which was the fundamental frequency of the transducer (Figure 3-4). In addition, the FFT magnitude spectrum showed activity at 2MHz and 3MHz. But this was expected as the transducer will have vibration modes at harmonics of the fundamental frequency. From the activity at 200kHz in the frequency spectrum (Figure 3-4) it can be assumed that the transducer is also vibrating in a sub-harmonic mode due to longitudinal vibrations in the PZT element.

It was necessary to prevent the transducer 'ringing' and allow the transducer to ideally produce only a single pulse having duration of 1µs. To suppress the 'ringing' an analysis in Matlab was done. The aim of the analysis was to find a drive pulse which gave a single isolated 1µS pulse from the PZT element.

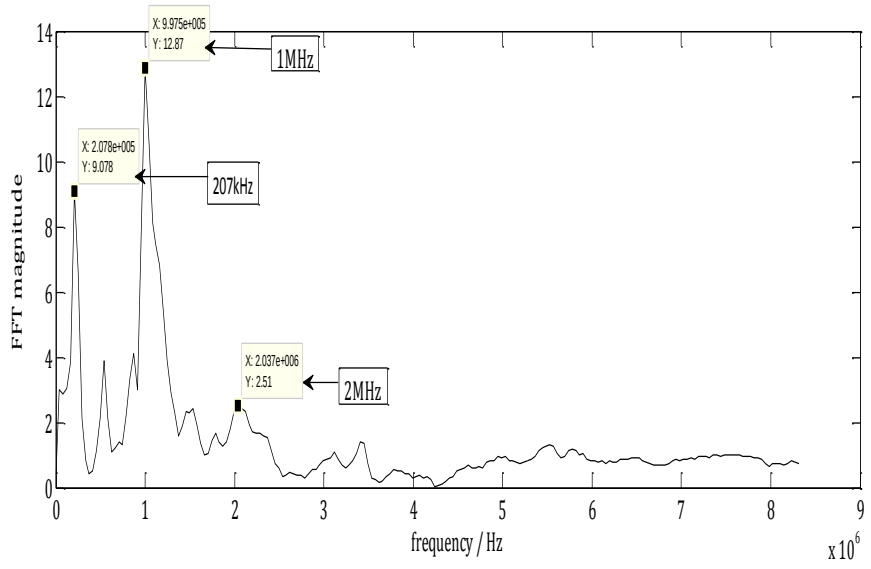

Figure 3-4 Frequency spectrum of the 10mm diameter circular element PZT transducer following excitation with 70ns pulse.

The analysis began by simulating a signal in Matlab that produced a wave similar to the 'ringing' seen at the output of the PZT transducer (Figure 3-3). The magnitude FFT spectrum of the transducer at and above 1MHz looks like the fundamental, 1st and 2nd harmonic of a triangular wave (Figure 3-4). If the excitation to the transducer is considered as a Dirac pulse, this (Figure 3-4) will be the frequency response of the transducer. As a first stage in the simulation process, a 1MHz triangular wave was generated (Figure 3-5a) as this had the same spectral components as those seen in the ultrasound transducer. For ease of analysis the triangular wave (Figure 3-5a) was created using a software waveform function generator and the resultant signal loaded in Matlab for analysis.

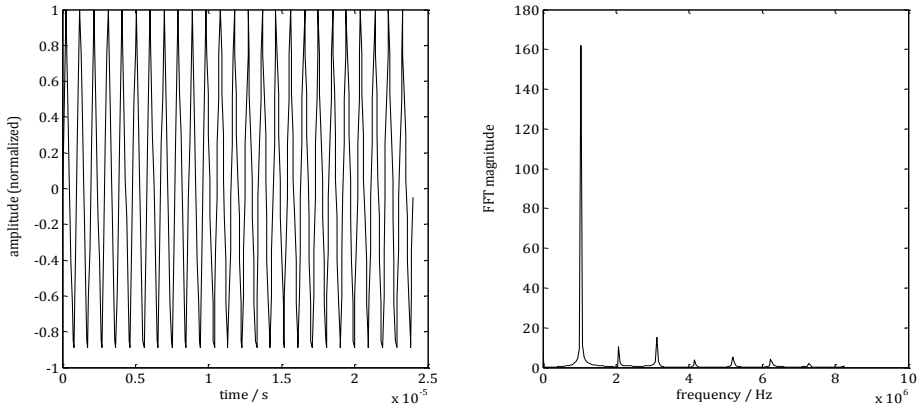

Figure 3-5 Triangular wave and FFT of the triangular wave (a) time domain signal (b) frequency domain signal

The triangular wave was then multiplied by a decaying exponential wave where time constant was set so that the amplitude was 2.5% of the maximum at 20µS. The composite signal (triangular wave multiplied by decaying exponential wave) produced a 'ringing' similar to the 'ringing' of the PZT transducer (Figure 3-6a) although the simulated signal was clearly more regular. The FFT of this 'composite signal' (Figure 3-6b) also looked somewhat similar to the FFT of the signal from the PZT transducer (Figure 3-4).

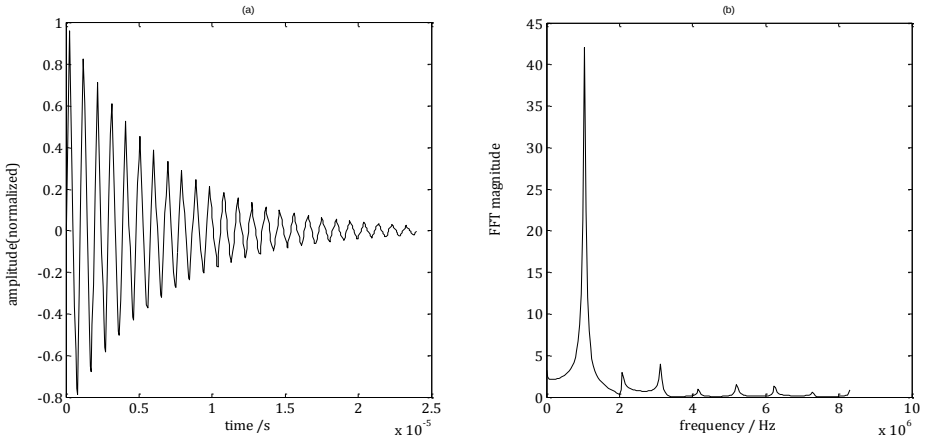

Figure 3-6 Triangular wave multiplied by a decaying exponential wave and its FFT magnitude (a) time domain signal (b) frequency domain signal.

The next stage in the simulation was to find a function that will reduce the power of the 1MHz component of the spectrum to zero to prevent the ringing of the transducer. Again a triangular pulse was used as a starting point. The duration or width of the pulse must be chosen carefully to ensure the 1st minimum in the FFT is at the right frequency. To find the effect of driving the PZT with a triangular pulse, it was necessary to convolve the decaying exponential signal shown in Figure 3-6 with a triangular pulse. The resultant time domain signal can be obtained by using the 'convolution theorem' (Bracewell, 1999). In this case, the FFT output of the '2µs triangular pulse' (Figure 3-7b) and the 'composite signal' (triangular wave multiplied by decaying exponential shown in the Figure 3-6b) were multiplied point-wise and then inverse FFT was taken which gave the signal in Figure 3-8. The resultant signal in Figure 3-8 is close to that required.

From simulation, it was observed that the triangular pulse can give zero power at 1MHz frequency if its width is made 2µS (Figure 3-7).

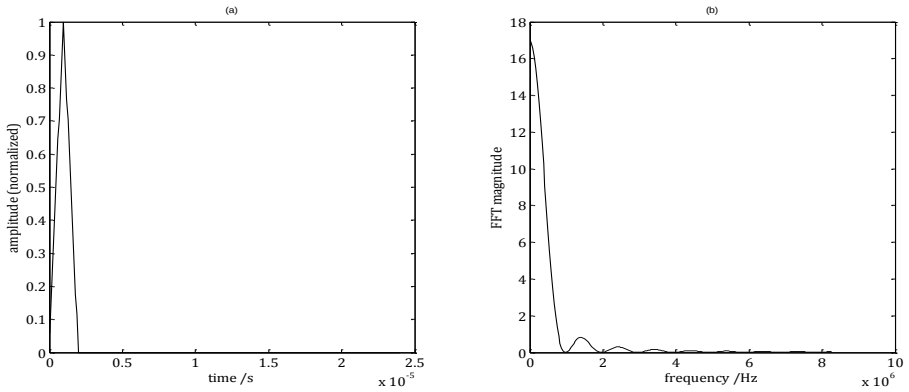

Figure 3-7 Triangular pulse of duration 2µs and the magnitude of its FFT(a) time domain signal (b) frequency domain signal.

So, a 2µs single pulse triangular wave (Figure 3-7) can be used as a drive pulse for the PZT transducer element which has the 'ringing' and frequency response like that in Figure 3-6. The result is the isolated triangular pulse of 1µS duration with only low amplitude ringing shown in Figure 3-8.

Whilst using a triangular pulse gives the right wave shape, in practice, a triangular pulse is difficult to generate in a high power electronic circuit.

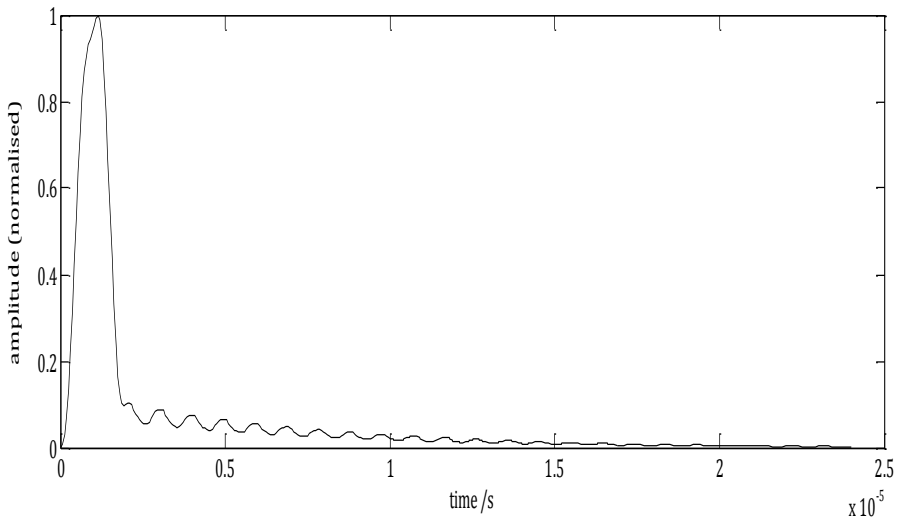

Figure 3-8 Showing the resultant time domain performance obtained using convolution theorem from Figure 3-6b and Figure 3-7b. The amplitude is the result of convolving a unit height impulse response with a unit high drive function.

It is much easier to generate a pulse with exponential rising and falling edges. Therefore, ''exponential pulses'' were loaded into Matlab from the software waveform function

generator. The pulse duration (pulse width) and time constant of the exponential pulses were carefully controlled to ensure that the first minimum in the FFT was obtained at a frequency of 1MHz.

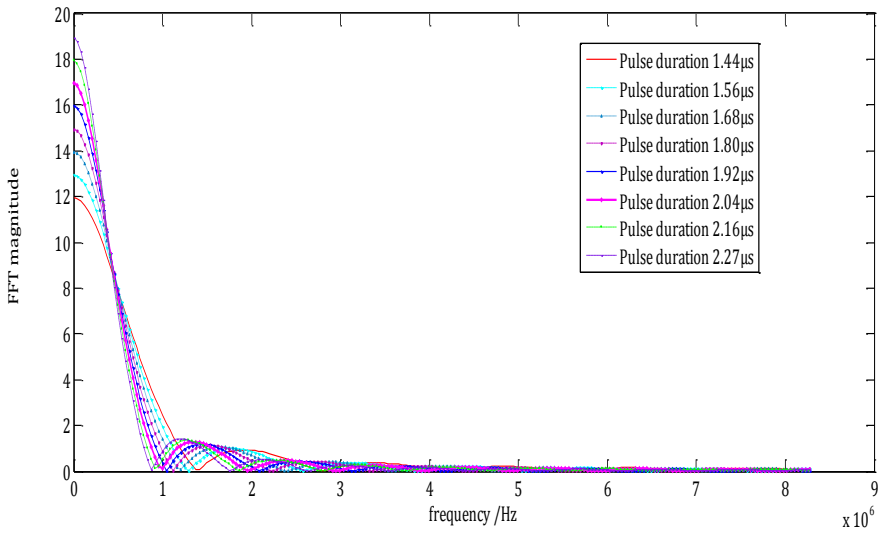

Figure 3-9 Effect of changes of pulse duration on the exponential drive pulse, keeping the time constant fixed. The magenta line at pulse duration about 2µs produces the first minima at 1MHz frequency.

It is clear from the Figure 3-9 that a pulse duration of about 2µs (the thick magenta line in Figure 3-9) can ensure to produce the first minima at exactly 1MHz. Next, the effect of the number of time constants on the amplitude of the pulse was investigated keeping the pulse duration fixed at 2µs.

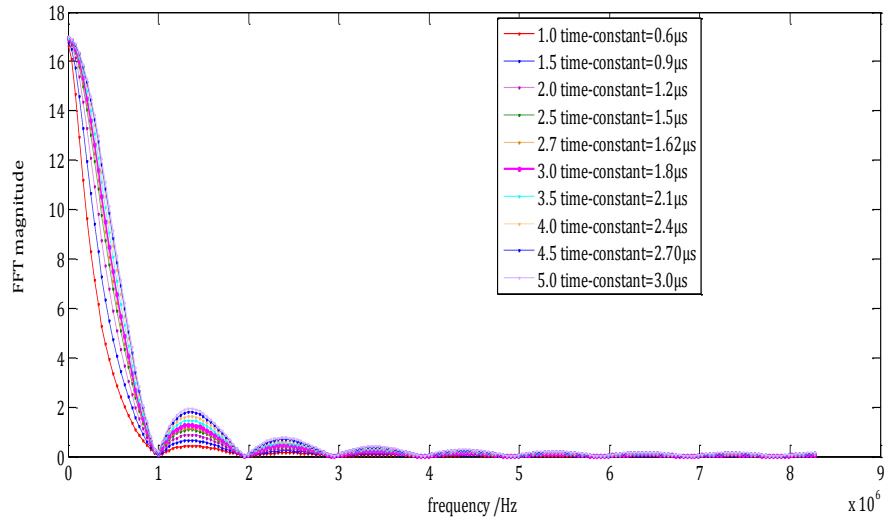

Figure 3-10 Effect of changes of times constant on the exponential drive pulse, keeping the pulse duration constant at about 2µs.

It is obvious that as the time constant increases, the charging time will increase which results in a decrease in the maximum output amplitude. So, it is necessary to use the lowest value of time constant possible, as this will increase the output amplitude. However, increasing the time constant will give a better approximation to the triangular wave. Therefore, as a compromise, 3 time-constant (3τ) (thick magenta line in Figure 3-10) was chosen for the exponential drive pulse of the ultrasound transducer. An exponential drive pulse of 2μs duration and with 3 time-constant (3τ) is shown in Figure 3-11 together with its frequency spectrum. Using this pulse to drive a transducer with the characteristics shown in Figure 3-6 gives the time domain pulse determined by using the convolution theorem which is shown in Figure 3-12.

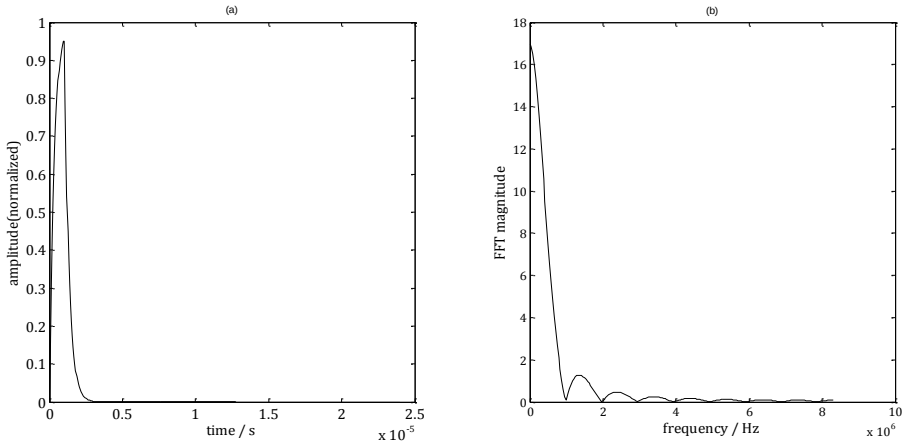

Figure 3-11 Exponential drive pulse of 2μs duration and 3 time constant (3τ); and its FFT magnitude (a) time domain signal (b) frequency domain signal.

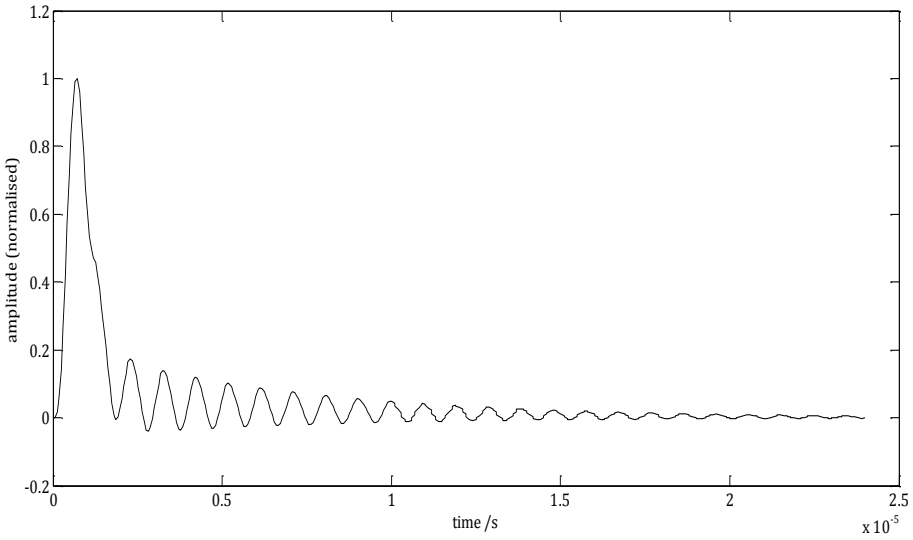

Figure 3-12 Resultant signal derived by using convolution theorem from the frequency domain signal of 2µs exponential drive pulse and composite signal (triangular wave multiplied by decaying exponential wave).

This is similar to the pulse shown in Figure 3-8 but it should be noted that for the exponential pulse the amplitude of the pulse returns to the baseline more quickly but the amplitude of the ringing is greater. Whilst creating an exponential pulse is simple electronically, it does involve reducing the energy delivered to the PZT element and therefore degrades the signal-to-noise ratio of the overall measurement system. As the time constants shown in Figure 3-10 decreases, the pulse more nearly approximates a square pulse. This is the simplest to produce from the pulse generator and therefore simulations on a square pulse were performed.

Figure 3-13 shows the 2µs wide square pulse and the magnitude of its frequency spectrum. Using the convolution theorem, the resultant time domain signal obtained from using a 2µs wide square pulse to drive a transducer with the characteristics shown in Figure 3-6 is shown in the Figure 3-14. However, for the 2µs wide square drive pulse, the 1st minimum in the FFT was not at 1MHz (Figure 3-13) and so it will not produce zero power at 1MHz.

Therefore, it produces a two 1µs pulses followed by large amplitude ringing (Figure 3-14).

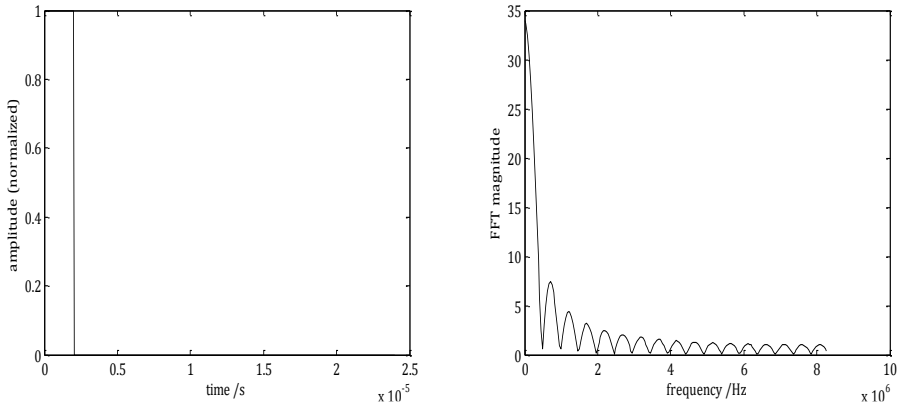

Figure 3-13 Showing the square drive pulse of 2µs duration and its frequency response.

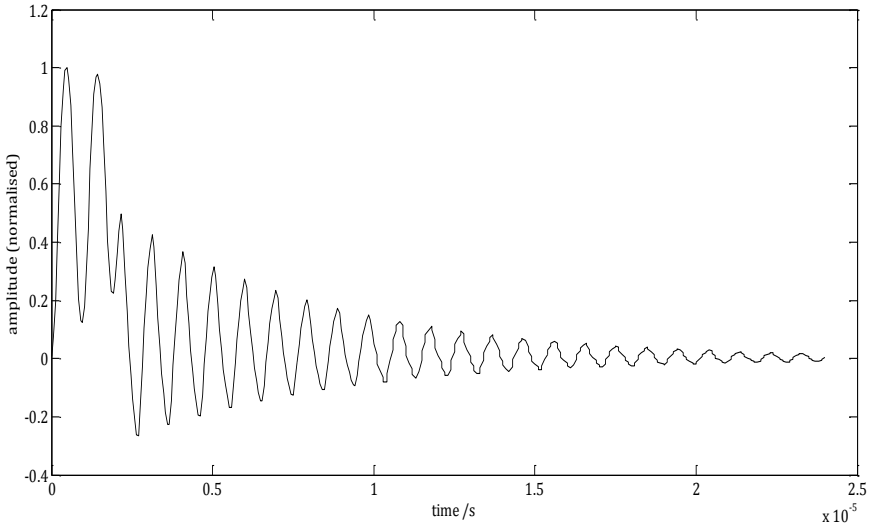

Figure 3-14 The resultant signal derived by using the convolution theorem from the frequency domain signal of the 2µs square pulse and the composite signal (triangular wave multiplied by decaying exponential wave).

To have zero power at 1MHz a 1 µs duration square pulse is required. The simulation results for a 1µs wide square pulse are shown in Figure 3-15 and Figure 3-16. The FFT of the 1µs wide square pulse gave the desired zero power and first minima at a frequency of 1MHz (Figure 3-15). The resultant time domain signal obtained from using a 1µs wide square pulse to drive a transducer with the characteristics shown in Figure 3-6 is shown in the Figure 3-16. Comparing this pulse to the pulse shown in Figure 3-13, it shows that they are broadly similar. Once again the amplitude rapidly returns to the baseline, but the amplitude of the ringing is slightly higher (25% rather than 20%).

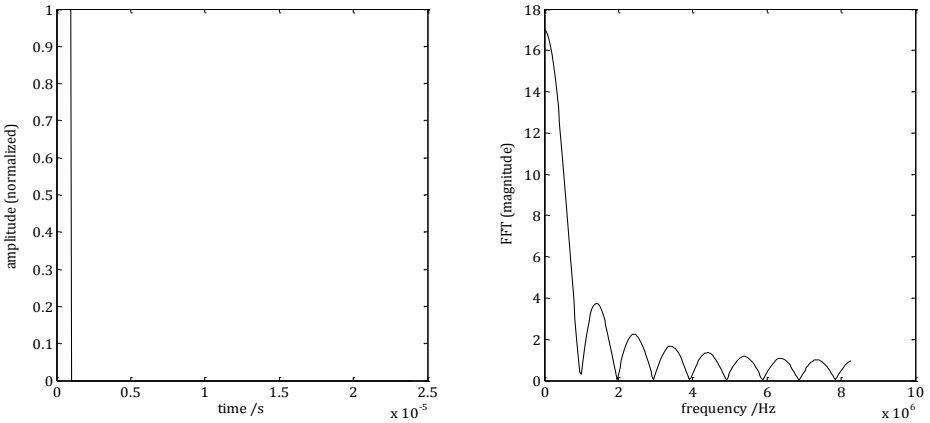

Figure 3-15 Showing the square drive pulse of 1µs duration and its frequency response.

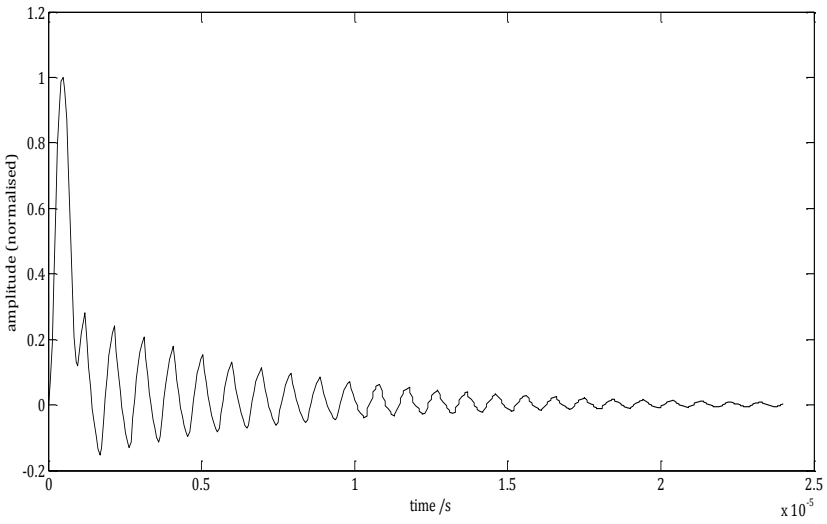

Figure 3-16 The resultant signal derived by using the convolution theorem from the frequency domain signal of the 1µs square pulse and the composite signal (triangular wave multiplied by decaying exponential wave).

Therefore, the transducer element is driven by the 1µs duration wide square pulse and the ringing following the excitation from the transducer is shown in the Figure 3-17.

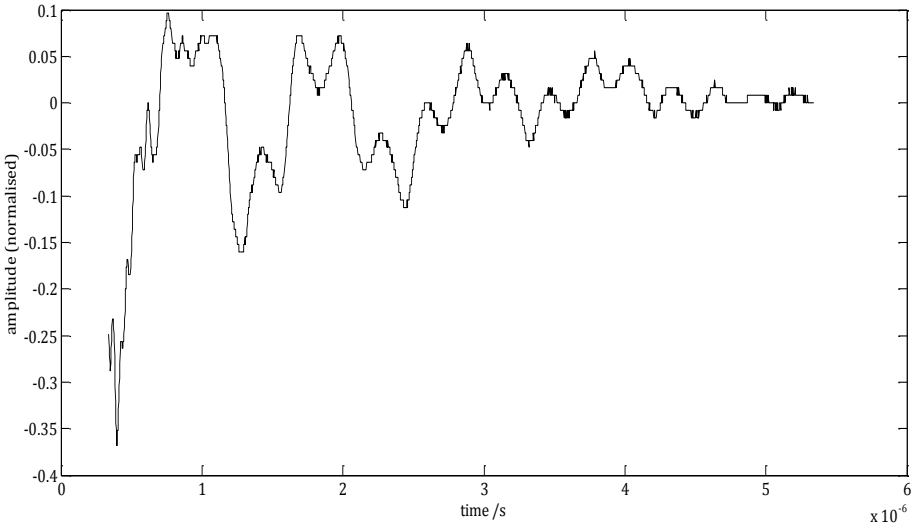

Figure 3-17 Showing the ultrasound signal from the PZT transducer following the excitation with a 1µs duration wide square pulse.

Figure 3-17 shows the multiple modes of vibration of the ultrasound transducer when driven with a 1µs square wave pulse. The first 1µ*s* pulse (ending at about 1.25µs) is the trigger pulse artefact and the pulse starting at about 1.25µs is the ultrasound pulse propagating into the media. The longitudinal mode giving the 200kHz vibration (sub harmonic mode) and a 3rd harmonic mode of vibration can be clearly seen.

3.2 Test Cell or sample chamber

3.2.1 Design and Construction of the Test-cell

To design and construct the test cell some design constraints were applied. The first and most important design constraint was that in making simultaneous electrical impedance and ultrasound propagation velocity measurements there should be similarity in spatial sensitivity between the two measurements. To ensure similarity between the spatial sensitivity of the two measurements, the diameter of the ultrasound element and the electrode spacing was selected so that the position of the last axial maximum in the centre line of the ultrasound field (based on a circular PZT element behaving as a piston) (Figure 3-18) is at the same depth as the peak in the average planar sensitivity for the tetrapolar electrical impedance measurements (section 2.2.3, published in (Islam *et al.*, 2010)).

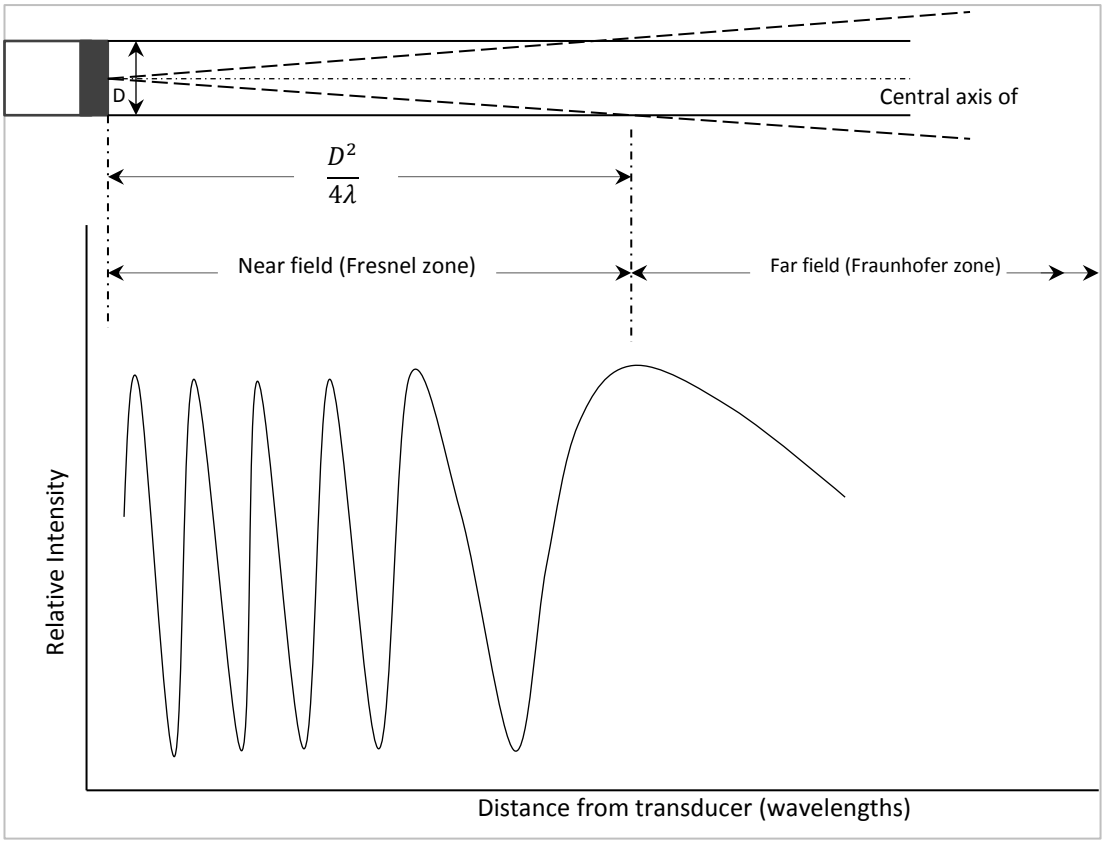

Figure 3-18 The field distribution of an ideal piston like source generating a continuous ultrasound wave. The near field (Fresnel zone) and far field (Fraunhofer zone) regions are shown in relation to the transducer's diameter (D) and wave length (λ). (Source:(Hedrick *et al.*, 1995))

Transparent Perspex, which is a premium grade acrylic, was chosen to make the test cell. The test cell, which was cylindrical in shape, holds the sample materials. The depth of the test cell had to be sufficient so that the distance from the base to the transducer was large compared to the wavelength of the ultrasound and that the time of flight for the reflection from the base was long compared to any 'ringing' from the transducer. Initial experiments done on the type of ultrasound transducer to be used (section 3.1.1) suggested that ringing following pulse excitation could last up to 30µs without an optimised drive pulse and 6µs with an optimised drive pulse. Therefore, the minimum time of flight from the transducer to a reflective surface was set to 30µs. This corresponds to a depth in the test cell of 22.5mm. This is approximately 13 times the wavelength of the ultrasound in soft tissue. This is small for time of flight measurements, so this was increased to approximately 25 times the wavelength giving a sample chamber depth of 36mm. The diameter of the sample chamber needs to be small to ensure even heating of the sample yet large to enable ultrasound propagation without reflection from the walls. In addition the sensitivity properties of the electrical impedance measurement assume a semi-infinite homogeneous

media. Therefore, as a compromise, a diameter of 40mm was selected for the test cell. The wall thickness of the cylindrical test cell was chosen to be 2mm as a compromise between robustness and thermal resistance.

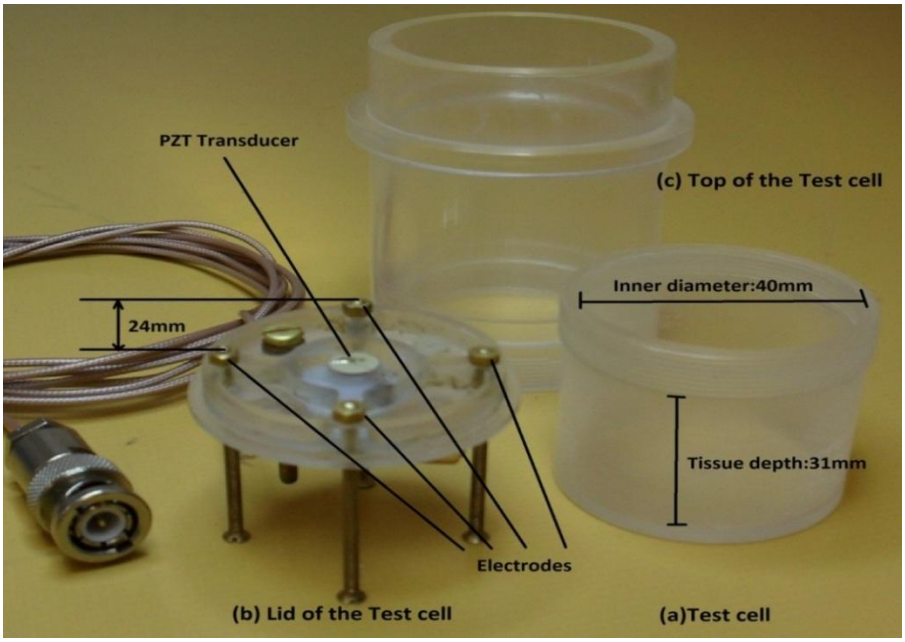

Figure 3-19 Perspex test cell showing position of the electrodes and PZT element - (a) Test cell (b) Lid of the test cell and (c) Top of the Test cell.

A cylindrical test cell having internal diameter of 40mm, height of 36mm, vertical walls and its base 2mm thick was constructed from Perspex with the help of the mechanical workshop of the department of Physics at Warwick University (Figure 3-19a). The test cell was threaded around the exterior wall from the top of its open ended side to a depth of 5mm. The lid of the test cell (Figure 3-19b) was designed to incorporate an ultrasound transducer and four electrodes so that simultaneous ultrasound and multi-frequency electrical impedance measurements can be taken. The ultrasound transducer was located at the centre of the lid and the four brass/stainless steel electrodes approximately 5mm in diameter were arranged in square centred on the transducer element. The four electrodes were equi-spaced at a radius of 17mm from the centre forming the corners of a square giving an electrode spacing of 24mm (Figure 3-19b). Apart from the four electrodes there was also an additional electrode for the common connection. Two holes were drilled at a radius of 15mm from the centre line of the lid for insertion of the thermocouple into sample materials to allow the temperature of these to be measured during experiments. Care had been taken to ensure that the positions of the thermocouples were away from the centre line of the test cell to avoid scattering of the ultrasonic waves generated by the

PZT transducer. Another hole and four recessed regions were cut outside the matching layer in the front side of the lid to allow filling the cell so that sample material made good contact with the electrodes and ultrasound transducer and to allow for its thermal expansion of the materials.

The top of the test cell was held in place by an open ended Perspex cylinder threaded at one end so that it could be screwed on to the threads at the top of the test cell (Figure 3-19c). An O-ring positioned between of lip on the inner surface of the cylinders just above the threaded portion around the top of the test cell in place and provided a seal against liquid ingress. The height of the cylinders, which can be seen in (Figure 3-19a) allowed the test sample to be fully immersed in a water bath for heating.

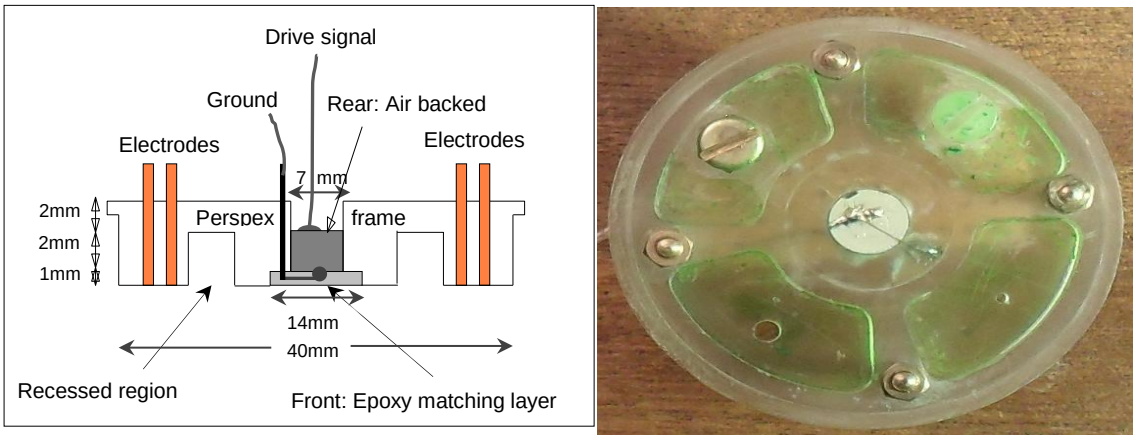

Figure 3-20 (a) Cross section of the perspex lid of the test cell. Electrode positions are shown as distorted so that al 4 electrodes are visible. (b) The completed Perspex lid – the PZT ultrasound transducer and the electrodes are fitted in the perspex lid.

The diameter of the ultrasonic transducer was chosen based on the sensitivity analysis of electrical impedance measurements discussed in chapter 2. In chapter 2, it was shown that sensitivity of the impedance measurement decreased with the increase of the receive electrode spacing. For a small electrode spacing a high value of sensitivity occurs beneath the electrodes edge. However, for small electrode spacing, the useful sensitivity extends to only a small depth directly beneath the electrodes' plane. On the other hand, for large electrode spacing, the useful sensitivity distribution extends to a greater depth beneath the electrodes' plane, but its value is smaller. In addition, the smaller the electrode spacing, the more the impedance measurements will be affected by the local tissue characteristics in the vicinity of the electrodes. From the experimental point of view, it was necessary to make a compromise between the magnitude of sensitivity and the electrode spacings and

to make a choice of the optimal electrode spacing for this work. Therefore, an electrode spacing of 24mm was chosen for the present electrical impedance measurement system. It was shown previously that for 4 electrodes arranged in a square, there is a peak in the average sensitivity of a plane at a depth of ⅓ of the electrode separation (section 2.2.3, published in (Islam *et al.*, 2010))- a depth of 8mm in the test cell.

The diameter of the circular element transducer was chosen so that it can produce maximum acoustic pressure amplitude at a distance of 8mm from the front face of the transducer along the centre line of the direction of propagation. If it is assumed that the circular transducer element behaves as a piston, then the axial intensity profile in the direction of propagation has the form of a Bessel function of the 1st type with the last axial maximum at $D^2/4\lambda$, where D is the radius of the transducer and λ is the wavelength in the media (Figure 3-18). If the frequency of oscillation of the transducer element considered as 1MHz, then the value of λ for 1MHz ultrasound in soft tissue is approximately 1.5mm (considering velocity of sound in soft tissue as 1500ms^{-1}) which gives a transducer diameter of 7mm to align the last axial maxima in the axial ultrasound intensity with the peak in the average sensitivity of a plane in the impedance data.

The Perspex-lid of the test cell was machined to house the circular transducer element. The lid incorporated one hole of 7mm diameter at the centre, into which the 7mm diameter transducer elements would be fitted. The front surface of the lid was recessed around the hole maintaining 14mm diameter and 1mm thickness. The recessed region allowed λ/4 matching layer to be incorporated for the transducer element. Four electrode positioning holes, each of 2.5mm diameters, maintaining 24mm distance between the adjacent holes were drilled in the lid. Another hole for common electrodes was also drilled in the lid of the test cell. Figure 3-20 shows the cross section of the Perspex lid and the completed Perspex lid with PZT and electrodes fitted in it.

3.2.2 Selection of the PZT element for the ultrasound transducer

Aitkenhead and co-workers (Aitkenhead *et al.*, 2008) have previously described a planar phased array ultrasound transducer with randomly distributed elements suitable for producing mild hyperthermia in solid tumours deep within the body. In this work (Aitkenhead *et al.*, 2008) the relationship between the size and position of the focus and the parameters of the array such as the size, shape and distribution of the individual elements was established. In the current work the aim was to use the same transducer for heating as for temperature measurement in mild hyperthermia. This transducer was air

backed allowing the PZT to ring undamped after application of a drive pulse avoiding any loss of energy due to absorption in the backing layer (Persson and Hertz, 1985).

PZT comes in a variety of compositions which are designed for a number of different applications. Of the possible compositions PZT-8 (e.g. PZT-4 is used for therapeutic applications, PZR-5A, PZT-5H, PVDF is used for diagnostic imaging purpose) is particularly suitable for high power applications having lower dielectric and mechanical losses than other compositions. With the ability to withstand high levels of electrical excitation and mechanical stress PZT-8 has been used by many workers in the construction of ultrasonic transducers intended for both mild hyperthermia (Sun *et al.*, 2003) and HIFU (Saleh and Smith, 2005b). So for the current ultrasound propagation velocity measurement work, PZT material of grade SP-8 from Sparkler Ceramics Pvt Ltd, Bhosari, Pune-411026, Maharashtra, INDIA was used. The PZT of grade SP-8 is equivalent to Navy type III ceramic materials. Key parameters for the PZT-8 materials are given in Table 3-1.

Table 3-1 Navy type III specifications for the PZT used in the transducer construction [U.S. Department of defence, 1995].

Property	***Symbol***	***Units***	***Typical Value***
Relative permittivity	k_3^T		1025±12.5%
Piezoelectric coefficient	d_{33}	$10^{-12}mV^{-1}$	215±15%
Planar frequency constant	N_p	Hz.m	2300±8.0%
Density	ρ	Kgm^{-3}	≥7450
Curie Temperature	T_C	°C	325

From the various shapes PZT elements available, the circular elements were chosen. This was because the circular PZT element vibrates closest to an ideal piston and the ultrasonic wavelength in the PZT is twice the thickness of the element. Given the planar frequency constant of PZT-8 in Table 3-1, for a resonant frequency of 1MHz, an element thickness of (2.30 ± 0.18) mm is required. In practice, the nearest suitable thickness readily stocked by the PZT suppliers is 2mm, corresponding to a resonant frequency of (1.15± 0.09) MHz. Therefore, for the present research a 7mm diameter, 1MHz resonant frequency, and 2mm thick circular PZT-8 element was used for the ultrasound transducer. Although, the resonant frequency is slightly above the drive pulse of a 1MHz element drive electronics, seeking to achieve a perfect match is impractical because the resonant frequency of PZT can decrease slightly as the element heats up during use (Martin *et al.*, 2003).

3.2.3 Fitting the PZT transducer and the electrodes in the lid

For mounting the PZT transducer in the test cell the same mounting arrangement was used as that in the planar phased array ultrasound transducer for creating mild hyperthermia described by Aitkenhead and co-workers (Aitkenhead *et al.*, 2008). The PZT transducer and the electrodes were mounted in the lid of the test cell. A copper wire having 1mm diameter and 10mm length was inserted through a hole in the lid of the test cell from the rear of the Perspex lid of the test cell. The tip of the copper wire was made flat using sand paper to allow a solder contact to be made. With the PZT elements held in the place in the lid, a thin wire was soldered between the front face of the PZT element and the tip of the copper wire in the recess. The solder contact on the front of the PZT element was kept small to ensure that it did not protrude above the surface level of the matching layer. This would allow for the matching layer which would later fill the recess and provide electrical insulation between this solder contacts and the medium. However, since the front face of the PZT element was electrically common and would be connected to ground, the electrical isolation provided by the matching layer would not be critical for safety if such an element is used in a clinical context. The high voltage drive was applied to the rear face of the PZT, precluding the possibility of a high voltage coming into contact with the medium.

Once the soldering has been completed at the front of the element, first Blu-Tack and then adhesive tape was applied to form a seal at the rear face of the PZT element with the rear of the Perspex lid. The alignment of the PZT element within the frame was checked repeatedly. The Blu-Tack was required to fill the free space of the back side of the PZT element. The tape and Blu-Tack will prevent the liquid epoxy from seeping through between the PZT elements and the Perspex frame. Once this sealing had been done, the recess on the front surface was filled with epoxy resin until it stood proud of the Perspex surface. Then it was allowed to cure at room temperature. Once cured the epoxy was ground back using wet abrasive paper until the surface was once again level with the Perspex frame. The surface of Perspex within the matching recession was abraded to ensure a reliable bond to form with the epoxy matching layer.

Araldite 2020 was chosen as a suitable epoxy due to its low viscosity in its liquid form and its water resistance nature in its cured state. It was mixed at a ratio of 100 : 35 (resin : hardener) by volume according to the manufacturer's recommendation. After filling the recess on the front surface, the araldite 2020 needed to allow 72 hours (or 24 hours at elevated temperature) at room temperature to cure properly. Enough time was needed to ensure adequate epoxy conversion (Karayannidou *et al.*, 2006). The low viscosity of

Araldite 2020 and slow curing allowed any gas bubbles formed during its application to rise to the surface of the epoxy. Grinding the protruding araldite 2020 layer with fine grade abrasive paper (P300A) and water allowed a smooth, level and air bubble free matching layer to be created.

The thickness of the matching layer was defined by the depth of the recess in Perspex lid. Once the epoxy was ground level with the lid surface, the thickness of the frame was measured with a micrometer at several points to ensure that it was an even thickness across the face of the array. The speed of sound in araldite 2020 is 2610 ms^{-1} (Ma *et al.*, 2007), and hence the wavelength of a 1MHz sound wave is 2.6 mm. To provide a matching layer of thickness λ/4 for optimal matching between the PZT and the medium, a layer of 0.65mm thickness was required. However, for construction of the transducer element a 1mm thick matching layer was used to ensure that the solder connections at the front of PZT lay entirely within the matching layer. It has been shown that the thickness of the matching layer is not critical to ensure adequate coupling into the medium (Wojcik *et al.*, 1996).

The completed Perspex top of the test cell was then ready for a drive signal to be applied to the PZT element. A 1.50m length of 50Ω coaxial cable (type RG178B/U) was used to supply the drive signals for the PZT elements. The cables entered the transducer from the back, connecting to sections of strip board fitted back Perspex top of the test cell. Wires from the PZT transducer element and the coaxial cable were connected at this strip board. The strip board ensured that the solder connections to the PZT were not stressed by the movement of the coaxial cables, making sure that the wiring of the transducer element was robust. The outer conductor of the coaxial cable was grounded to shield the inner conductor which carried the drive signal. The rear of the Perspex lid is shown in the Figure 3-21 where cable connections for the drive pulse are shown.

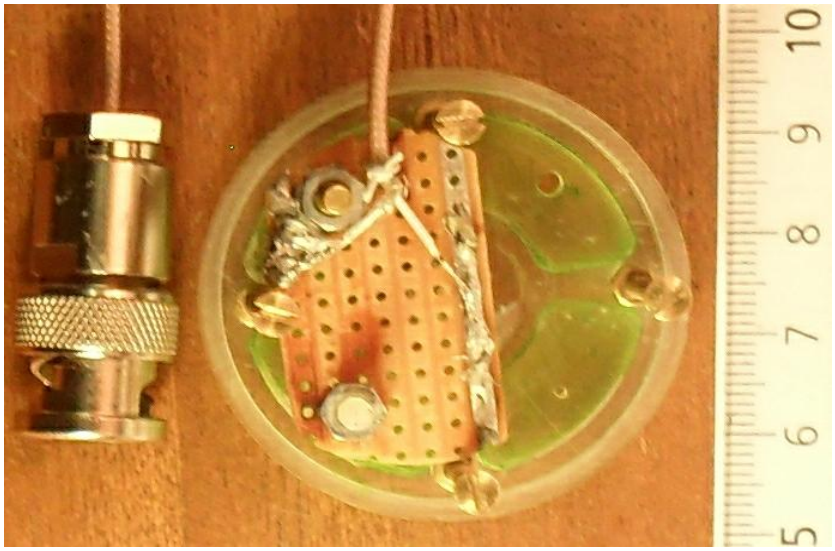

Figure 3-21 Showing the rear of the Perspex lid of the test cell. A coaxial cable is connected to a strip board fitted at the rear of the lid. Wires are connected from strip board to the back and front of the transducer to provide drive pulse to the transducer.

Four 8ba brass / stainless steel bolts were fitted to the threaded holes in the top of the test cell so that nuts fitted to the bolts formed the electrodes for electrical impedance measurements. The protrusions of the bolts into the medium were adjusted such that the nut face and end the bolt were flush.

3.2.4 Coupling media

For surface diagnostic and therapeutic ultrasound techniques a coupling medium (usually a gel) is required to ensure an air-free coupling between the ultrasound transducer and the surface of the skin since air is a poor conductor of ultrasound energy. When ultrasound probes are used within the body (e.g. during operations), then body fluids provide the coupling in the majority of applications.

For electrical impedance measurements made at the surface of the skin, an electrolyte is required between the metallic surface of the electrode and the surface of the tissue to be measured to convert the electronic conduction in the metal electrode to the ionic conduction in tissue. For surface measurements various coupling media including conducting gels and pastes are available, but naturally generated perspiration is used in some electrode systems. When intra-cavitary impedance measurements are made (e.g. in the cervix or oesophagus) the ionic fluids on the epithelial surfaces act as the electrolyte. In this research measurements were made on samples of tissue which is equivalent to making measurements within the body, therefore, no additional coupling media was necessary provided a good mechanical and electrical contact could be made between the

top of the tissue sample and the electrodes and ultrasound transducer mounted in the lid of the test cell. The lid of the test cell was recessed around the electrodes and ultrasound transducer element so that liquids and tissues could be displaced into these regions on fitting the lid to the test cell ensuring a good electrical and mechanical contact with the ultrasound transducer and electrodes within the lid.

The long term aim is to be able to make simultaneous electrical impedance and ultrasound velocity measurements from the surface of the body. In this case, a coupling gel will be required which will essentially be an ultrasound gel loaded with a soluble chloride compound so that it will support both types of measurement.

3.3 Electrical Impedance Instrumentation

The multi-frequency tetrapolar measurement system uses the same measurement technique as that used in the Sheffield Mk3.5 EIT system (Wilson *et al.*, 2001). The system used in this project is essentially a single channel version of that system. This system is intended for tetrapolar impedance measurement– using 4 separate electrodes, 2 are used as a drive electrode and the other 2 are used as the receive electrodes. Tetrapolar impedance measurement technique is chosen for this research over the focused impedance measurement techniques because it is the most common and widely used technique for impedance measurement in biological tissue. The device is capable of measuring electrical impedance simultaneously at 11 octave separated frequencies in the range 1kHz – 1024kHz. The drive signal consisted of repeated 1ms epochs of 11 summed sine waves such that repeated epochs provided a continuous sine wave at each frequency. Each frequency had a peak-to-peak amplitude of 200µA giving a maximum drive current of 1.2mA peak-to-peak. The voltage from the receive electrodes was amplified by a differential amplifier which had switchable levels of voltage gain of 10, 50 and 100. Before taking the measurement on a sample material, this voltage gain was switched to a particular level to give optimum level of voltage suitable for that measurement.

The block diagram of the electrical impedance measurement instrumentation is shown in Figure 3-22. The system has two components: a current drive component and a voltage measurement component. Current drive is achieved through a precision balanced voltage controlled current source (VCCS) which uses a modified Howland circuit (Bertemes-Filho *et al.*, 2000). The voltage measurement is done through a wideband differential amplifier constructed from 3 high speed op-amps. A brief description of each section of the multi-

frequency electrical impedance measurement instrument is given in the following paragraph.

The clock frequency is generated from a programmable crystal controlled oscillator chip set to deliver a frequency of 16.384MHz. This clock frequency is then divided by 2 to give a clock of 8.192MHz and this frequency is then used to drive a 13 stage binary ripple counter-divider. The binary outputs from the counter-divider circuit were used to cyclically address the first 8192 locations in the EPROM.

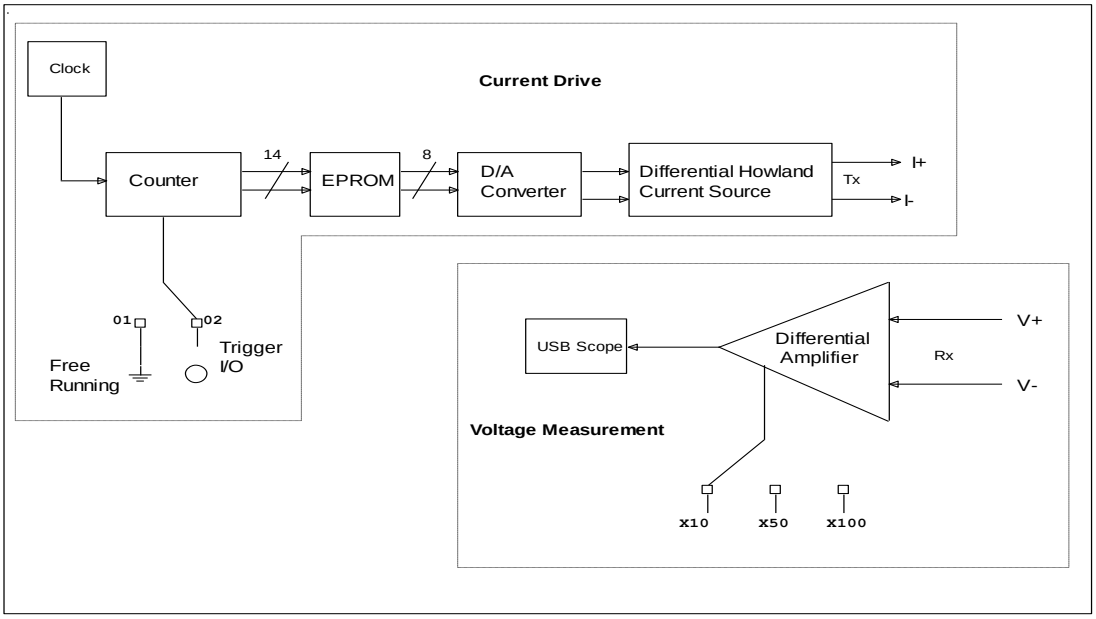

Figure 3-22 Block diagram representation of the Multi-frequency Electrical Impedance Measurement Instrument.

The EPROM contains the digital values for the 11 summed sine waves. The discrete values for 1ms periods of 11 sine waves with frequencies in the range 1kHz–1024kHz when clocked with a frequency of 8192kHz were generated in Matlab. The 11 frequencies were in a power of 2 sequence and each frequency contained an integer number of cycles within the 1ms period which contained 8192 data values. The lowest frequency (1kHz) gave 1 cycle which contained 8192 data values, whilst the highest frequency (1024kHz) gave 1024 cycles each of which contained 8 samples. The 11 sine wave signals were then summed to obtain the composite sine wave signal. The amplitude of the composite wave was then scaled so that the values were integers in the range 0–255. It should be noted that this scaling procedure meant all 11 sine waves had the same peak-to-peak amplitude in the composite signal. The scaled composite wave values were then converted to 8 bit data

format and saved as binary file. The binary values in this file were then programmed in to the EPROM by an EPROM programmer.

The 8 bit data clocked from the EPROM were converted to analogue signal by a digital to analogue converter (DAC). The unipolar differential current outputs from the DAC were converted to a bipolar voltage and then fed to two modified Howland current source circuits that provided a differential current drive. The sensitivity of the current source was set to provide 1.2mA peak-to-peak current for a binary value of 255 at the digital inputs to the DAC. This gave a current drive of 200μA for each frequency in the composite signal. The outputs from the Howland current source were AC coupled to the tissue to prevent electrolysis from DC potentials arising from offset voltages and currents. The output impedance of the current source was measured and found to be 316kΩ at 10kHz and 45kΩ at 1MHz.

The voltage measurement in the impedance measuring instrument was done through a differential amplifier. The differential amplifier used the standard 3 op-amp instrumentation amplifier configuration which was capable of gain adjustment through altering a single resistor as well providing very high input impedance. AC coupling was used at the input of the amplifier to prevent electrolysis in the tissue samples caused by DC potentials arising from voltage and current offsets in the devices. Low-noise, high bandwidth FET-Input operational amplifiers (OPA657) were used throughout.

3.4 Data acquisition

For data acquisition of the multi-frequency electrical impedance measurement and ultrasound propagation velocity measurement, a National Instrument high speed digitiser (USB-5133) was used. The schematic diagram of the experimental apparatus is given in the Figure 3-23. The USB-5133 was the capable of acquiring data at a maximum rate of 100MS/s. The digitiser has 2 channels with 8 bit resolution. The 2 channel digitiser was chosen in order to acquire ultrasound and impedance data simultaneously using both channels.

For interfacing the USB-5133 digitiser to a computer and collecting data functions were written in C which were implemented and called from Matlab (MEX-files) rather than using the National Instrument LabVIEW graphical programming language.

In this research several MEX-files were written in C to configure and control all the data acquisition parameters. The functions of the digitiser controlled included setting up the

channels, the sampling rate, the trigger type and trigger level. These MEX-files effectively interfaced the impedance and ultrasound measurement electronics with a computer through the USB-5133 high speed digitiser. In the present work the ultrasound and impedance data were digitised at 100MHz and 10MHz respectively.

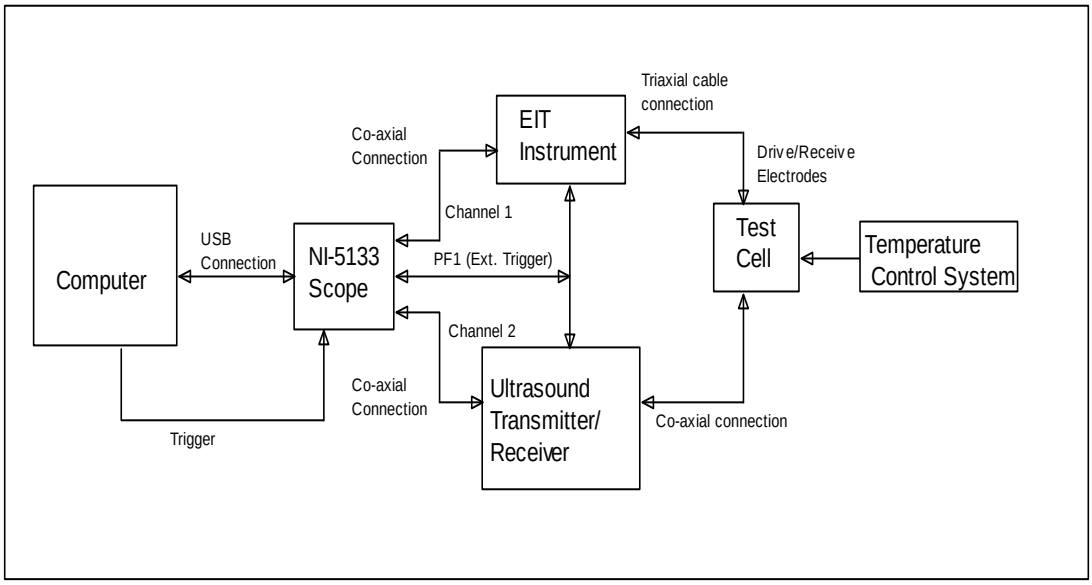

Figure 3-23 Showing the schematic diagram of the experimental apparatus. Interfacing to the computer and the EIT and the Ultrasound Instrument is done through programmes written in C.

For both cases 10,000 data points were acquired. The USB-5133 was programmed so that data acquisition was triggered externally from the computer. In this way the electrical impedance and ultrasound propagation velocity measurements remained under computer control, where the computer could trigger the simultaneous measurements by giving a digital signal through the PFI connection of the USB-5133 digitiser.

3.5 Temperature control

The purpose of this work was to observe the influence of temperature on the ultrasound propagation velocity and electrical impedance of tissue. For this, the ultrasound and impedance data from the sample materials need to be acquired with the change of temperature. To increase the temperature of the tissue sample within the test cell a thermostatically controlled hot plate with a magnetic stirrer from Fisher Scientific (Model no: 11-302-5008HP) was used. A water bath was created from a 1000ml beaker placed on the white ceramic coated aluminium top of the hot plate with magnetic stirrer inside the beaker (Figure 3-24). After filling the test cell with the sample materials required for a particular experiment, two thermocouples were inserted in the sample materials at approximately half the depth of the test cell. Here, general purpose K-type thermocouples

were used with a sensitivity of approximately 41μV/°C. Two thermocouples were used in order to minimize gradients in the temperature of the sample material. The other ends of the thermocouples were connected to a calibrated digital thermometer (Digitron Ltd, model 2038), which has temperature accuracy of (0.1% scale ± 0.2°C) for K type thermocouples. The test cell was then placed in a water bath through the integral ring-stand holder of the magnetic hotplate. The hotplate temperature could either be controlled from the temperature of the hotplate itself or by a temperature probe placed in the liquid being heated by the hotplate. For the measurement made in this project, the Teflon coated temperature probe of the hot plate was used and was placed into the water bath. A temperature display system on the hot plate indicated the actual temperature of the water bath. Then the stirrer was run for 10minutes at the maximum speed 1200rpm before setting up the temperature and stirring speed to 300rpm during the whole period of research. The stirring speed was chosen as 300rpm, since it gave uniform mixing of the water in water bath. Stirring speed higher than 300rpm produced a vortex down the test cell.

The temperature of the phantom materials was increased from room temperature to 50˚C. The ultrasound and electrical impedance measurements were made on the sample materials with temperature changing from 25 to 50˚C in 5°C increments. For tissue samples the upper temperature was limited to 50˚C to avoid any tissue damage. Beyond 50°C temperature irreversible tissue damage has been found to occur and for this reason some researchers proposed to heat up the tissue maximum at 50°C for mild hyperthermia treatment (Kerr *et al.*, 1994; ter Haar, 1999a). Figure 3-24 shows the complete experimental setup for simultaneous ultrasound and electrical impedance measurements with the change of temperature.

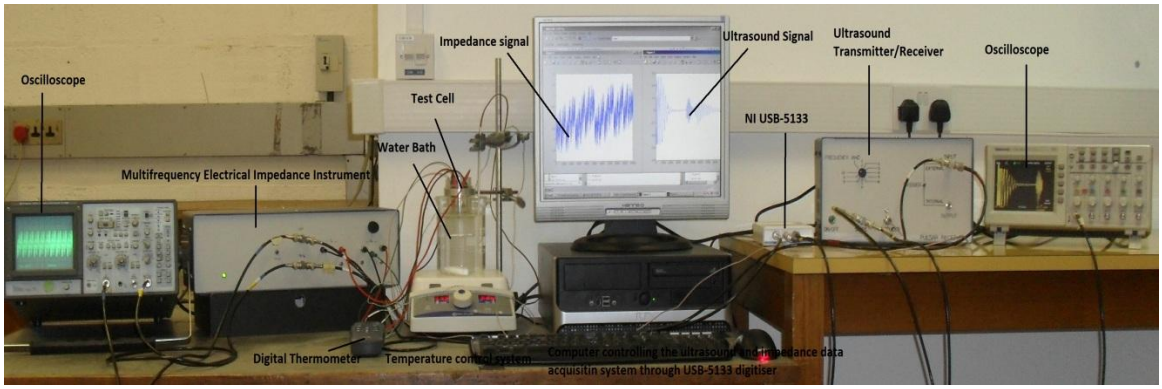

Figure 3-24 Showing the experimental setup for simultaneous ultrasound and electrical impedance measurement with the change of temperature. For data acquisition through the NI USB-5133 the interfacing to the computer and the EIT and Ultrasound transmitter/ receiver is done through functions written in C.

3.6 Data processing

3.6.1 Ultrasound

The ultrasound data were displayed and processed in Matlab. Several functions were written in Matlab to process the ultrasound data. To improve the signal-to-noise ratio averaged data from 20 multiple measurements were taken. Following averaging, the received ultrasound data were passed through a band pass filter. The equi-ripple FIR band pass filter was created using the Matlab signal processing tool box. The band pass filter had a length 284 samples and pass band range was 750kHz – 1.25kHz provided greater than 40dB attenuation of noise components (specifically, the 200kHz sub harmonic ringing of the transducer described in section 3.1.1 and shown in Figure 3-4). The filtered ultrasound data were then squared and smoothed using a median filter and peaks in the reflected signal were detected. The ultrasound propagation velocity in a sample material placed in in the test cell was calculated by using the formula given in equation 3-1.

$$v = 2d/t \qquad \text{3-1}$$

where,

d = distance from the transducer's front surface to the bottom of the test cell,

t = measured time of flight of the ultrasound signal reflected from the bottom of the test cell,

v = ultrasound propagation velocity in the sample material placed in the test cell.

3.6.2 Electrical impedance

The measured voltage from the tetrapolar electrical impedance measurements were also displayed and processed in Matlab. Several functions were written in Matlab to process

these data. To improve the signal-to-noise ratio, averaged voltage data from 20 multiple measurements were taken. An FFT was performed on the digitised average voltage data to determine the amplitude and phase spectrum for each of the drive frequencies. The amplitude and phase spectrum was then scaled to determine the real part of the transfer impedance in ohms and phase difference in degrees. The details of the impedance and phase calculations are explained in the following sections.

3.6.2.1.1 Impedance calculation from the FFT of the received signal

The FFT of the received voltage signal from a sample material gives a mirror image of the magnitude spectrum with each containing peaks different at 1, 2, 4, 8, 16, 32, 64, 128, 256, 512, and 1024kHz centred on half the sampling frequency. The relationship between the amplitude of the injected current and the magnitude of the amplitude spectrum of the received voltage signal is needed to calculate the transfer impedance and this is given in equation 3-2. The impedance at each measured frequency was calculated by using the equation 3-2.

$$\boldsymbol{Z = \frac{2A}{NG} \cdot \frac{1}{(I/nf)}} \qquad \textbf{3-2}$$

where,

Z = impedance in ohm,

A = single sided spectrum amplitude in volts,

nf = total number of discrete frequency,

N = number of data points,

G = switchable gain of the differential amplifier,

I = resultant peak to peak currents in ampere.

In the above formula, 2 is needed to convert the double sided spectrum amplitude to single sided spectrum amplitude. The value of nf was equal to 11, since the spectrum was received at 11 different frequencies. The number of data points, N was equal to 10,000 for impedance measurement. The value of the gain, G is switched to any value among 10, 50, and 100 before the start of the measurement. Since the original voltage signal is amplified by G times before the digitisation, the result should be divided by the gain of the amplifier which will give the actual magnitude of the voltage at each frequency. Finally, to get the impedance values at each frequency it was necessary to divide the voltage values by the resultant peak to peak input currents, which is fixed to 1.2mA for the electrical impedance

measurement instrument used in this research. The same steps will be followed to get the impedance values at each measured temperature.

It is noted that the amplitude of the individual sine waves that were summed to give the composite drive signal was set so that the o/p current for each was the same and equal to 200µA peak to peak. Because the composite signal was within an EPROM, the individual components were no longer directly visible. The peak to peak current could however be checked via an oscilloscope and resistor and thus was done as part of the routine quality assurance of equipment during the measurements. Therefore, the factor I/nf was used as an index of the average current in order to calculate the transfer impedance.

3.6.2.1.2 Phase calculation from the FFT of the received data

The phase information of biological tissue in electrical impedance measurements is always difficult to obtain (Smith, 1992; Osterman *et al.*, 2000; Koo *et al.*, 2007). For phase determination at the measured frequency, it was necessary to have a reference signal. The transmitted composite current signal which is programmed in the EPROM of the impedance measurement instrument (section 3.3) is used as the reference signal for phase calculation. The phase difference between the measured voltage signal and the injected current signal was determined at the designated 11 discrete frequencies. But, the expected phase difference between the current and the voltage signal for any sample materials gave unpredictable results on tissue, when the phase appeared to alter +180° at one of the higher frequency (>128kHz) measurements.

To investigate the source of this error – whether there was a problem with the test cell–a signal obtained across a tissue mimicking phantom constructed from resistors and capacitors was used. The circuit diagram and the impedance and phase response of this tissue mimicking phantom is shown in the Figure 3-25 and Figure 3-26 respectively. The value of the discrete component was chosen according to the Cole-Cole (Cole and Cole, 1941) model of the tissue, with 240Ω, and 20Ω were used as the extra- and intra-cellular impedance value, and 1nF was considered as the value for the membrane capacitance. These values were in line with measurements made using 4 electrodes with 20mm spacing in a human abdomen. Repeated measurements on this phantom gave no problem with discontinuity in the phase spectrum (Figure 3-26b). Therefore, it was concluded that it was the result of the measurement system.

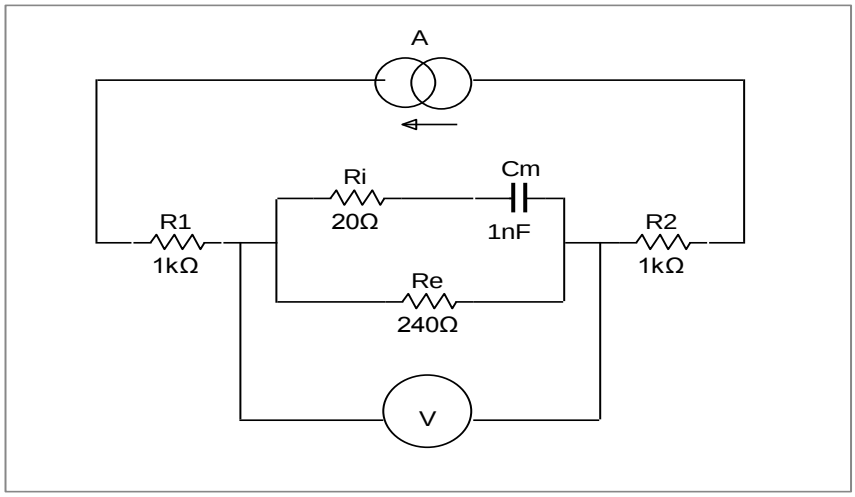

Figure 3-25 The circuit diagram of the cell mimicking phantom materials.

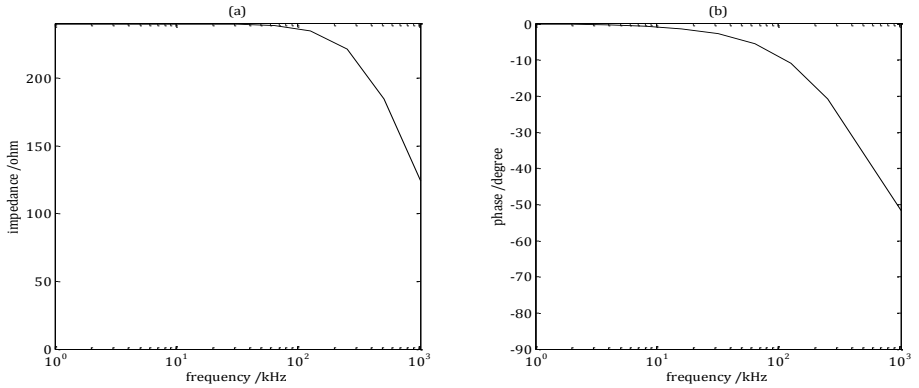

Figure 3-26 Showing the theoretical (a) impedance and (b) phase response of the tissue mimicking phantom materials.

Subsequently, measurements were made on a sample saline solution (σ = 1ms.cm^{-1}) in the test cell but it failed to produce the correct phase information on the saline solution, exhibiting the step change in phase at one of the higher frequencies. As the measurement system for this research was intended for simultaneous use of electrical impedance and the ultrasound propagation velocity measurements, the PZT transducer was present in the top of the cell on the same plane as the electrodes. The surface of the PZT closest to the sample was connected to earth (section 3.2.3). There may be some capacitive effect arising between the PZT element and the sample material which generated the problem– although why this should be intermittent remains unclear. A possible cause includes instability in the o/p stage of the high speed op-amp producing low level oscillations which can be load impedance critical. Essentially, the phase spectrum gave a discontinuity where the phase changes changed from a negative value to a positive value at high frequency. However, the phase changes always saturated to ±180°, so a code was written in Matlab to correct the

phase calculation. The Matlab script (or simply the algorithms) written to correct phase calculation followed the procedure illustrated in the flow diagram in Figure 3-27.

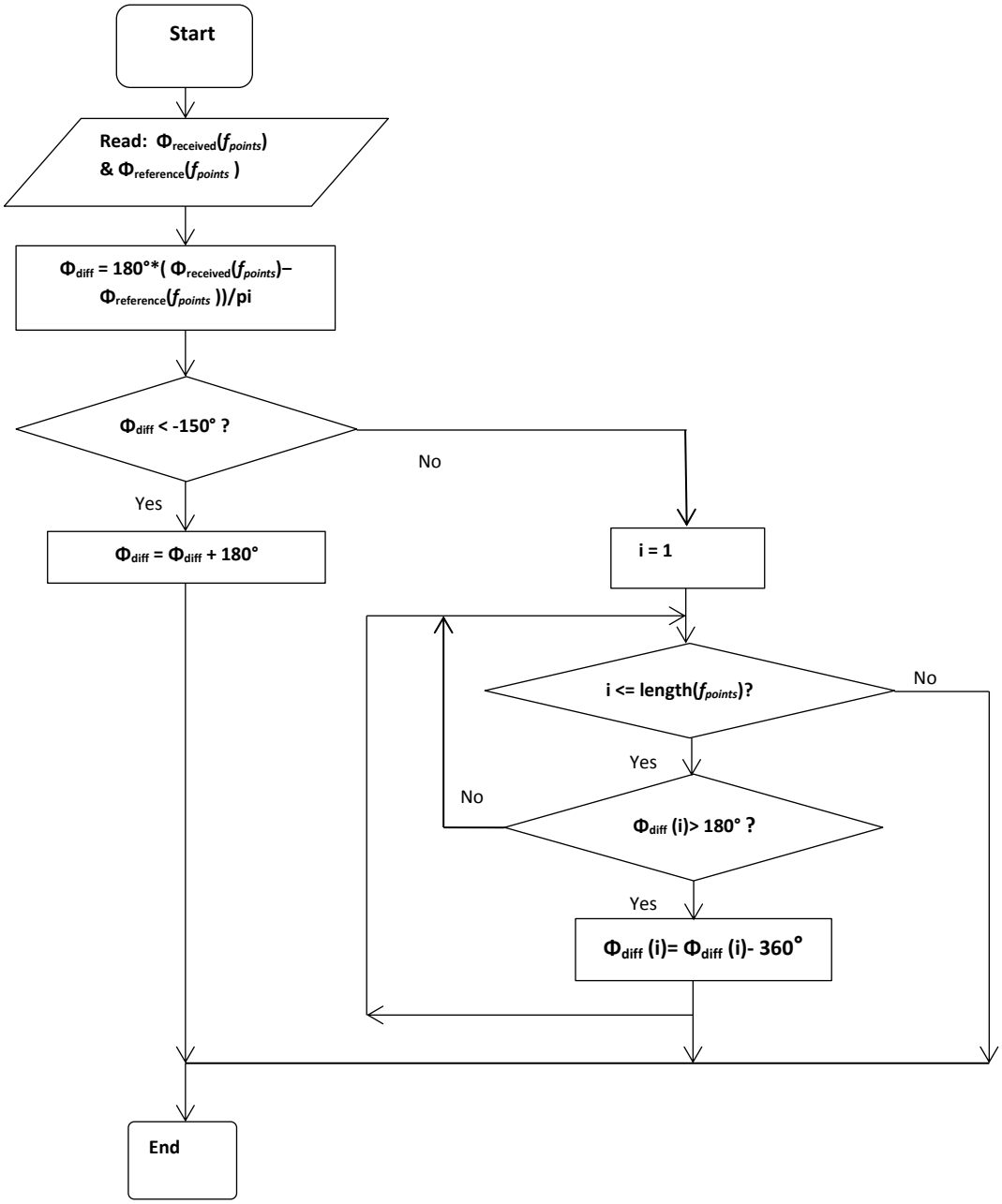

Figure 3-27 A flow chart illustrating the phase calculation and correction procedures.

The phase difference is measured with respect to a reference signal which in this project was calculated with respect to a reference signal measured in a purely conducting medium. Based on a Cole-Cole model of tissue, the phase difference for cellular tissue should lie in the range 0° to -90° for the frequency range 1kHz – 1MHz. For some phase determinations, values greater than -90° were obtained, usually close to -200°. Therefore, a phase correction procedure was introduced such that when the phase difference from the FFT

was less than -150°, 180° was added to the calculated phase difference. Occasionally phase differences of around +200° were obtained from the FFT: to correct such values, 360° was subtracted from the calculated phase value if the phase difference was greater than 150°.

3.7 Preliminary experiments

Prior to embarking a measurement on tissue, ultrasound propagation velocity (section 3.7.1.1) and electrical impedance (section 3.7.2) measurements were made on substances with known thermal properties to validate the measurement system and provide results against which tissue results can be compared and evaluated. As part of describing these preliminary experiments, the data acquisition (section 3.7.1.1.3) and signal processing (section 3.7.1.1.4) for the ultrasound measurements will be described in more details.

3.7.1 Ultrasound

Initially, the ultrasound propagation velocity measurements were taken by filling up the test cell with water. The ultrasound measurement showed a clear reflection from the base of the test cell. From the time of flight of the ultrasound signal and distance from the front surface of the ultrasound transducer to the base of the test cell, the ultrasound propagation velocity in water was measured using equation 3-1 given in section 3.6.1. For time of flight detection, the first peak of the reflected signal was counted. The calculated ultrasound propagation velocity in water, $1496 ms^{-1}$, was in agreement with the value published in literature (Hill *et al.*, 2004; Duck, 1990). Then, some copper wire stands of different height were made in order to place a metallic reflector at different depth inside the test cell filled with water. To make the copper wire stands, a single core PVC insulated cable with 1mm diameter rigid copper conductor was used (RS part number 694-1990). The insulation was removed and stands with different heights were made from the 1mm diameter copper wire stretched to work harden it and make it rigid. The ultrasound measurements were made by placing the metallic reflector in water at different depth inside the test cell. The ultrasound measurement showed reflection from the metallic reflector placed at different depths. The Figure 3-28a shows the ultrasound signal from a metal reflector placed at a distance 19mm inside the test cell from the front surface of the ultrasound transducer. The peaks of the full wave rectified reflected signals are also detected and shown in the Figure 3-28b.

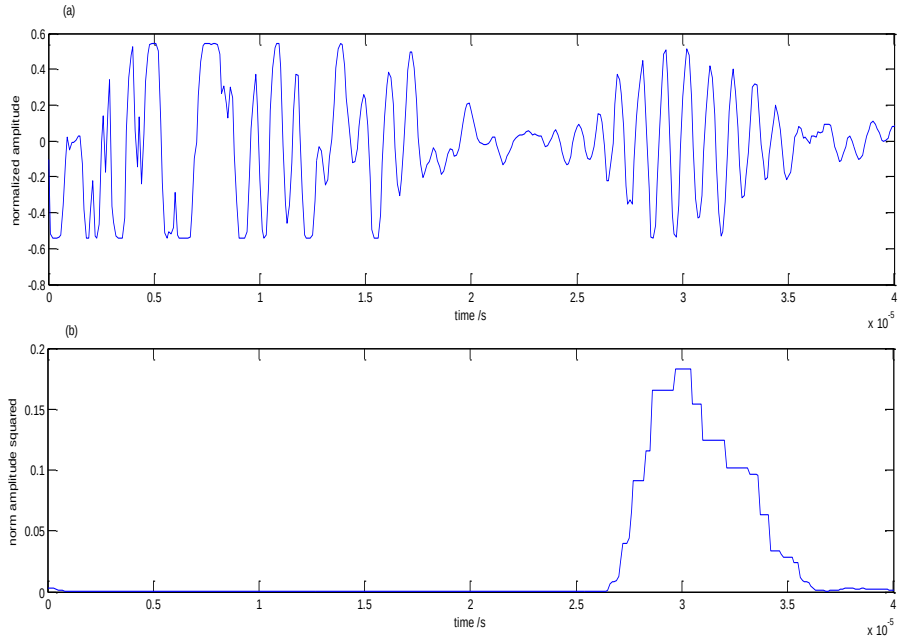

Figure 3-28 Showing (a) the reflected ultrasound signals and (b) its peaks from a reflector placed at 19mm distance from the transducer.

The ultrasound measurements on the vegetable fat (sunflower oil) sample were taken with changing the temperatures from 20°C to 55°C to verify the temperature measurement system. Having filled the test cell with vegetable fat, the thermocouples were inserted into the solution through the lid. The test cell was then placed in the water bath from the ring stand. The temperature of the vegetable fat sample was increased from room temperature to 50˚C using the thermostatically controlled hot plate and stirring the magnetic stirrer inside the water bath. The ultrasound measurements were done for temperature 20°C to 55°C in 5°C increments. Repeated measurements (5 times) were taken both during the heating and cooling session of the sample. Temperature measurements were made by the digital thermometer connected to thermocouples inserted into the test material (section 3.5). For each measured temperature, the ultrasound propagation velocity in vegetable fat was calculated using the time of flight information. As mentioned before, the first peak of the reflected pulse was considered for the time of flight detection. Similarly, for ultrasound propagation velocity calculation the equation 3-1 given in section 3.6.1 was used.

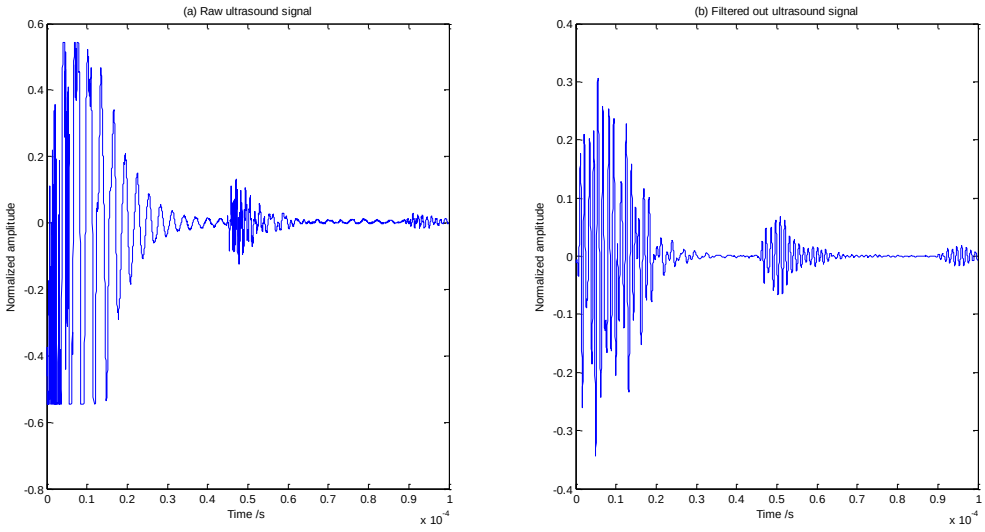

Figure 3-29 The ultrasound signal in the vegetable fat at 40°C showing the detection of the reflected pulse from the base of the chamber. (a) showing the raw ultrasound signal (b) showing the signal after application of the FIR band pass filter to remove the 200kHz component (section3.6.1). The reflection from the base of the test cell can be seen centred at 50µs.

The reflected ultrasound signal from the base of the test cell at temperature 40°C in the vegetable fat sample is shown in the Figure 3-29. The calculated ultrasound propagation velocities in vegetable fat were plotted against temperatures. Figure 3-30 shows the changes of ultrasound propagation velocity in the vegetable fat with temperature. From Figure 3-30 it can be observed that the ultrasound propagation velocity in vegetable fat decreased with increasing temperature indicating the negative temperature coefficients of ultrasound propagation velocity in fat (Figure 3-30). The magnitude and changes of ultrasound propagation velocity with temperature in vegetable fat were in agreement with the value obtained by McClements and Povey (1471.6ms^{-1} at 20°C and -0.23%°C^{-1} change with temperature) (McClements and Povey, 1988).

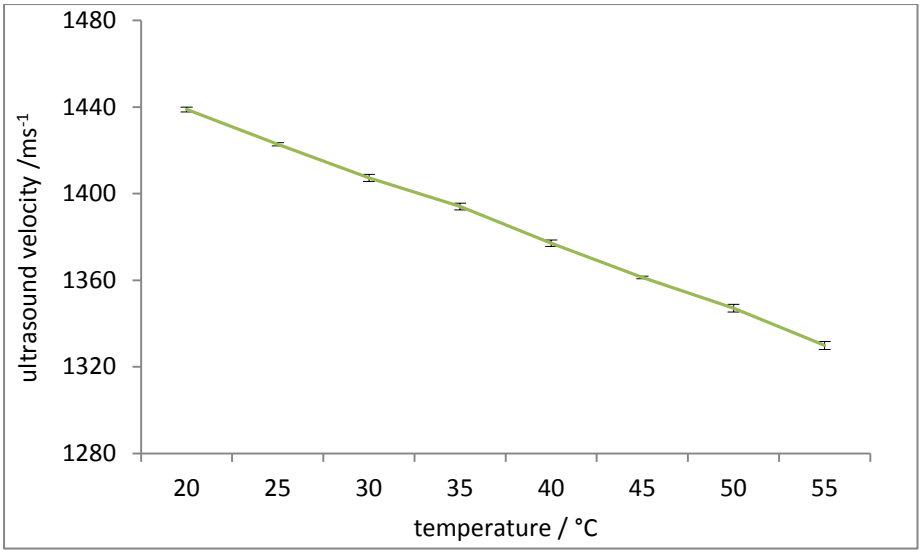

Figure 3-30 The changes of ultrasound propagation velocity with temperature in the vegetable fat (sunflower oil). The vertical error bars represent standard error of the mean.

3.7.1.1 Ultrasound Measurements in aqueous solution with different ion concentration

Ultrasound measurements on aqueous samples with varying ion concentrations (different conductivity level) were made. The aim of these measurements is to investigate one of the possible factors which cause the variation of ultrasound propagation velocity. To do this, first the effect of ion concentration on the ultrasound propagation velocity as well as theirs effects on changing the ultrasound propagation velocity with temperature were investigated. Moreover, since the purpose of this research is to use the electrical impedance and ultrasound measurements simultaneously and the former is based measuring the conductivity, therefore it is necessary to know the effect of ion concentration on the ultrasound propagation velocity.

3.7.1.1.1 Sample preparation:

Sample solutions with different percentage of ion concentration were prepared by varying the amount of NaCl added to de-ionized water. De-ionized water was chosen because it has no free ions. First, some amount of NaCl was taken in a glass beaker and its quantity was weighed by a high precision (0.1g resolution) scale (KERN EMB 500-1). The de-ionized water was then slowly poured into the beaker containing the salt and stirred to dissolve the salt completely. The volume of the deionized water used for each sample preparation was also recorded. The conductivity level of the solutions was measured by using a hand held conductivity meter (RS 180-7172). To achieve a particular conductivity value more deionized water or salt was added to the solution.

3.7.1.1.2 Calculation of ion concentration:

From the weight of NaCl and the volume of de-ionized water, the ion concentration of the sample solution with different conductivity levels was calculated in terms of molar concentration. The calculated values are tabulated in the Table 3-2.

Table 3-2 Ion concentration of the prepared experimental sample solution with different values of conductivity.

Conductivity σ, $mS.(cm)^{-1}$	Molar concentration, $mol.L^{-1}$	Ion concentration, $(molecules).L^{-1}$
σ_1=0	0	0
σ_2= 0.1	0.000906	$0.000906 \times 6.02 \times 10^{23}$
σ_3= 1	0.0107	$0.0107 \times 6.02 \times 10^{23}$
σ_4= 10	0.15	$0.15 \times 6.02 \times 10^{23}$
σ_5= 20	0.912	$0.912 \times 6.02 \times 10^{23}$

3.7.1.1.3 Ultrasound measurements:

The ultrasound measurements on aqueous ionic solutions were made following the same procedure used for the ultrasound measurement on vegetable fat sample (section 3.7.1). Having filled the test cell with ionic sample solution, the thermocouples were inserted into the solution through the lid. The test cell was then placed in the water bath and the temperature of sample solution was increased from room temperature to 50˚C. The ultrasound data were acquired for temperature range 20–50°C, in 5°C increments and data were collected both for the heating and cooling session. Temperature was measured by the digital thermometer connected to thermocouples inserted into the ionic solution (section 3.5). For each measurement at a measured temperature, an average of 20 raw data sets was taken (Figure 3-31). For each sample five sets of measurements were taken.

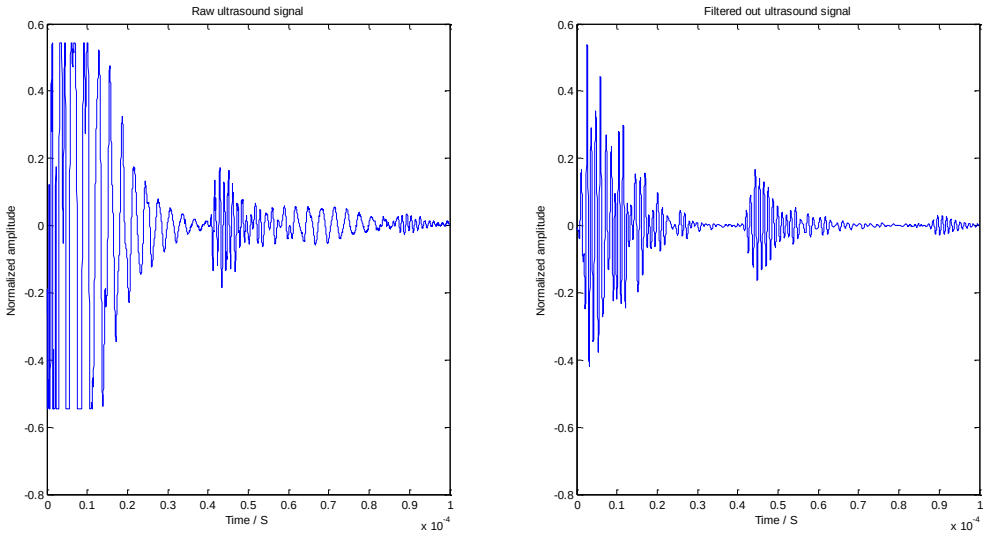

Figure 3-31 The ultrasound signal in 1mS(cm)$^{-1}$ deionized water at 40°C showing the detection of the reflected pulse from the base of the chamber. (a) showing the raw ultrasound signal (b) showing the ultrasound signal after application of the FIR band pass filter. The reflection from the base of the test cell can be seen centred at 45µs.

3.7.1.1.4 Ultrasound data processing:

The ultrasound data were processed in Matlab. Following data acquisition and averaging, the received ultrasound data were passed through the band pass filter (section 3.6.1). The filtered ultrasound signal is shown in the Figure 3-31b. The time of flight of the ultrasound signal from the transducer's front surface to the bottom of the test cell was measured considering the first peak of the reflected pulse. Since the distance from the transducer's front surface to the bottom of the test cell was known, the ultrasound velocity in the sample solution was calculated by using the equation 3-1 given in section 3.6.1. The ultrasound velocity data were then tabulated and the mean and standard error of the mean were calculated for the 5 set of measurements and plotted in a spread sheet to observe the change of velocity with the increase of temperature (Figure 3-32 and Figure 3-33). The mean ultrasound velocities at each measured temperature from the 5 different set of measurements were calculated. The percentage change of the ultrasound velocity per degree Celsius temperature for the measured temperature was also detected for each of the sample solution (Table 3-3). To detect the percentage change of ultrasound velocity at a particular measured temperature, the difference in ultrasound velocity at that temperature from the preceding measured temperature was detected. This difference gave

a change in ultrasound velocity for 5°C temperature change and later it was converted to percentage change of ultrasound velocity per degree Celsius.

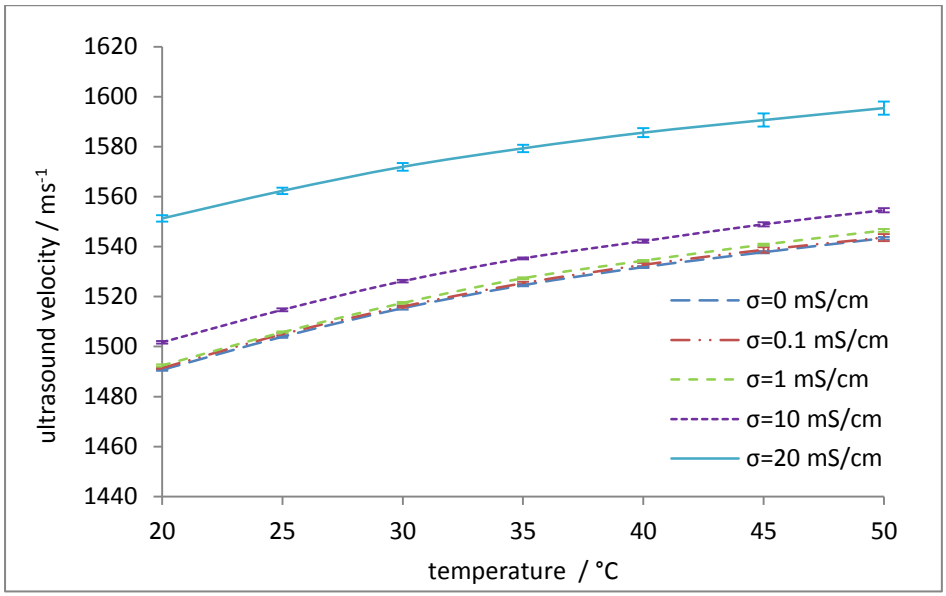

Figure 3-32 Showing the change of ultrasound velocity with temperature in aqueous solution having different levels of conductivity.

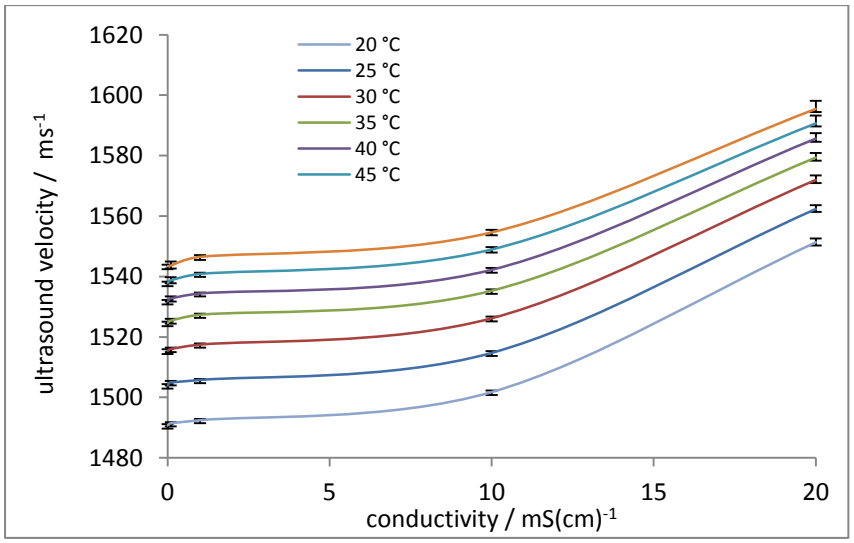

Figure 3-33 Ultrasound propagation velocity in ionic solution are plotted against conductivity at all the measured temperatures. The lines are guide to the eye to emphasise the profile of changes in propagation velocity with conductivity at different temperatures.

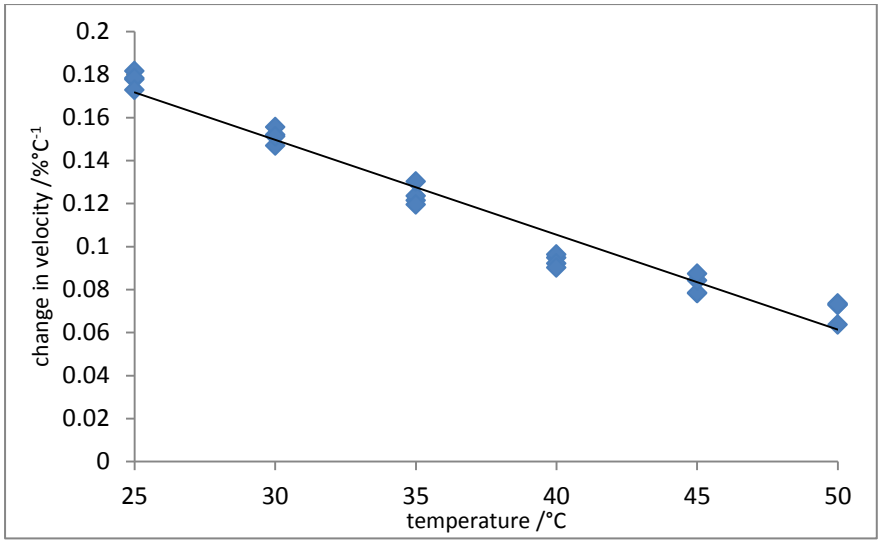

Figure 3-34 Showing the percentage change of ultrasound propagation velocity in the ionic solutions having conductivity levels in the physiological range (≤ 1mScm^{-1}). Line-of-best-fit is shown with individual data points.

Table 3-3 Percentage change of ultrasound propagation velocity in ionic solutions with temperature.

Temperature Co-efficient of Ultrasound Velocity /%°C^{-1}					
T / ◦C	σ =0mS(cm)$^{-1}$	σ =0.1mS(cm)$^{-1}$	σ =1mS(cm)$^{-1}$	σ =10mS(cm)$^{-1}$	σ =20mS(cm)$^{-1}$
25	0.18	0.18	0.18	0.17	0.14
30	0.15	0.15	0.16	0.15	0.12
35	0.12	0.12	0.13	0.12	0.09
40	0.09	0.10	0.09	0.09	0.08
45	0.08	0.08	0.08	0.09	0.06
50	0.07	0.07	0.07	0.07	0.06

3.7.1.1.5 *Results and discussions:*

The aqueous sample solution with different levels of conductivity or ion concentration showed positive change of ultrasound propagation velocity with increasing temperature for all conductivity values measured (Figure 3-32 and Figure 3-33). Figure 3-32 shows the ultrasound propagation velocity against temperature and Figure 3-33 shows the ultrasound velocity against conductivity. The vertical error bars in Figure 3-32 and Figure 3-33 represented the standard error of mean ultrasound propagation velocity for the ionic solutions. The standard errors of mean increased with increasing temperature as well as with increasing conductivity. The change of ultrasound propagation velocity with temperature is nearly independent of conductivity for values up to 1mScm^{-1} when compared with the results for 10 and 20mScm^{-1} (Figure 3-32 and Table 3-3). The magnitudes of the ultrasound propagation velocity in the sample solutions having

conductivity in the range 0 to 1mScm^{-1} were approximately equal and their corresponding rate of change of velocity with temperature was also same. However, whilst sample solutions having higher conductivity (σ = 10 and 20mScm^{-1}) gave a greater ultrasound propagation velocity than the corresponding values for lower conductivity solutions (σ = 0 – 1mScm^{-1}) (Figure 3-32 and Table 3-3). The aqueous solutions with different levels of conductivity have positive temperature coefficients of ultrasound propagation velocity. In the mild hyperthermia temperature range (40-45°C), the percentage change of ultrasound propagation velocity with temperature is almost same for the sample solution with conductivity level zero to 10mScm^{-1} (Table 3-2).

The majority of the ionic fluids within the body have conductivity less than 2mScm^{-1} (Duck, 1990). As for example, liver has conductivity around 1mScm^{-1} and fat has conductivity less than 0.2mScm^{-1} (Duck, 1990) and the mild hyperthermia community are primarily interested in cellular and fat tissue types. From Figure 3-33 it can be observed that the ultrasound propagation velocity in this conductivity range at all the measured temperature was independent of conductivity. Beyond that conductivity level, the ultrasound velocity increased with increasing of conductivity.

The rise of ultrasound propagation velocity with increasing temperature in the ionic sample solutions is due to positive temperature coefficients of ultrasound propagation velocity in the ionic solutions. The types of temperature coefficient of the ultrasound propagation velocity depend on the molecular components of the solution.

It should be noted that the test cell used for this research was a closed chamber and the thermal expansion of the Perspex chamber was negligible. So, thermal expansion of the sample solution will not produce an increase in distance to the reflecting surface. However, despite the closed chamber, the increasing temperature may decrease the density of the ionic solutions because the sample can expand.

Another cause of the change of ultrasound velocity could be the increase of equivalent conductance in the ionic solutions with increasing temperature. This may be due to two causes, firstly the increased mobility of the ions due to a lower viscosity of the solvent at the higher temperature, and secondly to the fact that the electrolyte when not completely dissociated, may dissociate more as the temperature raised (Coolidge and Bent, 1936). However, as seen from the Figure 3-32 and Figure 3-33 that the change of ultrasound propagation velocity with temperatures in the sample solutions having conductivity 0–

1mScm^{-1} is negligible. Therefore rise in conductivity with temperatures will have negligible effect on increasing the ultrasound velocity with temperatures.

Since, the ultimate target of this research is to predict tissue temperature as well as to characterise tissue based on the 'ultrasound' and 'electrical impedance measurements' during mild hyperthermia, the results presented here show 'ion concentrations' in the physiological range have negligible effects on the change of ultrasound velocity with temperature. The results show the percentage change of ultrasound velocity with temperature (mild hyperthermia temperature: 40–45°C) was almost same for sample solutions with conductivity levels in the range 0 – 1mScm^{-1} (Table 3-3).

3.7.1.2 Ultrasound Measurements in solutions with various percentage of fat

Ultrasound measurements on sample solutions with various percentages of fat were made to investigate the effect of fat on ultrasound propagation velocity with the change of temperature. In the previous measurements (Figure 3-30) on vegetable fat (100% fat), it has been shown that pure fat has negative temperature coefficients of ultrasound velocity. However, in this experiment the effect of change of percentage of fat on the temperature coefficients of ultrasound propagation velocity was investigated. It is difficult to create a sample tissue with known percentage of fat, therefore for this experiment, liquids with high fat content were chosen.

3.7.1.2.1 Sample preparation:

Liquids with a high content of fat molecules (double cream or single cream) were collected and several samples with varying fat content were created. The percentage of fat in the solution was calculated from known density values cited in the literature (Goff, 1993). Several sample solutions with various percentage of fat were prepared by mixing double cream or single cream with de-ionized water in different proportions. Sample solutions having fat percentages of 47% (double cream), 35.25% (3 part double cream + 1 part water), 31.33% (2 part double cream + 1 part water), 23.5% (1 part double cream + 1 part water), 18% (half cream),15.3% (1 part double cream + 2 part water), 9.4% (1 part double cream + 4 part water), 6% (1 part half cream + 2 part water) of fat were prepared. Milk with 4% (whole milk) and 2% (semi skimmed) fat provided two further sample solutions.

3.7.1.2.2 Ultrasound measurement and data processing:

Ultrasound measurements on fatty sample solutions were taken using the same procedure described in the section 3.7.1.1.3. Data were processed in Matlab according to the procedure described in section 3.7.1.1.4 to calculate the velocity from the time of flight of

ultrasound signal. The ultrasound velocity data were plotted against temperature (Figure 3-35). The percentage change in ultrasound velocity per degree Celsius changes in temperature were calculated (Table 3-4). The percentage change of ultrasound velocity with temperature was detected following the same methods that were followed for the sample solution with varying percentage of ion concentration (section 3.7.1.1.4).

3.7.1.2.3 Results and Discussion:

Figure 3-35 illustrates the change of ultrasound velocity with temperature in solutions with different percentages of fat. In solutions with a low percentage of fat (<18%), the ultrasound velocity increased with increasing temperature indicating a positive temperature coefficients for ultrasound propagation velocity. However, in solutions with a higher percentage of fat (>18%), the ultrasound velocity decreased with increasing temperature indicating a negative temperature coefficient for the ultrasound propagation velocity. The sensitivity of ultrasound propagation velocity change with temperature in the sample solution with 18% of fat content is almost zero. From these results, it can be observed that fat molecules in a solution have significant effects on the change in the ultrasound velocity with temperature. In particular, the direction of change in ultrasound propagation velocity changes with increasing fat content. The fat molecules not only reduce the rate of change of ultrasound propagation velocity with temperature but also become a factor in reducing the absolute value of ultrasound velocity at a particular temperature.

Table 3-4 Temperature coefficients of ultrasound velocity in solution with various percentage of fat.

	Fat / %									
	2	4	6	9.4	15.3	18	23.5	31.33	35.25	47
T / °C	Ultrasound Velocity Change / %°C^{-1}									
30	0.11	0.10	0.08	0.09	0.08	0.00	0.01	0.00	-0.03	-0.11
35	0.10	0.08	0.07	0.07	0.06	-0.02	0.00	-0.02	-0.05	-0.10
40	0.08	0.06	0.07	0.07	0.04	-0.02	-0.01	-0.05	-0.05	-0.09
45	0.08	0.06	0.06	0.03	0.00	-0.02	-0.05	-0.09	-0.08	-0.09

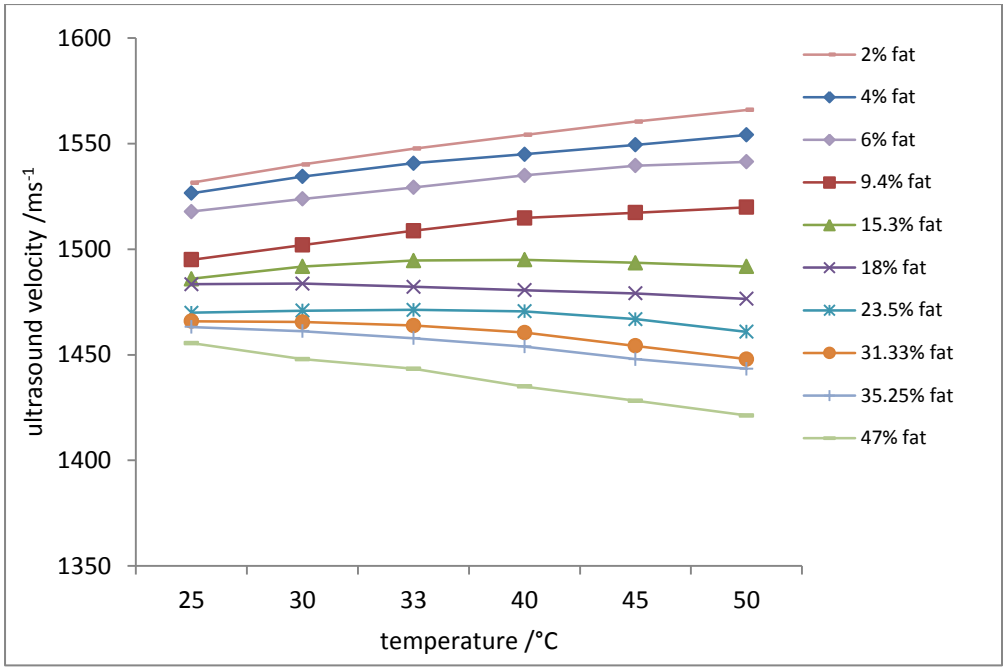

Figure 3-35 Change of ultrasound velocity with temperature in sample solutions as the percentage of fat in the solution was varied from 2% to 47%.

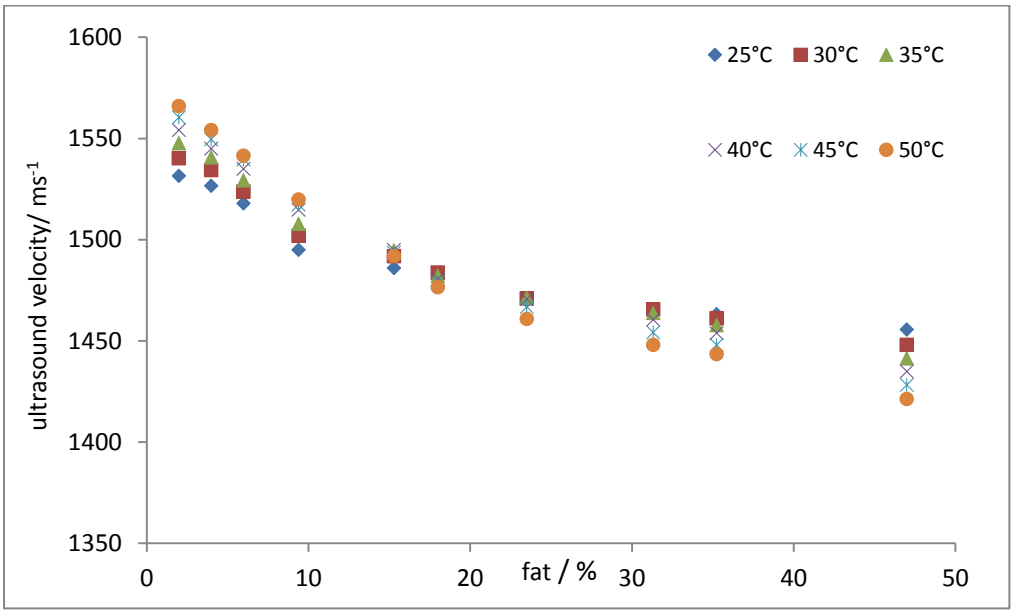

Figure 3-36 Change of ultrasound propagation velocity with the change of percentage of fat at the measured temperatures.

In the solutions with lower percentages of fat the increase of ultrasound velocity may be due to the decreased density of the samples solutions at higher temperature. However, in the solution with higher percentage of fat the negative temperature coefficients as being due to the fact that decreased bulk modulus is more than offset by the decrease in density with temperature (Kramer, 1973).

Figure 3-36 illustrates the change of ultrasound velocity with fat content in the sample solution at a particular temperature. The Figure 3-36 clearly shows that the ultrasound velocity decreased with increasing fat content. It also clearly shows that in samples with low percentage of fat, the ultrasound velocity increased with increasing temperature whereas samples with a higher percentage of fat show the reverse, a decrease of velocity with increasing temperature.

From these results, it can be observed that there is clearly a point at which the transition from positive temperature coefficients to negative temperature coefficients for the ultrasound velocity occurs. In this experiment, this transition was found at around 18% fat. Thus a sample with around 18% fat showed a negligible change in ultrasound propagation velocity as a function of temperature (Figure 3-35 and Figure 3-36). This is because the positive change in ultrasound velocity with temperature in water cancelled the negative change in ultrasound velocity in fat -resulting in negligible temperature dependence for the overall sample (Miller and Bamber, 2004).

From the result of this experiment it can be said that the 'percentage of fat' has very important effect on the ultrasound velocity change with temperature. The absolute value of ultrasound propagation velocity and the change of ultrasound propagation velocity with temperature will depend on the molecular component of the solution having different percentage of fat.

However, the sample solutions used in this experiment may not mimic animal or human tissues. The sample solutions prepared from milk/milk products and deionized water lacked the living cell structures found in tissues. So the numerical change of ultrasound velocity with temperature may not reflect the actual change of ultrasound velocity with temperature in animal or human tissues having the same ion and fat content. As noted at the start of this section that it is impossible to create tissue samples with a reproducible fat content and therefore, this experiment results a reproducible test bed for looking at the effects of fat content on ultrasound propagation velocity.

3.7.2 Electrical Impedance

Initially, multi-frequency tetrapolar electrical impedance measurements were made at room temperature on separate discrete electronic component phantoms and non-biological materials. The discrete component phantoms included resistive and resistive-capacitive circuits. Figure 3-37 shows the circuit diagram of a resistive and a resistive-capacitive phantom with the value of the individual discrete component. To construct the

resistive phantom (Figure 3-37a), the component value was chosen as 20Ω by keeping in mind the impedance value obtained for intra-cellular fluids from the 20mm electrode spacing tetrapolar impedance measurements on human lower abdomen. The resistive-capacitive phantom was constructed (Figure 3-37b) based on the Cole-Cole model (Cole and Cole, 1941) of tissue described in section 3.6.2.1.2 with the first dispersion frequency set to 61kHz and the second dispersion frequency set to 800kHz).

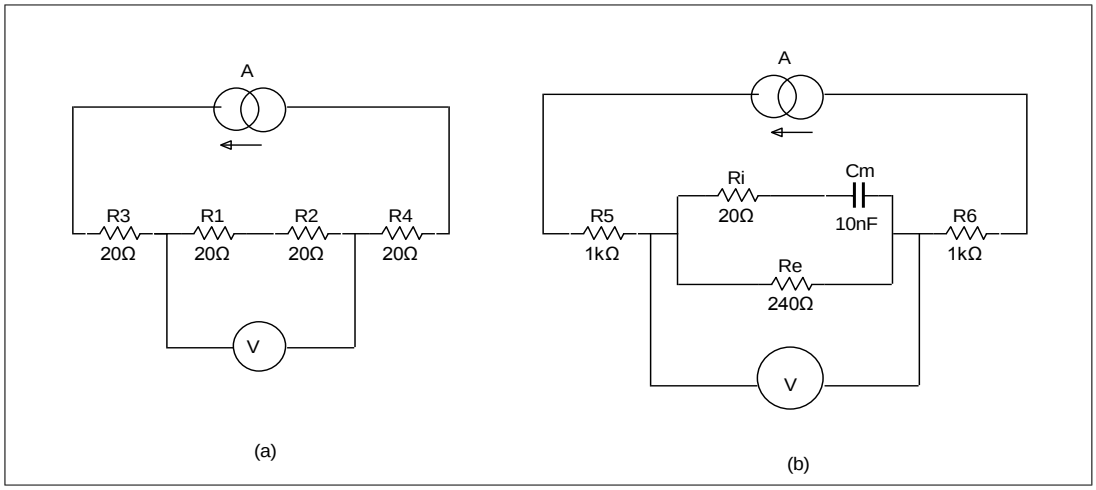

Figure 3-37 Circuit diagram of the discrete components phantom (a) phantom made from pure resistive components (b) phantom made from resistive and capacitive components.

In addition, physiological saline was used to mimic a resistive volume conductor in order to test the multi-frequency electrical impedance measurement system. Before taking the measurement on a sample material, the switchable voltage gain of the differential amplifier was switched to a particular level to give optimum level of voltage suitable for the measurement (section 3.6.2.1.2). The amplified voltage was then digitised using the 2nd channel of the National Instruments high speed digitiser at a sampling rate of 10MHz. Then, the digitised data was transferred from the digitiser to Matlab for further processing. This data transfer was controlled by a C-code routine called from Matlab. Detail of the electrical impedance data processing is given in section 3.6.2. In every electrical impedance measurement 10 epochs of measured data were summed to improve the signal-to-noise ratio of the measured data. The Figure 3-38 shows the receive voltage and its FFT spectrum from the multi-frequency electrical impedance measurements across a pure resistive phantom materials. The frequency spectrum at 11 discrete frequencies obtained from the impedance measurement across the resistive phantom is shown in the Figure 3-38b.

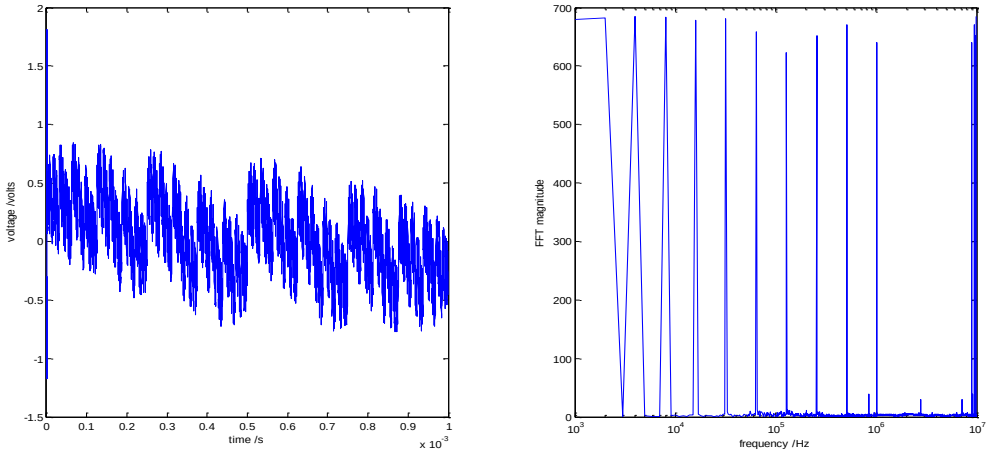

Figure 3-38 Showing the electrical measurements across a pure resistive phantom materials (shown in figure 3-36a) (a) showing the received voltage signals (b) showing the FFT magnitude of the received voltage signals.

However, it was unexpected that the FFT magnitude spectrum across the resistive phantom did not remain fixed throughout the measured frequency range–it showed a slight fall around 128kHz (Figure 3-38b). The measurement systems were checked several times and repeated measurements were taken on various phantoms but every time it gave a slight decrease in FFT magnitude around 128kHz. It was accepted as an instrumental artefact and a correction based on the spectrum obtained from a saline solution applied. This was also required for the determination of the phase angle (section 3.6.2.1.2). Figure 3-39 shows the normalized impedance and phase angle of a parallel connected resistive-capacitive phantom shown in Figure 3-37b. The impedance value was obtained by using the equation 3-2 described in section 3.6.2.1.1. Then, the impedance value was normalised to the impedance value at 1kHz and compared with the corresponding theoretical impedance value obtained from the empirical solution of the resistive-capacitive circuit shown in Figure 3-37b. The phase information was obtained from the measured data for the resistive-capacitive circuit and corrected using the procedure described in section 3.6.2.1.2. The measured phase information was also compared with the theoretical phase information of the resistive-capacitive circuit shown in Figure 3-37b. From Figure 3-37 it can be seen that the multi-frequency electrical impedance instrument used for this research is more accurate in measuring the impedance value (the percentage of error increased with frequency from 0.29% at 1kHz to 7.52% at 1MHz) than the phase information (the percentage of error increased with frequency from 0.26% at 1kHz to 17.21% at 1MHz).

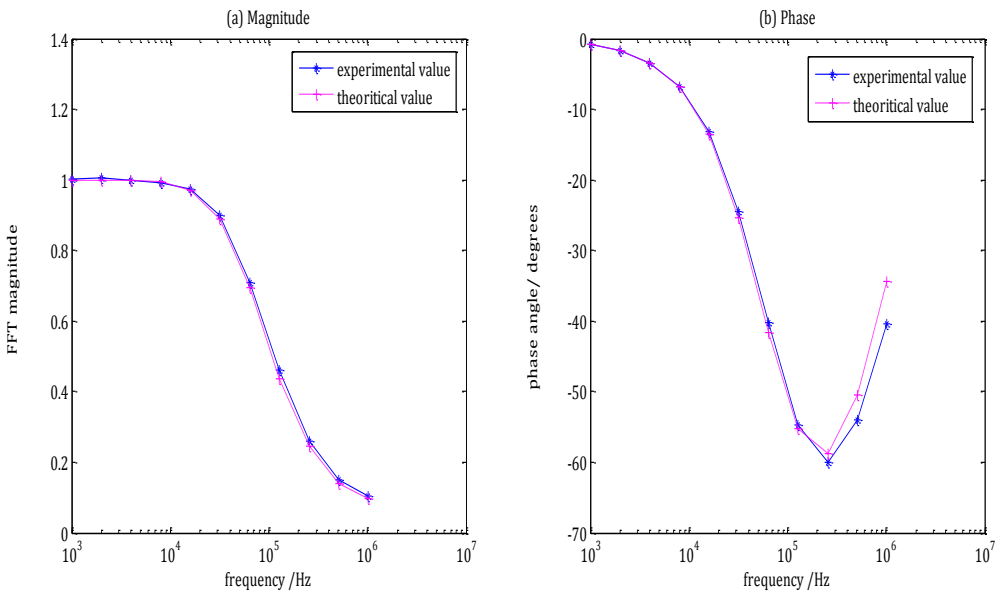

Figure 3-39 Impedance and phase angle of a phantom material made from combining resistive and capacitive materials in parallel.

4 Single Tissue Experiments

4.1 Experiments on liver

As discussed in Chapter 3, the ultrasound propagation velocity of aqueous solutions increases with increasing temperature whilst the ultrasound propagation velocity of fats decreases with increasing temperature. The effect of this difference on the propagation velocity measured in tissues can be seen in graphs of propagation velocity against temperature for different tissues (Bamber, 1997). In terms of using combined ultrasound and electrical impedance measurements to determine temperature, any technique must be able to work with tissue of an unknown fat content.

One of the primary targets for cancer treatment by high intensity focused ultrasound (HIFU) has been the liver: partly because both primary and secondary tumours in the liver are hard to treat by other techniques (ter Haar *et al.*, 1989) but also because the liver is readily accessible to a high intensity ultrasound field and is a relatively homogeneous organ. However, the liver does contain fat and large vacuoles of lipids (triglyceride) accumulate in liver cells. Fat accumulations in liver cells can progress to cirrhosis and can be associated with hepatocellular carcinoma (Angula, 2002). Therefore, liver and fat tissues were the test specimens for the experimental work described in this thesis. The mean fat content of normal and fatty liver has been reported to be 6% and 26% respectively and that of liver tumour to be 3% (Bamber *et al.*, 1981). In this chapter, separate simultaneous ultrasound propagation velocity and electrical impedance measurements on liver and fat samples are described and the results analysed in terms of the implication for using a combination of the two measurement technique to non-invasively determine temperature.

4.1.1 Procedure

4.1.1.1 Sample preparation

Liver from lambs was obtained as fresh (never frozen) samples from retail butchers. The liver tissue was cut into thin slices maintaining approximately 8mm thickness and 40mm diameter. Samples of liver tissues were taken from tissue, where there was no visible fat content. The sample tissues were then placed in the test cell in the form of layers – four slices were used to fill up the test cell (detail of the test cell is described in section 3.2, chapter 3). In the test cell four brass/ stainless steel electrodes were connected through the lid of the test cell – one pair of electrodes were the drive electrodes (current drive) and the other pair were the receive electrodes (voltage measurement) for the terapolar

impedance measurements. Before closing the test cell to make the measurements, all the electrodes were thoroughly cleaned using a hard brush to remove any oxidation deposits. After inserting the thermocouples half way into the liver tissues through the lid, the lid of the test cell was sealed using a rubber O-ring. Then, the test cell was placed in the water bath supported by the integral ring holder of the hot plate (a full experimental setup for the simultaneous ultrasound and electrical impedance measurement is shown in Figure 3-24).

4.1.1.2 Measurements

Ultrasound and multi-frequency electrical impedance measurements were made simultaneously on lambs liver as the temperature of the sample tissue increased from room temperature to 50°C. Before taking the measurements, the voltage gain of the electrical impedance measurement instrument was switched to 10, which gave optimum level of amplification for the measured voltage data from the liver tissue. The temperature in the sample tissues was raised using the thermostatically controlled hot plate and the temperature in the tissue was recorded using the digital thermometer. Details of the temperature changing and data recording procedures are described in section 3.5 and shown in Figure 3-24 in chapter 3. The ultrasound and impedance data were collected at a sampling rate of 100 and 10MHz respectively using the 1^{st} and 2^{nd} channel of the National Instruments high speed digitiser (USB-5133). Details of the data acquisition procedures are also described in section 3.4 and shown in Figure 3-24 in chapter 3. Both the ultrasound and tetrapolar electrical impedance measurements were made on liver tissue at temperatures from 25°C to 50°C in 5°C steps. The ultrasound and electrical impedance data were also recorded during the cooling period from 50°C to 25°C in 5°C steps. For each ultrasound measurement at a specific temperature, the average of twenty consecutive 100µs ultrasound data sets was taken to improve the signal-to-noise ratio. Similarly, for the multi-frequency electrical impedance measurements at a particular temperature, twenty 1ms epochs of measured voltage data were summed to improve the signal-to-noise ratio. The measurements were repeated at least five times on different tissue samples on different days to establish reproducibility. The Figure 4-1 and Figure 4-2 show examples of the raw ultrasound propagation velocity and tetrapolar electrical impedance data respectively.

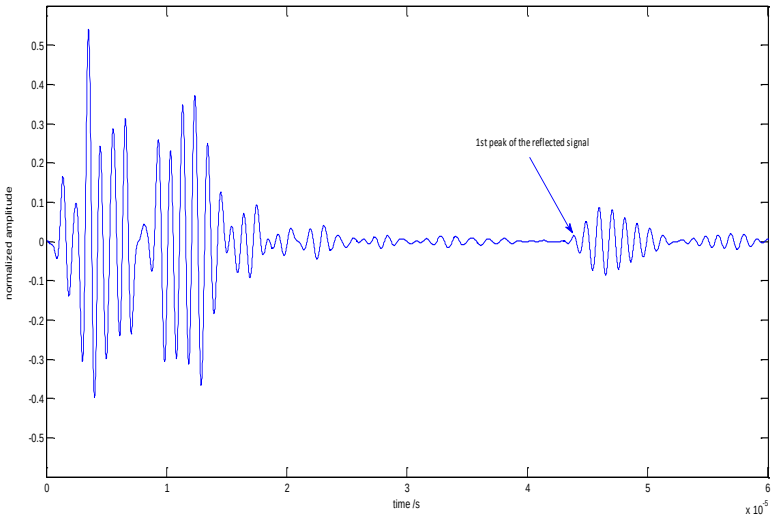

Figure 4-1 The ultrasound signal in liver at 40°C showing the reflected pulse at about 45µs from the base of the test cell after application of the FIR filter.

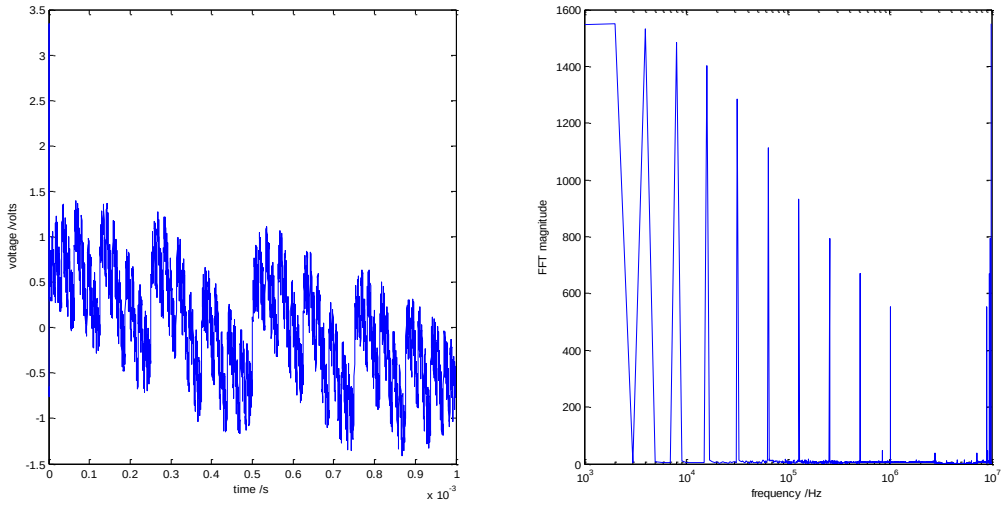

Figure 4-2 Showing the amplified received voltage signal in liver tissue and its frequency spectrum obtained from the multi-frequency electrical impedance measurements at temperature 40°C. The FFT amplitudes at each frequency were converted to impedances.

4.1.1.3 Data processing

4.1.1.3.1 Ultrasound data processing

Data from the liver tissue were processed and displayed in Matlab. After the application of the FIR filter (section 3.6.1, chapter 3), the time of flight of the ultrasound reflected pulse from the base of the test cell was measured. As mentioned in chapter 3, to detect the time of flight, the first peak of the reflected pulse was considered (Figure 4-1). From the time of

flight, the ultrasound propagation velocity in the liver tissue was calculated for each measured temperature for both during the heating and cooling phase using the equation 3-1 (section 3.6.1, chapter 3). The calculated ultrasound propagation velocity data for the heating and cooling duration were then averaged. So for each set of measurement, the ultrasound propagation velocity data at all the measured temperature consisted of the average of ultrasound propagation velocity data from the heating and cooling phase of the experiment. The mean and standard deviations of the ultrasound propagation velocity in liver tissue at each measured temperature were calculated from the five sets of measurement. A simple linear regression analysis was also performed to investigate the relationship between the ultrasound propagation velocity in the liver tissue and the temperature. A linear relationship between the ultrasound propagation velocity in liver tissue and the temperature was observed and a line-of-best-fit and the Pearson r correlation coefficient was determined (Figure 4-3). The average percentage change of the ultrasound propagation velocity per degree Celsius temperature in liver tissue was also determined from the slope of line-of-best-fit. To determine the average percentage change of ultrasound propagation velocity per °C, the slope of line-of-best-fit was divided by the averaged ultrasound propagation velocity data across all the measured temperature.

4.1.1.3.2 Electrical Impedance data processing

The amplified received voltage signal (10 times of the original signal) at each measured temperature in liver tissue was processed in Matlab. An FFT was performed on the digitised averaged voltage data to determine the amplitude and phase spectrum in the liver tissue for each of the 11 drive frequencies. The raw voltage signal and the frequency spectrum obtained from the FFT for the liver tissue are shown in the Figure 4-2. The amplitude and phase spectrum was then scaled to determine the real part of the transfer impedance in ohms and phase difference in degrees. The details of the impedance and phase calculation procedures were described in the sections 3.6.2.1.1 and 3.6.2.1.2 respectively in chapter 3. Each measurement for the each measured temperature both during the heating and cooling phase was processed in this way. The impedance data from the heating and cooling duration were then averaged. So for each set of measurement, the impedance data at all the measured temperature consisted of the average of impedance data from the heating and cooling phase of the experiment. Similarly, the phase at all the measured temperature consisted of the average of phase from the heating and cooling duration of the experiment. From the five set of measurements, the mean impedance and phase value at each measured temperature for all the frequencies were determined for the liver tissue. The

standard deviations of the impedance and phase value and their respective standard error of means were also calculated. The impedance values for the liver tissue are plotted against the measured temperatures and frequencies in Figure 4-5 and Figure 4-6 respectively. The phase values for the liver tissue at each measured temperature are also plotted against frequencies in Figure 4-7. From the mean impedance and phase information, the real and imaginary part of the impedances in liver tissue were separated and plotted in Figure 4-14.

The temperature coefficients or the temperature sensitivity of the magnitude of impedances for the liver tissue were calculated at each measured frequency. The temperature coefficients were calculated based on the impedances at 40°C as follows: firstly the difference between the impedances at the lowest measured temperature (the highest impedance) and the highest measured temperature (the lowest impedance) was determined for each measured frequency; secondly this difference was then divided by the impedances at 40°C and thereafter, converted to percentage temperature coefficients or temperature sensitivity at each measured frequency. The mean and standard deviation of the temperature sensitivity of electrical impedance in liver were calculated across all the frequencies measured. A simple linear regression analysis was performed to investigate the relationship between the temperature coefficients and measured frequencies for the liver tissue.

Determining the repeatability of measurements on a single sample in this part of the work was impossible because heating caused irreversible changes in the tissue and the characteristics of the tissue changed with time when held at a constant temperature. Therefore the variability in liver tissue was assessed in terms of multiple samples (e.g. Figure 4-4). There was a high variability in the magnitude of impedance values for different samples of liver tissue measured on different days. This variability was due to variations in the liver samples themselves and will include freshness, age of the sample and interstitial fat content. However, the shapes of the impedance spectra obtained from the different samples of liver tissue were similar at the measured frequencies. Therefore, it was necessary to normalise the impedance spectra to the impedance at a single frequency to produce a standardised measurement. The impedance measurements were subsequently normalized to the impedance at 8kHz (section 4.3.2) as part of the procedure for combining electrical impedance and ultrasound measurement for the non-invasive determination of tissue temperature. The normalized impedance spectra of liver tissues were plotted in Figure 4-8 and Figure 4-9 against frequency and temperature. The temperature sensitivity

or the temperature coefficients of these normalised impedances was also determined across the measured temperature range. The mean and standard deviation of the temperature sensitivity of the normalised impedances for all measured frequencies were also determined.

4.1.2 Results

4.1.2.1 Ultrasound

The change in ultrasound propagation velocity with temperature in liver tissues was shown in the Figure 4-3. The results showed a positive change of ultrasound propagation velocity with temperature. The mean ultrasound propagation velocity (± standard deviation) of the five set of measurements in liver tissue was (1523 ± 4) ms^{-1} and (1547 ± 11) ms^{-1} at 25°C and 50°C respectively.

From Figure 4-3 it can be seen there was a large variation in the ultrasound propagation velocity between different samples of liver due to the variation in properties of the liver samples such as freshness, interstitial fat content etc. (section 4.1.3.1). All samples show a rise in propagation velocity with temperature and the slopes for individual samples determined using a linear regression analysis gave slopes in the range 0.35ms^{-1} °C^{-1} to 1.35 ms^{-1} °C^{-1} (Figure 4-4).

In line with the approach used by other workers in this area (Bamber, 2004) a linear regression analysis was performed on the 5 samples shown in figure 4.3 was used to obtain a typical value for the change in ultrasound propagation velocity with temperature. This showed a positive correlation between the ultrasound propagation velocity and the temperature (r^2 = 0.56 and $p < 0.01$). The linear relationship between the ultrasound propagation velocity in liver and the temperature can be expressed as, $y = 0.94x + 1501$, where y and x represent the ultrasound propagation velocity and temperature respectively. The mean slope and intercept of the line-of-best-fit were 0.95 and 1500ms^{-1} respectively. The average percentage change of ultrasound propagation velocity in liver tissue was 0.06%°C^{-1}.

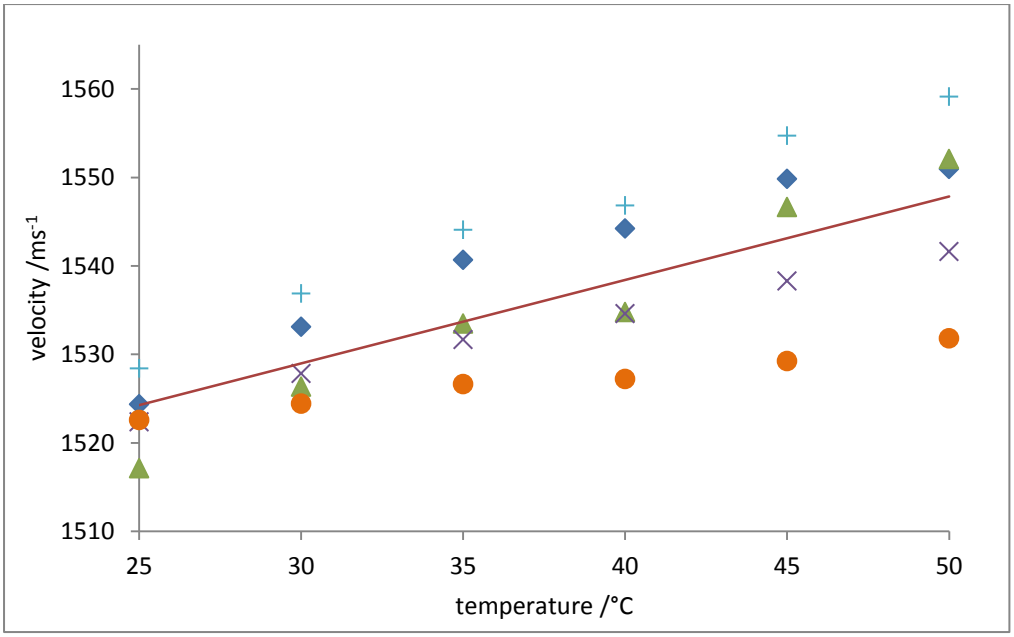

Figure 4-3 Individual ultrasound propagation velocity data points in liver tissue with the mean line-of-best-fit are shown in the graph against temperature. Each symbol represents a different liver tissue sample.

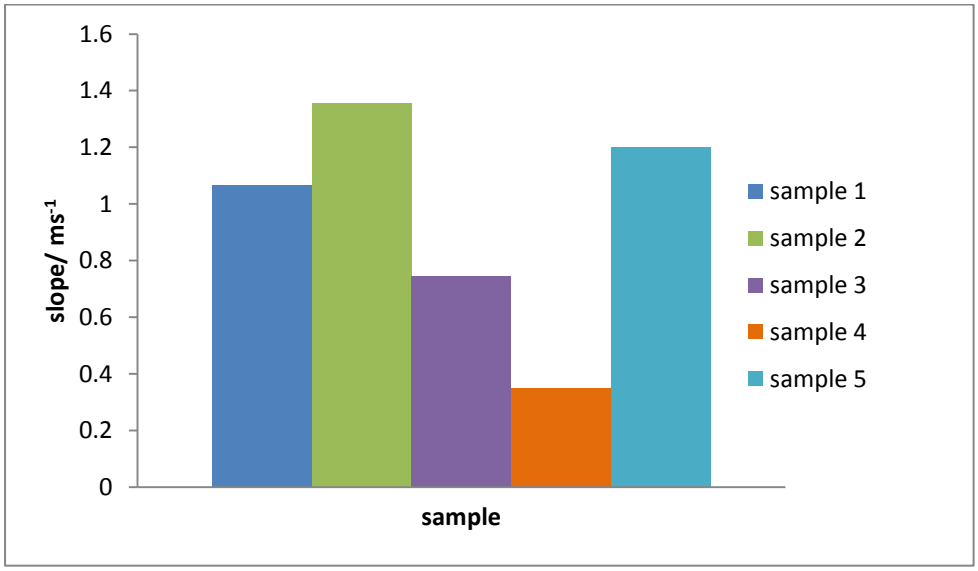

Figure 4-4 Showing the variation of slopes of the line-of-best-fit of different liver samples. The colours of the bars match the colours of the symbols in Figure 4-3 for the identification of individual samples.

4.1.2.2 Electrical impedance

Figure 4-2 shows the received voltage signal from the electrical impedance measurements in the liver tissue together with the magnitude of its frequency spectrum. The electrical impedance of the liver tissue is shown in Figure 4-5 and Figure 4-6, where the magnitude of the impedance is plotted against frequencies and temperatures respectively. It can be seen from Figure 4-5 that there is a single dispersion in the electrical impedance spectra within the frequency range measured with the roll off starting at about 8kHz. Above 8kHz, the

electrical impedance of liver tissue decreased with increasing frequency. This high frequency sensitivity of the electrical impedances in liver tissue decreased with increasing temperatures (Figure 4-5 and Figure 4-6).

Figure 4-7 shows the phase spectra of the liver tissue as the temperatures of the sample is raised from 25°C to 50°C in 5°C steps. The phase difference in liver tissue increased with increasing of frequency and it reached a turning point at about 512kHz and the phase change decreased thereafter (Figure 4-7). Above 4kHz the phase difference in liver tissue decreased with increasing temperature (Figure 4-7).

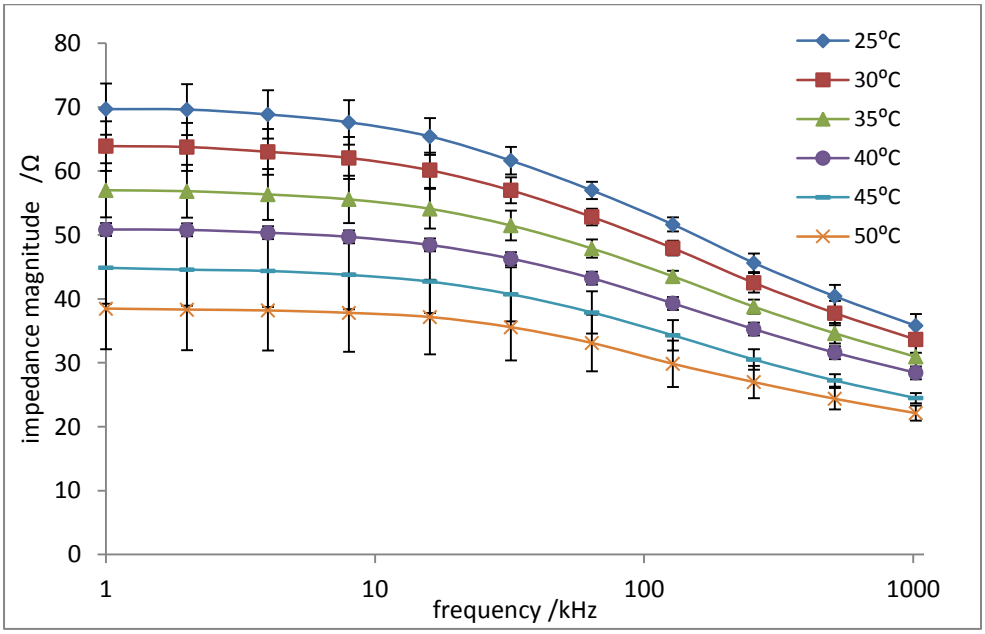

Figure 4-5 The average electrical impedance in the liver tissues are shown with the changes of frequency at different temperatures. The vertical error bars in the figure indicates standard error of the mean.

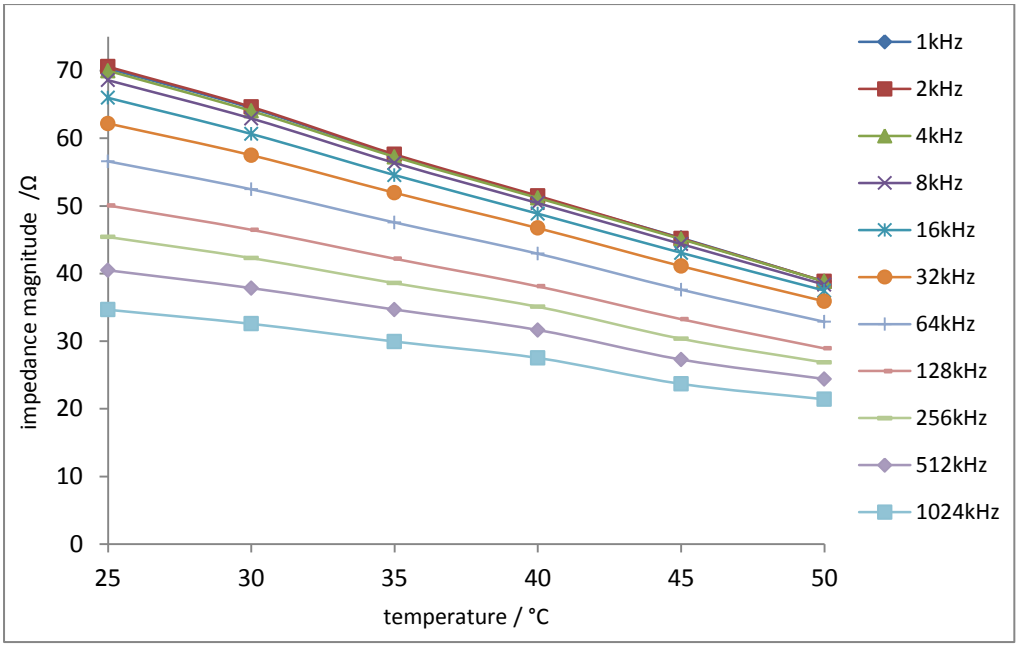

Figure 4-6 Changes in magnitude of the impedance in liver tissues with the change in temperatures at different frequencies.

In these experiments, the mean and standard deviation of sensitivity of the electrical impedance measurements to temperature across all frequencies measured for liver tissues was found to be -2.3±0.18 %°C^{-1}. Figure 4-6 shows the changes of impedance in liver tissue with temperature. It can be seen from Figure 4-6 that the impedance in liver tissue linearly decreases with temperature and is independent of frequency up to 8kHz. However, at the highest frequency measured –1MHz– the rate of decrease of impedance with temperatures is the lowest indicating a decrease in temperature sensitivity of electrical impedance with increasing frequency.

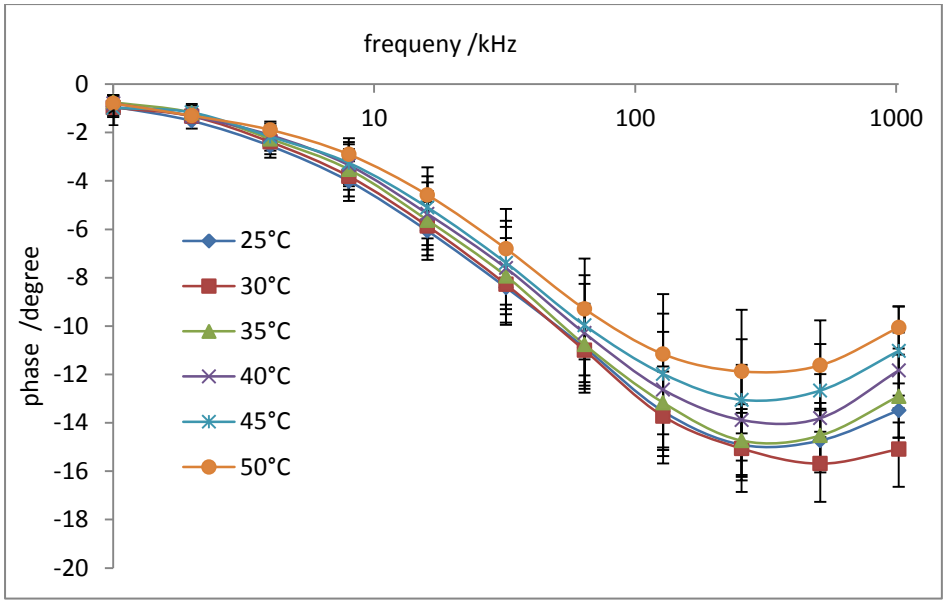

Figure 4-7 The phase differences in the liver tissue are shown against frequencies at different temperatures. The vertical error bars in the figure represent standard error of the mean.

The error bars in Figure 4-5 and Figure 4-7 showed the standard error in impedance and phase measurements for the liver tissue. From the Figure 4-5, it can be observed that the variability in the measured impedance decreased with increasing frequency at all temperatures and increased with increasing temperature for all the measured frequencies for the liver tissue. Figure 4-8 shows the normalised impedance against 8kHz at all temperatures measured. The normalization of the impedance spectra to the impedance at 8kHz as described in section 4.3.2 reduced the temperature sensitivity of the measurements for liver tissue to 0.17±0.18 $\%°C^{-1}$ across all frequencies measured. The temperature sensitivity of the normalized impedances at frequencies 16kHz to 1MHz can be observed from the Figure 4-9, where the normalised impedances are plotted against temperatures.

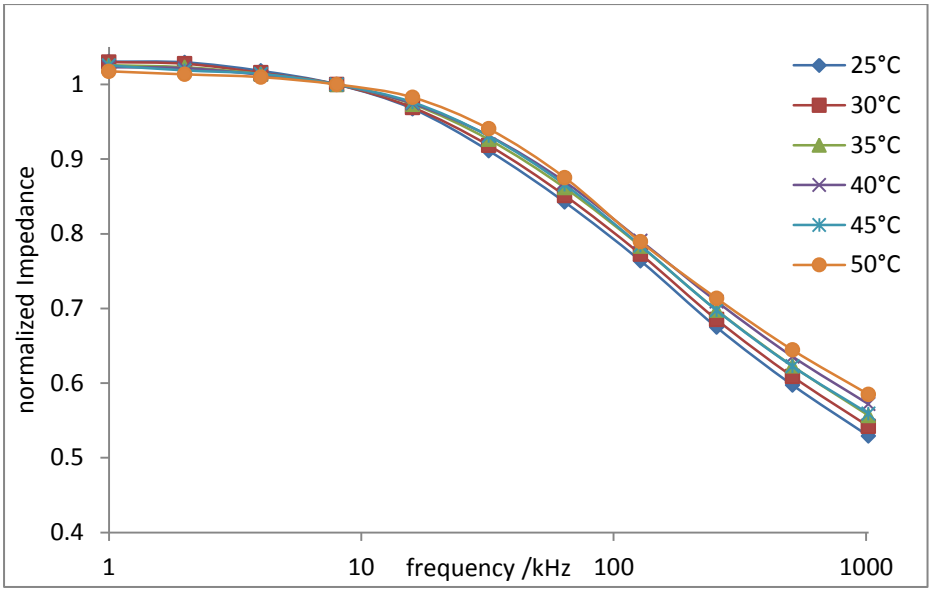

Figure 4-8 Showing the normalized impedance changes of liver tissue with the change of frequency at the measured temperature.

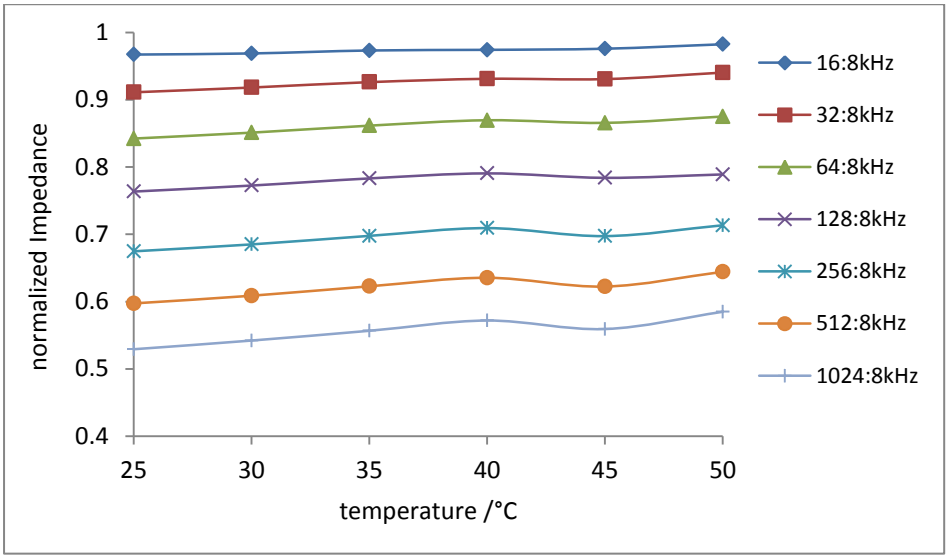

Figure 4-9 Showing the normalized impedance of liver tissue against temperature. The impedance at 8kHz was used for the normalisation.

4.1.3 Discussion

4.1.3.1 Ultrasound

The temperature coefficient of the ultrasound propagation velocity in liver tissue is positive in the temperature range 25–50°C. During the experiments a small but measurable decrease in the ultrasound propagation velocity was noticed when the temperature rose above 50°C. This is consistent with the findings from the other researchers' work, who reported heat induced denaturation and coagulation in the tissue above this temperature

are responsible for this small decrease in velocity (Miller and Bamber, 2004; Hill *et al.*, 2004). The ultrasound propagation velocity against temperature graph for the liver tissue (Figure 4-3) showed similar behaviour to that for aqueous salt solution (Figure 3-32, section 3.7.1.1, Chapter 3). However, in liver tissue the ultrasound velocity is slightly higher than the corresponding value for aqueous salt solution due to the protein content, particularly the structural protein collagen that is present in moderate amount in liver tissues (Miller *et al.*, 2002). The measured values for the changes of ultrasound propagation velocity with temperature in liver tissues were in agreement with the values reported in the literature (Duck, 1990; Miller and Bamber, 2004). However, there was a large variation in values between samples and this highlights the problem of using changes in ultrasound propagation velocity to measure temperature. Samples with no visible fat content were taken from the livers and therefore whilst interstitial fat content may contribute to the variability seen, it is unlikely to completely explain it. Therefore origin of the observed variability needs to be understood as part of refining the propagation velocity measurement to create a new measure of temperature.

It should be noted that the standard deviations or the standard errors of ultrasound propagation velocity increased with temperatures. As noted by Bamber (Bamber, 2007), the time of flight method for determining the ultrasound propagation velocity is dependent on being able to reproducibly detect the time of arrival of the reflected signal (e.g. to identify the first peak in the reflected ultrasound signal). The amplitude of the reflected ultrasound signal decreased with increasing temperature and for the liver tissue experiments, the average decrease of the peak to peak amplitude of ultrasound signal with temperature was 1.5%°C^{-1} which has the effect of producing errors in the time of flight detection from the first peak of the reflected signal (Figure 4-10). Hence, due to the decrease in amplitude of the reflected ultrasound signal with increasing temperature, the errors in the propagation velocity determination increased as the temperature increased.

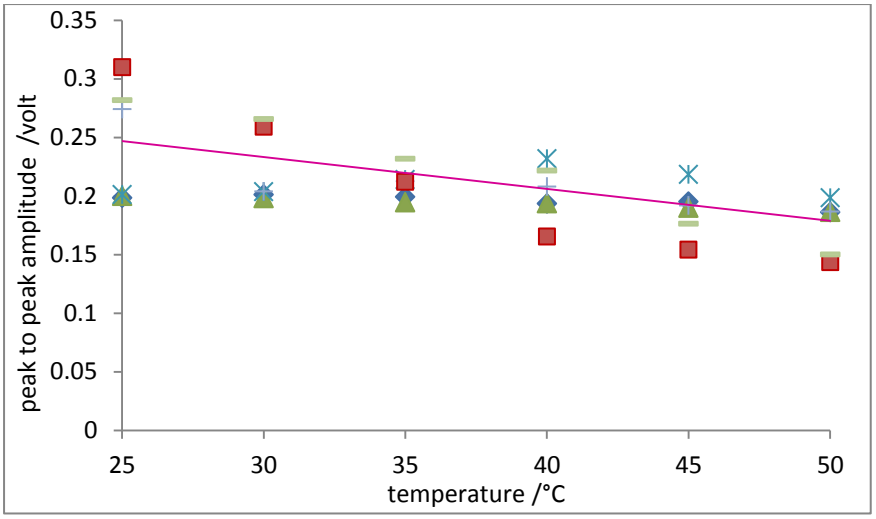

Figure 4-10 The change of peak to peak amplitudes of the ultrasound signal with temperatures in the liver tissue experiments. Individual data points were shown along with the line-of-best-fit.

It is also noted that the change of ultrasound propagation velocity in liver tissue with temperature was not exactly same during the heating and cooling phase of the measurements. It was observed that the ultrasound propagation velocity against temperature curve during the heating phase (25°C–50°C) did not follow the same path as that of the cooling phase (50°C–25°C). This may be due to some irreversible tissue damage (hysteresis) occurred during the heating period as the temperature was raised above 45°C. However, for this experiment the averaged ultrasound propagation velocity from the heating and cooling phase was considered

4.1.3.2 Electrical impedance

The impedance values obtained for liver tissue (Figure 4-5) are in consistent with a Cole-Cole model (Cole and Cole, 1941) of cellular tissue. The Cole-Cole model is an electrical analogue of a tissue, where the extra-cellular resistance of cellular tissue is connected in parallel with the intra-cellular resistance and membrane capacitance (Figure 4-11). The empirical equation for the Cole-Cole model is also given in equation 4-1.

$$Z = R_\infty + \frac{R_0 - R_\infty}{1+(j\omega\tau_z)^\alpha} \qquad 4\text{-}1$$

Where, R_∞ and R_0 is equivalent to the intra- and extra-cellular resistance respectively at high and low frequency; ω = angular frequency, τ_z = relaxation time constant, and α ($1 \geq \alpha \geq 0$) is a parameter which measures the deviation from an ideal resistor and capacitor in the equivalent circuit.

Therefore, in the Cole-Cole model the electrical conductivity of cellular membrane decreases as the frequency of measurement increases reducing the measured electrical impedance of the sample as the current is conducted through the membrane and thus the current path includes both the intra-cellular fluid and the extra-cellular fluid (Figure 4-12). As the frequency increases further, the impedance of the cellular membranes reduces to the level where it is much less than the impedance of the intra- and extra-cellular fluids in parallel resulting in no further change in impedance with increasing frequency (Figure 4-13).

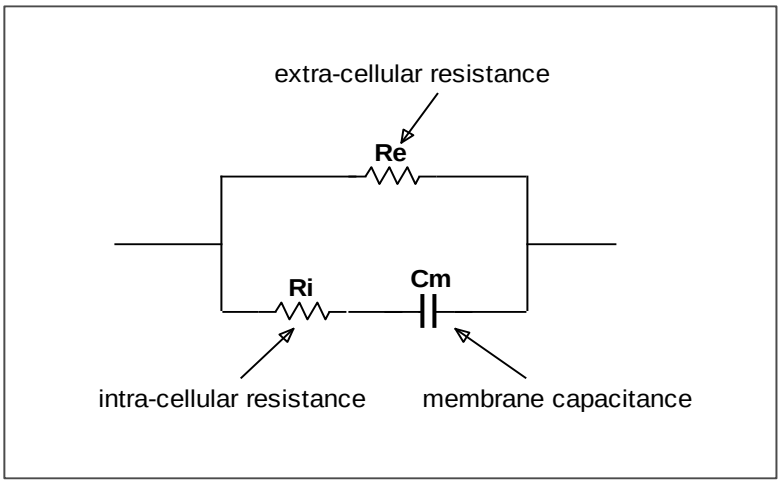

Figure 4-11 The equivalent electrical circuit diagram of Cole-Cole model for cellular tissue.

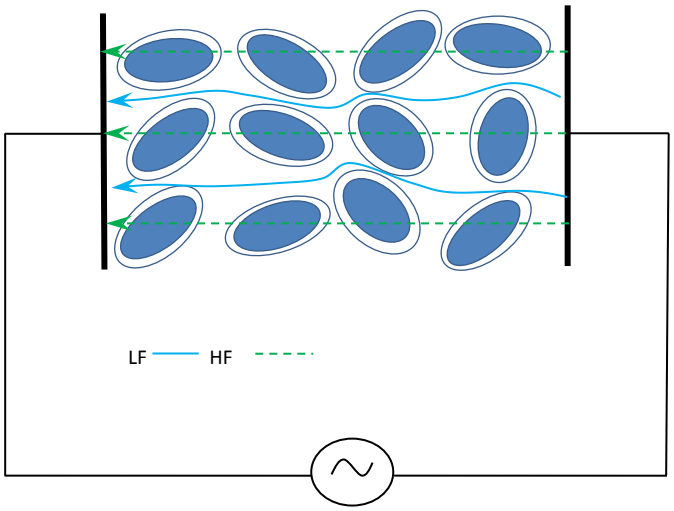

Figure 4-12 Showing the low frequency (LF) and high frequency (HF) current paths in tissue. The high frequency current passes through the intra- and extra-cellular fluids in tissue. However, the low frequency current cannot penetrate the cell membrane and follows a tortuous path in the extra-cellular fluids.

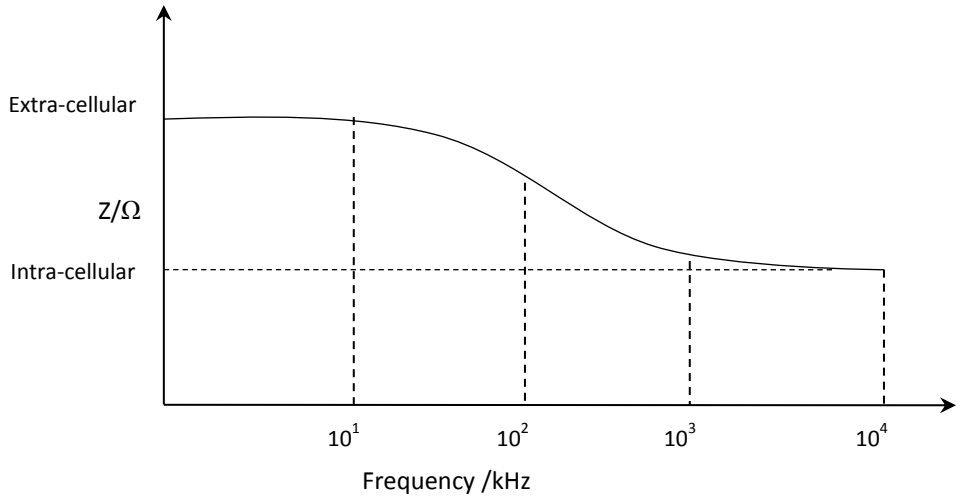

Figure 4-13 Theoretical impedance diagram showing the dispersion for the liver tissue.

The highest frequency that could be measured in this experiment was 1MHz and this is close to the frequency at which the impedance in lamb liver plateaus. It should be noted that 1MHz is the highest frequency that can realistically be measured with surface electrodes and discrete components due to the problem of stray capacitance (McEwan *et al.*, 2007). Due to lack of measurements above 1MHz frequency, data obtained from the lamb liver tissue could not be analysed by fitting the equation of a Cole-Cole model (Cole and Cole, 1941) to the data as other workers characterising tissue have done (Brown *et al.*, 2000a; Gonzalez-Correa *et al.*, 1999; Parramon *et al.*, 2007). This can also be observed from the Cole-Cole plot (also termed as the Complex plane plot or Wessel plot) shown in Figure 4-14 of the liver tissue data obtained from this experiment, where the resistive component of impedance data of the liver tissue is plotted against the imaginary or reactive data. If the measurement data above 1MHz were available, this plot would give a complete half-moon shaped curve with both ends having near zero reactive parts and the minima below the real axis corresponds to the first dispersion starting at about 8kHz (Figure 4-5 and Figure 4-7).

The phase values obtained from the electrical impedance measurement on lamb liver are consistent with the values obtained by Parramon and co-workers (Parramon *et al.*, 2007) from multi-frequency tetrapolar electrical impedance measurements on rat liver.

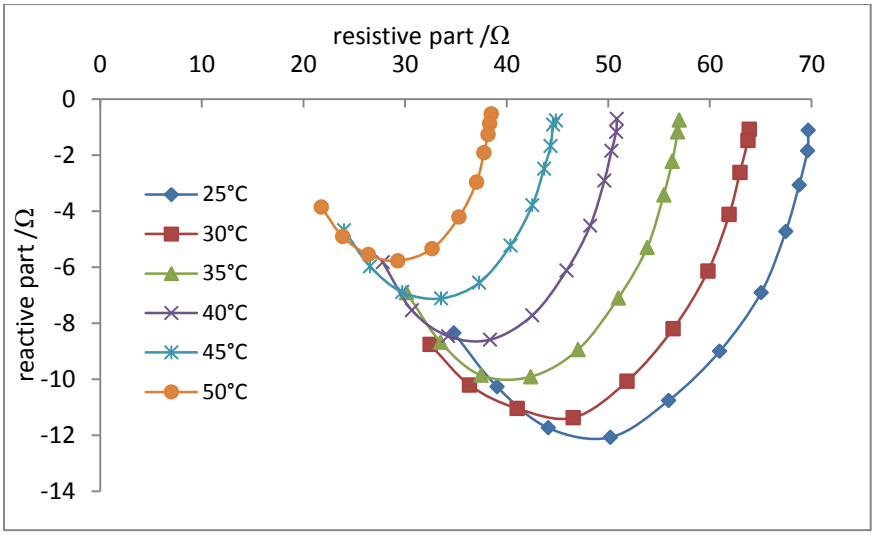

Figure 4-14 Showing the Cole-Cole or Wessel plot of liver tissue. The resistive (real) and the reactive (imaginary) part of the impedances in liver tissue were obtained from the mean impedance and phase information.

The results for liver tissue samples showed a decrease in the variability of the measured impedance with increasing frequency. However, the variability of the measured phase differences showed the opposite results, with an increase in the variability of the measured phase difference with frequency. The origins of the variabilities are unclear. The findings in the variability of the absolute impedance in different samples may be due to the differences in the volume of extra-cellular fluid in different samples. The variability of the phase differences is more difficult to identify but may be due to the thickness differences in the cellular membrane layers between samples (Marder *et al.*, 1984; Janesick, 2001).

The impedance measurements have been done on lamb liver that is not living. The tissue response to heating may differ for living and non-living tissue due to changes in cell permeability, shift of fluids, blood flow, glucose, oxygen, ATP or pH. However, the value for the temperature coefficient of the impedance obtained for liver tissue is consistent with that of physiological saline (-2% $°C^{-1}$, (Duck, 1990)). The temperature coefficients for electrical impedance may be different for different tissue types (Gersing *et al.*, 1995). It is unclear whether these differences in different tissue types are the result of differences in the non-electrolyte components of the tissue or the result of metabolic changes associated with heating (e.g. changes in blood flow and membrane conductivity).

4.2 Experiments on fat

4.2.1 Procedure

4.2.1.1 Sample preparation

Fresh (never frozen) fat samples from lamb were obtained from domestic butchers and tissue samples for the simultaneous ultrasound and multi-frequency electrical impedance measurements were prepared according to the same procedure followed for the liver samples in section 4.1.1.1.

4.2.1.2 Measurements

The ultrasound and multi-frequency electrical impedance measurements on fat were made simultaneously using the same procedure that was followed for the measurements on liver tissue samples in section 4.1.1.2. However, for the measurements on fat the gain of the differential amplifier in the electrical impedance measurement instrument was switched to 50. The ultrasound and electrical impedance measurements were made at temperatures 25°C to 50°C in 5°C steps both during the heating and cooling phase. To establish reproducibility, the measurements were repeated at least five times on different tissue samples on different days.

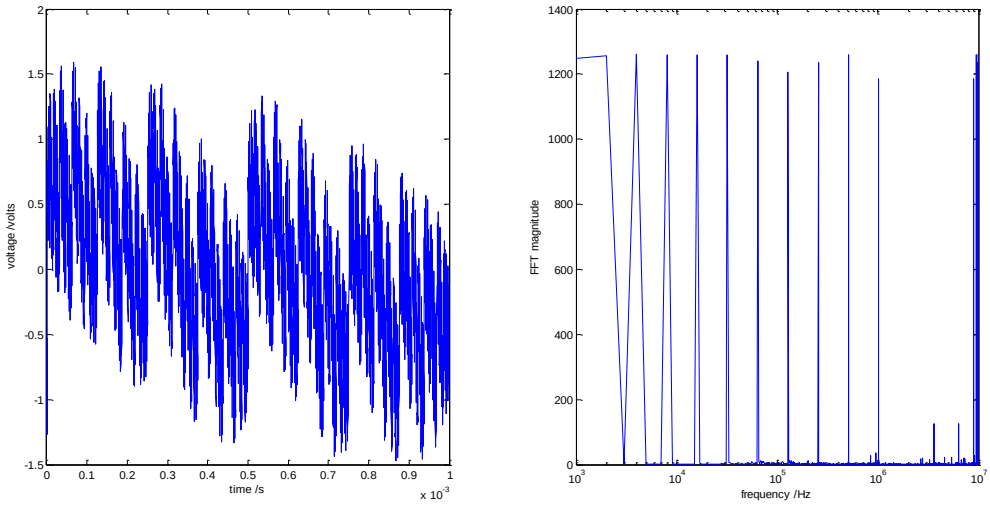

Figure 4-15 Showing the amplified (50 times) received voltage signal and its frequency spectrum from the multi-frequency electrical impedance measurements on a fat sample at 40°C.

4.2.1.3 Data processing

4.2.1.3.1 Ultrasound data processing

The ultrasound data for fat were processed according to the methods followed for the liver tissues in section 4.1.1.3.1. The ultrasound propagation velocities in fat were determined at the measured temperatures for both during the heating and cooling phase of the experiment and then data from the heating and cooling duration were averaged. So for each set of measurement on fat, the ultrasound propagation velocity data at all the measured temperature consisted of the average of ultrasound propagation velocity data from the heating and cooling phase of the experiment like that of the liver tissue. The mean ultrasound propagation velocity and the standard deviations were determined from the five sets of measurement for fat. The percentage change in ultrasound propagation velocity with temperature was determined for fat. A simple linear regression analysis was performed between the ultrasound propagation velocity data and the measured temperatures to investigate the relationship between the temperature and the propagation velocity in fat. The linear relationship was quantified between the propagation velocity and temperature with a line-of-best-fit and Pearson r correlation coefficient (Figure 4-16). The average percentage change of ultrasound propagation velocity per degree Celsius temperature in fat was also determined from the slope of line-of-best-fit. As mentioned in section 4.1.1.3.1 for liver tissue measurement, to determine the average percentage change of ultrasound propagation velocity per °C, the slope of line best of fit was divided by the averaged ultrasound propagation velocity data across all the measured temperature.

4.2.1.3.2 Electrical Impedance data processing

The electrical impedance data for fat were also processed according to the same procedures followed for the liver tissues in section 4.1.1.3.2. The impedance magnitude and phase difference in fat for the measured frequencies were determined from the measured voltage data. The temperature coefficients or the temperature sensitivities of impedance for each measured frequency in fat were then calculated across all temperature measured. The mean and standard deviation of the temperature coefficients of the electrical impedance to temperature across all the frequencies measured were detected. Details of the temperature coefficients or temperature sensitivity calculations are described in section 4.1.1.3.2. As discussed in liver tissue measurements (section 4.1.1.3.2), normalisation can minimise the effect of temperatures in the impedance spectra, the impedance data in fat were normalised to the impedance at 8kHz using the same

procedure as used for the liver tissue experiment (section 4.3.2). Again, the mean and standard deviation of the temperature coefficients of normalised impedances to temperature across all frequencies were detected for fat.

4.2.2 Results

4.2.2.1 Ultrasound

Figure 4-16 shows the change of ultrasound propagation velocity with temperatures in fat samples obtained from lambs. The ultrasound measurements on fat samples showed that the propagation velocity in fat decreased with increasing temperature. The mean ultrasound propagation velocity (with standard deviation) from the five sets of measurement on fat was (1453±19) ms^{-1} and (1326±32) ms^{-1} at 25°C and 50°C respectively which was much lower than the corresponding values of ultrasound propagation velocity obtained for the aqueous salt solutions and the liver tissue (section 3.7.1.1 and section 4.1.2.1). There was a good negative correlation between the ultrasound propagation velocity in fat and the temperature (r^2 = 0.80 and p<0.01).

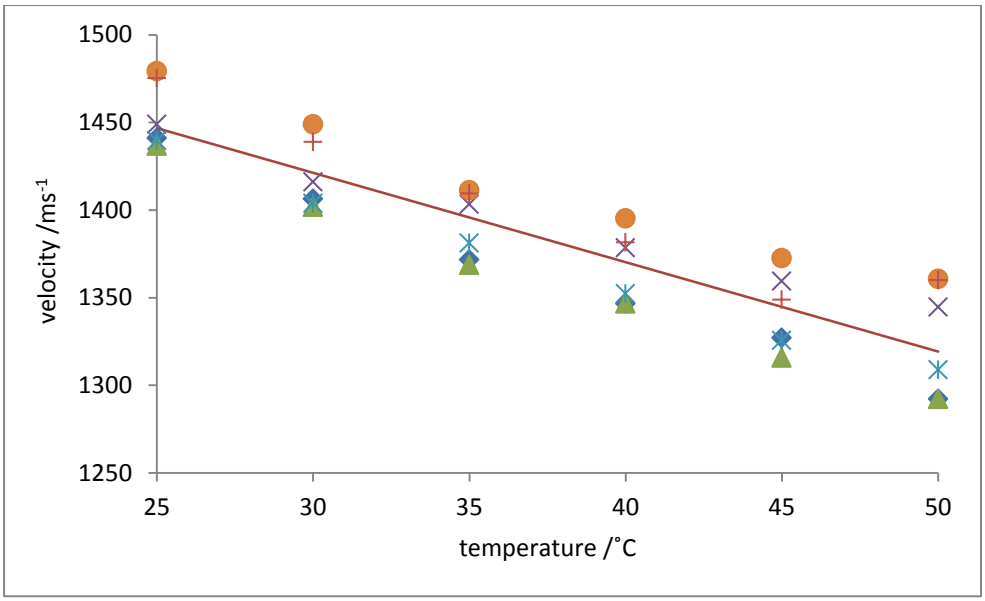

Figure 4-16 Showing the change of ultrasound propagation velocity with increasing temperatures. Individual ultrasound propagation velocity data points in fat tissue are shown with the line-of-best-fit. Each symbol represents data from a different fat sample.

Fat showed a negative percentage change or temperature coefficient of ultrasound propagation velocity. The magnitude of the temperature coefficients or average percentage change in ultrasound propagation velocity in fat was -0.43%°C^{-1}. The magnitude of the temperature coefficients or the average percentage change in ultrasound

propagation velocity in fat was much higher than the corresponding values for liver or aqueous salt solutions (Chapter 3, Table 3-3), although the change in velocity with temperature was in the opposite direction to liver.

It should be noted that there was a significant variability in the fat data between different samples due to the variation in the properties of the fat samples such as freshness, or cellular structure, size etc.. So, the linear regression analysis gave a significant variation in slopes (0.35 to 1.35) between fat samples which is shown in Figure 4-17 to indicate the range of fractional change of ultrasound velocity in fat with temperature.

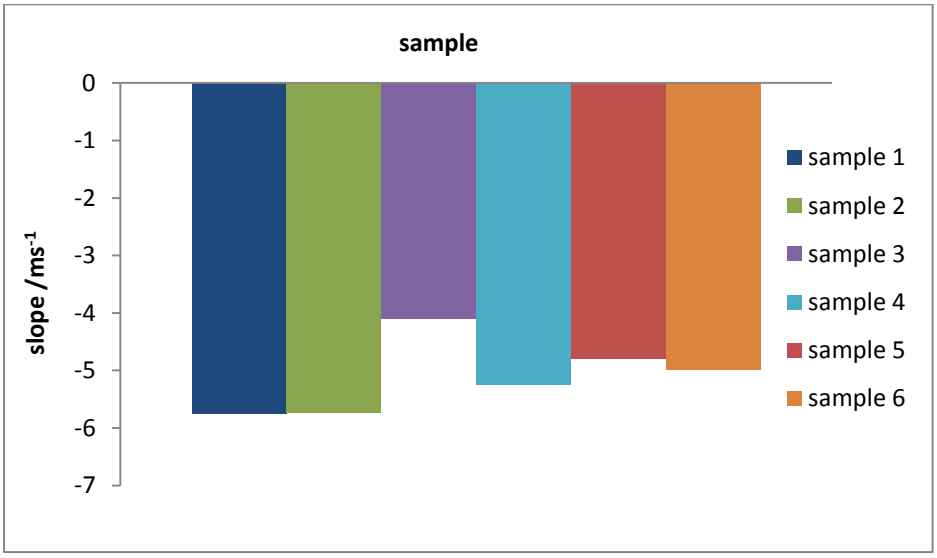

Figure 4-17 Showing the variation of slopes of the line-of-best-fit of different fat sample samples. The colours of the bars match the colours of the symbols in Figure 4-16 for the identification of individual samples.

4.2.2.2 Electrical Impedance

Figure 4-15 shows the received voltage signal from the impedance measurements in fat together with the magnitude of its frequency spectrum. The results presented in Figure 4-18 and Figure 4-19 are the electrical impedances from fat as the temperature is raised from 25°C to 50°C in 5°C steps. The error bars in Figure 4-18 and Figure 4-19 are the standard errors of mean. The results show that the electrical impedance of fat is largely independent of frequency up to 512kHz, but there is a decrease in impedance at 1MHz, the highest frequency measured in this experiment. The mean and standard deviation of the sensitivity of the electrical impedance measurements to temperature across all frequencies measured for fat was -2.3±0.43 %°C^{-1}. Figure 4-20 shows the phase difference in fat against frequency at all the measured temperatures. The phase difference in fat increased with increasing frequency. The error bars in Figure 4-20 are also standard error of mean. From

Figure 4-20, it can be seen that the phase difference in fat is independent of temperature below 64kHz, thereafter it decreases with temperature.

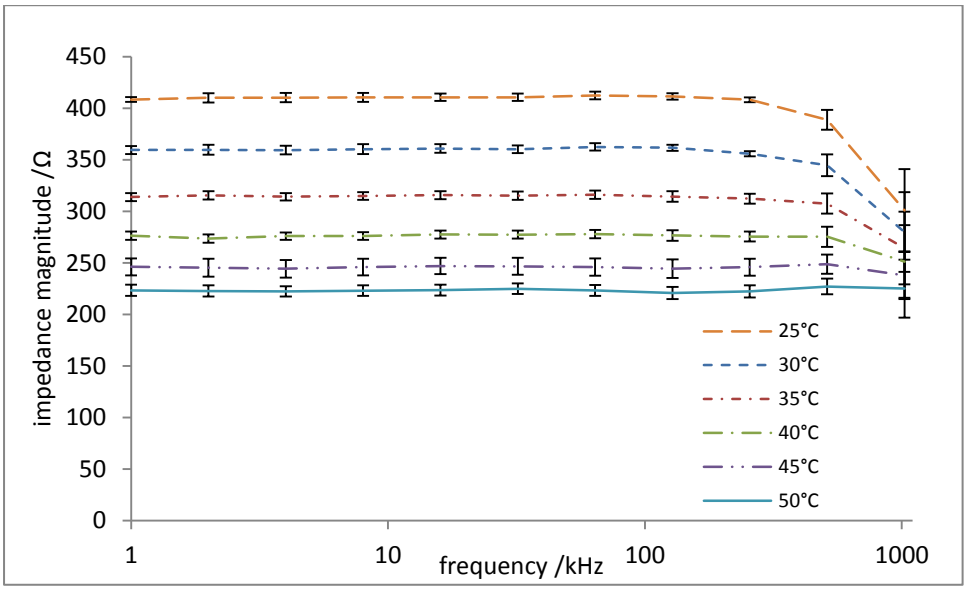

Figure 4-18 Measured Impedance value at 11 discrete frequencies in fat with the change of temperature

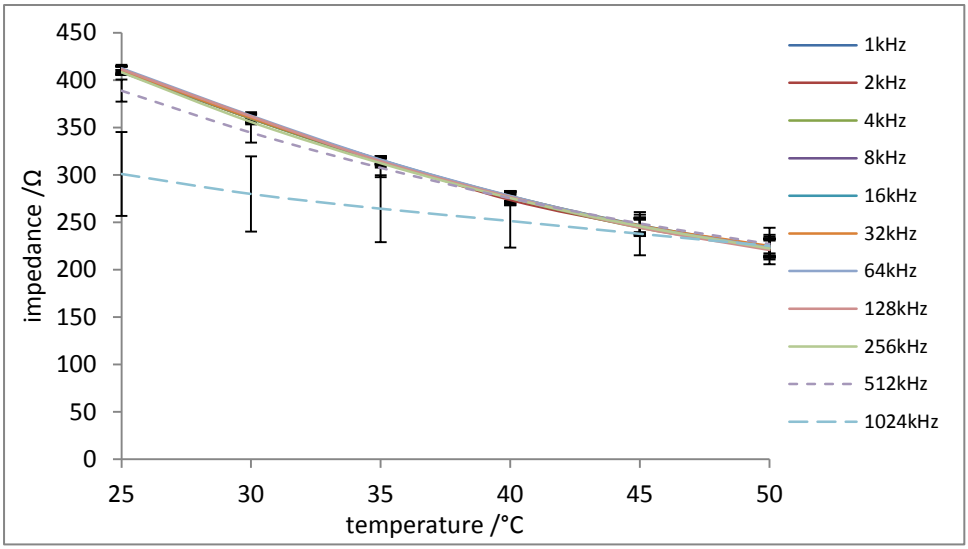

Figure 4-19 The change of impedances in fat with temperatures at different frequencies.

The Figure 4-18 and Figure 4-19 show that below 512kHz the variability of the impedance measurements is small– for frequencies up to 256kHz this variability rises from a maximum of 1% at 25°C to 4% at 50°C. At and above 512kHz the variability is much larger having a maximum value of 13% for 1024kHz at 25°C. The Figure 4-21 and Figure 4-22 show the normalised impedances in fat for the measured temperatures. The normalization of the impedance spectra to the impedance at 8kHz reduced the temperature sensitivity of the measurements for fat to 0.14±0.38 %°C^{-1}. It is clearly shown in Figure 4-21 and Figure 4-22

that there is a significant temperature sensitivity of the normalized electrical impedance of fat at 512kHz and at 1MHz.

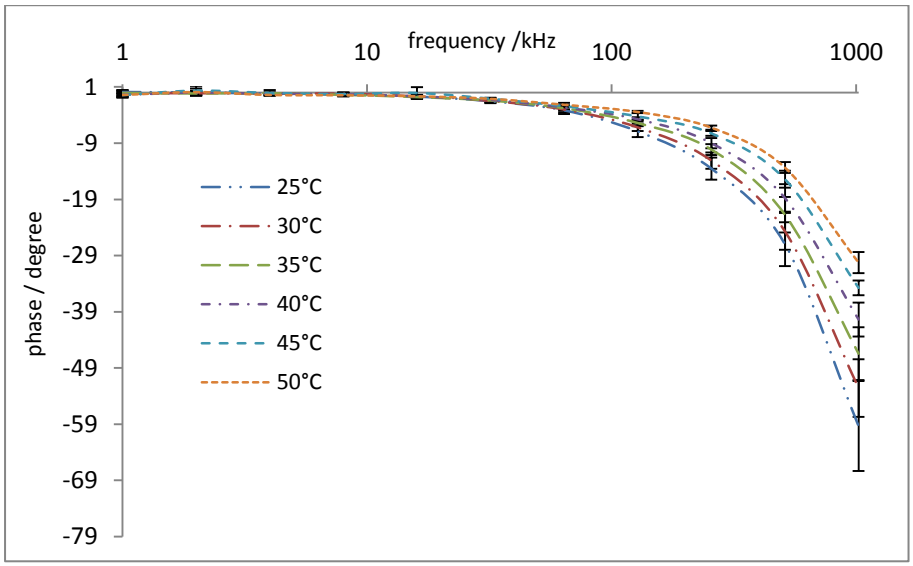

Figure 4-20 Phase changes in fat with increasing frequency are shown at the temperature measured. The vertical error bars in the figure represent standard error of the mean.

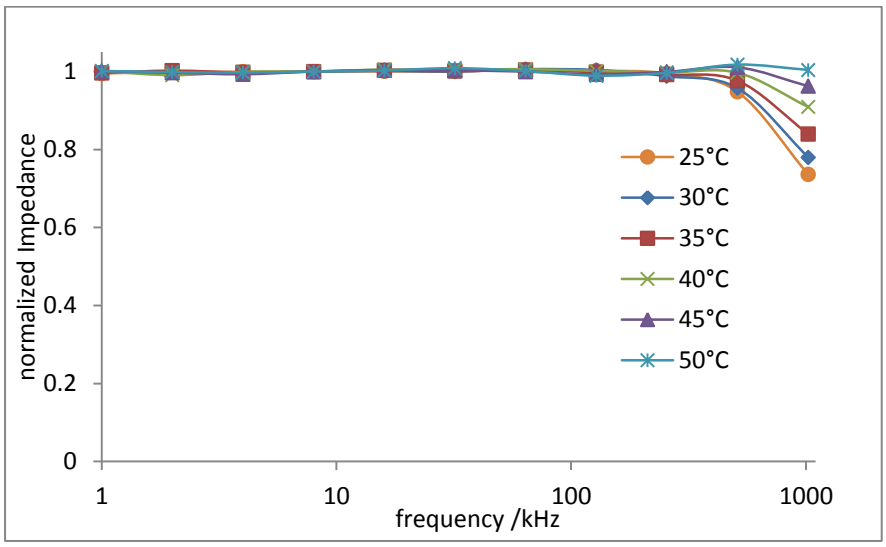

Figure 4-21 The normalized impedance in fat to the impedance at 8kHz are shown against frequency.

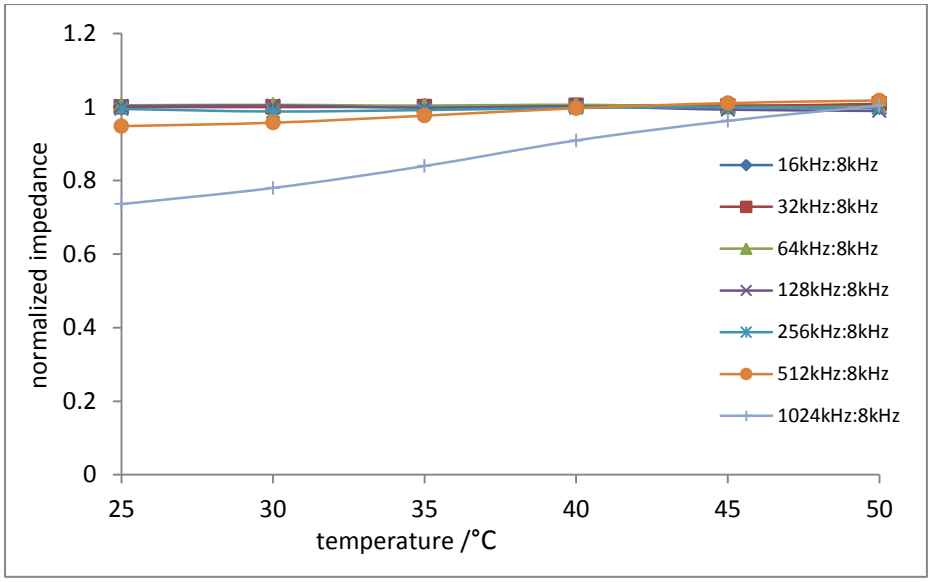

Figure 4-22 Temperature sensitivity of the normalised impedance to the impedance at 8kHz from the measurements on fat. The normalized impedances below 8kHz are not shown.

4.2.3 Discussion

4.2.3.1 Ultrasound

The ultrasound measurements showed that fat has a lower ultrasound propagation velocity when compared with the corresponding values for aqueous solutions (section 3.7.1.1, chapter 3) and liver tissue (section 4.1.2.1). Unlike these other materials (aqueous solution and liver), the temperature coefficient of ultrasound propagation velocity in fat is negative in the temperature range 25–50°C. The ultrasound propagation velocity measurements on fat showed similar behaviour to other non-aqueous liquids measured within this project (e.g. cooking oil (Figure 3-30, section 3.7.1, chapter 3), double cream and single cream fat solutions (section 3.7.1.2, chapter 3)). The measured absolute values of ultrasound propagation velocity in fat from lambs are consistent with the findings of others (McClements, 1997; Miles, 1985) in fat from animal and fish. The average percentage change of ultrasound propagation velocity per °C in fat from lambs are in agreement with the values obtained by others (e.g. (Duck, 1990; Miles, 1985)).

As with the liver tissue experiments (Figure 4-10, section 4.1.3.1), the amplitude of the reflected ultrasound signal in fat also decreased with increasing temperature, which has the effect of producing an increasing error in the propagation velocity determination as the temperature increased. However, in fat the decrease in peak to peak amplitude of the reflected ultrasound signal was 0.5%°C^{-1}, this value is lower than the corresponding

percentage drop of peak to peak amplitude in liver tissue, which resulted in less error in the ultrasound propagation velocity measurement in fat comparing to the liver tissue.

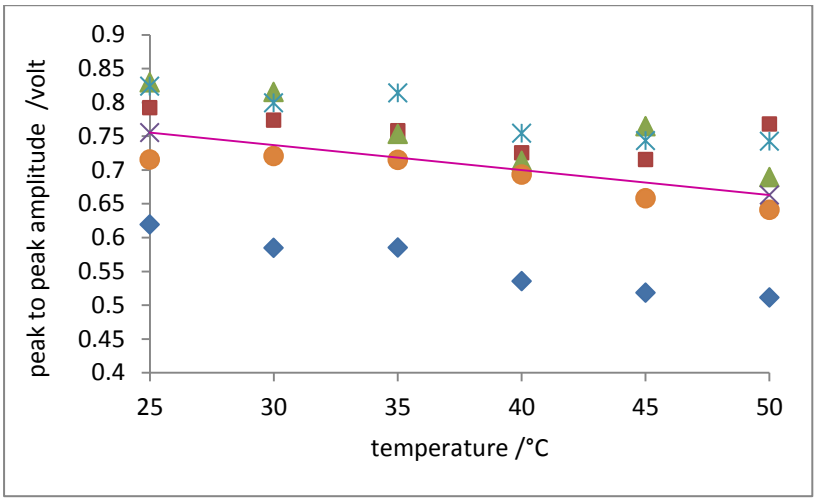

Figure 4-23 Showing the changes of peak to peak amplitude of the ultrasound signal in fat with temperature. Individual data points are shown along with the line-of-best-fit.

The magnitude and the temperature coefficients of ultrasound propagation velocity or the percentage change of ultrasound propagation velocity for fat depend on whether it is solid, liquid or in semi-solid state; and all three phases are believed to be present in the body (Hill *et al.*, 2004). This is clearly observed if the ultrasound propagation velocity from this measurement on solid fat is compared with the ultrasound propagation velocity measurements on cooking oil (section 3.7.1 and Figure 3-30, chapter 3), double and single cream (section 3.7.1.2, chapter 3), which are liquid in nature. Normally fat is considered as solid (or semisolid) at room temperature, whereas oil is liquid. Triglycerides or more specifically fatty acids are the main constituents of fat and oils, which are defined by the number of carbon atoms and the number of double bonds between carbon atoms in each molecule and these play a major role in determining their overall bulk properties, such as viscosity, density, and melting characteristics (Miller and Bamber, 2004; Shannon *et al.*, 2004). The ultrasound propagation velocity on a fat samples depends on the type and proportion of fatty acids it contains and from the knowledge of composition of fatty acid the ultrasound propagation velocity can also be determined (Javanaud and Rahalkar, 1988).

4.2.3.2 Electrical Impedance

The tetrapolar impedance measurements on fat gave higher magnitude of electrical impedance values comparing to the impedance values in liver tissue. The origin of this high impedance lies in the structural difference of fat from the liver tissue. Fat has small amount

of fluid in the extra-cellular space, since the bulk of the cell is occupied by a large spherical (approximately 0.1mm diameter) fat droplet surrounded by cytoplasm with the nucleus flattened and located on the periphery. The impedance value showed a minimal change in impedance with frequency up to 512kHz, which is consistent with fat cells having no intra-cellular fluid. However, the lipid within fat cells is a dielectric and this could result in a decrease in impedance at 1MHz. The Cole-Cole model applies to cellular tissues, but there is no equivalent for fat. To investigate the impedance findings on fat a lumped parameter model was developed and its impedance determined using the National Instrument Multisim Circuit Design software (Figure 4-25).

For the modelling work, the membrane capacitance and extra-cellular resistance of the fat cell was needed and calculated assuming fat cell having 0.1 mm diameter spherical shape and has no intra-cellular fluid. To obtain the capacitance value of a single fat cell, the theory of parallel plate capacitor ($C = \varepsilon_0 \varepsilon_r \frac{A}{d}$), was applied, where two square shaped plates having sides 0.1mm surrounded the 0.1mm diameter spherical fat cell. The value of the relative permittivity of fat cell was taken from the literature (Duck, 1990) as $5X10^4$. The area of the square shaped plate was calculated and 0.1mm, which is the diameter of the fat cell, was used for calculation as the distance between the two parallel plates.

To calculate the extra-cellular resistance, at first the total volume of a single fat cell (volume between the two parallel plates in Figure 4-24) was determined considering a cube with sides 0.1mm. Then, the volume of the extra-cellular region was determined by subtracting the volume of the spherical region from the total volume of fat cell. This volume of the extra-cellular region was then converted to the area of the extra-cellular region. Then, using the resistance formula ($R = \rho \frac{l_{ecf}}{A_{ecf}}$), the resistance of the extra-cellular region of fat cell was determined, where resistivity, ρ, is the inverse of conductivity, σ, ($\rho = 1/\sigma$) and l_{ecf} and A_{ecf} represent the length and area of the extra-cellular region. For the calculation the value of conductivity for the extra-cellular region was taken from the literature (e.g. Duck) as $1mScm^{-1}$.

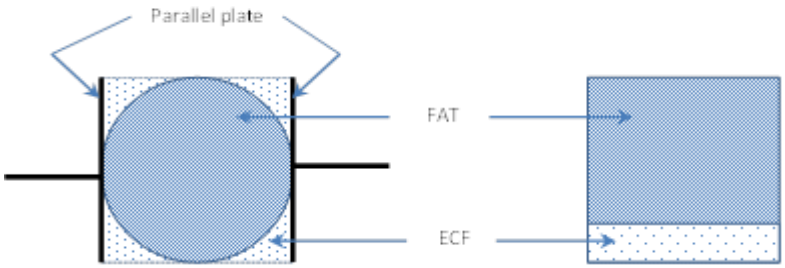

Figure 4-24 Showing the spherical fat cell and extra-cellular regions between two parallel plates, where ECF means the extra-cellular fluid.

From calculation the value of membrane capacitance and extra-cellular resistance obtained as 44pF and 2.1kΩ respectively and these values were used in the modelling work for fat. The circuit diagram of fat tissue consisting of (9X9X9) fat cells is shown in Figure 4-25. The fat modelling works showed similar type of impedance and phase response with increasing frequency (Figure 4-26) as that of the experimental results. It should be noted that the magnitude of impedance primarily depends on the sample size and the measurement technique. Figure 4-25 represents a 0.9mm sided cube of fat whereas the results given in Figure 4-18 were from a cylindrical sample 40mm in diameter and 31mm long. Furthermore, the simulation used to determine the impedance for the circuit shown in Figure 4-25 was essentially a bipolar impedance measurement whereas the measurements on the tissue sample were tetrapolar. Thus there was a large difference between the modelled impedance and the experimental data. However, irrespective of the sample size and measurement technique, the dispersion frequency will be the same. Therefore, the magnitude results from the fat measurement at 25^{o}C (Figure 4-18) and the simulation (Figure 4-26a) were normalized and compared (Figure 4-27). This shows the good agreement between the measured and simulated values in terms of the dispersion frequency.

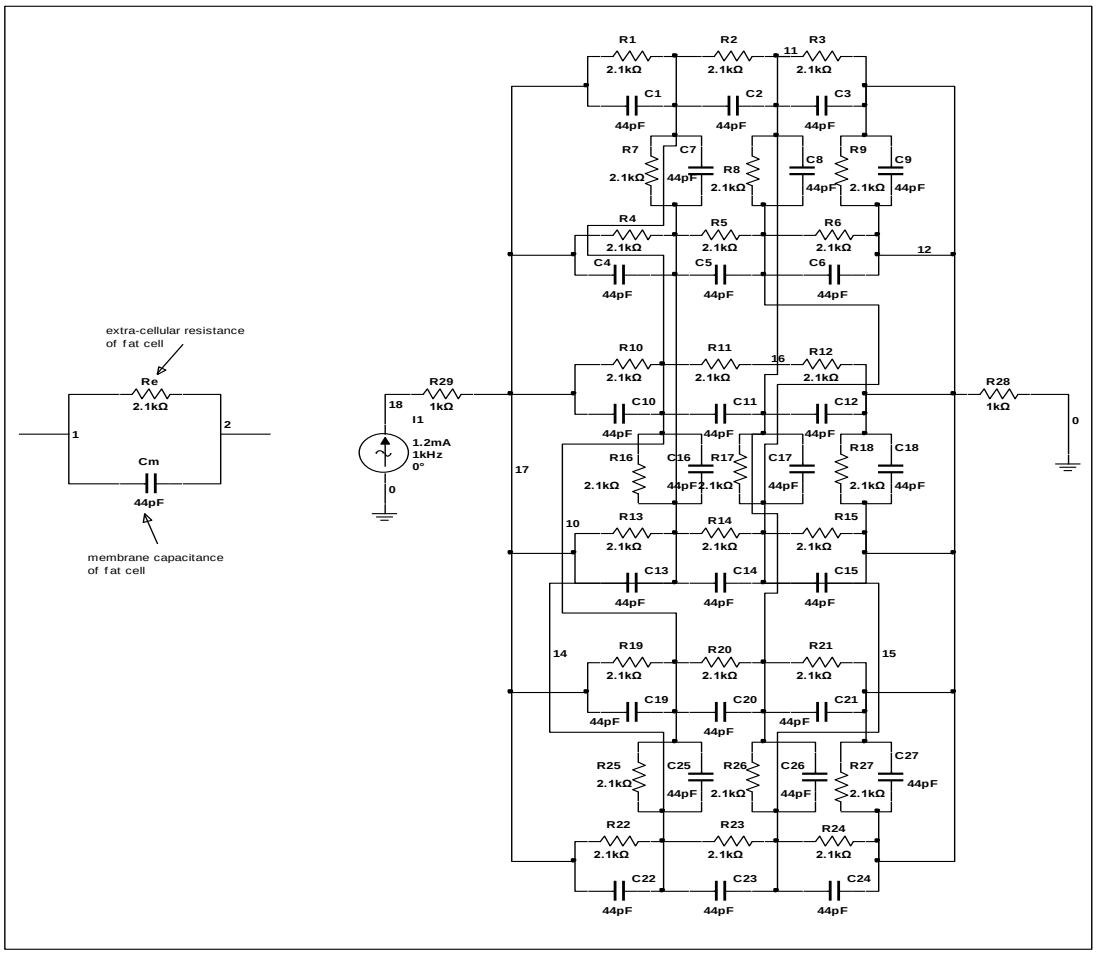

Figure 4-25 Showing the circuit diagram of a 9X9X9 fat cells. The value of extra-cellular impedance and membrane capacitance were calculated considering fat cell having 0.1mm diameter spherical shape.

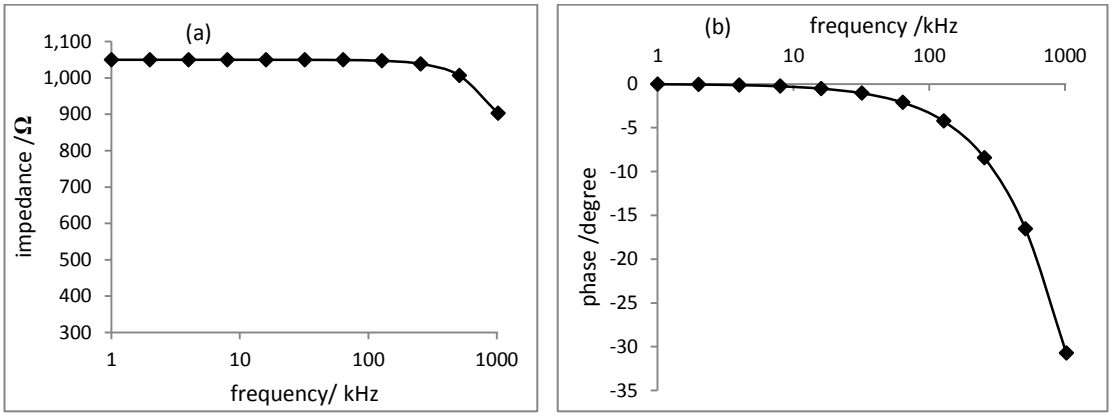

Figure 4-26 The impedance and phase response of fat tissue (considering 9X9X9 fat cells) from the modelling works–(a) showing the impedance spectra (b) showing the phase spectra.

The electrical impedance measurements on fat gave higher phase differences (Figure 4-20) than those obtained for liver tissue (Figure 4-7). The reason for this high phase difference in fat is that the lipid within the fat cell acts as a dielectric, which has high dielectric constant than the dielectric constant value for the intra-cellular fluid in liver tissue. The high phase

difference in fat from lamb is consistent with the results obtained from multi-frequency electrical impedance measurements on fat from rat by Parramon and co-workers (Parramon *et al.*, 2007). The lumped parameter modelling work done in Multisim for fat also gave higher phase difference (Figure 4-26b).

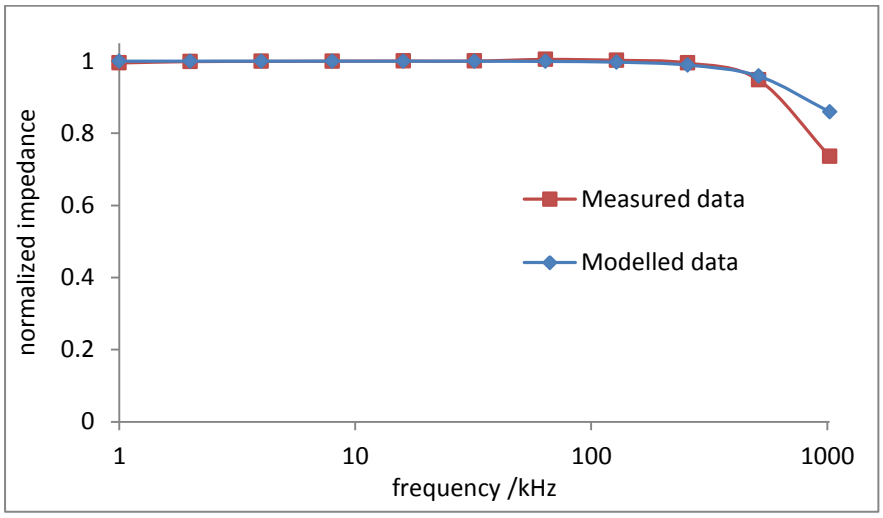

Figure 4-27 Normalised data from the fat modelling works are compared with the measured data from fat.

The variability in the impedance measurements for the fat samples was much smaller than the corresponding variability in liver tissue and independent of frequency. The origin of this small variability between samples is unclear but may reflect the fact that in a fat cell the space for extra-cellular fluid is very small with the majority of the space occupied by large, spherical fat droplets. The variability of the measured phase differences increased with frequency, the origin of which is also unclear but this could be due to the size and spatial distribution of fat cells.

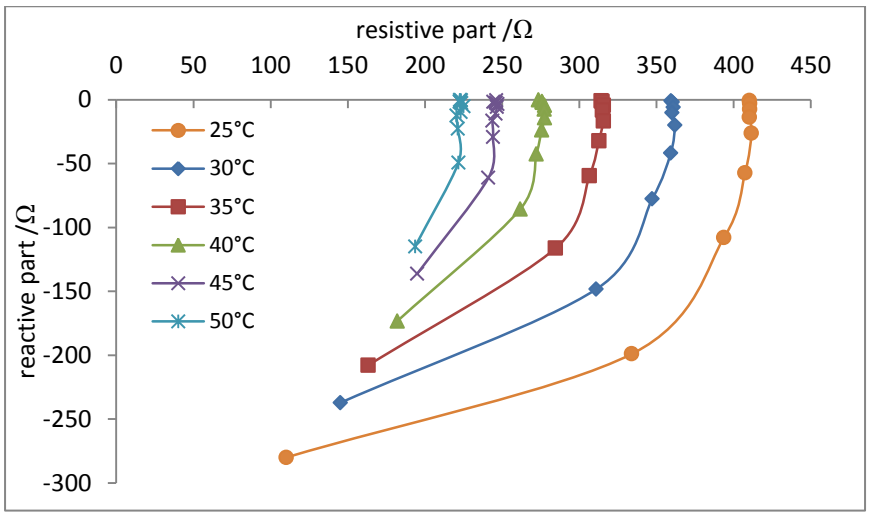

Figure 4-28 Showing the Cole-Cole or Wessel plots of the fat data

The fat data (resistive and reactive component (Figure 4-28)) could not be analysed by fitting to the equation of a Cole-Cole model, because the Cole-Cole model is used for the cellular tissue. Therefore, the fat data was analysed with the data from lumped parameter modelling works which showed similar shapes of Cole-Cole or Wessel plot for fat tissue (Figure 4-29).

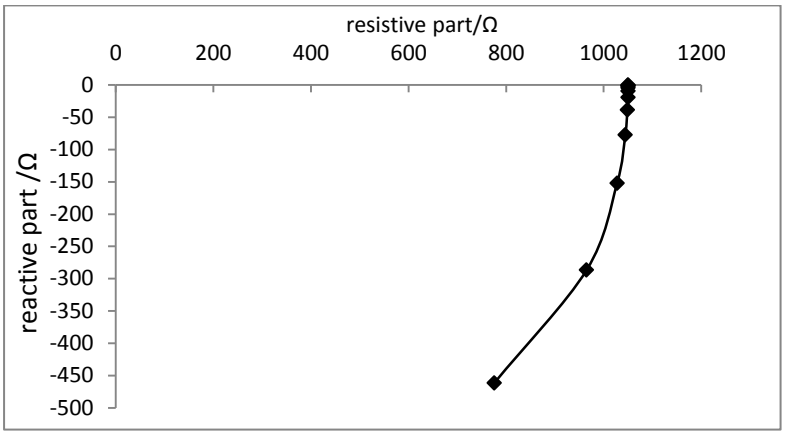

Figure 4-29 Showing the Cole-Cole or Wessel plot of fat obtained from the modelling work

4.3 Implications for temperature measurements on fatty liver

In this section the results from the ultrasound and electrical impedance measurements on liver and fat samples will be considered together in terms of using a combination of the measurements for the non-invasive estimation of temperature in the mild hyperthermia range.

4.3.1 Implications from the Ultrasound measurement

The results from the liver sample showed a linear positive change in ultrasound propagation velocity with temperature of $0.94 ms^{-1}°C^{-1}$ corresponding to $0.06\%°C^{-1}$ (r^2 = 0.43, Figure 4-3) across all the measured temperatures, whilst the results for fat sample showed a linear negative change in ultrasound propagation velocity of $-4.7 ms^{-1}°C^{-1}$ corresponding to $-0.43\%°C^{-1}$ (r^2 = 0.64, Figure 4-16) across all the measured temperatures. Therefore, the percentage change of ultrasound velocity in fatty liver tissue would lie in between the percentage change of liver and fat. These percentage changes of ultrasound velocity can be related to the percentage of fat in the fatty liver tissue, which can either be used to predict the temperature in tissue during mild hyperthermia treatment or to determine the tissue type by predicting the percentage of fat in a tissue.

4.3.2 Implications from the Impedance measurements

The main difference between the electrical impedance spectra of fat and liver samples lies in the decrease in impedance with increasing frequency for liver tissue. The mean and standard deviation of the sensitivity of the electrical impedance measurements to temperature across all frequencies measured for liver and fat were almost the same (-2.3±0.18 %°C^{-1} and -2.3±0.43 %°C^{-1} respectively). To investigate whether the difference between the temperature sensitivity in liver and fat samples was statistically significant, a Student's t-test were performed on these temperature coefficients or temperature sensitivity data. There was no statistical difference between the average temperature coefficients for fat and liver tissue (Student's t-test, $p = 0.55$). This analysis was only for the average temperature coefficients and there is a need to examine how the temperature coefficients changes within temperature range of interest (25–50°C). Below 512kHz there was no correlation between the temperature coefficient and the logarithm of the frequency for fat ($r^2 = 0.001$, $p = 0.92$) however, there was a positive linear correlation between the temperature coefficient and frequency for liver tissue ($r^2 = 0.95$, $p < 0.01$) with the slope of the line-of-best-fit being 0.17%°C^{-1} log(kHz)$^{-1}$ (Figure 4-30). Therefore, the similarity between the temperature coefficients for fat and liver coupled with the different impedance spectra between fat and liver suggest that an appropriate way of combining the two measurements is to use the impedance measurements to quantify the fat composition and the ultrasound measurements to determine the temperature.

As discussed before (section 4.1.2.2) there was a large variability in the impedance spectrum for liver tissue. In addition, it was also shown in section 4.1.2.2 that temperature has the effect of increasing the variability in the magnitude of high frequency impedance values in liver tissue. Therefore, to reduce both the variability in magnitude of the impedance and the effect of temperature, normalisation was required. To use the fat and liver spectra together the same normalisation must be applied to the impedance data from liver and fat. Similarly, the linear increase in the temperature coefficient with frequency for liver sample also results in increased temperature sensitivity of a high to low frequency ratio as the difference between two frequencies increases. Therefore, the highest frequency below the roll-off in impedance for the liver tissue should be selected to minimise the temperature sensitivity. The highest frequency measured below the cut off frequency is 8kHz (Figure 4-5) and normalised magnitude spectra for fat and liver are given in Figure 4-8 and Figure 4-21, respectively. It was also shown (section 4.2.2.2 and Figure 4-18) that fat has a small variability in impedance below 512kHz; and above 512kHz the

variability is much larger (as high as 13% for 1024kHz). Thus, normalisation can also minimise the effect of temperatures in the impedance spectra for fat samples. As mention previously (section 4.2.3.2) for the impedance measurement in fat, the normalisation frequency can be chosen from any frequency below 512kHz. The normalisation of the impedance spectra to the impedance at 8kHz significantly minimised the effect of temperature and reduced the temperature sensitivity of the impedance measurements for liver and fat to 0.17±0.18 % $°C^{-1}$ and 0.14± 0.38 % $°C^{-1}$, respectively.

Having normalized the impedance measurements to 8kHz, analysis was also done to select the normalized frequency to be used to determine the percentage of fat in the sample. The candidate frequencies are those above the roll-off frequency in the spectrum for liver (8kHz). It has been shown in section 4.2.2.2 that there is a temperature sensitivity of the normalized electrical impedance of fat at 512kHz and at 1MHz. Therefore, the frequency selected could be one of those measured between 8kHz and 256kHz.

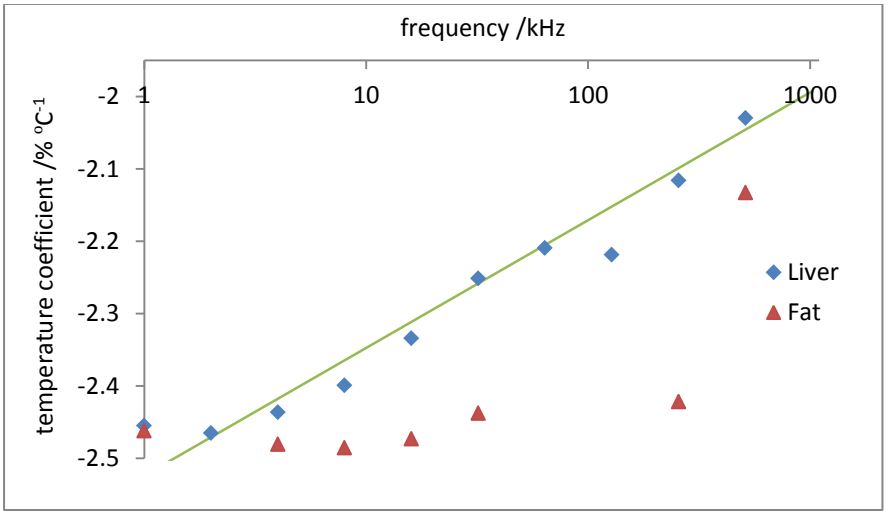

Figure 4-30 Showing the temperature sensitivity of liver and fat with the change of frequency. The temperature coefficients were averaged around temperatures 25°C to 50°C.

To use the electrical impedance measurements to determine the percentage of fat in a tissue sample, the ratio of the normalised impedance values for fat and liver must be independent of temperature. To investigate this, the ratio between the normalized electrical impedances for liver and fat samples were determined for each measured frequency for temperatures 25°C–50°C in 5°C increments. This analysis showed that up to 512kHz, the ratios were almost independent of temperature (r^2 = 0.05 & p =0.55) but that a temperature sensitivity existed at 1MHz (Figure 4-31).

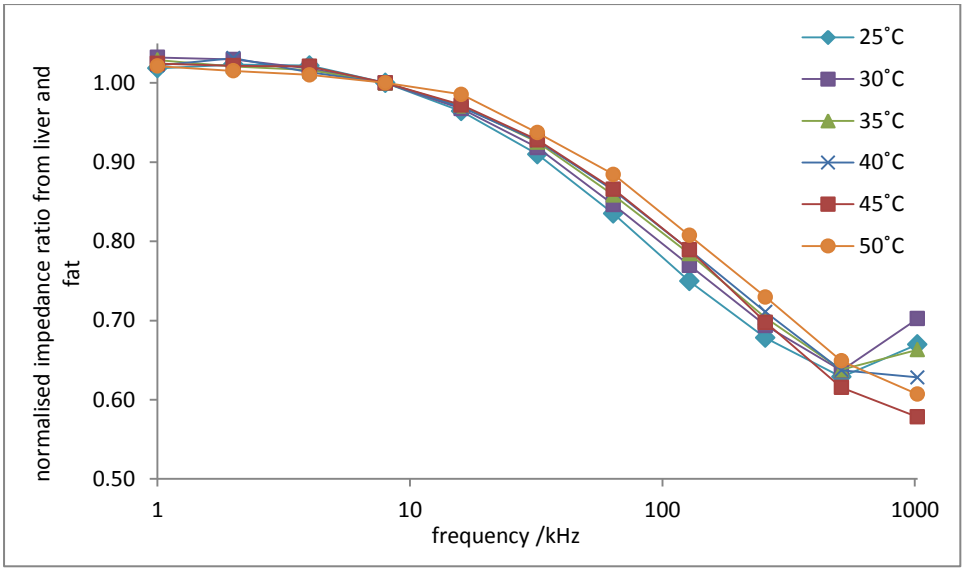

Figure 4-31 The ratio of the normalised impedances at each measured temperature from the liver and fat samples are shown against frequency.

The temperature independence of this normalized impedance ratio of fat and liver supports the approach of using normalized electrical impedance measurements to determine tissue type in mild hyperthermia. However, in that case again a good correlation between the normalized impedance and the percentage of fat in the sample is required to use the measurement predictively.

5 Layer tissue experiments

In the previous chapter a large variability in the magnitude of the electrical impedance for liver and fat tissue with temperature was found which increased with increasing frequency (section 4.3.2, chapter 4). It was shown that normalising the values against a single frequency value can minimise the effect of temperature on the impedance data from both fat and liver tissue. The temperature independence of the normalised electrical impedance magnitude measurements in fat and liver tissue supports an approach of using normalised electrical impedance measurements for determining the percentage of fat in the tissue. However, in order to do this it is necessary to know the relationship between the normalised impedance measurements and the percentage of fat in the tissue. Considering the fat and liver tissue results together, it was also shown in the previous chapter that the changes in ultrasound propagation velocity is also related to the percentage of fat in tissue as well as the temperature of the sample (section 4.3.1, chapter 4). Therefore, if the ultrasound propagation velocity is to be used for predicting the temperature in tissue during mild hyperthermia treatment, the percentage of fat in the tissue must be known or measurable. In this chapter, the proposed approach of tissue characterisation using normalised impedance and predicting the temperature in tissue based on the change in ultrasound propagation velocity have been evaluated by making measurements on simulated fatty tissue samples with known percentages of fat constricted from fat and liver tissue.

An important lesson learned from the liver tissue measurements in the previous chapter is that the maximum temperature in the tissue sample should be restricted to 45°C to minimize the tissue damage. If the temperature in the tissue sample is raised beyond 45°C, some irreversible damage can occur to the tissue due to heat induced denaturation and coagulation in the tissue. This irreversible tissue damage was clearly observed in the ultrasound measurements on the tissue samples while the temperature in the tissue sample was cooled down from 50°C to 25°C in 5°C steps (section 4.1.3.1, chapter 4).

5.1 Procedure

5.1.1 Sample preparation

Liver and fat tissues from lambs obtained from a domestic butcher were used in the layered tissue experiments described in this chapter. For the layered tissue experiments, the same procedures were followed as those used in for the single tissue measurement (section 4.1.1.1 and section 4.2.1.1; chapter 4). However, for the layered tissue

experiments, first the densities of fat and liver tissue that were used for the experiments had to be determined in order to determine the percentage of fat in the sample. To determine the density of both types of tissue, a small block of fat or liver tissue was cut from the bulk tissue. The mass of the small block of liver or fat was measured using a precision scale (KERN EMB 500-1). The volume of the small block of fat or liver was determined from the displacement of water when the sample was inserted in a volumetric flask. From the mass and the volume, the density of fat or liver tissue used for the experiments was determined. These density values were then used to calculate the percentage of fat and liver by volume in a particular layered tissue experiment before the measurement.

For the layered tissue experiments, thin layers of liver and fat were cut from the bulk tissue using a very sharp knife; details of these procedures are also described in the previous chapter (section 4.1.1.1 and 4.2.1.1, chapter 4). The mass of each thin layer of fat and liver tissue used for a particular experiment was measured using the precision scale. The thin tissue layers were placed in the test cells in an alternate fashion of fat and liver tissue. In this research fat that is within the liver is the focal interest and therefore, the top layer in these layered fat-liver tissue experiments was always made liver. The thickness and the number of fat and liver tissue layers were varied to simulate liver tissue containing different proportions of fat. Then, from the mass and density of each type of tissue placed in the test cell for the experiments, the percentage of liver and fat in the sample tissues were determined and expressed as the percentage by volume before the measurement. In addition, the proportion of fat and liver in the final sample can also be expressed as a percentage by weight.

18 layered tissue samples (mean % of fat and liver: x ± y, range: 0% - 100%) containing different percentage of fat and liver tissues were prepared. As described previously (section 4.1.1.2 and section 4.2.1.2) each of these tissue samples was prepared to take simultaneous ultrasound and electrical impedance measurements. For each experiment the layered tissue sample consisted of 4 layers from the liver and fat tissue. The measurements were performed on different days using liver and fat tissues collected from different animals.

5.1.2 Measurements

The ultrasound and the multi-frequency electrical impedance measurements were made simultaneously on the layered fat-liver tissues samples placed in the test cell as the

temperature in the tissue sample was raised from room temperature to 45°C. As discussed at the beginning of this chapter that following the results from the liver tissue experiments in chapter 4, the maximum temperature was restricted to 45°C for the layered tissue experiments to minimize the irreversible tissue damage (section 4.1.3.1, chapter 4). The temperature of the sample tissues were increased and recorded using the same procedures that were followed for the single tissue measurements described in the previous chapter (section 4.1.1.2, chapter 4; details of temperature change procedure with technical detail in section 3.5, chapter 3). The ultrasound propagation velocity and tetrapolar electrical impedance measurements were made simultaneously on the layered tissue samples at temperatures from 25°C to 45°C in 5°C steps during both the heating and cooling phase. The electrical impedance and ultrasound data were acquired simultaneously using the two channels of the National Instruments high speed digitiser (USB-5133) at a sampling rate of 100 and 10MHz respectively (details of which are described in section 3.4, chapter 3). Similar to the measurements on the single tissues (chapter 4), each measurement on the layered tissue samples at each temperature was the average of twenty consecutive 100µs ultrasound data sets and twenty 1ms epoch of measured voltage data for the ultrasound and electrical impedance measurements respectively to improve the signal-to-noise ratio.

5.1.3 Data analysis

5.1.3.1 Ultrasound data analysis

The ultrasound data were processed in Matlab following the same procedures described in section 3.6.1 in chapter 3. The ultrasound propagation velocity was calculated from the time of flight of the reflected ultrasound signal from the base of the test cell as it passed through the layered fat-liver tissue samples. The ultrasound propagation velocity data from the sample tissues with various percentage of fat were plotted against temperature for each tissue composition used to investigate the change of propagation velocity with the change of temperature and also to understand how the fat content of the sample affected the propagation velocity (Figure 5-1). The ultrasound propagation velocity data were also plotted against the percentage of fat in the layered tissue samples at all the temperature measured (Figure 5-2). Simple linear regression analyses were performed on the calculated ultrasound propagation velocity data at each measured temperature (25°C–45°C) to investigate the relationship between the sample composition, specifically the percentage of fat in the layered tissue samples and the ultrasound propagation velocity. Pearson r correlation coefficients were determined between the ultrasound propagation velocity at the measured temperatures and the percentage of fat in the sample tissues used for the

layered tissue experiments to investigate the correlation between ultrasound propagation velocity and the percentage of fat in the sample. The relationship between the sample compositions and the ultrasound propagation velocity at each measured temperature for the layered fat-liver samples was quantified using a line-of-best-fit determined by the least squares methods (Figure 5-2).

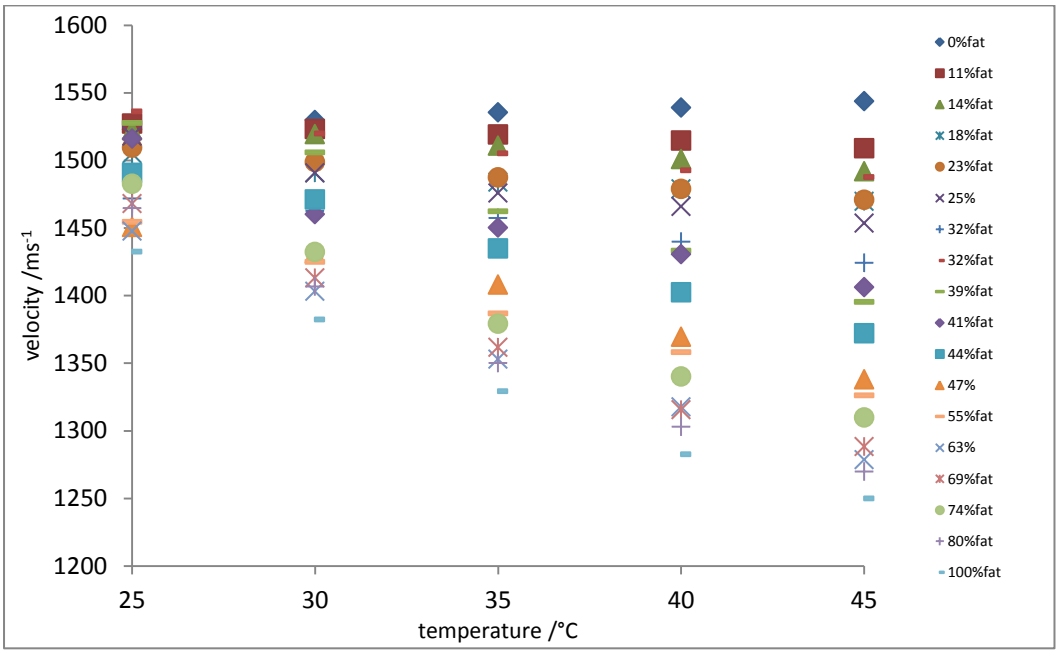

Figure 5-1 Changes of ultrasound propagation velocity with temperature in the layered tissue samples produced by varying the percentage of fat and liver tissue.

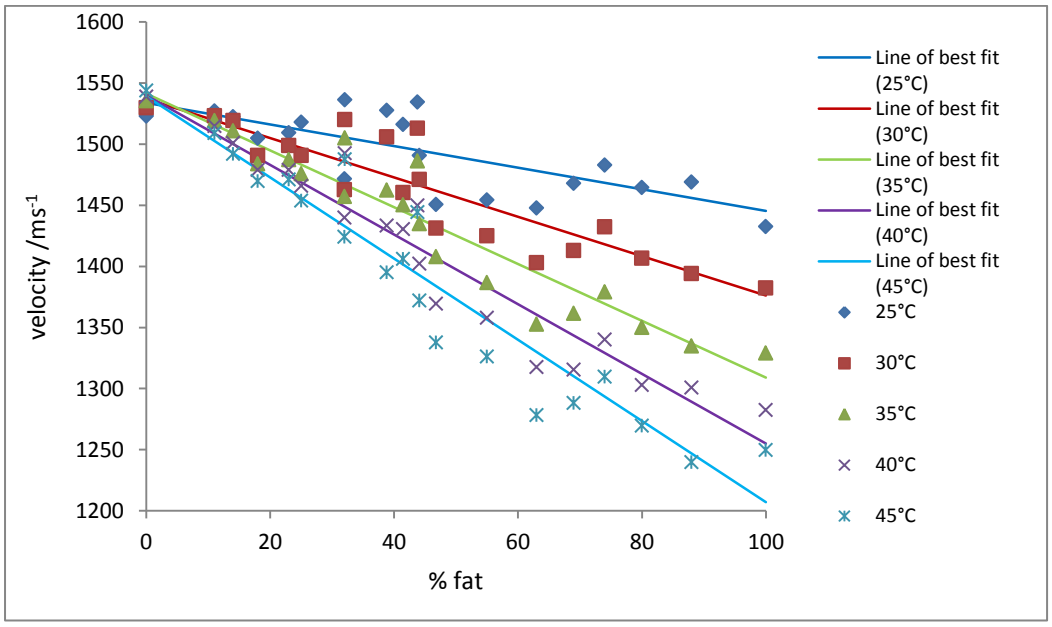

Figure 5-2 Changes of ultrasound propagation velocity with the percentage change of fat content in the layered tissue samples at the measured temperatures.

The average change of ultrasound propagation velocity per degree Celsius temperature for each sample composition across all the temperature measured was estimated and plotted against the percentage of fat in the layered tissue samples (Figure 5-3). The average change of ultrasound propagation velocity per degree Celsius temperature was calculated from the slope of the line-of-best-fit of the ultrasound propagation velocity in the layered tissue samples against the measured temperature curves (Figure 5-1). These average changes of ultrasound propagation velocity per degree Celsius data from the layered tissue samples were also converted to the percentage changes of ultrasound propagation velocity per degree Celsius. To calculate the percentage change of ultrasound propagation velocity per degree Celsius, the measured ultrasound propagation velocity at temperature 35°C (considering 35°C as the middle value of the measured temperature range 25°C–45°C) was used. The percentage changes of ultrasound propagation velocity per °C in the layered tissue samples were again plotted against the percentage of fat in the layered fat-liver tissue composition (Figure 5-4).

A linear regression analysis was also performed between the change in ultrasound propagation velocity per °C data and the percentage of fat in the layered tissue samples and a linear relationship is established with a line-of-best-fit and the Person r correlation coefficients determined (Figure 5-4). Similarly, a linear regression analysis was also performed between the percentage change in ultrasound propagation velocity per °C data and the percentage of fat in the layered tissue samples. Again a linear relationship was established between the percentage change in ultrasound propagation velocity per °C data and percentage of fat in the layered tissue samples with a line-of-best-fit and the Person r correlation coefficients determined.

5.1.3.2 Impedance data analysis

The measured voltage data from the multi-frequency electrical impedance measurements on the layered fat-liver tissue samples were processed in same way as that was used to process the data from the single tissue measurements (section 4.1.1.3.2). The magnitude and phase of the transfer impedance for the layered fat-liver tissue samples were also obtained using the method described in the previous chapter for the single tissue measurements (section 4.1.1.3.2). Detail of the determination of the magnitude and phase of the transfer impedance is described in section 3.6.2 in chapter 3. However, as discussed in section 3.6.2.1.2 in chapter 3, the phase information in biological tissue is always difficult to obtain therefore, only the amplitude information for the layered tissues measurements was taken forward for further analysis. Moreover, the results obtained from the fat and

liver tissue impedance measurements in the previous chapter show that the phase information doesn't provide useful additional information (section 4.1.3.2 and 4.2.3.2, chapter 4).

As discussed in chapter 4 the variability of the impedance measurements in liver and fat samples (section 4.1.1.2 and 4.2.1.2, chapter 4) resulted in the magnitude values of the transfer impedance being normalised to 8kHz (section 4.1.1.3.2 and 4.2.1.3.2, chapter 4). Moreover, it was also shown in the previous chapter (section 4.1.2.2 and 4.2.2.2, chapter 4) that the normalisation process reduced the temperature sensitivity of the impedance measurements. Therefore, as part of processing the layered tissue impedance data the magnitudes of the transfer impedance of the layered fat-liver samples were also normalised to the impedance at 8kHz. From the normalized impedance data, the temperature coefficients for each of the layered fat-liver tissue samples were determined for each measured frequency. For none of the frequencies measured was there a statistically significant correlation between the temperature coefficient of the normalised impedance and the percentage of fat in the sample ($r^2 < 0.02$, $p > 0.05$). A simple linear regression analyses were performed between the averaged normalised impedance data at each measured frequency and the percentage of fat in the layered tissue samples. The linear relationships between the averaged normalised impedances and the percentages of fat were obtained only at frequencies 64kHz, 128kHz, and 256kHz, which are shown in Figure 5-5, Figure 5-6, and Figure 5-7 and for these frequencies a line-of-best-fit and Pearson r correlation coefficients were determined.

5.2 Results

5.2.1 Ultrasound

Figure 5-1 shows the changes of ultrasound propagation velocity in the layered fat-liver tissue samples with the change of temperature. It can be seen from the Figure 5-1 that in samples with the lowest percentage of fat, the change in ultrasound propagation velocity with temperature was positive; however as the percentage of fat increased, the change in ultrasound propagation velocity with temperature becomes negative.

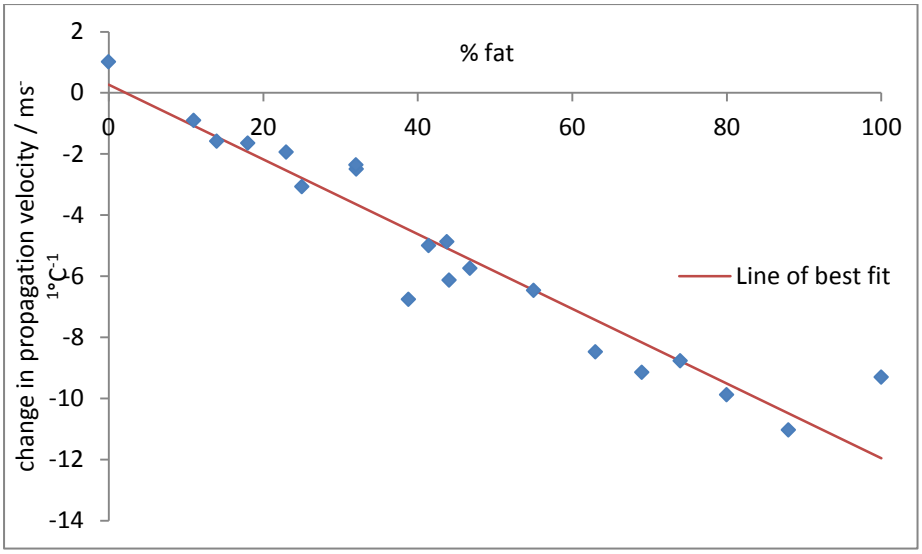

Figure 5-3 Changes in ultrasound propagation velocity per degree Celsius temperature with the percentage change of fat in the layered tissue samples. Here, velocity data at 35°C were considered. Individual velocity data points were shown with the line-of-best-fit.

The changes of ultrasound velocity with the change of percentage of fat content in the layered fat-liver tissue samples at the measured temperatures are also shown in the Figure 5-2, where it can be seen that the ultrasound propagation velocity at each measured temperature decreases linearly with the increasing percentage of fat in the layered tissue samples. The slopes of the lines of best fit between the ultrasound propagation velocity and the percentage of fat in the sample fell with increasing temperature from -0.88 ms^{-1} $\%^{-1}$ (r^2 = 0.56) at 25°C to -3.32 ms^{-1} $\%^{-1}$ (r^2 = 0.91) at 45°C. The Pearson r correlation coefficients between the ultrasound propagation velocity and the percentage of fat in the layered tissue samples increased with increasing temperature (the value of r^2 increased from 0.56 at 25°C to 0.91 at 45°C).

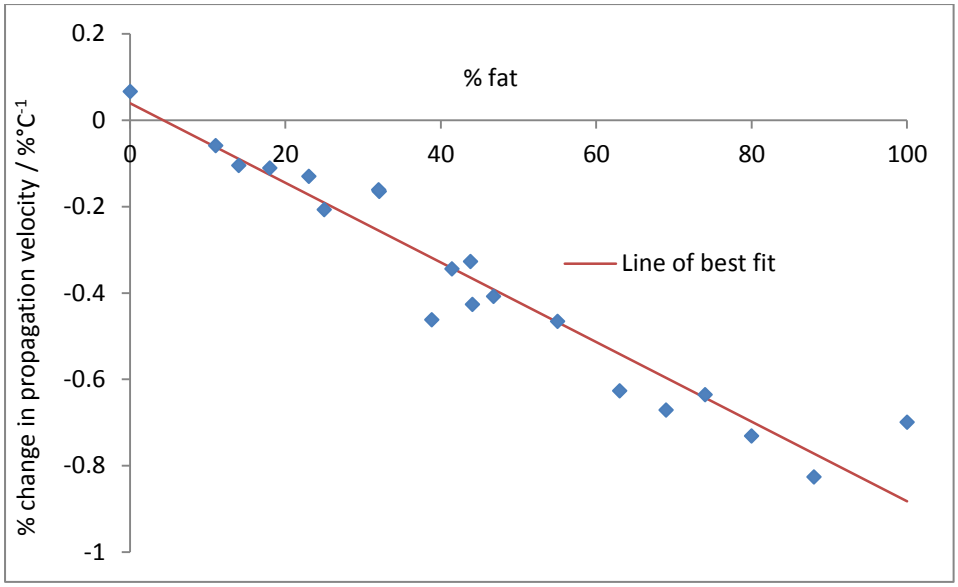

Figure 5-4 Changes in the ultrasound propagation velocity expressed as percentage with the percentage change of fat in the samples. Line-of-best-fit is shown with the individual data points.

The changes in ultrasound propagation velocity per °C as a function of the percentage of fat in the layered tissue samples are shown in the Figure 5-3. These data can also be expressed as the percentage change in propagation velocity per °C with the percentage change in fat in the layered tissue samples as shown in Figure 5-4. The regression analysis showed that there was a linear relationship between the percentage of fat in the sample and the change in ultrasound propagation velocity per °C (r^2 = 0.93). The linear relationship is shown in the Figure 5-3 and has a line-of-best-fit with a gradient of 0.12 $ms^{-1}°C^{-1}\ \%^{-1}$, which correspond to a percentage change in propagation velocity with percentage of fat of -0.009%$°C^{-1}\ \%^{-1}$ (Figure 5-4). The data on the change in ultrasound propagation velocity per °C can be used either to determine the percentage of fat or the temperature in a fatty tissue. The slope in the line-of-best-fit from Figure 5-3 or Figure 5-4 provides the way of determining the change in temperature or percentage of fat in the fatty tissue sample. If the starting temperature and the percentage of fat in a tissue sample in known, then the change in temperature of a tissue sample can be determined using the gradient obtained from Figure 5-1. Alternately, if the change in temperature is known, the percentage of fat in tissue sample can be determined.

5.2.2 Electrical impedance

The analysis in section 5.1.3.2 showed that the temperature coefficients of the normalized impedances with the change of percentage of fat in the layered tissue samples. The correlation analysis between the temperature coefficients of the normalised impedances at

each measured frequency and the percentage of fat in the tissue samples gave very small correlation coefficient values which were not statistically significant (r^2 = 0.007, p >0.05). The value of r^2 and p value at each measured frequency are shown in Table 5-1. Therefore, no statistically significant correlation was found between the temperature coefficients of the normalized impedances at the measured frequencies and the temperature in the layered tissue samples.

Table 5-1 Showing the value of r^2 and p value from the correlation analysis between the temperature coefficients of the normalised impedances at each measured frequency and the percentage of fat in the tissue samples.

Frequency/kHz	p	r^2
1kHz:8kHz	0.93	6E-04
2kHz:8kHz	0.95	2E-04
4kHz:8kHz	0.84	0.003
Reference		
16kHz:8kHz	0.39	0.054
32kHz:8kHz	0.34	0.064
64kHz:8kHz	0.56	0.025
128kHz:8kHz	0.67	0.013
256kHz:8kHz	0.75	0.007
512kHz:8kHz	0.93	6E-04
1024kHz:8kHz	0.67	0.013

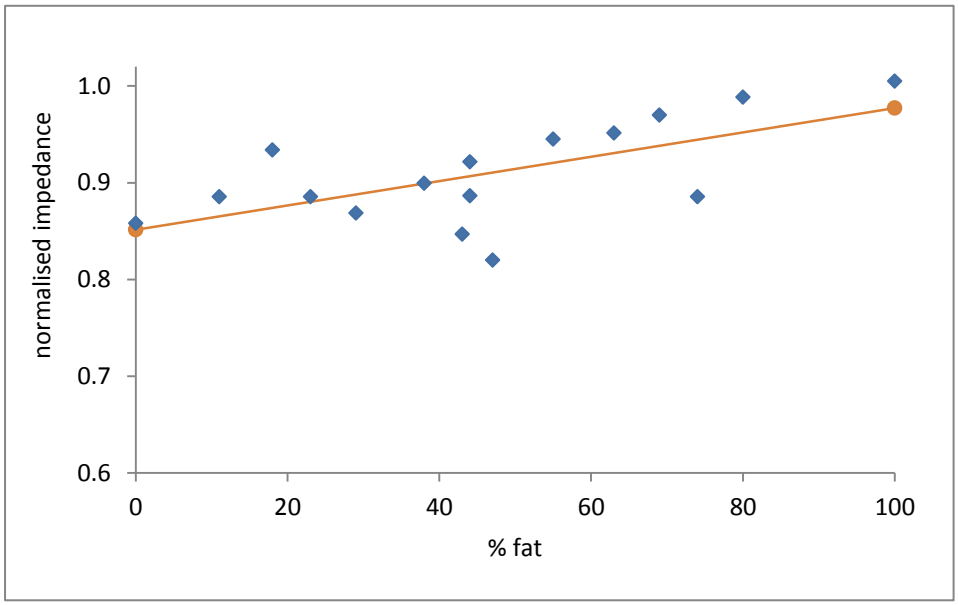

Figure 5-5 The averaged normalized impedances at the frequency ratio 64kHz to 8kHz over the measured temperatures with the change of percentage of fat in the layered fat-liver tissue samples.

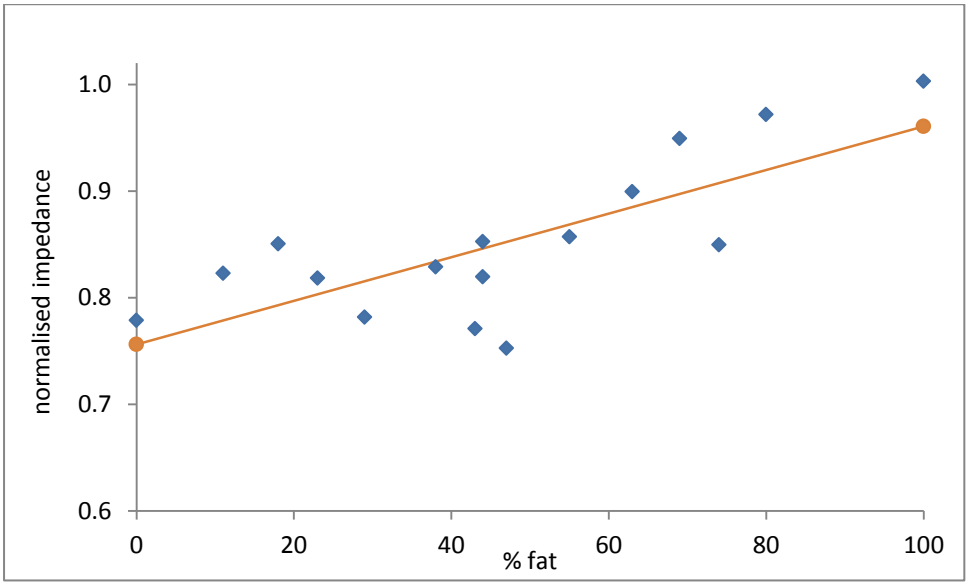

Figure 5-6 The averaged normalized impedances at the frequency ratio 128kHz to 8kHz over the measured temperatures with the change of percentage of fat in the layered fat-liver tissue samples.

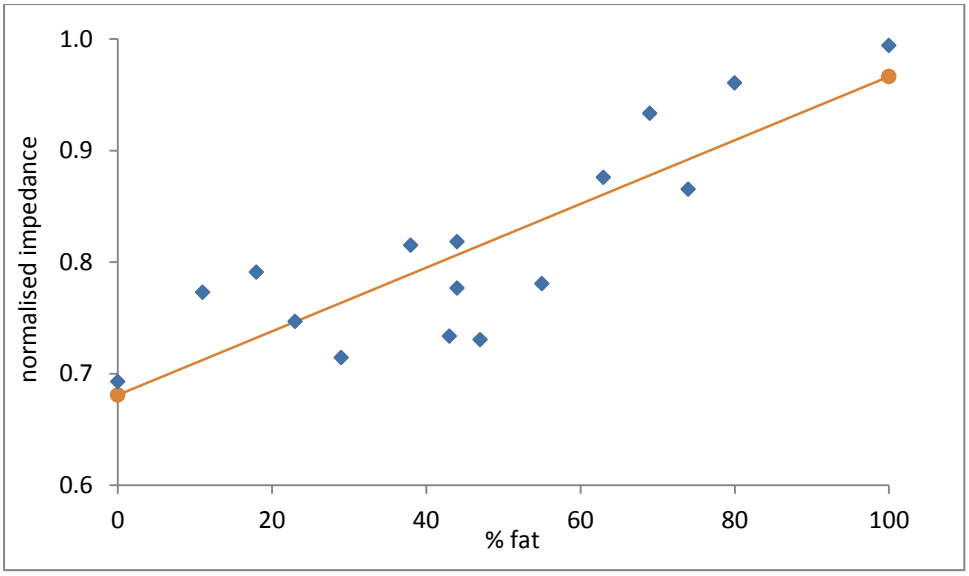

Figure 5-7 The averaged normalized impedances at the frequency ratio 256kHz to 8kHz over the measured temperatures with the change of percentage of fat in the layered fat-liver tissue samples.

It was shown in the previous chapter that the tetrapolar electrical impedance measurements on single tissues (section 4.1.3.2, chapter 4) could be normalized to reduce the temperature sensitivity up to measurement frequency of 512kHz. The Figure 5-5, Figure 5-6, and Figure 5-7 show the averaged normalized impedances over the measured temperature range (25°C– 45°C) at 64kHz, 128kHz, and 256kHz against the percentage of fat for the layered tissue measurements. The regression analysis showed that there was a positive linear relationship between the averaged normalized impedances at high frequency and the percentages of fat in the layered tissue samples. The value of correlation coefficient increases with increasing frequency (e.g. values of r^2 equal to 0.41, 0.56, and 0.72 at frequency 64kHz, 128kHz, and 256kHz respectively and the value of p less than 0.01 at all these frequencies). For completeness the value of r^2 and p value from the regression analysis between the averaged normalized impedances at each measured frequency and the percentage of fat in the layered tissue samples are shown in Table 5-2.

Table 5-2 Showing the values of r^2 and p from the correlation analysis between the averaged normalised impedances at each measured frequency and the percentage of fat in the tissue samples.

Frequency/kHz	p	r^2
1kHz:8kHz	0.766	0.007
2kHz:8kHz	0.31	0.073
4kHz:8kHz	0.091	0.191
Reference		
16kHz:8kHz	0.08	0.203
32kHz:8kHz	0.014	0.363
64kHz:8khz	0.007	0.413
128kHz:8kHz	7E-04	0.57
256kHz:8kHz	3E-05	0.72
512kHz:8kHz	3E-05	0.722
1024kHz:8kHz	7E-05	0.687

5.3 Discussion

5.3.1 Ultrasound

The ultrasound measurements on the layered fat-liver tissue samples demonstrated that the temperature coefficient for the ultrasound velocity varies linearly with the percentage of fat in the sample tissue. In samples having a very low percentage of fat, the ultrasound velocity increased with increasing temperature due to the positive temperature coefficients of ultrasound propagation velocity and in the samples with higher percentage of fat content, the ultrasound velocity decreased with increasing temperature due to negative temperature coefficients of ultrasound propagation velocity. Since the temperature coefficients of the ultrasound propagation velocity changes sign as the percentage of fat increases, there will be a tissue composition at which there is no change in ultrasound propagation velocity with temperature. The percentage of fat at which the temperature coefficients of ultrasound propagation velocity changes sign was around 10% (Figure 5-1) of fat which is much lower that the percentage of fat (18%) giving zero change in velocity with temperature found in solution of liquid fat (section 3.7.1.2, chapter 3). The difference in the percentage of fat at which zero change in ultrasound propagation velocity occurs may be due to the nature of the fat used. A solid form of fat containing a cellular structure was used in the layered tissue experiments whilst a liquid form of fat without a

defined cellular structure was used in the previous measurements (section 3.7.1.2, chapter 3).

The statistical analysis of the ultrasound data from the layered tissue measurements showed a linear correlation between the percentage of fat content in the sample and the ultrasound propagation velocity at all the measured temperatures. This finding is in agreement with the findings of Shannon and co-workers (Shannon *et al.*, 2004), who proposed a weighted sum model of tissue constituents for determining the propagation velocity and experimentally showed a linear correlation between ultrasound propagation velocity and the lipid content of salmon muscle. The findings of the ultrasound measurements on layered tissue samples are also in agreement with the assumptions made by Miller and co-workers (Miller *et al.*, 2004), who modelled the effects of fat content on the ultrasound propagation velocity of fatty liver containing 3.6%, 15.5%, and 27.4% of fat. Their finding (Miller *et al.*, 2004) about the negligible change in ultrasound propagation velocity with temperature in fatty liver tissue containing intermediate fat content (15.5% fat) is also in broad agreement with the finding of this work about the intersection percentage of fat at which the temperature coefficients of ultrasound propagation velocity changes sign. The propagation velocity of ultrasound in soft tissues is determined at the molecular level and thought to be independent of cellular or higher level structures (Bamber, 2007). The temperature dependence of the correlation coefficients obtained for the ultrasound propagation velocity against percentage of fat (r^2 = 0.56 at 25^{o}C to r^2 = 0.91 at 45^{o}C) in this research whilst being considerably better than that obtained by Shannon and co-workers (Shannon *et al.*, 2004) on salmon muscle (r^2 = 0.53 above 30^{o}C) support a view that multiple factors are responsible for determining the change in propagation velocity with temperature, some of which are tissue structure or fluid content dependant. There is a large difference in scattering coefficients between the liver and fat tissue and the scattering coefficient in fatty tissue (fatty scatterers) is strongly temperature dependent (Bamber, 1997). Moreover, changes in scattered energy with temperature also occur at tissue interfaces (Arthur *et al.*, 2005). Therefore, whilst tissue interfaces affect the energy of the reflected signal, they have little impact on the speed of propagation. Thus, number or arrangement of layers within the samples used within this project will have minimal impact on the propagation velocity and hence on the results reported in this thesis.

There was a good correlation between the percentage change of ultrasound propagation velocity per °C and the percentage of fat in the layered tissue samples (r^2 = 0.93). However, there is a large variation in ultrasound propagation velocities among the individual ultrasound measurement on the sample layered tissues (Figure 5-2), differences which may be due to the natural variation in the tissue itself (Shannon *et al.*, 2004). However, it is also possible that the large variation in ultrasound propagation velocity in different percentage of fat samples may be caused by the natural variation of the fat and liver tissue structure (Bamber, 2004; Shannon *et al.*, 2004).

It should be noted that in the layered tissue experiments, the measurements for a certain percentage of fat in the sample tissue could not be repeated for multiples times to establish reproducibility in a similar way to the single tissue measurements on fat and liver tissue. Due to the nature of the layered liver and fat samples, it was not always possible to accurately reproduce the percentage of fat in the different samples. However, in the layered tissue experiments the reproducibility was maintained based on the number of fat and liver layers in each sample used for the experiments.

5.3.2 Electrical Impedance

The aim of the multi-frequency electrical impedance measurements on layered samples of fat and liver tissue was to characterise the percentage of fat in the tissue as well as part of estimating the temperature during mild hyperthermia. Since there was a large variation in the magnitude of impedance among tissue samples, the approach of using normalized electrical impedance was used to determine the percentage of fat. However, a good correlation between the normalized impedance and the percentage of fat in the sample is required to use the measurement predictively. Of the frequencies examined, the normalized value at 64kHz, 128kHz, and 256kHz gave a statistically significant correlation coefficient (r^2 equal to 0.41, 0.56 and 0.72 at 64kHz, 128kHz, and 256kHz respectively and $p < 0.01$ at these frequencies). It is quite reasonable to use the largest r^2 value of the normalized impedance at 256kHz to determine the percentage of fat (0.003 $\%^{-1}$, r^2 = 0.72). However, the correlation between the normalized impedance and the percentage of fat is not as strong as that might have been expected. This may be due to one of the underlying problems with the tetrapolar impedance measurement technique: that of a complex sensitivity distribution coupled with regions of negative sensitivity between the drive and receive electrodes (Islam *et al.*, 2010; Brown *et al.*, 2000b). It was previously shown (section 2.2.3.2 in chapter 2; published in (Islam *et al.*, 2010)) that the sensitivity

distribution can be improved through summing multiple measurements made using different combinations of electrodes over the region of interest (Rabbani and Karal, 2008).

6 Conclusions and suggestions for further work

6.1 Key findings

The work presented in this thesis has investigated the potential for determining the temperature in a deep body solid tumour during mild hyperthermia by combining the ultrasound propagation velocity and electrical impedance measurement techniques. Previous studies in this area have considered the use of ultrasound propagation velocity (e.g.(Seip and Ebbini, 1995; Miller *et al.*, 2002; Arthur *et al.*, 2005; Maass-Moreno and Damianou, 1996)) and electrical impedance (e.g. (Esrick and McRae, 1994; Gersing, 1999; Paulsen *et al.*, 1994)) independently as the potential methods for determining the temperature of deep body tissue during hyperthermia treatment. This is the first time two different measures have been combined to produce a potential new measurement technique to address the long standing problem of determining deep body tissue temperature during hyperthermia. The focus of this work was the mild hyperthermia temperature and the key findings are:

- that the ultrasound propagation velocity for fat and liver tissues vary linearly with temperature but there is a large variability in the temperature coefficient between samples;
- that the change in ultrasound propagation velocity with temperature of simulated fatty liver tissue varies linearly with the percentage of fat in the sample;
- that the magnitude of the electrical impedance of simulated fatty liver tissue measured at 256kHz ($|Z_{256kHz}|$) normalised to the magnitude of measurement at 8kHz ($|Z_{8kHz}|$) varies linearly with the percentage of fat in the tissue sample and that the normalised impedance value is independent of temperature; and
- that the determination of fat content of the sample through an electrical impedance measurement will allow determination of the temperature change through an ultrasound propagation velocity measurement.

The major problem with the application of the results of this work to determine the temperature of a tissue sample is the intra-sample variability of the temperature coefficient of the individual tissue samples. A second problem with the application of the technique to tissue samples lies with the spatial sensitivity of the tetrapolar electrical measurements. The proposed improvement in the spatial sensitivity through using the FIM technique (Rabbani *et al.*, 1999; Rabbani and Karal, 2008) has been quantified in this work

through simulation. However, it still does not allow the measurement of the electrical impedance of a localised region deep within a large volume of tissue.

6.2 Discussion

One of the problems of investigating the techniques for non-invasive temperature measurement is having an experimental procedure from which reproducible results can be obtained as the measurement techniques are developed. Essentially, this means having test samples with reproducible properties. Whilst those working with a simple measurement technique have identified inorganic materials (e.g. the use of rubber for ultrasound measurement (Seip and Ebbini, 1995)); there was no obvious inorganic material that could be used in the current work that would mirror both the electrical impedance and ultrasound properties of tissue. Therefore, an experimental system was devised that enabled reproducible measurement to be made on excised tissue samples. Initially, the accuracy and precision of the ultrasound propagation velocity and electrical impedance measurements made on this measurement system were determined by using samples of materials with known properties e.g. water, saline, oil for the ultrasound measurement system, and, in addition, resistive and resistive-capacitive phantoms for the electrical impedance measurement system (section 3.7.1 and 3.7.2, chapter 3).

The ultrasound propagation velocity is reported to be determined at the molecular level (Bamber, 1997) and the electrical impedance properties are dependent on the ion concentration of the intra- and extra-cellular fluids. Therefore, the effect of ion concentration on the ultrasound propagation velocity was investigated (section 3.7.1.1, chapter 3). The results showed that the change in the ultrasound propagation velocity with temperature was independent of ion concentration for ion concentration in the physiological range.

The liver has long been a potential target for high intensity focused ultrasound (HIFU) treatments partly as result of its anatomical position, size and consistent structure and partly because liver metastases are difficult to treat by other techniques. As a result, considerable work has been done on non-invasive temperature determination in the liver (e.g.(Miller *et al.*, 2002)). Therefore, liver was used as the tissue to be studied in the work described in this thesis. Liver also contains fatty deposits (Miller *et al.*, 2002) and therefore fat was chosen as the second tissue to be used in this work. Liver and fat from the lamb were used in all experimental works involving tissue. Both the ultrasound propagation velocity and electrical impedance measurements were made on liver (section 4.1, chapter

4) and fat (section 4.2, chapter 4) samples as the temperature was raised above the upper limit of the mild hyperthermia range (50°C). Measurements were also made on the layered fat-liver tissue samples prepared from the combination of thin slices of fat and liver tissue from lambs (chapter 5). In the layered tissue experiments, the upper limit for the temperature rise was set to 45°C, the upper limit of the mild hyperthermia range; because evidence from the single tissue measurement showed that structural change to the liver tissue occurred above this temperature (section 4.1.3, chapter 4). From the layered tissue measurements a good correlation was obtained between the percentage of fat in the sample and the change in ultrasound propagation velocity at different temperatures which supports the hypothesis that a combination of ultrasound propagation velocity and electrical impedance has the potential to measure deep body temperature if the percentage of fat in the sample can be determined from electrical impedance measurements.

From the ultrasound measurements, it was shown that basal ultrasound propagation velocity was very variable between samples, but that the change in propagation velocity per °C was reproducible and therefore this could be used to determine the temperature in liver tissue in a non-invasive way if the fat content was known. The ultrasound propagation velocity measurements confirmed that the biological tissues have both positive and negative temperature coefficients of ultrasound propagation velocity depending on the composition of the tissue (Bamber, 1997). Moreover, it was also found that there are some tissue compositions which have temperature coefficients of ultrasound propagation velocity close to zero resulting in a negligible change in ultrasound propagation velocity as a function of temperature. These findings are consistent with view that water, the main constituent of soft tissue is mainly responsible for the positive temperature coefficients of ultrasound propagation velocity in liver tissue whilst fat has a negative temperature coefficient due to its main structural component which is fatty acids (Miller *et al.*, 2004; Shannon *et al.*, 2004). The cancellation of the positive and negative temperature coefficients of ultrasound propagation velocity results in a negligible change in propagation velocity change with temperature in a soft tissue having intermediate percentage of fat (Miller and Bamber, 2004). It is noted that the definition of intermediate fat content tissue that has a negligible temperature coefficients of ultrasound propagation velocity varies in literature (Miller *et al.*, 2002; Phinney *et al.*, 1994; Thorne *et al.*, 2010; Bozkurt *et al.*, 2012). As for example, Miller and co-workers (Miller *et al.*, 2002) termed the fatty liver tissue having 15.5% of fat as the intermediate fat content tissue, Phinney and co-workers

(Phinney *et al.*, 1994) considered the fatty liver with fat in the range of 6 –14% as the intermediate fat content. However, this depends on the nature of the fat and in this research for solid fat, 10% was found to give no change in propagation velocity with temperature (section 5.3.1, chapter 5) whilst for liquid fat, 18% was found to give no change in propagation velocity with temperature (section 3.7.1.2.3, chapter 3). It was impossible to produce layered tissue samples with a reproducible level of fat (section 5.3.1, chapter 5); therefore, the definition of intermediate fat content based on this work lies in the range 10 – 18%.

From the multi-frequency electrical impedance measurements, the temperature coefficients were determined for both the single and layered tissue samples. However, it was found that there was no statistical difference in the average temperature coefficients between fat and liver tissue in the mild hyperthermia temperature range. Furthermore, it was found that the values for the temperature coefficient of the impedance obtained from the fat, liver and layered fat-liver measurements were consistent with that of physiological saline (-2% $°C^{-1}$,(Duck, 1990)). Whilst there was no statistical difference in the average temperature coefficients measured across all frequencies, there was a difference in the temperature coefficients for fat and liver at individual frequencies and therefore, this limits the ability to predict temperature from electrical impedance measurements in fatty tissues. No simple relationship was found between fat content and the temperature coefficient for electrical impedance (section 5.2.2, chapter 5).

An approach of using the normalized impedance spectra to characterise the amount of fat in tissue is proposed in this research. It was shown that normalisation of the impedance data to a single frequency reduced the temperature sensitivity and that normalised impedances are independent of temperature up to frequency 512kHz (section 4.3.2, chapter 4). The temperature independence of the normalised impedances supports the approach of using normalised impedances at high frequency to detect the percentage of fat in tissue. However, in order to do this a good correlation between the percentage of fat in tissue and the normalised impedances were required and of the frequencies examined the normalized value at 256kHz gave the best correlation coefficient ($r^2 = 0.72$, $p = 0.03$).

6.3 Suggestions for further work

In this research a new method for non-invasive determination of temperature in a deep body solid tumour during mild hyperthermia has been investigated by combining ultrasound propagation velocity and electrical impedance measurement techniques. The key area where further work is required is to understand the origin of the variability in the temperature coefficient of ultrasound propagation velocity between tissue samples. Once an understanding of this variability is achieved, new measurement technique can be investigated to minimise it. In terms of the measurements made in this thesis, further work is required on the signal processing of the reflected ultrasound signal to improve reflection detection. The key work required on the tetrapolar impedance measurement technique is the development of a technique for localising the measurement to a specific region within a large volume of tissue. Electrical impedance imaging has failed to provide adequate spatial resolution or measurement accuracy and therefore the use of a chemical contrast agent or nano-particles that can be constrained to a specific tissue region should be considered.

7 References

Adler A, Arnold J H, Bayford R, Borsic A, Brown B, Dixon P, Faes T J C, Frerichs I, Gagnon H, Gärber Y, Grychtol B, Hahn G, Lionheart W R B, Malik A, Patterson R P, Stocks J, Tizzard A, Weiler N and Wolf G K 2009 GREIT: a unified approach to 2D linear EIT reconstruction of lung images *Physiological Measurement* **30** S35

Aisenberg A C 1961 *The glycolysis and Respiration of Tumours* (New York: Academic Press, Inc.)

Aitkenhead A H 2008 The use of Ultrasound to create Tissue Hyperthermia to support the Treatment of Cancer *Dostoral thesis, Departement of Physics, University of Warwick*

Aitkenhead A H, Mills J A and Wilson A J 2008 The Design and Characterization of an Ultrasound Phased Array Suitable for Deep Tissue Hyperthermia *Ultrasound in Medicine & Biology* **34** 1793-807

Algan Ö, Fosmire H, Hynynen K, Dalkin B, Cui H, Drach G, Stea B and Cassady J R 2000 External beam radiotherapy and hyperthermia in the treatment of patients with locally advanced prostate carcinoma *Cancer* **89** 399-403

Angula P 2002 Nonalcoholic fatty liver disease *N Eng J Med* **346** 1221-31

Arthur R M, Straube W L, Trobaugh J W and Moros E G 2005 Non-invasive estimation of hyperthermia temperatures with ultrasound *International journal of hyperthermia : the official journal of European Society for Hyperthermic Oncology, North American Hyperthermia Group* **21** 589-600

Atanackovic D, Pollok K, Faltz C, Boeters I, Jung R, Nierhaus A, Braumann K M, Hossfeld D K and Hegewisch-Becker S 2006 Patients with solid tumours treated with high-temperature whole body hyperthermia show a redistribution of naive/memory T-cell subtypes *Am J Physiol Regul Integr Comp Physiol* **290** 27

Bamber J C 1997 *Acoustical characateristics of biological media* (New York: Wiley and Sons)

Bamber J C 2004 *Physical Principles of Medical Ultrasonics,* ed Hill C R, Bamber J C, ter Haar G R (West Sussex, England: John Wiley & Sons, Ltd) p 180

Bamber J C 2007 *Encyclopedia of Acoustics* ed Crocker M J (John Wiley & Sons, Inc.) pp 1703-26

Bamber J C, Hill C R and King J A 1981 Acoustic properties of normal and cancerous human liver—II Dependence on tissue structure *Ultrasound in medicine & biology* **7** 135-44

Barber D C and Brown B H 1984 Applied Potential Tomography *J. Phys. E. Sci. Instrum.* **17** 723-34

Barber D C and Brown B H 1986 Recent developments in applied potential tomography-apt *Information Processing in Medical Imaging ed S L Bacharch* 106-21

Baronozio G F and Hager E D eds 2006 *Hyperthermia in cancer treatment: A primer, chapter 22 - Future perspectives of interstitial and perfusional hyperthermia*: SpringerLink 338-360

Beaney R P, Jones T, Lammertsma A A, McKenzie C G and Halnan K E 1984 Positron Emission Tomography for in-vivo measurement of regional blood flow, oxygen utilisation, and blood volume in patients with breast carcinoma *The Lancet* **323** 131-4

Bendz H, Ruhland S C, Pandya M J, Hainzl O, Riegelsberger S, Brauchle C, Mayer M P, Buchner J, Issels R D and Noessner E 2007 Human heat shock protein 70 enhances tumour antigen presentation through complex formation and intra-cellular antigen delivery without innate immune signaling *J Biol Chem* **282** 31688-702

Bernestein C A and Casadio T E 1996 Integral geometry in hyperbolic spaces and electrical impedance tomography *SIAM J. Appl. Math.* **56** 755-64

Bertemes-Filho P, Brown B H, Smallwood R H and Wilson A J 2003 Stand-off electrode (SoE): a new method of improving the sensitivity distribution of a tetrapolar probe *Physiol. Meas.* **24** 517-25

Bertemes-Filho P, Brown B H and Wilson A J 2000 A comparison of modified Howland circuits as current generators with current mirror type circuits *Physiological Measurement* **21** 1-7

Bertsch F, Mattner J, Stehling M K, Müller-Lisse U, Peller M, Loeffler R, Weber J, Messmer K, Wilmanns W, Issels R and Reiser M 1998 Non-invasive temperature mapping using MRI: comparison of two methods based on chemical shift and T1-relaxation *Magn Reson Imaging.* **16** 393-404

Bicher H I and Wolfstein R S 1990a Clinical use of regional hyperthermia *Adv Exp Med Biol.* **267** 1-20

Bicher H I and Wolfstein R S 1990b Local hyperthermia for superficial and moderately deep tumours– factors affecting response *Adv Exp Med Biol.* **267** 353-67

Bicher H I and Wolfstein R S 2006 Thermoradiotherapy with curative intent- Breast,Head and Neck and Prostate tumours *German Journal of Oncology, (Deutsche Zeitschrift für Onkologie)* **38** 116-22

Blazickova S, Rovensky J, Koska J and Vigas M 2000 Effect of hyperthermic water bath on parameters of cellular immunity *Int J Clin Pharmacol Res* **20** 41-6

Bleier A R, Jolesz F A, Cohen M S, Weisskoff R M, Dalcanton J J, Higuchi N, Feinberg D A, Rosen B R, McKinstry R C and Hushek S G 1991 Real-time magnetic resonance imaging of laser heat deposition in tissue *Magn Reson Med* **21** 132-7

Bleifuss E, Bendz H, Sirch B, Thompson S, Brandl A, Milani V, Graner M W, Drexler I, Kuppner M, Katsanis E, Noessner E and Issels R 2008 Differential capacity of chaperone-rich lysates in cross-presenting human endogenous and exogenous melanoma differentiation antigens *International Journal of Hyperthermia* **24** 623-37

Bloembergen N, Purcell E M and Pound R V 1948 Relaxation Effects in Nuclear Magnetic Resonance Absorption *Physical Review* **73**

Borcea L 2001 Nonlinear multigrid for imaging electrical conductivity and permittivity at low frequency *Inverse prob.* **17** 329-59

Borcea L, Berryman J G and Papanicolaou G C 1996 High-contrast impedance tomography *Inverse Problems* **12**

Bozkurt L, Göbl C S, Tura A, Chmelik M, Prikoszovich T, Kosi L, Wagner O, Roden M, Pacini G, Gastaldelli A and Kautzky-Willer A 2012 Fatty Liver Index Predicts Further Metabolic Deteriorations in Women with Previous Gestational Diabetes *PLoS ONE* **7** e32710

Bracewell R 1999 *The Fourier Transform and Its Applications* (New York: McGraw-Hill)

Brown B H, Barber D C, Wang W, Lu L, Leathard A D, Smallwood R H, Hampshire A R, Mackay R and Hatzigalanis K 1994 Multi-frequency imaging and modelling of respiratory related electrical impedance changes *Physiological Measurement* **15** A1-A12

Brown B H, Tidy J A, Karen B, Blackett A D, Smallwood R H and Frank S 2000a Relation between tissue structure and imposed electrical current flow in cervical neoplasia *The Lancet* **355** 892-5

Brown B H, Wilson A J and Bertemes-Filho P 2000b Bipolar and tetrapolar transfer impedance measurements from volume conductor *Electronics Letters* **36** 2060-2

Burd R, Dziedzic T S, Xu Y, Caligiuri M A, Subjeck J R and Repasky E A 1998 Tumour cell apoptosis, lymphocyte recruitment and tumour vascular changes are induced by low temperature, long duration (fever-like) whole body hyperthermia *Journal of Cellular Physiology* **177** 137-47

Cain C A and Umemura S 1986 Concentric-Ring and Sector-Vortex Phased-Array Applicators for Ultrasound Hyperthermia *Microwave Theory and Techniques, IEEE Transactions on* **34** 542-51

Calderwood S K and Ciocca D R 2008 Heat shock proteins: Stress proteins with Janus-like properties in cancer *International Journal of Hyperthermia* **24** 31-9

Calderwood S K, Theriault J R and Gong J 2005 How is the immune response affected by hyperthermia and heat shock proteins? *Int J Hyperthermia* **21** 713-6

Cheever E A and Foster K R 1992 Microwave radiometry in living tissue: what does it measure? *IEEE Trans Biomed Eng* **39** 563-8

Chen Q, Appenheimer M M, Muhitch J B, Fisher D T, Clancy K A, Miecznikowski J C, Wang W C and Evans S S 2009 Thermal facilitation of lymphocyte trafficking involves temporal induction of intravascular ICAM-1 *Microcirculation* **16** 143-58

Chen Q, Fisher D T, Clancy K A, Gauguet J M, Wang W, Unger E, Rose-John S, von Andrian U H, Baumann H and Evans S S 2006 Fever-range thermal stress promotes lymphocyte trafficking across high endothelial venules via an interleukin 6 trans-signaling mechanism *Nature Immunology* **7** 1299-308

Cheney M, Isaacson D, Newell J C, Simske S and Goble J 1990 NOSER: An algorithm for solving the inverse conductivity problem *International Journal of Imaging Systems and Technology* **2** 66-75

Cole K S and Cole R H 1941 Dispersion and absorption in dielectrics *J. Chem. Phys.* **9** 341-51

Coley W B 1991 The Classic: The Treatment of Malignant Tumours by Repeated Inoculations of Erysipelas: With a Report of Ten Original Cases *Clinical Orthopaedics and Related Research* **262** 3-11

Constable R T, Dunscombe P, Tsoukatos A and Malaker K 1987 Perturbation of the temperature distribution in microwave irradiated tissue due to the presence of metallic thermometers *Med Phys* **14** 385-8

Conway J 1987 Electrical impedance tomography for thermal monitoring of hyperthermia treatment: an assessment using in vitro and in vivo measurements *Clin. Phys. Physiol. Meas.* **8** 141-6

Conway J, Hawley M S, Seagar A D, Brown B H and Barber D C 1985 Applied potential tomography (APT) for noninvasive thermal imaging during hyperthermia treatment *Electronics Letters* **21** 836-8

Coolidge A S and Bent H E 1936 The Conductance of Non-Aqueous Solutions. II. The Temperature Coefficient of Conductivity *Journal of the American Chemical Society* **58** 505-6

Curley S A 2001 radio frequency ablation of malignant liver tumours *The Oncologist* **6** 14-23

Damianou C A, Sanghvi N T, Fry F J and Maass-Moreno R 1997 Dependence of ultrasonic attenuation and absorption in dog soft tissues on temperature and thermal dose *J Acoust Soc Am* **102** 628-34

Daum D R and Hynynen K 1999 A 256-element ultrasonic phased array system for the treatment of large volumes of deep seated tissue *Ultrasonics, Ferroelectrics and Frequency Control, IEEE Transactions on* **46** 1254 -68

Dayanc B E, Beachy S H, Ostberg J R and Repasky E A 2008 Dissecting the role of hyperthermia in natural killer cell mediated anti-tumour responses *International Journal of Hyperthermia* **24** 41-56

De Bree J, Lagendijk J J, Raaymakers B W, Bakker C J, Hulshof M C, Koot R W, Hanlo P W, Struikmans H, Ramos L M and Battermann J J 1998 Treatment planning of brain implants using vascular information and a new template technique *IEEE Trans Med Imaging* **17** 729-36

De Poorter J, De Wagter C, De Deene Y, Thomsen C, Stahlberg F and Achten E 1995 Noninvasive MRI thermometry with the proton resonance frequency (PRF) method: in vivo results in human muscle *Magn Reson Med* **33** 74-81

de Wit R, van der Zee J, van der Burg M E, Kruit W H, Logmans A, van Rhoon G C and Verweij J 1999 A phase I/II study of combined weekly systemic cisplatin and locoregional hyperthermia in patients with previously irradiated recurrent carcinoma of the uterine cervix *Br J Cancer.* **80** 1387-91

Deardorff D L and Diederich C J 2000 Ultrasound applicators with internal water-cooling for high-powered interstitial thermal therapy *IEEE Trans Biomed Eng.* **47** 1356-65

Debicki P S, Okoniewski M, Okoniewska E, Shrivastava P N, Debicka A M, Baert L V and Petrovich Z 1995 Cooled microwave transrectal applicator with adjustable directional beam for prostate treatment *Int J Hyperthermia* **11** 95-108

Dewhirst M W, Viglianti B L, Lora-Michiels M, Hanson M and Hoopes P J 2003 Basic principles of thermal dosimetry and thermal thresholds for tissue damage from hyperthermia *Int J Hyperthermia* **19** 267-94

Diederich C J 1996 Ultrasound applicators with integrated catheter-cooling for interstitial hyperthermia: theory and preliminary experiments *Int J Hyperthermia* **12** 279-97

Diederich C J and Hynynen K 1990 The development of intracavitary ultrasonic applicators for hyperthermia: A design and experimental study *Medical Physics* **17**

Diederich J and Hnynen K 1989 Induction of Hyperthermia Using an Intracavitary Multielement Ultrasonic Applicator *IEEE Transaction on biomedical engineering, IEE Proc. Sci. Meas. Technol* **36**

Dobson D C and Santosa F 1994 An image-enhancement technique for electrical impedance tomography *Inverse Problems* **10** 317-35

Duck F A 1990 *Physical properties of tissue : a comprehensive reference book* (London; San Diego: Academic Press)

Dudar T E and Jain R K 1984 Differential Response of Normal and Tumour Microcirculation to Hyperthermia *Cancer Research* **44** 605-12

Dunscombe P B, Cetas C T, Connor G W, Douple E B, Hetzel F W, Lee K W, Loshek D, Nussbaun H G, Roemer R, Saylor K T, Strobehn W J and Waterman M F 1989 Hyperthermia Treatment Planning *AAPM Report* **27** 1-57

Dunscombe P B, Constable R T and McLellan J 1988 Minimizing the self-heating artefacts due to the microwave irradiation of thermocouples *Int J Hyperthermia* **4** 437-45

Edrich J, Jobe W E, Cacak R K, Hendee W R, Smyth C J, Gautherie M, Gros C, Zimmer R, Robert J, Thouvenot P, Escanye J M and Itty C 1980 Imaging thermograms at centimeter and millimeter wavelengths *Ann N Y Acad Sci* **335** 456-74

El-Sharkawy A M, Schar M, Bottomley P A and Atalar E 2006 Monitoring and correcting spatio-temporal variations of the MR scanner's static magnetic field *Magma* **19** 223-36

Engler M, Dewhirst M W, Winget J M and Oleson J R 1987 Automated temperature scanning for hyperthermia treatment monitoring *Int J Radiat Oncol Biol Phys* **13** 1377-82

Esrick M A and McRae D A 1994 The effect of hyperthermia-induced tissue conductivity changes on electrical impedance temperature mapping *Phys Med Biol.* **39** 133-44

Evans S S, Wang W, Bain M D, Burd R, Ostberg J R and Repasky E A 2001 Fever-range hyperthermia dynamically regulates lymphocyte delivery to high endothelial venules *Blood* **97** 2727-33

Fajardo L F 1984 Pathological effects of hyperthermia in normal tissues *Cancer Res* **44** 4826s-35s

Fessenden P, Lee E R and Samulski T V 1984 Direct temperature measurement *Cancer Res* **44** 4799s-804s

Fjield T, Fan X and Hynynen K 1996 A parametric study of the concentric-ring transducer design for MRI guided ultrasound surgery *J. Acoust. Soc. Am.* **100** 1220-30

Fossheim S L, Il'yasov K A, Hennig J and Bjornerud A 2000 Thermosensitive paramagnetic liposomes for temperature control during MR imaging-guided hyperthermia: in vitro feasibility studies *Acad Radiol* **7** 1107-15

Foster K R and Cheever E A 1992 Microwave radiometry in biomedicine: A reappraisal *Bioelectromagnetics* **13** 567-79

Gavrilov L R and Hand J W 2000 A theoretical assessment of the relative performance of spherical phased arrays for ultrasound surgery *IEEE Trans Ultrason Ferroelectr Freq Control* **47** 125-39

Gellermann J, Weihrauch M, Cho C H, Wlodarczyk W, Fähling H, Felix R, Budach V, Weiser M, Nadobny J and Wust P 2006 Comparison of MR-thermography and planning calculations in phantoms *Med Phys.* **33** 3912-20

Gellermann J, Wlodarczyk W, Ganter H, Nadobny J, Fähling H, Seebass M, Felix R and Wust P 2005 A practical approach to thermography in a hyperthermia/magnetic resonance hybrid system: Validation in a heterogeneous phantom *International journal of radiation oncology, biology, physics* **61** 267-77

Gerad H, van Echo D A, Whitacre M, Ashman M, Helrich M, Foy J, Ostrow S, Wiernik P H and Aisner J 1984 Doxorubicin, cyclophosphamide, and whole body hyperthermia for treatment of advanced soft tissue sarcoma *Cancer* **53** 2585-91

Germain D, Vahala E, Ehnholm G J, Vaara T, Ylihautala M, Savart M, Laurent A, Tanttu J and Saint-Jalmes H 2002 MR temperature measurement in liver tissue at 0.23 T with a steady-state free precession sequence *Magnetic Resonance in Medicine* **47** 940-7

Gersing E 1999 Monitoring Temperature-Induced Changes in Tissue during Hyperthermia by Impedance Methods *Annals of the New York Academy of Sciences* **873** 13-20

Gersing E, Kruger W, Osypka M and Vaupel P 1995 Problems involved in temperature measurements using EIT *Physiol Meas* **16** A153-60

Gerweck L E 1977 Modification of Cell Lethality at Elevated Temperatures The pH Effect *Radiation Research* **70** 224-35

Gerweck L E 1985 Hyperthermia in cancer therapy: the biological basis and unresolved questions *Cancer Research* **45** 3408-14

Gerweck L E, Dahlberg W K, Epstein L F and Shimm D S 1984 Influence of Nutrient and Energy Deprivation on Cellular Response to Single and Fractionated Heat Treatments *Radiation Research* **99** 573-81

Geselowitz D B 1971 An application of electrocardiographic lead theory to impedance plethysmography *IEEE Trans. Biomed. Eng.* **18** 38-41

Gibbs F A 1983 Thermal mapping in experimental cancer treatment with hyperthermia *Int. J. Radiat. Onc. Biol. Phys.* **9** 1057-63

Globe J 1990 The three-dimensional inverse problem in electric current computed tomography *PhD thesis, Rensselaer Plytechnic Institute, NY, USA*

Godik E E and Gulyaev Y V 1991 Functional imaging of the human body *IEEE Eng Med Biol Mag* **10** 21-9

Goff H D and Hill A R 1993 *Dairy Science and Technology Handbook, Vol. 1, Principles and Properties,* ed Y H Hu (New York: VCH Publishers) pp 1-81

Goldhaber D M, Deli M, Mineyev M I, Gronemeyer D H W, Kramer D M, Avram H E, Seibel R M M and Kaufman L 1993 Measurement of Tissue Temperature by MRI *Nuclear Science Symposium and Medical Imaging Conference, 1993., 1993 IEEE Conference Record.* **3** 1702-5

González-Correa C A, Brown B H, Smallwood R H, Kalia N, Stoddard C J, Stephenson T J, Haggie S J, Slater D N, Bardhan K D 1999 Virtual biopsies in Barrett's esophagus using an impedance probe *Ann N Y Acad Sci.* **873** 313-21

Graham B M and Adler A 2007 Electrode placement configurations for 3D EIT *Physiol Meas.* **28** S29-44

Grimnes S and Martinsen Ø G 2000 *Bioimpedance and bioelectricity basics (*Academic Press)

Gustov A V and Troitsky V S 1985 Investigation of cranio-cerebral temperature with microwave radiometry *Human physiology* **11** 151-4

Habash R W, Bansal R, Krewski D and Alhafid H T 2006 Thermal therapy, part 1: an introduction to thermal therapy *Crit Rev Biomed Eng.* **34** 459-89

Hacker A, Kohrmann K U, Back W, Kraut O, Marlinghaus E, Alken P and Michel M S 2005 Extracorporeal application of high-intensity focused ultrasound for prostatic tissue ablation *BJU Int* **96** 71-6

Han J W, van Leeuwen G M, Mizushina S, van de Kamer J B, Maruyama K, Sugiura T, Azzopardi D V and Edwards A D 2001 Monitoring of deep brain temperature in infants using multi-frequency microwave radiometry and thermal modelling *Phys Med Biol* **46** 1885-903

Hand J W, Shaw A, Sadhoo N, Rajagopal S, Dickinson R J and Gavrilov L R 2009 A random phased array device for delivery of high intensity focused ultrasound *Phys Med Biol* **54** 5675-93

Hedrick W R, Hykes D L and Starchman D E 1995 *Ultrasound physics and instrumentation : practice examinations* (St. Lois [u.a.]: Mosby)

Hekmatyar S K, Kerkhoff R M, Pakin S K, Hopewell P and Bansal N 2005 Noninvasive thermometry using hyperfine-shifted MR signals from paramagnetic lanthanide complexes *Int J Hyperthermia* **21** 561-74

Hildebrandt B, Hegewisch-Becker S, Kerner T, Nierhaus A, Bakhshandeh-Bath A, Janni W, Zumschlinge R, Sommer H, Riess H and Wust P 2005 Current status of radiant whole-body hyperthermai at temperatures > 41.5 C and practical guidelines for treatmetn of adults. The German 'Interdiscipinary working Group on Hyperthermia' *Int J of Hyperthermia* **21** 169-83

Hildebrandt B and Wust P 2007 *Peritoneal Carcinomatosis,* ed W Ceelen (Springer US) pp 171-84

Hildebrandt B, Wust P, Ahlers O, Dieing A, Sreenivasa G, Kerner T E, Felix R and Riess H 2002 The cellular and molecular basis of hyperthermia *Critical reviews in oncology/hematology* **43** 33-56

Hill C R, Bamber J C and ter Haar G R 2004 eds *Physical Principle of medical ultrasonics (* John Wiley & Sons), pp 167-186

Hindman J C 1966 Proton Resonance Shift of Water in the Gas and Liquid States *J. Chem. Phys.* **44** 4582-93

Horseman P R, Law D J, Dunscombe P B, Gammampila K and Southcott B M 1983 A microcomputer-based multithermocouple system for use in microwave fields *J Med Eng Technol* **7** 96-100

Hu Z, Yang X Y, Liu Y, Sankin G N, Pua E C, Morse M A, Lyerly H K, Clay T M and Zhong P 2007 Investigation of HIFU-induced anti-tumour immunity in a murine tumour model *Journal of translational medicine* **5** 34

Hynynen K 1992 The feasibility of interstitial ultrasound hyperthermia *Med Phys* **19** 979-87

Hynynen K, Colucci V, Chung A, and Jolesz F 1996 Noninvasive arterial occlusion using MRI-guided focused ultrasound *Ultrasound Med Biol* **22** 1071–7

Hynynen K, Martin C J, Watmough D J and Mallard J R 1983 Errors in temperature measurementn by thermocouple probes during ultrasound induced hyperthermia *Brit. J. Radiol.* **56** 969-70

Hynynen K, McDannold N, Mulkern R V and Jolesz F A 2000 Temperature monitoring in fat with MRI *Magn Reson Med* **43** 901-4

Ishihara Y, Calderon A, Watanabe H, Okamoto K, Suzuki Y, Kuroda K and Suzuki Y 1995 A precise and fast temperature mapping using water proton chemical shift *Magnetic Resonance in Medicine* **34** 814-23

Islam N, Rabbani K S and Wilson A 2010 The sensitivity of focused electrical impedance measurements *Physiological Measurement* **31** S97-S109

Issels R D, Lindner L H, Verweij J, Wust P, Reichardt P, Schem B C, Abdel-Rahman S, Daugaard S, Salat C, Wendtner C M, Vujaskovic Z, Wessalowski R, Jauch K W, Durr H R, Ploner F, Baur-Melnyk A, Mansmann U, Hiddemann W, Blay J Y and Hohenberger P 2010 Neo-adjuvant chemotherapy alone or with regional hyperthermia for localised high-risk soft-tissue sarcoma: a randomised phase 3 multicentre study *Lancet Oncol* **11** 561-70

Janesick J R 2001 Scientific charge-coupled devices (SPIE Press Book)

Javanaud C and Rahalkar R R 1988 Velocity of Sound in Vegetable Oils *Lipid / Fett* **90** 73-5

Johnson J E, Neuman D G, Maccarini P F, Juang T, Stauffer P R and Turner P 2006 Evaluation of a dual-arm Archimedean spiral array for microwave hyperthermia *Int J Hyperthermia* **22** 475-90

Jolesz F A, Bleier A R, Jakab P, Ruenzel P W, Huttl K and Jako G J 1988 MR imaging of laser-tissue interactions *Radiology* **168** 249-53

Kaipio J P, Kolehmainen V, Somersalo E and Vauhkonen M 2000 Statistical inversion and Monte Carlo sampling methods in electrical impedance tomography *Inverse Problems* **16** 1487

Kallman J S and Berryman J G 1992 Weighted least square criteria for electrical impedance tomography *IEEE Transactions on medical imaging* **11** 284-92

Kampinga H H and Dikomey E 2001 Hyperthermic radiosensitization: mode of action and clinical relevance *Int J Radiat Biol* **77** 399-408

Karayannidou E G, Achilias D S and Sideridou I D 2006 Cure kinetics of epoxy–amine resins used in the restoration of works of art from glass or ceramic *European Polymer Journal* **42** 3311-23

Kerr J F R, Winterford C M and Harmon B V eds 1994 *Morphological criteria for identifying apoptosis* (San Diego, USA: Academic Press)

Knorr C, Meyer T, Janssen T, Goehl J and Hohenberger W 2006 Hyperthermic isolated limb perfusion (HILP) in malignant melanoma. Experience with 101 patients *EJSO* **32** 224-7

Koch C J, Kruuv J, Frey H E and Snyder R A 1973 Plateau Phase in Growth Induced by Hypoxia *International Journal of Radiation Biology* **23** 67-74

Kohn R V and McKenney A 1990 Numerical implementation of a variational method for electrical impedance tomography *Inverse Problems* **6** 389-414

Kohn R V and Vogelius M 1987 Relaxation of a variational method for impedance computed tomography *Communications on Pure and Applied Mathematics* **40** 745-77

Koo H, Oh T I and Woo E J 2007 Calibration of Multi-frequency EIT system. In: *13th International Conference on Electrical Bio-impedance and 8th Conference on Electrical Impedance Tomography*, ed H Scharfetter and R Merwa (Springer Berlin Heidelberg) pp 332-5

Kramer A and Szezesniak A S 1973 *Texture Measurement of Foods: Phychophysical Fundamentals: Sensory, Mechanical and Chemical Procedures, and Their Interrelationships*

Kuroda K 2005 Non-invasive MR thermography using the water proton chemical shift *Int J Hyperthermia* **21** 547 -60

Lagendijk J J W 1982 The influence of bloodflow in large vessels on the temperature distribution in hyperthermia *Physics in Medicine and Biology* **27** 17-23

Lagendijk J J W 2000 Hyperthermia treatment planning *Phys Med Biol* **45** R61-R76

Lee C K, Song C W, Rhee J G, Foy J A and Levitt S H 1995 Clinical experience using 8 MHZ radiofrequency capacitive hyperthermia in combination with radiotherapy: Results of a phase I II study *International journal of radiation oncology, biology, physics* **32** 733-45

Leroy Y, Bocquet B and Mamouni A 1998 Non-invasive microwave radiometry thermometry *Physiol Meas* **19** 127-48

Lewa C J and Majewska Z 1980 Temperature relationships of proton spin-lattice relaxation time T1 in biological tissues *Bull Cancer* **67** 525-30

Li G C and Werb Z 1982 Correlation between sysnthesis of heat shock proteins and development of thermotolerance in Chinese hamster fibrobllasts. *Proc Natl Acad Sci U S A* **79** 3218-22

Lionheart W R B 2004 EIT Reconsruction Algorithms: Pitfalls, Challenges and Recent Developments *Physiol. Meas.* **25** 125-42

Lionheart W R B 1999 Uniqueness, shape and dimension in EIT *Annals New York Acad Sci* **873** 466-71

Lyons B E, Samulski T V and Britt R H 1985 Temperature measurements in high thermal gradients: I. The effects of conduction *Int J Radiat Oncol Biol Phys* **11** 951-62

Ma J, Lowe M J S and Simonetti F 2007 Feasibility study of sludge and blockage detection inside pipes using guided torsional waves *Measurement Science and Technology* **18** 2629-41

Maass-Moreno R and Damianou C A 1996 Noninvasive temperature estimation in tissue via ultrasound echo-shifts. Part I. Analytical model *J Acoust Soc Am* **100** 2514-21

Maass-Moreno R, Damianou C A and Sanghvi N T 1996 Noninvasive temperature estimation in tissue via ultrasound echo-shifts. Part II. In vitro study *J Acoust Soc Am* **100** 2522-30

Marder M, Frisch H L, Langer J S and McConnell H M 1984 Theory of the intermediate rippled phase of phospholipid bilayers *Proc Natl Acad Sci U S A* **81** 6559-61

Marino C and Cividalli A 1992 Combined radiation and hyperthermia: effects of the number of heat fractions and their interval on normal and tumour tissues *Int J Hyperthermia* **8** 771-81

Martin R W, Vaezy S, Proctor A, Myntti T, Lee J B and Crum L A 2003 Water-cooled, high-intensity ultrasound surgical applicators with frequency tracking *IEEE Trans Ultrason Ferroelectr Freq Control.* **50** 1305-17

McClements D and Povey M 1988 Ultrasonic velocity measurements in some liquid triglycerides and vegetable oils *Journal of the American Oil Chemists' Society* **65** 1787-90

McClements D J 1997 Ultrasonic characterization of foods and drinks: Principles, methods, and applications *Critical Reviews in Food Science and Nutrition* **37** 1-46

McEwan A, Cusick G and Holder D S 2007 A review of errors in multi-frequency EIT instrumentation *Physiological Measurement* **28** S197

McRae D A and Esrick M A 1993 Changes in electrical impedance of skeletal muscle measured during hyperthermia *International Journal of Hyperthermia* **9** 247-61

Metherall P, Barber D C, Smallwood R H and Brown B H 1996 Three-dimensional electrical impedance tomography *Nature* **380** 509-12

Miles C A, Fursey G A J and Jones R C D 1985 Ultrasonic estimation of solid/liquid ratios in fats, oils and adipose tissue *J. Sci. Food Agric.* **36**

Miller N R and Bamber J C 2004 Ultrasonic measurement of the temperature distribution due to absorption of diagnostic ultrasound: potential and limitations *Journal of*

Physics: Conference Series, Advanced Metrology for Ultrasound in Medicine **1** 128-33

Miller N R, Bamber J C and Meaney P M 2002 Fundamental limitations of noninvasive temperature imaging by means of ultrasound echo strain estimation *Ultrasound Med Biol.* **28** 1319-33

Miller N R, Bamber J C and ter Haar G R 2004 Imaging of temperature-induced echo strain: preliminary in vitro study to assess feasibility for guiding focused ultrasound surgery *Ultrasound Med Biol.* **30**

Mizushina S, Shimizu T, Suzuki K, Kinomura M, Ohba H and Sugiura T 1993 Retrieval of Temperature-Depth Profiles in Biological Objects from Multi-Frequency Microwave Radiometric Data *Journal of Electromagnetic Waves and Applications* **7** 1515-48

Montreuil J and Nachman M 1991 Multiangle method for temperature measurement of biological tissues by microwave radiometry *Microwave Theory and Techniques, IEEE Transactions on* **39** 1235-9

Moreno-Ramirez D, Cruz-Mrino L D L, Ferrandiz L, Villegas-Portero R and Nieo-Garcia A 2010 Isolated Limb Perfusion for Malignant Melanoma: Systematic Review on Effectiveness and Safety *The Oncologist* **15** 416-27

Morvan D, Leroy-Willig A, Malgouyres A, Cuenod C A, Jehenson P and Syrota A 1993 Simultaneous temperature and regional blood volume measurements in human muscle using an MRI fast diffusion technique *Magn Reson Med* **29** 371-7

Moskowitz M J, Paulsen K D, Ryan T P and Pang D 1994 Temperature field estimation using electrical impedance profiling methods. II. Experimental system description and phantom results *Int J Hyperthermia* **10** 229-45

Moss R W 1996 Serious Consideration of Alternative Ideas *The Cance Chronicles* **7** 34-5

Muller R N, Vander Elst L and Laurent S 2003 Spin transition molecular materials: intelligent contrast agents for magnetic resonance imaging *J Am Chem Soc* **125** 8405-7

Nagy J A, Chang S H, Dvorak A M and Dvorak H F 2009 Why are tumour blood vessels abnormal and why is it important to know[quest] *Br J Cancer* **100** 865-9

Nau W H, Diederich C J and Stauffer P R 2000 Directional power deposition from direct-coupled and catheter-cooled interstitial ultrasound applicators *Int J Hyperthermia* **16** 129-44

Newman D G and Callister R 1999 The non-invasive assessment of stroke volume and cardiac output by impedance cardiography: a review *Aviat Space Environ Med* **70** 780-9

Nielsen O S, Horsman M and Overgaard J 2001 A future for hyperthermia in cancer treatment? *European Journal of Cancer* **37** 1587-9

Ostberg J R, Gellin C, Patel R and Repasky E A 2001 Regulatory potential of fever-range whole body hyperthermia on Langerhans cells and lymphocytes in an antigen-dependent cellular immune response *J Immunol* **167** 2666-70

Ostberg J R and Repasky E A 2000 Comparison of the effects of two different whole body hyperthermia protocols on the distribution of murine leukocyte populations *Int J Hyperthermia* **16** 29-43

Osterman K S, Kerner T E, Williams D B, Hartov A, Poplack S P and Paulsen K D 2000 Multi-frequency electrical impedance imaging: preliminary in vivo experience in breast *Physiol Meas* **21** 99-109

Overgaard J, Gonzalez D G, Hulshof M C C H, Arcangeli G, Dahl O, Mella O and Bentzen S M 1996 Hyperthermia as an adjuvant to radiation therapy of recurrent or metastatic malignant melanoma. A multicentre randomized trial by the European Society for Hyperthermic Oncology *International Journal of Hyperthermia* **12** 3-20

Pakin S K, Hekmatyar S K, Hopewell P, Babsky A and Bansal N 2006 Non-invasive temperature imaging with thulium 1,4,7,10-tetraazacyclododecane-1,4,7,10-tetramethyl-1,4,7,10-tetraacetic acid (TmDOTMA-) *NMR Biomed* **19** 116-24

Parker D L, Smith V, Sheldon P, Crooks L E and Fussell L 1983 Temperature distribution measurements in two-dimensional NMR imaging *Med Phys.* **10** 321-5

Parramon D, Erill I, Guimerà A, Ivorra A, Muñoz A, Sola A, Fondevila C, García-Valdecasas J C and Villa R 2007 In vivo detection of liver steatosis in rats based on impedance spectroscopy *Physiological Measurement* **28** 813

Paulides M M, Bakker J F, Neufeld E, van der Zee J, Jansen P P, Levendag P C and van Rhoon G C 2007 The HYPERcollar: a novel applicator for hyperthermia in the head and neck *Int J Hyperthermia* **23** 567-76

Paulsen K D and Jiang H 1997 An enhanced electrical impedance imaging algorithm for hyperthermia applications *Int J Hyperthermia* **13** 459-80

Paulsen K D, Moskowitz M J and Ryan T P 1994 Temperature field estimation using electrical impedance profiling methods. I. Reconstruction algorithm and simulated results *Int J Hyperthermia* **10** 209-28

Persson H W and Hertz C H 1985 Acoustic impedance matching of medical ultrasound transducers *Ultrasonics* **23** 83-9

Peterson H I ed 1978 *Tumour blood flow compared with normal tissue blood flow* (Boca Raton: CRC Press)

Phinney S, Fisler J, Tang A and Warden C 1994 Liver fatty acid composition correlates with body fat and sex in a multigenic mouse model of obesity *The American Journal of Clinical Nutrition* **60** 61-7

Polydorides N and Lionheart W R B 2002 A Matlab toolkit for three-dimensional electrical impedance tomography: a contribution to the Electrical Impedance and Diffuse Optical Reconstruction Software project *Measurement Science and Technology* **13** 1871-83

Raaphorst G P 1990 Fundamental aspects of hyperthermic biology. In: *An Introduction to the Practical Aspects of Clinical Hyperthermia,* ed S B Field and Hand J W (London: Taylor and Francis) pp 10-54

Rabbani K S and Kabir A M 1991 Studies on the effect of the third dimension on a two-dimensional electrical impedance tomography system *Clin Phys Physiol Meas.* **12** 393-402

Rabbani K S and Karal M A S 2008 A New Four-Electrode Focused Impedance Measurement (FIM) System for Physiological Study *Annals of Biomedical Engineering* **36** 1072-7

Rabbani K S, Sarker M, Akond M H R and Akter T 1999 Focused Impedance Measurement (FIM): A New Technique with Improved Zone Localization *Annals of the New York Academy of Sciences* **873** 408-20

Rieke V and Pauly K B 2008 Echo combination to reduce proton resonance frequency (PRF) thermometry errors from fat *J Magn Reson Imaging* **27** 673-7

Rieke V and Pauly K B 2008 MR thermometry *Journal of magnetic resonance imaging : JMRI* **27** 376-90

Riu P, Rosell J, Lozano A and Pallà-Areny R 1995 Multi-frequency static imaging in electrical impedance tomography: Part 1 instrumentation requirements *Medical and Biological Engineering and Computing* **33** 784-92

Riu P J, Rosell J, Lozano A and Pallas-Areny R 1992 A broadband system for multi-frequency static imaging in electrical impedance tomography *Clinical physics and physiological measurement : an official journal of the Hospital Physicists' Association, Deutsche Gesellschaft fur Medizinische Physik and the European Federation of Organisations for Medical Physics* **13 Suppl A** 61-5

Roemer R B 1999 Engineering aspects of hyperthermia therapy *Annu Rev Biomed Eng* **1** 347-76

Rowland I J, Rivens I, Chen L, Lebozer C H, Collins D J, ter Haar G R and Leach MO, 1997 MRI study of hepatic tumours following high intensity focused ultrasound surgery *British. J. Radiol.* **70** 144-53

Saleh K Y and Smith N B 2005 A 63 element 1.75 dimensional ultrasound phased array for the treatment of benign prostatic hyperplasia *Biomed Eng Online* **4** 39

Salloum M, Ma R and Zhu L 2009 Enhancement in treatment planning for magnetic nanoparticle hyperthermia: optimization of the heat absorption pattern *Int J Hyperthermia* **25** 309-21

Salomir R, de Senneville B D and Moonen C T W 2003 A fast calculation method for magnetic field inhomogeneity due to an arbitrary distribution of bulk susceptibility *Concepts in Magnetic Resonance Part B: Magnetic Resonance Engineering* **19B** 26-34

Samulski T V, Fessenden P, Valdagni R and Kapp D S 1987 Correlations of thermal washout rate, steady state temperatures, and tissue type in deep seated recurrent or metastatic tumours *Int J Radiat Oncol Biol Phys* **13** 907-16

Sanghvi N T, Foster R S, Bihrle R, Casey R, Uchida T, Phillips M H, Syrus J, Zaitsev A V, Marich K W and Fry F J 1999 Noninvasive surgery of prostate tissue by high intensity focused ultrasound: an updated report *Eur J Ultrasound* **9** 19-29

Santosa F and Vogelius M 1990 A backprojection algorithm for electricla impedance imaging *SIAM J. Appl. Math.* **50** 216-43

Schueller G, Stift A, Friedl J, Dubsky P, Bachleitner-Hofmann T, Benkoe T, Jakesz R and Gnant M 2003 Hyperthermia improves cellular immune response to human hepatocellular carcinoma subsequent to co-culture with tumour lysate pulsed dendritic cells *Int J Oncol.* **22** 1397-402

Segal K R, Van Loan M, Fitzgerald P I, Hodgdon J A and Van Itallie T B 1988 Lean body mass estimation by bioelectrical impedance analysis: a four-site cross-validation study *The American Journal of Clinical Nutrition* **47** 7-14

Seip R and Ebbini E S 1995 Noinvasive Estimation of Tissue Temperature Response to Heating Fields Using Diagnostic Ultrasound *IEEE Transactions on Biomedical Engineering* **42** 828-39

Shallof A M and Barber D C 1997 Multi-frequency electrical impedance tomography: tissue characterization and image quality. ed Y Kim (Newport Beach, CA, USA: SPIE) pp 699-707

Shannon R A, Probert-Smith P J, Lines J and Mayia F 2004 Ultrasound velocity measurement to determine lipid content in salmon muscle; the effects of myosepta *Food Research International* **37** 611-20

Shi H, Cao T, Connolly J E, Monnet L, Bennett L, Chapel S, Bagnis C, Mannoni P, Davoust J, Palucka A K and Banchereau J 2006 Hyperthermia Enhances CTL Cross-Priming *The Journal of Immunology* **176** 2134-41

Shibata H R and MacClean L D 1966 Blood flow to tumours *Progess Clin. Cancer* **2** 33-47

Skibba J L, Jones F E and Condon R E 1982 Altered hepatic disposition of doxorubicin in the perfused rat liver at hyperthermic temperatures *Cancer Treat Rep* **66** 1357-63

Skitzki J J, Repasky E A and Evans S S 2009 Hyperthermia as an immunotherapy strategy for cancer *Curr Opin Investig Drugs* **10** 550-8

Smith N B, Merrilees N K, Dahleh M and Hynynen K 2001 Control system for an MRI compatible intracavitary ultrasound array for thermal treatment of prostate disease *Int J Hyperthermia* **17** 271-82

Smith R W M, Freeston I L, Brown B H and Sinton A M 1992 Design of a phase-sensitive detector to maximize signal-to-noise ratio in the presence of Gaussian wideband noise *Measurement Science and Technology* **3** 1054-62

Somersan S, Larsson M, Fonteneau J F, Basu S, Srivastava P and Bhardwaj N 2001 Primary Tumour Tissue Lysates Are Enriched in Heat Shock Proteins and Induce the Maturation of Human Dendritic Cells *The Journal of Immunology* **167** 4844-52

Song C W 1984 Effect of local hyperthermia on blood flow and microenvironment: a review *Cancer Res* **44** 4721s-30s

Song C W, Kang M S, Rhee J G and Levitt S H 1980 The effect of hyperthermia on vascular function, pH, and cell survival *Radiology* **137** 795-803

Song C W, Park H J, Lee C K and Griffin R 2005 Implications of increased tumour blood flow and oxygenation caused by mild temperature hyperthermia in tumour treatment *Int J Hyperthermia* **21** 761-7

Song C W M, Shakil A, Griffin R F and Okajima K 1997 Improvement of tumour oxygenation status by mild temperature hyperthermia alone or in combination with carbogen *Semin Oncol* **24** 626-32

Straube W L and Arthur R M 1994 Theoretical estimation of the temperature dependence of backscattered ultrasonic power for noninvasive thermometry *Ultrasound in medicine & biology* **20** 915-22

Strohbehn J W and Douple E B 1984 Hyperthermia and Cancer Therapy: A Review of Biomedical Engineering Contributions and Challenges *Biomedical Engineering, IEEE Transactions on* **BME-31** 779-87

Sun L, Schiano J and Smith N B 2003 Novel adaptive control system for ultrasound hyperthermia treatment of prostate disease. In: *Ultrasonics, 2003 IEEE Symposium on,* pp 1274-7 Vol.2

Takahashi T, Mitsuhashi N, Sakurai H and Niibe H 1995 Modifications of tumour-associated antigen expression on human lung cancer cells by hyperthermia and cytokine *Anticancer Res.* **15** 2601-6

Takeda T, Fukunaga K, Miyazawa K, Takahashi T, Takeda H, Takeda Y, Tanigawa K, Morisaki T, Yamamoto I and Hasegawa T 2008 [Hyperthermic immuno-cellular therapy-basic and clinical study] *Gan To Kagaku Ryoho* **35** 2244-6

Tamura Y, Tsuboi N, Sato N and Kikuchi K 1993 70 kDa heat shock cognate protein is a transformation-associated antigen and a possible target for the host's anti-tumour immunity *J Immunol.* **151** 5516-24

Tanaka K, Ito A, Kobayashi T, Kawamura T, Shimada S, Matsumoto K, Saida T and Honda H 2005 Intra-tumoural injection of immature dendritic cells enhances anti-tumour effect of hyperthermia using magnetic nanoparticles *Int J Cancer* **116** 624-33

Techavipoo U, Varghese T, Chen Q, Stiles T A, Zagzebski J A and Frank G R 2004 Temperature dependence of ultrasonic propagation speed and attenuation in excised canine liver tissue measured using transmitted and reflected pulses *J Acoust Soc Am* **115** 2859-65

ter Haar G 1999 Therapeutic ultrasound *European Journal of Ultrasound* **9** 3-9

ter Haar G 2007 Therapeutic applications of ultrasound *Progress in biophysics and molecular biology* **93** 111-29

ter Haar G, Sinnett D and Rivens I 1989 High intensity focused ultrasound– a surgical technique for the treatment of discrete liver tumours *Physics in Medicine and Biology* **34** 1743

Thomlinson R H and Gray L H 1955 The Histological Structure of Some Human Lung Cancers and the Possible Implications for Radiotherapy *Br J Cancer* **9** 539-49

Thorne A, Lofgren P and Hoffstedt J 2010 Increased visceral adipocyte lipolysis– a pathogenic role in nonalcoholic fatty liver disease? *J Clin Endocrinol Metab* **95** 21

Todryk S M, Melcher A A, Dalgleish A G and Vile R G 2000 Heat shock proteins refine the danger theory *Immunology* **9** 334-7

Togawa T 1985 Body temperature measurement *Clin Phys Physiol Meas* **6** 83-108

Tseng H Y, Lee G B, Lee C Y, Shih Y H and Lin X Z 2009 Localised heating of tumours utilising injectable magnetic nanoparticles for hyperthermia cancer therapy *IET Nanobiotechnol* **3** 46-54

Valdagni R and Amichetti M 1994 Report of long-term follow-up in a randomized trial comparing radiation therapy and radiation therapy plus hyperthermia to metastatic lymph nodes in stage IV head and neck patients *Int J Radiat Oncol Biol Phys* **28** 163-9

van den Berg A P, Wike-Hooley J L, van den Berg-Block A F, van der Zee J and Reinhold H S 1982 Tumour pH in human mammary carcinoma *European Journal of Cancer and Clinical Oncology* **18** 457-62

van der Zee J 2002 Heating the patient: a promising approach? *Annals of Oncology* **13** 1173-84

van der Zee J, Gonzalez Gonzalez D, van Rhoon G C, van Dijk J D, van Putten W L and Hart A A 2000 Comparison of radiotherapy alone with radiotherapy plus hyperthermia in locally advanced pelvic tumours: a prospective, randomised, multicentre trial. Dutch Deep Hyperthermia Group *Lancet* **355** 1119-25

van der Zee J, van der Holt B, Rietveld P J, Helle P A, Wijnmaalen A J, van Putten W L and van Rhoon G C 1999 Reirradiation combined with hyperthermia in recurrent breast cancer results in a worthwhile local palliation *Br J Cancer* **79** 483-90

Van Leeuwen G M, Kotte A N, Raaymakers B W and Lagendijk J J 2000 Temperature simulations in tissue with a realistic computer generated vessel network *Phys Med Biol* **45** 1035-49

Vauhkonen M, Karjalainen P A and Kaipio J P 1998 A Kalman filter approach to track fast impedance changes in electrical impedance tomography *Biomedical Engineering, IEEE Transactions on* **45** 486-93

Vauhkonen P J, Vauhkonen M and Kaipio J P 2001 Fixed-lag smoothing and state estimation in dynamic electrical impedance tomography *International Journal for Numerical Methods in Engineering* **50** 2195-209

Vaupel P, Kallinowski F and Okunieff P 1989 Blood flow, oxygen and nutrient supply, and metabolic microenvironment of human tumours: a review *Cancer Res* **49** 6449-65

Vaupel P W and Kelleher D K 1990 *Thermoradiotherapy and thermochemotherapy* ed J-C Bolomey

Vaupel P W and Keller D K eds 1995 *Metabolic status and reaction to heat of normal and tumour tissue.* vol 2 (Berlin Sringer Verlog)

Vernon C C, Hand J W, Field S B, Machin D, Whaley J B, van der Zee J, van Putten W L, van Rhoon G C, van Dijk J D, Gonzalez Gonzalez D, Liu F F, Goodman P and Sherar M 1996 Radiotherapy with or without hyperthermia in the treatment of superficial localized breast cancer: results from five randomized controlled trials. International Collaborative Hyperthermia Group *International journal of radiation oncology, biology, physics* **35** 731-44

Verwaal V J, van Ruth S, de Bree E, van Slooten G W, van Tinteren H, Boot H and Zoetmulder F A N 2003 Randomized Trial of Cytoreduction and Hyperthermic Intraperitoneal Chemotherapy Versus Systemic Chemotherapy and Palliative Surgery in Patients With Peritoneal Carcinomatosis of Colorectal Cancer *Journal of Clinical Oncology* **21** 3737-43

Waterman F M 1985 The response of thermometer probes inserted into catheter *Med. Phys.* **12** 368-72

Waterman F M, Nerlinger R E and Leeper J B 1990 Catheter induced temperature artifacts in ultrasound hyperthermia *Int J Hyperthermia* **6** 371-81

Weidensteiner C, Quesson B, Caire-Gana B, Kerioui N, Rullier A, Trillaud H and Moonen C T 2003 Real-time MR temperature mapping of rabbit liver in vivo during thermal ablation *Magn Reson Med.* **50** 322-30

Welz S, Hehr T, Lamprecht U, Scheithauer H, Budach W and Bamberg M 2005 Thermoradiotherapy of the chest wall in locally advanced or recurrent breast cancer with marginal resection *International Journal of Hyperthermia* **21** 159-67

Weng L, Reid J M, Shankar P M, Soetanto K and Lu X M 1992 Nonuniform phase distribution in ultrasound speckle analysis. I. Background and experimental demonstration *IEEE Trans Ultrason Ferroelectr Freq Control* **39** 352-9

Wexler A, Fry B and Neuman M R 1985 Impedance-computed tomography algorithm and system *Appl. Opt.* **24** 3985-92

Wickersheim A K and Mei H S 1987 Fiber optic thermometry and its application *J Microwave Power* 84-94

Wilson A J, Milnes P, Waterworth A R, Smallwood R H and Brown B H 2001 Mk3.5: A modular, multi-frequency successor to the Mk3a EIT/EIS System *Physiol. Meas.* **22** 49-54

Witkamp A J, de Bree E, Kaag M M, Boot H, Beijnen J H, van Slooten G W, van Coevorden F and Zoetmulder F A N 2001 Extensive cytoreductive surgery followed by intra-operative hyperthermic intraperitoneal chemotherapy with mitomycin-C in patients with peritoneal carcinomatosis of colorectal origin *European Journal of Cancer* **37** 979-84

Wlodarczyk W, Boroschewski R, Hentschel M, Wust P, Monich G and Felix R 1998 Three-dimensional monitoring of small temperature changes for therapeutic hyperthermia using MR *J Magn Reson Imaging* **8** 165-74

Wlodarczyk W, Hentschel M, Wust P, Noeske R, Hosten N, Rinneberg H and Felix R 1999 Comparison of four magnetic resonance methods for mapping small temperature changes *Phys Med Biol* **44** 607-24

Woessner D E, Zhang S, Merritt M E and Sherry A D 2005 Numerical solution of the Bloch equations provides insights into the optimum design of PARACEST agents for MRI *Magn Reson Med* **53** 790-9

Wojcik G, DeSilets C, Nikodym L, Vaughan D, Abboud N and Mould J, Jr. 1996 Computer modeling of diced matching layers. In: *Ultrasonics Symposium, 1996. Proceedings., 1996 IEEE,* pp 1503-8 vol.2

Wolf P 2008 *Innovations in Biological Cancer Therapy*: NaturaSanitas

Woo E J, Hua P, Webster J G and Tompkins W J 1993 A robust image reconstruction algorithm and its parallel implementation in electrical impedance tomography *IEEE Trans Med Imaging* **12** 137-46

Wu F, Chen W Z, Bai J, Zou J Z, Wang Z L, Zhu H and Wang Z B 2001 Pathological changes in human malignant carcinoma treated with high-intensity focused ultrasound *Ultrasound Med Biol* **27** 1099-106

Wu F, Chen W Z, Bai J, Zou J Z, Wang Z L, Zhu H and Wang Z B 2002 Tumour vessel destruction resulting from high-intensity focused ultrasound in patients with solid malignancies *Ultrasound Med Biol* **28** 535-42

Wust P, Cho C H, Hildebrandt B and Gellermann J 2006a Thermal monitoring: Invasive, minimal-invasive and non-invasive approaches *International Journal of Hyperthermia* **22** 255-62

Wust P, Gneveckow U, Johannsen M, Bohmer D, Henkel T, Kahmann F, Sehouli J, Felix R, Ricke J and Jordan A 2006b Magnetic nanoparticles for interstitial thermotherapy--feasibility, tolerance and achieved temperatures *Int J Hyperthermia* **22** 673-85

Wust P, Hildebradnt B, Sreenivasa G, Rau B, Gellermann J, Riess H, Felix F and Schlag P M 2002 Hyperthermia in combined treatmetn of cancer *The Lancet Oncology* **3** 487-97

Wust P, Stahl H, Löffel J, Seebass M, Riess H and Felix R 1995 Clinical, physiological and anatomical determinants for radiofrequency hyperthermia *International Journal of Hyperthermia* **11** 151-67

Wyatt C R 2010 Developement of MR Thermometry Strategies for Hyperthermia of Extremity and Breast Tumours *Doctoral Thesis, Department of Biomedical Engineering, Duke University*

Yonezawa M, Otsuka T, Kato T, Moriyama A, Kato K H, Asai K and Matsui N 2002 Hyperthermic induction of apoptosis in malignant fibrous histiocytoma cells: possible involvement of a p53-independent pathway in the induction of bax gene *Journal of Orthopaedic Science* **7** 117-22

Yuhua P, Honghong D and Xiaoying T 2010 Noninvasive temperature measurement using MRI based on T2 relaxation time. In: *Bioinformatics and Biomedical Engineering (iCBBE), 2010 4th International Conference on,* pp 1-3

Zanker K S and Lange J 1982 Whole body hyperthermia and natural killer cell activity *Lancet* **1** 1079-80

Zhang Y, Qu M, Webster J G, Tompkins W J, Ward B A and Bassett D R 1986 Cardiac Output Monitoring by Impedance Cardiography During Treadmill Exercise *Biomedical Engineering, IEEE Transactions on* **BME-33** 1037-42